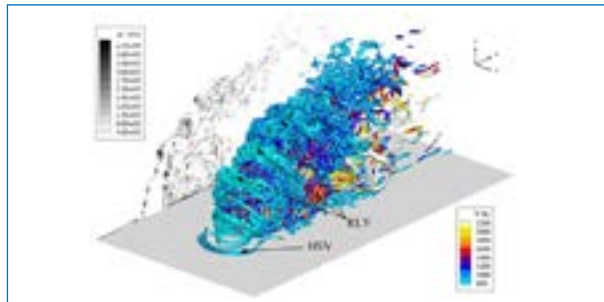
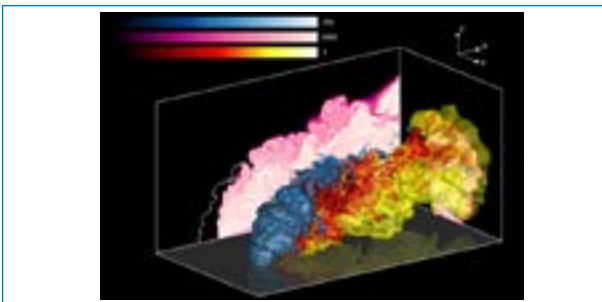
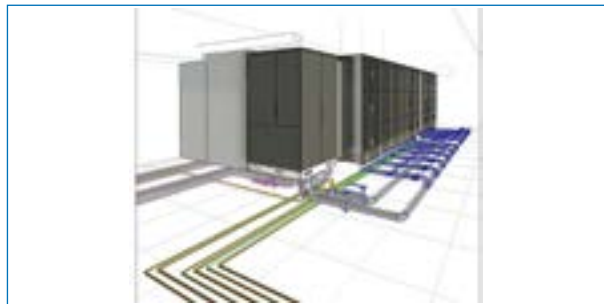
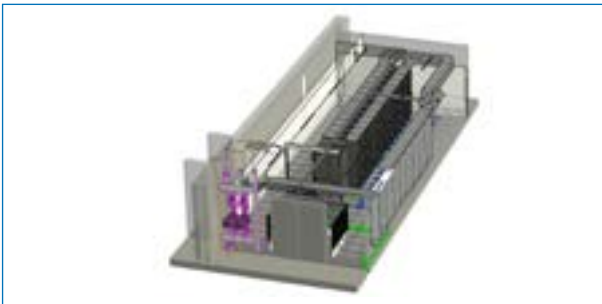
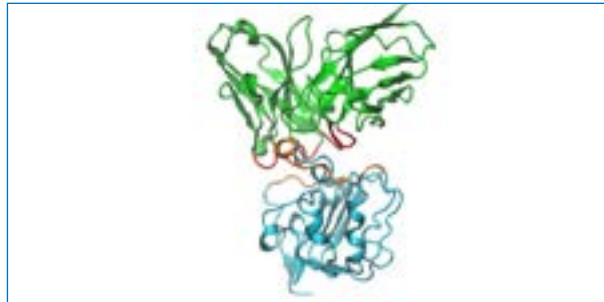
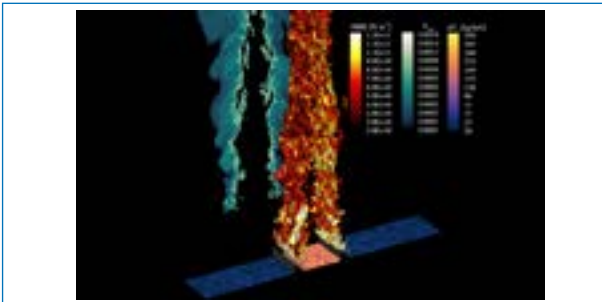


High Performance Computing on CRESCO infrastructure: research activities and results 2023





ITALIAN NATIONAL AGENCY FOR
NEW TECHNOLOGIES, ENERGY AND
SUSTAINABLE ECONOMIC DEVELOPMENT

High Performance Computing on CRESCO Infrastructure: research activity and results 2023

December 2024

High Performance Computing on CRESCO Infrastructure: research activity and results 2023

Contributions provided by a selection of users of the CRESCO infrastructure

Scientific Editor: Beatrice Calosso, ENEA, TERIN-ICT-HPC e

Luigi Bucci, ENEA, TERIN-ICT-HPC

Cover: Amedeo Trolese, ENEA, TERIN-ICT, CR Frascati

ISBN: 978-88-8286-494-1

Figure captions on the cover CrescoReport 2023

First on the left. *Volume rendering of the isosurface at $c=0.76$ coloured with the HRR, NO slice at $z=0$, and momentum fluctuations slices at the slot inlet. Instantaneous taken at $t=0.0052$ s from the start of the simulation.*

First on the right. *Structural representation of the mAb:Ag complex. Upper (green) the monoclonal antibody (mAb). Lower (cyan) the antigen (Ag). The interacting residues are coloured in red (mAb) and orange (Ag).*

Second on the left. *Structural representation of the mAb:Ag complex. Upper (green) the monoclonal antibody (mAb). Lower (cyan) the antigen (Ag). The interacting residues are coloured in red (mAb) and orange (Ag).*

Second on the right. *Cresco8, rack layout*

Third on the left. *Volume rendering of temperature and NH₃ mass fraction, and HRR slices at $z = 0$ and $x = 7d$.*

Third on the right. *Visualization of instantaneous iso-surface of the Q-criterion coloured by the local value of temperature, and vorticity magnitude projected from the mid-plane at $z = 0$. The snapshot refers to $t = 0.00646$ s from the start of the simulation.*

INDEX

Forward	5
New HPC ENEA CRESCO Deployment	7
Francesco Iannone and <i>CRESCO team</i>	7
Integrating Enterprise 4.0 Knowledge in Generative Artificial Intelligence: from Bag-of-words to Multilingual Large Language Models	19
Daniela Alderuccio, Rossana Cotroneo	19
Optimization for Efficient and Accurate Radiative Transfer Modelling.....	23
Livio Bernardini, Paolo Scaccia, and Paolo Antonelli	23
Evaluation of the capabilities of the AMS-MINNI system to simulate air quality in Italy during the calendar year 2019.....	29
Gino Briganti, Andrea Bolignano, Andrea Cappelletti, Ilaria D’Elia, Massimo D’Isidoro, Mihaela Mircea, Antonio Piersanti, Felicita Russo, Maria Gabriella Villani, Lina Vitali	29
A Robust Statistical Process Monitoring Framework	35
Christian Capezza, Fabio Centofanti, Antonio Lepore, Biagio Palumbo	35
High Pressure Direct Numerical Simulation of Turbulent Premixed NH ₃ /H ₂ /N ₂ – Air Slot Flame at High Equivalence Ratio	41
Donato Cecere, Matteo Cimini, Simone Carpenella and Eugenio Giacomazzi	41
Extreme Mediterranean cyclones in an atmosphere-only vs an ocean-coupled regional model	45
Marco Chericoni, Alessandro Anav, Giorgia Fosser and Gianmaria Sannino	45
Steered Molecular Dynamics Simulations for Antibody-Drug Conjugate Candidate Discovery .	49
Valerio Chiarini, Sara Marchio, Simone Giusepponi, Paolo Roberto Saraceni, Caterina Arcangeli, Giuseppe Roscilli and Mariateresa Mancuso	49
High Fidelity Numerical Simulations of Ammonia-Hydrogen-Nitrogen Jet in Cross Flow	55
Matteo Cimini, Donato Cecere, Simone Carpenella and Eugenio Giacomazzi	55
Ab initio study of the surface stability of Ni-rich oxides.....	59
Andrea Cioffi, Valeria Sperati, Mariarosaria Tuccillo, Priscilla Reale, Sergio Brutti	59
Product and manufacturing process optimization using advanced calculation models on hpc and cloud platforms	63
Leonardo Cosma, Antonio Gerardi, Annalisa Cassinelli, Rosario Dotoli and Alberto Scalise .	63
Scale-resolving simulations of the flow field developing around circular cylinders in tandem configuration for far-field aeroacoustic prediction	69
Valerio D’Alessandro and Matteo Falone	69
Preliminary CFD simulation results of the NACIE-UP wire wrapped pin bundle for the IAEA NACIE-CRP	75
Roberto Da Vià, Francesco Lodi, Giacomo Grasso	75

Simulating 3D chromosome structure through Polymer Physics and High-Performance Computing	79
Florinda Di Pierno, Alex Abraham, Sougata Goha, Francesca Vercellone, Andrea Fontana, Simona Bianco, Andrea Maria Chiariello, Mattia Conte and Andrea Esposito	79
Nuclear Analyses for Equatorial Port 12 in ITER	89
Davide Flammini, Andrea Colangeli, Nicola Fonnesu, Michele Lungaroni, Fabio Moro, Simone Noce, Alberto Previti, Rosaria Villari.....	89
Preliminary studies on DTT TOKAMAK with hymagyc and the Hamiltonian mapping technique... 93	
V. Fusco, S. Briguglio, G. Vlad, C. Di Troia, G. Fogaccia, X. Wang.....	93
Classical Molecular Dynamics Simulations Of A Pm 0.1 Model And Its Interaction With Raft-Like And Non-Raft-Like Biological Membranes.....	97
Sara Giordan ¹ , Federico Iacovelli, Alice Romeo, Davide Pietrafesa, Mattia Falconi, Barbara Benassi and Caterina Arcangeli.....	97
High-fidelity numerical simulations of reacting flows	103
Davide Laera, Francesco Gabriele Schiavone, Raffaele Intranuovo, Christophe Vankelekom, Sergio Mario Camporeale, and Marco Torresi.....	103
Non-covalent binding of Nirmatrelvir to the SARS-CoV-2 main protease	107
Marina Macchiagodena, Marco Pagliai, Piero Procacci	107
First-Principles Metadynamics Simulations of PEO/(101)-TiO ₂ Anatase Interfaces	115
Arianna Massaro, Francesca Fasulo, Ana B. Muñoz-García and Michele Pavone	115
Nuclear analyses in support of ITER ex-port Radial Neutron Camera design.....	119
Fabio Moro, Daniele Marocco, Francesco Belli, Dariusz Bocian, Giorgio Brolatti, Silvia Cesaroni, Andrea Colangeli, Davide Flammini, Nicola Fonnesu, Davide Falco, Giada Gandolfo, Ryszard Kantor, Jerzy Kotula, Domenico Marzullo, Simone Noce, Enrico Occhiuto, Rafal Ortwein, Alberto Previti, Dustin Sancristóbal, Rosaria Villari and Basilio Esposito	119
SASE X-ray Free-Electron Laser driven by Resonant Multi-Pulse Ionization acceleration scheme	123
Federico Nguyen, Paolo Tomassini, Leonida A. Gizzi, Luca Giannessi and Anna Giribono... 123	
Natural Antioxidants as potential inhibitors of proteases from SARS-CoV-2	127
Carla Orlando , Giada Ciardullo , Mario Prejanò , Nino Russo and Tiziana Marino.....	127
First-principles insights on solid-state phase transitions in P2-na _x mno ₂ -based high energy cathode	133
Michele Pavone, Aniello Langella, Arianna Massaro and Ana B. Muñoz-García	133
Hexagonal NaCl atom-thin layer structuring on methylammonium lead iodide perovskite: a first-principles investigation.....	137
Adriana Pecoraro, Ana Belén Muñoz-García, Gennaro Vincenzo Sannino, Paola Delli Veneri and Michele Pavone.....	137
Neutronic Model to Find Promising Candidates As Burnable Poisons in Fast Reactors	141
Roberto Pergreffi, Francesco Lodi, Giacomo Grasso.....	141

Development of a multiphase MHD openFOAM solver for fusion reactor analysis	145
Sonia Pignatiello, Lorenzo Melchiorri, Simone Siriano and Alessandro Tassone	145
Modelling the potential interaction between airborne particulate matter and the SARS-CoV-2 Spike protein	149
Alice Romeo, Roberto Pellegrini, Maurizio Gualtieri, Barbara Benassi, Massimo Santoro, Federico Iacovelli, Milena Stracquadanio, Mattia Falconi, Carmela Marino, Gabriele Zanini, Caterina Arcangeli	149
Multipartite Entanglement and Quantum Frustration: Simulation and Applications	155
Paolo Scarafile, Angelo Mariano, Saverio Pascazio	155
Monte Carlo Simulation for Reactor Calculations to Medical Terbium-161 production	161
Lucrezia Spagnuolo, Luigi Lepore, Giada Gandolfo, Marco Capogni	161
Accurate calculations of the exchange interactions in molecular qubits and organic radicals in the bulk phase and in the presence of an electric field	167
Federico Totti, Prem Prakash Sahu, and Maksim Arsentev	167
Atomistic simulations of quantum dots and other nanocrystals.....	171
Juliette Zito, Iyyappa R. Panneerselvam, Roberta Pascazio, and Gabriele Saleh	171

FORWARD

During the year 2023, the CRESCO high performance computing clusters have provided 120 million hours of “core” computing time, at a high availability rate, to about 200 users, supporting ENEA research and development activities in many relevant scientific and technological domains. In the framework of joint programs with ENEA researchers and technologists, computational services have been provided also to academic and industrial communities. The slight decrease in computing power delivered in 2023 compared to 2022 confirming the negative trend, highlights the aging of the current CRESCO HPC systems and the need for a technological upgrade.

This report, the fifteenth of a series started in 2008, is a collection of 31 papers illustrating the main results obtained during 2023 using the CRESCO/ENEAGRID HPC facilities. The significant number of contributions proves the importance of the HPC facilities in ENEA for the research community. The topics cover various fields of research, such as materials science, efficient combustion, climate research, nuclear technology, plasma physics, biotechnology, aerospace, complex systems physics, geophysical flow, renewable energies, environmental issues, HPC technology and quantum computing. The report shows the wide spectrum of applications of high-performance computing, which has become an all-round enabling technology for science and engineering.

Since 2008, the main ENEA computational resources are located near Naples, in Portici Research Centre. This is a result of the CRESCO Project (Computational Centre for Research on Complex Systems), co-funded, in the framework of the 2001-2006 PON (European Regional Development Funds Program), by the Italian Ministry of Education, University and Research (MIUR).

The CRESCO Project provided the financial resources to set up the first HPC x86_64 Linux cluster in ENEA; a major computing installation for both the Italian and the International context: it ranked 126 in the HPC Top 500 June 2008 world list, with 17.1 Tflops and 2504 cpu cores. It was later decided to keep CRESCO as the name for all the Linux clusters in the ENEAGRID infrastructure, which integrates all ENEA scientific computing systems, and is currently distributed in six Italian sites.

CRESCO computing resources were later upgraded in the framework of PON 2007-2013 with the project TEDAT and the cluster CRESCO4, 100 Tflops computing power. In 2020 the ENEAGRID computational resources consist of ~25000 computing cores and a raw data storage of about 5 PB.

In 2015 ENEA and CINECA, the main HPC institution in Italy, signed a collaboration agreement to promote joint activities and projects in HPC. In this framework, CINECA and ENEA are providing HPC services for the nuclear fusion researcher community until 2023. In this framework, the new system MARCONI-FUSION started the operations in July 2016 with 1 Pflops computation power and they have been extend until 2029 with PITAGORA that has a power peak of 14 PFlops of conventional processors AMD Turin and 20 PFlops of accelerated GPU NVIDIA H100. The extension of the HPC services for EUROfusion has allowed to deploy new HPC systems in Portici: CRESCO7 and in Frascati: XCRESCO, described in this report

The ENEA-CINECA agreement was the key basis for ENEA HPC developments in the past. The CRESCO6 cluster has been installed in 2018 and its own 1.4 PFlops peak computing power, ranked 420th in November 2018 Top500 list. CRESCO6 has been a challenge in HPC co-design system thanks to implement a multi-fabric network able for working Infiniband and Omni-Path on a single GPFS cluster using the same storage systems of CRESCO data centre. New project opportunities in 2024 have allowed to scale the ENEA HPC tier0 with the deployment of CRESCO8 in Portici.

The success and the quality of the results produced by CRESCO stress the role that HPC facilities can play in supporting science and technology for all ENEA activities, national and international collaborations, and the ongoing renewal of the infrastructure provides the basis for an upkeep of this role in the forthcoming years.

*Dipartimento Tecnologie Energetiche e Fonti Rinnovabili,
Divisione per lo Sviluppo di Sistemi per l'Informatica e l'ICT - CRESCO Team*

NEW HPC ENEA CRESCO DEPLOYMENT

Francesco Iannone* and *CRESCO team*:

L.Acampora, D.Alderuccio, F.Adagna, F.Ambrosino, G.Baldassarre, T.Bastianelli, F.Bianchi, G.Bracco, L.Bucci, F.Buonocore, M.Caiazzo, B.Calosso, G.Cannataro, M.Caporicci, G.Carretto, M.Casa, G.Cascone, M.Catillo, M.Celino, M.Chinnici, R.Clemente, D. De Chiara, M.De Rosa, D.Di Mattia, S.D’Onofrio, M.Faltelli, S. Ferlito, G.Ferro, M.Fois, M.Fratarcangeli, A.Funel, F.Genovesi, S.Giusepponi, G.Guarnieri, M.Gusso, W.Lusani, M.Marano, S.Marchio, A.Mariano, M.Mongelli, P.Palazzari, F.Palombi, S.Pecoraro, S.Pierattini, G.Ponti, E.Rossi, G.Santomauro, A.Scalise, F.Simoni, M.Steffè

*Energy Technologies & Renewable Sources Department - Information Communication Technologies,
Lungotevere Thaon di Revel, 76, 00196 Rome Italy*

* Corresponding author. E-mail: francesco.iannone@enea.it

ABSTRACT. This report presents the deployment of new High-Performance Computing (HPC) clusters at ENEA Cresco, featuring a 100 Gbps Infiniband fabric and a modernized software stack. The operating environment has been upgraded to AlmaLinux 9, ensuring a robust and stable foundation for computational workloads. Resource management and job scheduling are handled by the Slurm workload manager replacing IBM Spectrum LSF suite, which has been finely tuned to optimize the performance of the new infrastructure. In addition to the primary cluster, a heterogeneous architecture cluster has also been integrated into the HPC ecosystem. This cluster leverages Nvidia V100 GPUs alongside IBM Power9 CPUs, providing a specialized platform for GPU-accelerated workloads and applications that benefit from heterogeneous computing environments. These advancements significantly enhance the computational capabilities of ENEA Cresco, enabling more efficient and scalable solutions for scientific and industrial applications. Furthermore, these operative environments, deployed on these HPC systems, shall facilitate the transition to the new ENEA TIER-0 Cresco8 system, scheduled for deploying in 2024, ensuring a seamless upgrade in computational power and resources.

1 Introduction

The Cresco project [1],[2] launched in 2008, marked the beginning of ENEA's journey into High-Performance Computing (HPC) systems, utilizing an architecture based on multicore and multiprocessor nodes connected by low-latency, high-bandwidth networks. This architectural approach has been consistently maintained across various stages of scaling ENEA's HPC systems, with advancements closely aligned with the evolution of CPU technology. As a result of this strategic growth, a robust user community, both within ENEA and externally, has steadily expanded, leading to a significant increase in the demand for computing time. Figure 1(a) illustrates the growth in millions of core-hours over approximately a decade, beginning in 2008 with the first HPC systems, Cresco1-2, which delivered a peak performance of 25 Tflops. This was followed by the installation of Cresco4 in 2015, achieving a peak power of 100 Tflops, and later, Cresco6, which reached a peak of 1.4 Pflops in 2018. In Figure 1(b), the same upward trend is shown for Cresco usage, divided between internal ENEA

users and external users. By 2023, the utilization of Cresco HPC systems reached around 122 million core-hours, equivalent to approximately €1.5 million when compared to the cost of running a similar node configuration on Amazon Web Services Ec2 instance.

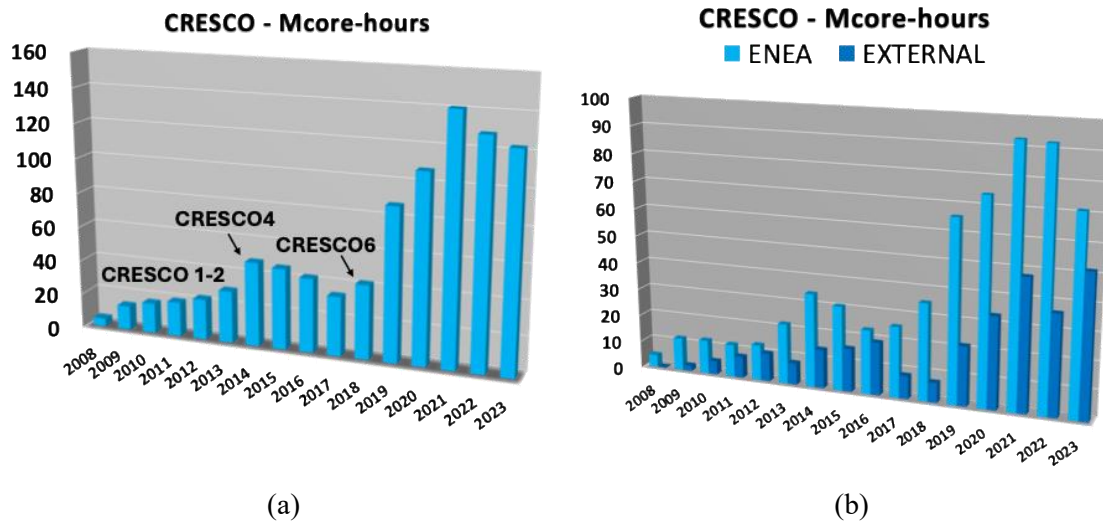


Fig.1: (a) CRESCO usage since 2008; (b) CRESCO usage since 2008 break down in ENEA internal and External Users.

To complete the statistics of the Cresco6 operations in 2023, the figure 2(a) shows the availabilities of TIER0 Cresco6 in 2020 and in 2023 respectively 97.7 and 88.3 % as annual mean, whilst the figure 2(b) shows the wait main time of the jobs in the TIER0 Cresco6 queues respectively in 2020 and 2023.

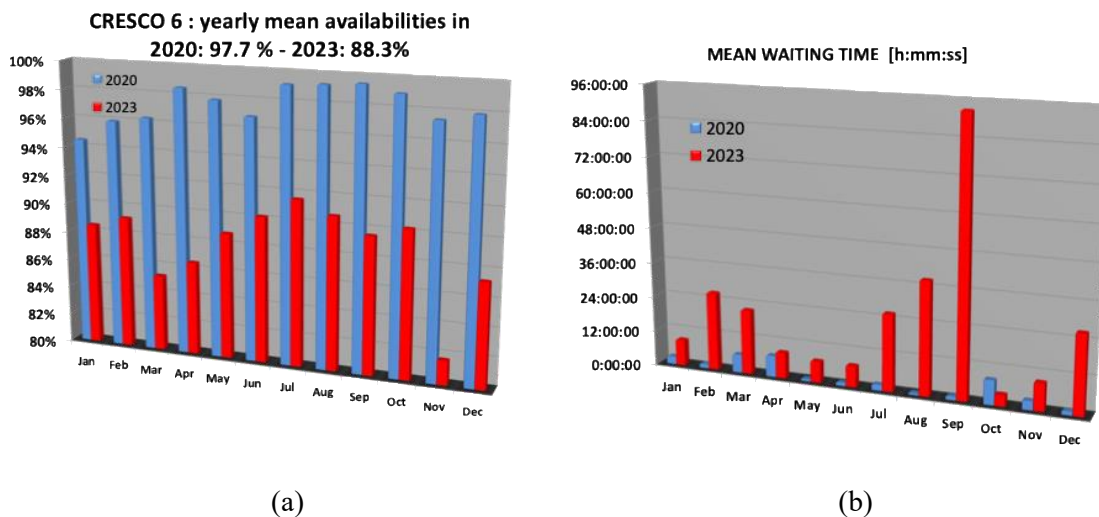


Fig.2: (a) CRESCO6 availability in 2020 and 2023; (b) CRESCO6 mean waiting time in the queues in 2020 and 2023.

The Fig. 2(a) illustrates the monthly mean availability of the TIER0 Cresco6 HPC cluster over a three-year period, comparing data from 2020 and 2023. The metric of interest is the percentage of time the HPC system was operational and available for computational tasks. In 2020, the availability was notably high, maintaining an operational status for approximately 98% as yearly mean. This high level of availability reflects the system's relative newness, with minimal hardware-related failures and

downtime. Routine maintenance and software updates were the primary causes of any observed interruptions.

By 2023, however, a marked decline in availability is evident, with the system operational for only 88% as yearly mean. This reduction can be attributed to the aging hardware, which has increasingly led to unplanned outages due to component failures, decreased system efficiency, and longer repair times. As infrastructure ages, the risk of hardware degradation and failure increases, contributing to extended downtimes and reduced reliability. Additionally, the increasing complexity of managing aging systems may have further compounded this decrease in availability. The data underscores the critical impact that hardware aging can have on the reliability and performance of HPC infrastructures, emphasizing the need for timely upgrades and maintenance strategies to mitigate availability loss over time.

The Fig.2(b) presents the monthly average queue waiting times in the Cresco6 HPC cluster for the years 2020 and 2023. The data reveals a significant increase in the waiting times over this three-year period, pointing to changes in system usage and resource availability. In 2020, the average waiting times in the queue remained relatively low, with most months recording monthly mean waiting times under 3 hours. This reflects a balanced system load, where computational demand was well-aligned with available resources. The system's hardware was still operating efficiently, and maintenance was adequately managed, ensuring optimal performance and minimal delays. However, by 2023, a clear upward trend in queues waiting times is observed, with averages reaching as high 24 hours in some months. This substantial increase is attributed to two primary factors. First, there was a notable rise in computational workload, driven by increased demand from users, which exceeded the system's capacity to efficiently distribute jobs. Second, the reduced availability of computational resources due to aging hardware significantly impacted the system's performance. The degradation of hardware components, coupled with the absence of a proper maintenance service, led to more frequent downtimes and slower recovery times, further exacerbating the backlog of queued jobs. This combination of higher demand and lower resource availability illustrates the critical challenges faced by HPC infrastructures as they age, especially when maintenance is not adequately sustained. The graph highlights the importance of both capacity planning and timely hardware upgrades to ensure the continued efficiency of HPC resources.

In 2023, two new HPC clusters were successfully installed in ENEA's data centers as part of the organization's ongoing efforts to enhance computational resources for scientific research and technological development.

Both these new cluster have been configured with a new software stack, designed to ensure for users a transition seamlessly to the new HPC clusters. This software environment is tailored to help users gradually adapt to the new operative conditions of ENEA's upcoming TIER-0 supercomputer, Cresco8, which is scheduled for deploy at the end of 2024. The new stack will facilitate compatibility and minimize disruption, allowing users to fully leverage the advanced capabilities of these cutting-edge systems as they prepare for the Cresco8 deployment.

2 New HPC clusters deployed

The first new cluster Cresco7, has been deployed in the Portici data center. It is based on the same node architecture as its predecessor, Cresco6, but with the significant addition of Infiniband fabric, which provides a high-speed, low-latency interconnect, thereby improving the system's performance and scalability in parallel computing tasks. The second new cluster Xcresco, was installed at the Frascati data center. Xcresco features a heterogeneous architecture that combines IBM Power9 CPUs with Nvidia V100 GPUs, designed to handle a wide range of computational workloads, including those that require both traditional CPU power and advanced GPU acceleration for artificial intelligence and machine learning applications

CRESCO7 configuration

Cresco7 is built upon the same compute node architecture as its predecessor, Cresco6, utilizing x86-64 processors from the Intel Xeon Sky-Lake series, known for their balance of core density, energy efficiency, and memory bandwidth. These processors are well-suited for a variety of parallel workloads and have extensive support for vectorized instructions (Avx-512). Each compute node in the Cresco7 cluster consists of dual-socket motherboards, housing two Intel Xeon Platinum 8160 @2.10GHz processors per node and 144 compute nodes hosted in 3 racks (Fig.3).



Fig.3 CRESCO7 cluster

The compute nodes feature up to 48 CPU cores per node, allowing highly parallelizable tasks to be efficiently distributed across a large number of compute cores. Each computing node is configured with 192 GB of DDR4 RAM per node. The memory bandwidth is optimized to support high-throughput workloads, such as large-scale simulations and data-intensive operations. One of the major enhancements in Cresco7 over its predecessor is the adoption of an Infiniband EDR (Enhanced Data Rate) interconnect fabric capable of achieving data transfer speeds up to 100 Gbps, Infiniband EDR delivers low-latency, high-bandwidth communication among the 144 compute nodes. A fat-tree topology on two levels with a 2.4:1 no-blocking is implemented to minimize communication bottlenecks, providing non-blocking bandwidth between critical node groups. The cluster leverages a High-performance Parallel Storage system (HPS), providing a shared, scalable storage environment with high throughput. The HPS is based on DDN ES400NVX-R-HDR100 appliance EXAScaler 400NVX with 24x NVMe drive slots, SAS expansion ports, 8 host ports HDR100 IB / 100GbE, integrated ExaScaler parallel file system (Lustre) and integrated MDS and OSS. The total raw capacity is 1 PB and a bandwidth aggregate of 10 GiB/s in read/write mode. The peak electric power is about 50 kW and the cooling system is composed of 2 CRAC unit Vertiv PIO062DD with cooling capacity of 73 kW and 1 CRAC unit Vertiv PX054DD with cooling capacity of 55 kW, hosted in CED2 hall of Cresco Data Center.

The software stack is completely open source. It operates on AlmaLinux 9.2[3]: a redhat-like distribution popular in HPC ecosystems for its stability and extensive support in scientific and enterprise use cases.

Cresco7 is totally integrated in EneaGrid [4] software stack with OpenAFS v.18.1[5] and Kerberos V5 MIT 1.15.1[6]. The parallel filesystem is Lustre v.2.14.0[7]. Cresco7 The cluster uses Slurm (Simple Linux Utility for Resource Management) v.23.11.5[8], a job scheduler for resource allocation and workload management that replaces LSF used on the previous HPC clusters. Slurm handles job queuing, resource reservation, and fair share scheduling, allowing efficient distribution of computational

resources across users and projects. As Slurm doesn't support Kerberos, in order to integrate it, the capabilities of the Slurm Plug-in Architecture for Node and job Control (Spank) has been used on Cresco7 cluster. Spank provides a very generic interface for stackable plug-ins which may be used to dynamically modify the job launch code in Slurm. Spank plugins may be built without access to Slurm source code. They need only be compiled against Slurm's *spank.h* header file, added to the Spank config file *plugstack.conf*, and they will be loaded at runtime during the next job launch. Thus, the Spank infrastructure provides administrators and other developers a low cost, low effort ability to dynamically modify the runtime behaviour of Slurm job launch. The plugins are shared libraries written in C, loaded at runtime by Slurm during job execution and their C-functions can be executed at the corresponding job stage, as example: *slurm_spank_init*, called when the job starts; *slurm_spank_user_init*, called after privileges are temporarily dropped; *slurm_spank_exit*, called when the job is done. Other functions like *spank_getenv*, *spank_setenv*, *spank_unsetenv* can view and modify job's environment. In order to integrate Kerberos authentication in Slurm, a Spank plugin has been developed using Auks [9]. Auks is a distributed credential delegation system that provides: *i*) Remote cache of Kerberos credentials, used to pull or push granted tickets; *ii*) Regular renewal of cached tickets; *iii*) Kerberized service, to ensure authentication and privacy of exchanges. Spank plugin (*auks.so*) allows to use all these functionalities within Slurm, thanks to its easily integration in other applications (C or command line client). Auks is composed of the following components:

- *auksd*: main auks daemon. It is a multi-thread server written in C and it provides: *i*) receives add(store in cache)/get(retrieve from cache)/remove(delete cache) Kerberos Ticket Granting Ticket (TGT) requests from clients; *ii*) provides a kerberized service, authenticates client requests. *iii*) stores TGTs in a cache directory, one per user.
- *auksdrenewer*: daemon implementing TGT renewal mechanism. Separate component due to thread safety issues in Kerberos libraries
- *aukspriv*: daemon ensuring credentials cache is accessible to: *i*) Slurm, for proper credential get action during job execution (via auks Spank plugin); *ii*) *auksdrenewer*, for proper renew logic.
- *auks*: command line client using Auks API to request add/get/remove TGT to *auksd*.

During the job prolog phase (right before the job starts executing on the compute node), the Slurm Spank plugin interacts with the Auks service. The following steps take place:

- Ticket Transfer: Auks securely retrieves the user's Kerberos ticket from the credential cache on the Slurm controller node.
- Ticket Injection: Auks injects the ticket into the environment of the job being executed. This ensures that the compute node where the job runs has access to a valid Kerberos ticket.
- Environment Variable Setup: The Spank plugin sets the KRB5CCNAME environment variable on the compute node, pointing to the credential cache that contains the Kerberos ticket.
- This process ensures that any application run as part of the job has access to the Kerberos ticket and can authenticate itself when accessing secure resources.

As a Slurm job needs a AFS token in EneaGrid in order to access to AFS filesystem, a command *aklog* has to be wrapped in the Auks Spank plugin when a Kerberos TGT is valid. Auks allows to add support for user Helper Script option with the API: *auks_api_run_helper* (Fig.4(a)) on which a script running the command *aklog* can be insert. The Helper Script is implemented in the Auks Spank plugin as shown in the diagram blocks of the complete integration of Auks in Slurm (Fig. 4(b)). A potential issue of this integration of AFS in Slurm is due to the shared tokens in a multiple jobs scenario, where a command to destroy a AFS token execute in a job destroys all the other tokens jobs. In order to avoid it, the *aklog* script is executed in *pagsh* shell.

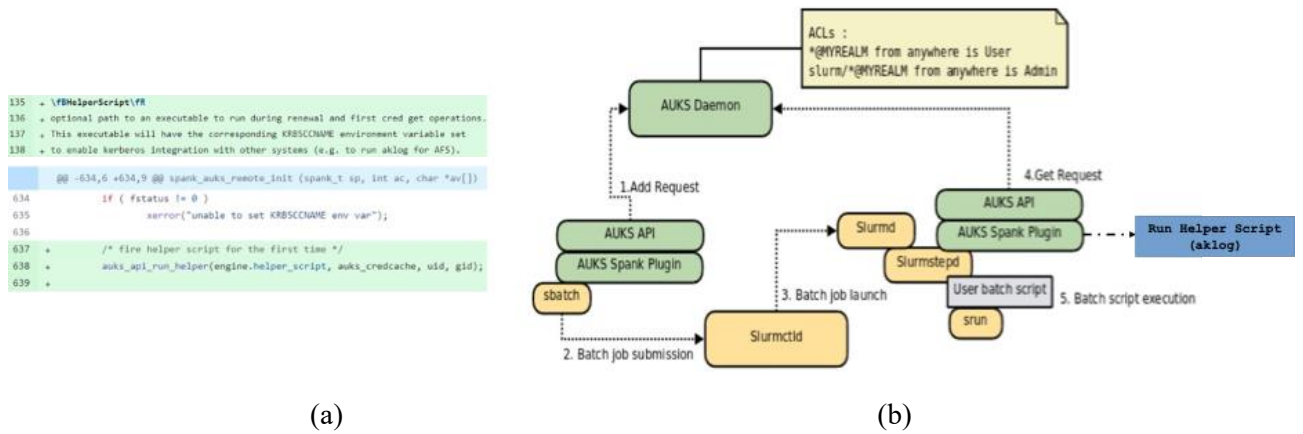


Fig.4: (a) helper Script support for Auks. (b)

XCRESCO configuration

The Xcresco HPC cluster, installed at the ENEA Frascati Data Center in 2023, is a cutting-edge system designed to tackle a wide range of computational workloads, from traditional simulations to AI and machine learning applications. Its architecture is built to support both CPU-intensive and GPU-accelerated tasks, making it a versatile and powerful addition to ENEA's high-performance computing infrastructure. Xcresco is based on a heterogeneous architecture and it is composed of 60 compute nodes in 3 racks (Fig.5), utilizing IBM Power9 processors as its primary computing units.



Model: IBM Power AC922 (Whiterspoon)
Racks: 3 total
Nodes: 60
Processors: 2x16 cores IBM POWER9 AC922 at 2.6(3.1) GHz
Accelerators: 4 x NVIDIA Volta V100 GPUs/node, Nvlink 2.0, 16GB
Cores: 32 cores/node, Hyperthreading x4
RAM: 256 GB/node (242 usable)
Peak Performance: about 1.9 Pflop/s, 32 TFlops per node
Internal Network: Mellanox IB EDR 100Gb/s
Disk Space: 140TB usable NFS storage

Fig.5: XCRESCO hardware configuration

The IBM Power9 CPUs are known for their high memory bandwidth, excellent multi-threading capabilities, and support for a wide variety of workloads, especially in data-intensive and parallel computing environments. Each node is equipped with 2 IBM Power9 CPUs, each providing up to 32 physical cores and 64 threads at 3 GHz as clock frequency. Each node is configured with up to 256 TB of DDR4 memory, offering substantial memory bandwidth for large-scale applications. As complement to the CPU architecture, Xcresco includes Nvidia V100 GPUs for accelerating specific tasks such as deep learning, machine learning, and HPC simulations that benefit from GPU parallelism. Nvidia V100 GPUs are based on the Volta architecture and provide up to 640 Tensor Cores per GPU, making them highly efficient for AI workloads. These GPUs also feature 16 GB of HBM2 memory, optimized for handling large datasets with high memory bandwidth. Infiniband EDR fabric is used to interconnect the 60 compute nodes within Xcresco providing high-speed, low-latency communication between compute nodes in one level ring topology. The scratch disk area is composed of 120 TB available via NFS

provided by a storage server with a throughput of ~1GB/s. The peak electric power is ~90 kW and the cooling system is composed of a rear door water cooling system supplied by a chiller of ~170 kW cooling power.

The software stack is similar to Cresco7 with Almalinux/Kerberos/Openafs/Slurm for *ppc64le* platform. The cluster provides a variety of compilers, including GCC, IBM XL, and NVIDIA compilers, including the old PGI, optimized for both CPU and GPU workloads. Xcresco is optimized for GPU-accelerated applications and comes with popular GPU programming libraries such as CUDA and cuDNN, for deep learning and AI applications. Xcresco supports a wide range of AI and machine learning frameworks, including TensorFlow, PyTorch leveraging the Nvidia V100 GPUs for deep learning model training and inference. The cluster is pre-configured with software packages widely used in scientific research available via modules tools, such as Gromacs [10], Cp2k [11] and Quantum Espresso (QE) [12] for molecular dynamics, and Lammmps [13] for materials science simulations. Furthermore the IBM Qiskit [14] for quantum computing emulations is available with GPU support. Singularity is supported or running containerized environments, allowing users to package and run their applications in isolated environments without conflicts. It is particularly useful for ensuring compatibility with different software stacks and managing complex dependencies for scientific applications.

A new user friendly graphical access to EneaGrid HPC resources has been developed for the future cluster deployment. It is based on Open OnDemand [14], an open-source framework that provides HPC infrastructures with the underlying structure and portal capabilities needed to offer a customizable range of interactive HPC services via a web interface. Using Open OnDemand is simpler than the traditional approach to HPC resources. It is command line free, offers a file management module, a job submission template composer, job monitoring, interactive applications and remote desktop access. All major features of Open OnDemand have been tested after successfully configuring Kerberos authentication and OpenAFS authorization permissions.

A set of benchmarks have been carried out in order to test the performance of some scientific applications, such as: Cp2k, Gromacs, Lammmps and QE.

Cp2k: The benchmark has been carried out on 16 compute nodes with 192 MPI tasks and 4 OpenMP threads using the input file: *H2O-2048.inp*. It is a CP2K input file for molecular dynamics (MD) simulations involving a large system of water molecules, typically 2048 in this case. This file is likely used for simulating properties of bulk water or studying hydrogen bonding, diffusion, or thermodynamic properties in a relatively large simulation box. The timestep is 0.5 fs for 10 steps with a total time to solution of 26818.45 s.

Gromacs: the benchmark is designed to test performance of GROMACS when simulating large biological systems composed of complex macromolecules like lignocellulose a composite of lignin, cellulose, and hemicellulose found in plant biomass. This kind of benchmark is useful for assessing the efficiency of Gromacs in handling large, heterogeneous systems that include both rigid polymeric structures (like cellulose) and more flexible, amorphous regions (like lignin). The benchmark was carried out on 4 compute nodes in 200000 time steps with 16 MPI tasks and 32 OpenMP threads. The total time solution is 1406 s.

Lammmps: The Lennard-Jones (LJ) benchmark is commonly used to evaluate the performance of the LAMMPS (Large-scale Atomic/Molecular Massively Parallel Simulator) code when simulating atomic systems governed by the Lennard-Jones potential, one of the most fundamental interaction models in molecular dynamics. This benchmark tests the scalability and efficiency of LAMMPS across various processor configurations and is frequently used for large-scale simulations of simple atomic or molecular systems, such as noble gases or non-bonded atomic systems. The benchmark was carried out on 16 compute nodes with 256 MPI tasks and 8 OpenMP threads. A loop time of 2897.36 sec. on 8192

cores/threads for 10000 steps with 101648736 atoms and timesteps of 0.01 μ s., that means 3.451 timesteps/s with a time to solution of 2904 s.

Quantum Espresso: the benchmark is the self-consistent field (SCF) calculations of a 2x2 supercell of tantalum pentoxide (Ta_2O_5) with 552 atoms. The maximum number of SCF iterations allows is 200 and the run was carried out on 8 compute nodes with 32 MPI tasks and 8 OpenMP threads. The time to solution to run the benchmark is 1881 s. The table 1 shows the above benchmarks carried out on Xcresco.

Scientific Application	benchmark	#nodes	MPI/OpenMP	Time to solution [sec.]
CP2K	H2O-2048	16	192/4	26818
GROMACS	lignocellulose	4	16/32	1406
LAMMPS	Lennard-Jones	16	256/8	2904
QE	Ta_2O_5	8	32/8	1881

Tab.1: XCRESCO scientific applications benchmarks. The details are described in the text.

3 New Tier-0 ENEA CRESCO8

Within the framework of the NextGeneration EU funding plan a new ENEA supercomputer is being deployed in 2024 to support the plasma physics modelling and new materials research relevant for nuclear fusion reactors. The new ENEA supercomputer, CRESCO8, shall provide HPC resources for DTT, Divertor Tokamak Test facility: a fusion experiment under construction at the Frascati ENEA Research Center.

ENEA is upgrading to 5th Gen Intel® Xeon® Platinum 8592+ processors, with built-in accelerators including Intel® Advanced Vector Extensions 512 (Intel® AVX-512) and Intel® Advanced Matrix Extensions (Intel® AMX). For acceleration, ENEA is deploying 30 additional 5th Gen Intel® Xeon® Platinum 8592+ processors with 60 Intel® Data Center GPU Max 1550 accelerators attached. The cluster also includes 32 Intel® Xeon® Max 9480 processors with high-bandwidth memory (HBM) for bandwidth-constrained workloads.

OneAPI enables researchers to run the same application code across the heterogeneous architecture, spanning CPUs, CPUs with HBM, and GPUs. The operative environments are similar to Cresco7 and Xcresco with Redhat 9 as operating, Kerberos/Openafs as Single-Sign-On and network filesystem, Slurm as resource management system and 10 PBytes of DDN/Lustre ES400NVX2 as high performance parallel filesystem with a throughput of 50 GB/s. The three partitions are described in the Table 2.

Partition	#nodes	CPU	Memory	Network
Lenovo EMR	758	2x Intel 8592+ Emerald Rapids (64c @ 1.9GHz)	16x 32GB (DIMM @ 5600MHz)	nVidia NDR400 SharedIO
Lenovo SPR HBM	16	2x CPU Intel Max 9480 (56c @ 1.9GHz)	2x 64GB HBM (DIMM @ 4800MHz)	nVidia NDR400 SharedIO
Lenovo PVC	15	2x Intel 8592+ Emerald Rapids (64c @ 1.9GHz) + 4x Intel Max 1550	16 x 32GB (DIMM @ 5600 MHz)	nVidia NDR400 SharedIO

Tab.2: CRESCO8 hardware partitions.

For the Cresco8 HPC cluster, ENEA chose a solution proposed by Lenovo. Most of the cluster comprises 5th Gen Intel® Xeon® Platinum 8592+ processors with 64 cores. These processors have built-in acceleration for workloads including AI, with Intel® Advanced Vector Extensions 512 (Intel® AVX-

512), Intel® Data Streaming Accelerator (Intel® DSA), and Intel® Advanced Matrix Extensions (Intel® AMX). The cluster has 30 additional processors with 60 Intel® Data Center GPU Max 1550 accelerators attached. Many applications across physics, biological and chemical sciences, and AI work out of the box on these accelerators. These include GENE, GROMACS, and CP2K, which ENEA uses and requested benchmarks for. Memory bandwidth constrains some workloads, so the cluster includes Intel® Xeon® Max processors with high-bandwidth memory (HBM). HBM can be used without code changes for workloads of up to 64GB or for caching DDR5 memory. It can also be combined with DDR5 memory for workloads that require large memory capacity. In that case, code changes may be needed to optimize performance. The new cluster brings Lenovo Neptune, a direct liquid cooling technology, to ENEA for the first time. Direct liquid cooling is more efficient than air cooling and helps to reduce energy use while supporting the Cresco8 HPC that has a 700kW of electrical power consuming. A Vertiv dry cooler of 1 MW with inlet temperature of 45 °C guarantee a Power Usage Effectiveness (PUE) of 1.045.

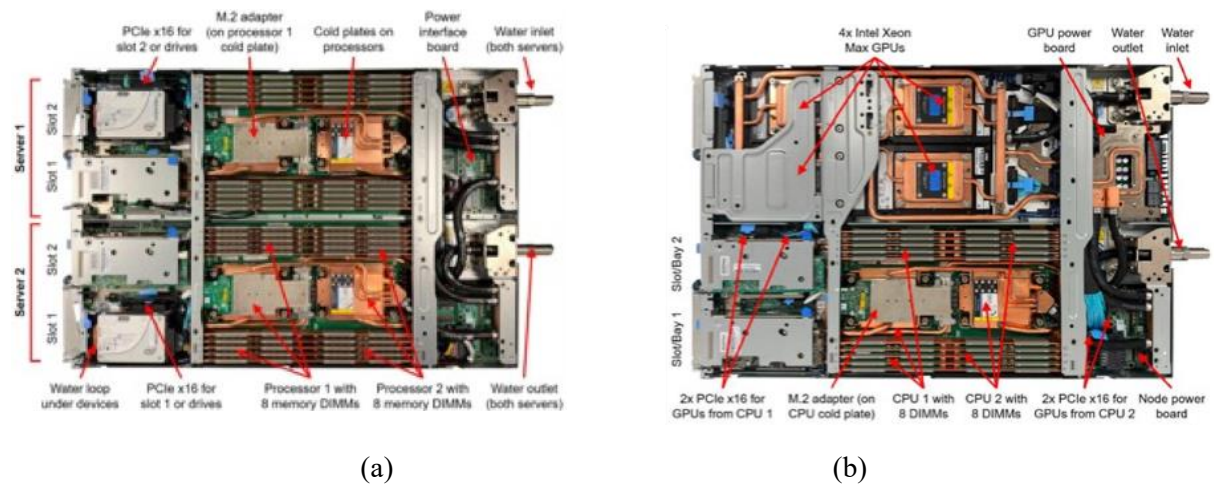


Fig.6: CRESCO8: Lenovo platform: (a) SD650 V3 for EMR partition. (b) SD650-I V3 for PVC partition

The compute node of the EMR partition is based on Lenovo platform SD650 V3, depicted in Fig.6 (a), whilst the accelerated partition is based on Lenovo platform SD650-I V3 as depicted in Fig.6 (b).

Cresco8 increases ENEA’s computing capacity from 1.01 PFlops on CRESCO 6 to more than 6.5 PFlops. That comprises about 5.4 PFlops in the general-purpose processor partition and 1.18 PFlops in a new accelerated partition with Intel Data Center GPU Max 1550 accelerators. More details on the Cresco8 technical hardware specification are reported in the Table 3.

Partition		
Lenovo EMR + SPR HBM 774 nodes	Technology Peak Performance Memory/node Memory/core Network	X86_64 – ThinkSystem SD650 V3 6 PFlops EMR: 512 GB – SPR: 1024 GB + 128 GB HBM 4 GB/core Nvidia NDR400 SharedIO
Lenovo PVC 15 nodes	Technology Peak Performance Memory/node Memory/GPU Network	Intel Max Pontevecchio – ThinkSystem SD650-I V3 3 PFlops 512 GB 32 GB HBM2 (Interna single GPU) Nvidia NDR400 SharedIO
High Performance Storage (scratch,work)	Technology Capacity (raw) Bandwidth	DDN ES400NVX2/Lustre 10 PN +50 GB/s
Service/login nodes		management nodes: SLURM, XCAT, RHEL, Energy Aware Runtime login nodes for terminal sessions Advanced Graphic cards and NX session

Tab.3: CRESCO8 technical specifications.

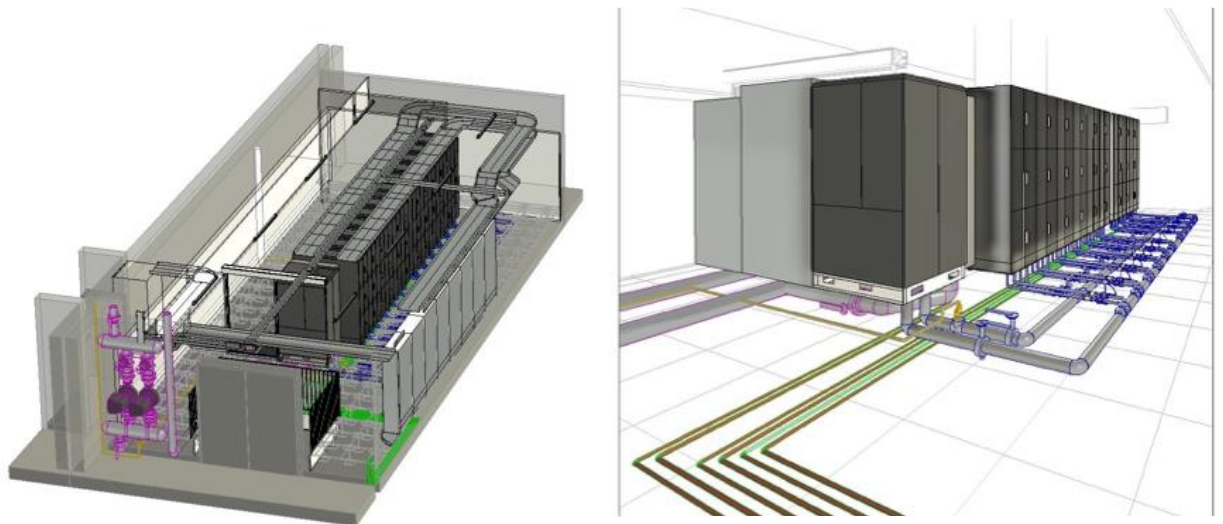


Fig.7: CRESCO8 rack layout

The new ENEA TIER-0 HPC cluster, Cresco8, is being installed in a dedicated room of approximately 150 square meters, specifically designed to host a direct liquid cooling HPC system. The rack layout has been carefully designed, as shown in Fig. 7, to optimize space and cooling efficiency. In addition, a new 1250 kVA medium-to-low voltage electrical substation has been constructed to power both Cresco8 HPC cluster and its cooling facilities.

ENEA carried out testing using several of its application benchmarks, measuring the performance of the latest generation CPU against ENEA’s Cresco6 and Xcresco. The results showed in Tab.4, provide performance accelerations of up to 8x with the same number of nodes.

Scientific Application (EMR)	#nodes	CRESCO6 Time to solution [sec.]	CRESCO8 Time to solution [sec.]	Boost
QE	16	3186.95	376.4	Up to 8x
GROMACS	16	1659.224	264.9	Up to 6x
ANSYS FLUENT	4	379	87	Up to 4x
OPENFOAM	16	193.06	72.2	Up to 2x
LAMMPS	16	1160	255.9	Up to 4x
Scientific Application (PVC)	#nodes	XCRESCO Time to solution [sec.]	CRESCO8 Time to solution [sec.]	Boost
CP2K	8	26818	1892.2	> 14x
LAMMPS	8	5316	128	> 41x

Tab.4: CRESCO8 benchmark results.

4 Conclusions

Cresco7 and Xcresco are a highly scalable and efficient HPC clusters designed to support a diverse range of workloads. The combination of high-performance Intel processors, IBM Power9 CPUs and Nvidia V100 GPUs, paired with a high-speed Infiniband EDR interconnect and optimized software environments, make them a highly capable and flexible HPC systems for research and development. Their configurations provide a seamless path for users to transition to the even more advanced capabilities of the upcoming CRESCO8, ensuring that ENEA remains at the forefront of computational science.

Acknowledgements

The hardware resources of Cresco7 and Xcresco belong to Cineca – ENEA collaboration agreement within the Project Implementing Agreement of HPC for EUROfusion (2024-2029).

References

- [1] G.Ponti et al. *The role of medium size facilities in the HPC ecosystem: The case of the new CRESCO4 cluster integrated in the ENEAGRID infrastructure*. Proceedings of the 2014 International Conference on High Performance Computing and Simulation, HPCS 2014 6903807, pp. 1030-1033
- [2] F.Iannone et alt. *CRESCO ENEA HPC clusters: A working example of a multifabric GPFS Spectrum Scale layout*. Open Access International Conference on High Performance Computing and Simulation, HPCS 2019 9188135, pp. 1051-1052
- [3] <https://almalinux.org/>
- [4] S. Migliori, G. Bracco, P. D'Angelo *L'architettura di ENEA GRID, infrastruttura distribuita per la condivisione di risorse informatiche per il calcolo scientifico* Conferenza GARR 2005 "La rete daPERTutto", Pisa, 1013/5/2005
- [5] <https://www.openafs.org/>
- [6] <https://web.mit.edu/kerberos/>
- [7] <https://www.lustre.org/>
- [8] <https://www.schedmd.com/>
- [9] <https://github.com/hautreux/auks/blob/master/HOWTO>

[10] <https://www.gromacs.org/>

[11] <https://www.cp2k.org/>

[12] <https://www.quantum-espresso.org/>

[13] <https://www.lammps.org>

[14] Dave Hudak, Doug Johnson, Alan Chalker, Jeremy Nicklas, Eric Franz, Trey Dockendorf, and Brian L. McMichael. Open ondemand: *A web-based client portal for hpc centers*. *Journal of Open Source Software*, 3(25):622, 2018

INTEGRATING ENTERPRISE 4.0 KNOWLEDGE IN GENERATIVE ARTIFICIAL INTELLIGENCE: FROM BAG-OF-WORDS TO MULTILINGUAL LARGE LANGUAGE MODELS

Daniela Alderuccio ^{[1]*}, Rossana Cotroneo^[2]

¹ENEA, TERIN-ICT-HPC, Rome, Italy¹

²ENEA, TTEC-KTM-GOT, Rome, Italy

ABSTRACT. In this paper we investigated Enterprise 4.0 Knowledge and its integration with generative AI (Large Language Models - LLMs), for competing in the age of Artificial Intelligence. Enterprise Knowledge is a mix of tacit and explicit Knowledge, evolving in time and space (embedded both in documents, repositories and in organizational routines, processes, practices and norms (brand/enterprise heritage). In the Digital Transition of Enterprise 4.0, pillars are: (i) data value Awareness; (ii) Trust in fair open data reuse/sharing in neutral e-infrastructure, in safe data spaces; (iii) and Integration of Technologies and Knowledge in cross-cultural perspective. The actual shift from Data Democratization to Technology Democratization and then to Knowledge Democratization is a complex process. This long journey started first from awareness of data value and its knowledge; then through the acquisition of control both over own enterprise's data and its reuse (granting/ revoking consent) and over technology evolution (from Bag-of-Words to LLMs approach); finally, guaranteeing a fair equal access to multicultural content. The discussion will cover legal, technological and multicultural perspectives. Our ongoing research focuses on training a cultural-aware language technology. In this first phase, our goal is to find how language and culture impacts in LLMs in domain-specific task (enterprise knowledge). Expected results will lead to an explainable and reliable genAI for applications in Enterprise 4.0. This evolution looks promising in facing the challenge for a sustainable, trustworthy, responsible, ethical, sustainable and safe, generative AI, where likely "AI won't replace Enterprise, but Enterprise with AI will replace Enterprises without AI".

Keywords: Enterprise 4.0; Generative Artificial Intelligence; cross-culture LLMs; Data Analytics; Digital Transition; Data/Technology/Knowledge Democratization

1 Introduction

In 2025 Global data volume will grow from 33 zettabytes (2018) to 175 zettabyte (530%). By 2028 Euro 270 billion is the expected EU-27 additional GDP thanks to new Data Rules. "*Companies investing in data driven innovation exhibit faster productivity growth by 5%-10%*"². The EU will boost the development of trustworthy data-sharing systems where Europeans decide what happens to their data (balancing data altruism and privacy concerns with neutrality of data intermediaries). By 2028 the new measures could increase the annual economic value of data sharing by up to Euro 7-11 billion. In addition, the new rules will have a wider impact on the EU economy and society as a whole: in 2027 Euro 1.3 trillion in increased productivity in manufacturing through IoT data; and Euro 120 billion/year of savings in the EU health sector^[3]. Great attention is to be paid to ethical and privacy concerns, biases and fairness problems, carbon footprints and massive computational costs.

¹ Corresponding author. E-mail: daniela.alderuccio@enea.it

² [Data Act — Factsheet | Shaping Europe's digital future \(europa.eu\)](#)

³ Osservatorio Big Data & Business Analytics. Politecnico di Milano (2024)

2 Enterprise 4.0 Knowledge

“Knowledge is a flux mix of framed experiences, values, contextual information and expert insight that provides a framework for evaluating and incorporating new experiences and information. It originates and is applied in the minds of knowers. In organizations, it often becomes embedded not only in documents or repositories but also in organizational routines, processes, practices, and norms”. [2]. Enterprise Knowledge is affected by: *Velocity* (the speed with which knowledge moves through an organization) and *Viscosity* (the thickness of the knowledge transferred). From a cross-cultural perspective, [Wang, 2018] compared tacit and explicit knowledge: *Tacit Knowledge* is subjective, simultaneous (here and now) analogue (practice); whereas *Explicit Knowledge* is objective, sequential (there and then); it is knowledge of rationality (mind), and it is digital knowledge (theory). As far a philosophical perspective is related, Wang [3] also reported tacit knowledge as more aligned with the Eastern philosophical tradition (Zen Buddhism), whereas explicit knowledge is more aligned with the Western philosophical tradition (scientific methods influenced by positivism).

3 Data Analytics in Enterprise 4.0

Data Analytics has a theoretical framework integrating the three phases of data analytics (knowledge discovery, creation, and application^[4]), with the three dimensions (Technology, People, and Organization), and the three paradigms (positivism, constructivism, and pragmatism). *“Data analytics with the goal of informing decision-making and supporting problem solving is not a onetime effort. The data analytics process is incremental and iterative in nature. The whole process of knowledge discovery, creation, and application continues in a spiral, and forms the basis for continuous process improvement.”*. *“Knowledge conversion (is) the process in which “human knowledge is created and expanded through social interaction between tacit knowledge and explicit knowledge”*^[5]. Applying knowledge conversion to data analytics, *“We consider data as explicit knowledge since they represent codified, explicit measures of properties of entities or events of interest. This can be applied to any type of data including structured (tabular), semi-structured, and unstructured (textual, audio, video, etc.). Analytics resulting from the application of statistical models and computational algorithms are considered information which is also considered explicit knowledge”* [3]. The use of statistical conventional models and artificial intelligence model to uncover trends and patterns of data from various sources represents the technical dimension of the data analytics process. It is the process of knowledge integration by systemizing data (explicit knowledge) from diverse sources to form a broader base of explicit knowledge of the problem at hand. Critical forces driving data analytics are the engagement and collaboration of individual and organizations, professionals and academia experts, integrating social values and organizational strategies. In this paper, we investigated Enterprise Knowledge and its link with generative AI LLMs for competing in the AI age. LLMs are Large Language Models performing a variety of NLP tasks. LLMs relies on complex deep learning models^[6],

⁴“(…) decisionmakers and stakeholders are involved, and the new tacit knowledge created from the previous phase is assessed against organizational values and business strategies. The application of knowledge leads to informed decisions and plan of actions aimed at improving situations and solving problems. The resultant decisions and actions can be viewed as explicit knowledge stemming from collective wisdom of experts, decisionmakers, stakeholders, and anyone else involved. In this phase, (...) mostly organization-oriented, organizational values and business strategies are the key considerations. This phase represents the application of the pragmatist worldview that emphasizes the practical application of knowledge (...). This phase takes the explicit knowledge discovered through the positivist approach, and the tacit knowledge created through the constructivist approach, and applies them in practical problem solving. The three phases of the data analytics process align well with the three eras of knowledge management: Era one, leveraging explicit knowledge; era two, leveraging experiential knowledge; and era three, leveraging collective knowledge” (Dixon, 2018) in [Wang, 2018].

⁵ This process has 4 modes of knowledge conversion: Socialization (Tacit to Tacit) “is the process of converting new tacit knowledge through shared experiences”; Externalization (Tacit to Explicit) “is the process of articulating tacit knowledge into explicit knowledge”; Combination (Explicit to Explicit) “is the process of converting explicit knowledge into more complex and systematic sets of explicit knowledge”; Internalization (Explicit to Tacit) “is the process of embodying explicit knowledge into tacit knowledge” [Wang, 2018]

⁶ LLMs models are: Discriminative (predicting the probability of a word and classification) trying to tag the tokens by classifications and combine the taggers to recognize entities; or Generative (generating new sequences) focusing on generating

requiring significant computational complexity and data. Our research covers different levels: legal, technological and multicultural level. **(a) legal level**: today citizens/enterprise data exchanges use data intermediation provided by private data platforms (not always neutral) which grant and revoke consent for the reuse of data to final data user, by adopting legal contracts; if we shift the right of giving and revoking consent to use data from the data provider platform to the data owner(producer/originator), the latter will regain the “power” on own data and on the reuse of enterprise data, by: (i) balancing enterprise (economic) interests and trust; (ii) preserving data sovereignty and visibility; (iii) assuring data safety and privacy; (iv) feeding an healthy and productive data economy for a wealth Society. **(b) technological level**: the shift from the data democratization to technology democratization is a complex process started from awareness of data value. Enterprise will gain control over their own data and reuse by: (i) customizing LLMs by their own using RAG (Retrieval Augmented Generation) on their enterprise data (and sharing with partners every output), so protecting the enterprise data privacy, obtaining effective outputs on up-to-date data so gaining a competitive advantage respect to competitors (i.e. enterprise without AI); (ii) crypting data before reuse and decrypting data only for selected data user for selected aims (defined in specific contracts between enterprise data producer and data users); (iii) balancing asymmetry of information access (for SME’s); (iv) granting a fair competition in the AI age. With the creation of European Data Spaces^[7], Data Owner, Data Provider and Data User are Data-Endpoints, adhering to a common sharing space where each participant trust each other because they all adhere to a common trust framework It is expected that: (i) the evolution from Data Silos to End-to-End Data Chains; (ii) the KG integration (static/dynamic, temporal, event) with LLMs [4]; as well as (iii) the Integration of enterprise domain-specific knowledge with general knowledge will be likewise fruitful and will lead to an explainable and trustworthy genAI for applications in Enterprise 4.0. **(c) multicultural and multilingual level**: the long path started from data democratization to Knowledge democratization is challenging. Cultural and multilingual asymmetries in English-centric LLM can be overcome, guaranteeing a world-wide fair equal access, eliminating disparities. On-going research on LLMs and RAG application in enterprise 4.0 domain is in progress, also improving traceability and certification of LLMs sources in domain-specific applications. Future directions of research are related to the implementation of LLMs also in Italian language and to the testing of prompt engineering for research/test purposes. The applicability of GenAI to real enterprise use cases is influenced not only by availability of high-quality data, data management/sharing policy, compliance to legal rules (GDPR), explainability, results accountability, deployability, scalability; even more relevant is precision: (i) both in understanding (within own culture and in mother tongue); (ii) and in mining/generating reliable results, avoiding "hallucinations". For this purpose, our on-going research focuses on training a culturally aware language technology, uncovering the semantics of concepts, the semantic alignment and cultural bias in LLMs. Our goal is to find how language and culture impacts in LLMs in domain-specific task (enterprise knowledge). Now LLMs: (i) are general, (based on general knowledge, they perform worst in domain-specific topics); (ii) they show monolingual English-centric ability, due to the overwhelming English textual training datasets adopted; (iii) and they are inclined to reflect western-centric culture. “Modello Italia”^[8] (the Italian LLMs created by CINECA and I-Genius in 2024, on Italian textual corpora and reflecting Italian culture) will provide a test bed for measuring cultural and economic impacts and gaining enterprise competitiveness.

4 Conclusions

The Digital Transition of Enterprise 4.0 has Awareness, Trust and Integration as pillars: data value Awareness, Trust in fair open data especially reuse/sharing in neutral e-infrastructure, in safe data spaces; and Integration of Data, of Technology and of Knowledge in cross-cultural perspective. EU data strategy^[9] aims at balancing the flow and wide use of data, (preserving high privacy, security, safety

a new sequence with additional token markers According to the embedding LLMs can be classified into: Static-embeddings-based methods (representative models: word2vec, BERT); or Contextualized-embedding-based methods.

⁷ European Data Spaces <https://digital-strategy.ec.europa.eu/en/policies/data-spaces>

⁸ “Modello Italia” – LLMs italiano - <https://www.cineca.it/temi-caldi/modello-italia>

⁹ [EU Commission package of measures](#) to support European startups and SMEs in the development of trustworthy Artificial Intelligence (AI) that respects EU values and rules (January 2024).

and ethical standards) and paves the way for facing the challenge for European Enterprises of competing in the AI age. Engagement and collaboration of individual and organizations, professionals and academia experts, integrating social values and organizational strategies are critical forces driving data analytics. In this context, ENEA supports both Training and Skills Development for Enterprises and Test-before-Invest Innovation in the EDIH I-Nest^[10] EU Project for the digital transition of businesses and the Public Administration, supporting enterprises and PAs in the knowledge and application of Artificial Intelligence, High Performance Computing (HPC), Information Security (CS) technologies. In these decades where dataism (belief in data) has spread, we are witnessing the transition from the democratization of data to the democratization of technology; and the evolution from Bag-of-Words approach to customized LLMS on enterprise domain-specific knowledge. The actual shift from Data Democratization to Technology Democratization and then to Knowledge Democratization is a long journey started first from awareness of data value; then through gaining control over enterprise's data and reuse (granting and revoking consent); finally guaranteeing an equal fair access to multicultural content, eliminating disparities. In this paper we investigated the Enterprise Knowledge and its link with generative AI (LLMs) for competing in the age AI. The discussion covered legal, technological and multicultural levels. In this complex process, from data democratization to technology and knowledge democratization, Enterprises will gain control: (i) over their own Data and its reuse; (ii) over Technology adoption and (iii) over own Enterprise Knowledge. Expected Results will show how (a) the evolution from Data Silos to End-to-End Data Chains; (b) the integration of KG with the LLLMs; (c) as well as the integration of enterprise multicultural multilingual domain-specific knowledge with general knowledge (also integrating enterprise data in RAG); they all will lead to a reliable, explainable, trustworthy generative AI application in Enterprise 4.0, facing the limitations of current LLMS (ethical and privacy concerns, cultural biases and fairness problems, carbon footprints and massive computational costs). The challenge for a multicultural, sustainable, responsible, ethical and safe Generative AI is to be faced, because AI won't replace Enterprise, but likely Enterprise without AI will be replaced by Enterprises with AI^[11].

References

- [1] Alderuccio D., EDIH-I-Nest – Tematica Tecnologica 4: IA e Tecnologie Semantiche – Corso “Analisi Testi - Text Mining per la Transizione Digitale Industry 4.0 Enterprise” (giugno 2024)
- [2] Davenport T.H., Prusak L., Working Knowledge: How Organizations Manage What They Know. EBSCO Collection-Knowledge Management, Harvard Business Press, ISBN 9780875846552 (1998)
- [3] Wang Chaojie, [Integrating Data Analytics & Knowledge Management: a conceptual model](#). In *Issue in Information Systems*, pp. 208-216 - https://doi.org/10.48009/2_iis_2018_208-216 (2018)
- [4] Xuhui Jiang et al., [On the Evolution of Knowledge Graphs: A Survey and Perspective](#). In [arxiv.org](#) - <https://arxiv.org/pdf/2310.04835.pdf> DOI: <https://doi.org/10.48550/arXiv.2310.04835> (2023)

¹⁰ [EDIH I-Nest](#) (the Italian National hub Enabling and Enhancing networked applications & Services for digitally Transforming SMEs and Public Administration), Resp. ENEA: Ing. G. D'Agostino - <https://inest-digital.eu/> -

¹¹ “[AI won't replace Humans – but Humans with AI will replace Humans without AI](#)” in *Business & Society* - Harvard Business Review – August 4th, 2023

OPTIMIZATION FOR EFFICIENT AND ACCURATE RADIATIVE TRANSFER MODELLING

Livio Bernardini^{1*}, Paolo Scaccia², and Paolo Antonelli²

¹*Himet S.r.l, Via della Rocchetta, 20, L'Aquila, Italy*¹²

²*AdaptiveMeteo S.r.l., Via Fatebenefratelli 19, Milano, Italy*

ABSTRACT. This paper presents advancements in optimizing satellite communication systems, particularly for interplanetary missions like BepiColombo, a joint mission between ESA and JAXA for the exploration of Mercury. Efficient satellite data transmission is essential, especially under challenging conditions imposed by atmospheric attenuation and the large distances between Earth and space probes. The integration of weather forecasting models with radio propagation models allows for dynamic adjustments to satellite transmission parameters, ensuring greater efficiency. Simulations performed on the CRESCO6 HPC cluster at ENEA-Portici generated daily weather forecasts and atmospheric attenuation estimates over a 15-month period for three ground stations: Cebreros (Spain), Malargue (Argentina), and New Norcia (Australia), using the Weather and Research Forecast (WRF) and the Goddard-Satellite Data Simulator Unit (G-SDSU) models, respectively. These data are fundamental for optimizing signal transmission in the X and Ku bands under varying atmospheric conditions.

Moreover, this study explores the possibility of replacing the traditional Microwave Radiative Transfer Model with Artificial Neural Networks (ANNs). As universal approximators of nonlinear functions, ANNs are particularly well-suited for simulating the radiative transfer equation in the atmosphere, offering a more computationally efficient alternative to the traditional model. This approach has the potential to significantly reduce computational load, enabling real-time or near-real-time transmission optimization, particularly in resource-limited environments such as satellites or cloud architectures. The results highlight the system's adaptability and its potential for implementation on lighter computational architectures in future space missions.

1 Optimization of Satellite Transmission Based on Radio Propagation Models in Interplanetary Missions

Optimizing satellite transmission plays a crucial role in interplanetary missions, where communications between space probes and ground stations must overcome significant challenges related to distance and atmospheric conditions. A prime example is the BepiColombo mission, a collaboration between the European Space Agency (ESA) and the Japan Aerospace Exploration Agency (JAXA), aimed at exploring Mercury, the innermost planet in the Solar System. This mission, launched in 2018, involves sending two probes to Mercury, the closest of which will provide critical data on its surface and atmosphere.

However, communications between the probe and Earth face unique challenges, including interference from Earth's atmosphere. The X and Ku frequency bands used for these communications are sensitive to meteorological phenomena such as rain and humidity, which can attenuate the signal and reduce transmission quality. In this context, optimizing satellite transmissions requires the tight integration of radio propagation models with weather forecasts,

¹² Corresponding author. E-mail: livio.bernardini@himet.it.

allowing for dynamic adjustment of transmission parameters (e.g., signal power and modulation) according to atmospheric conditions (**Fig.1**).

In the past, the CRESCO6 cluster has been used to perform daily weather forecasts, two runs a day of the WRF model [1] (<https://www.mmm.ucar.edu/models/wrf>), over a 15-month period. These forecasts were employed to estimate atmospheric signal attenuation in the X and Ku bands using the G-SDSU model [2] (<https://opensource.gsfc.nasa.gov/projects/G-SDSU>). These attenuation estimates are essential to ensure that signals sent from probes, such as in the case of BepiColombo, reach Earth efficiently without significant data loss.

The integration of numerical weather prediction (NWP) models with radio propagation models enables the prediction of transmission quality in advance and the adjustment of operational parameters, thus reducing the risk of communication interruptions during critical mission phases. This leads to improved efficiency in interplanetary transmissions, particularly for complex missions like BepiColombo, which require a constant flow of data from the probe to Earth throughout the mission's duration.

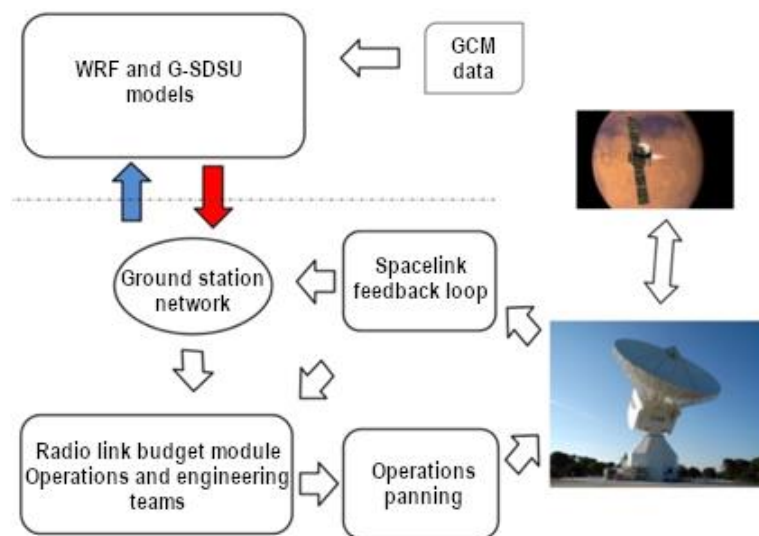


Fig.1: Radio Propagation System.

2 Use of CRESCO6 for Simulation on Lightweight Architectures and Optimization of Satellite Communication Systems

The CRESCO6 cluster has been a key tool for analyzing satellite communication systems and proposing potential improvements. One of the main objectives of this work was to analyze possible improvements in the portability and efficiency of the system, making it compatible with lighter architectures than traditional ones. This is particularly important for applications that require intensive computational resources, such as interplanetary missions, where ground stations must communicate with satellites located millions of kilometers away from Earth.

One of the main challenges was ensuring that the system could operate not only on high-performance computing platforms like CRESCO6 but also on lighter architectures, such as cloud platforms or embedded systems, which offer fewer computational resources but are more flexible and accessible. During 15 months of continuous operations on four nodes of the cluster, CRESCO6 enabled complex simulations that provided valuable insights into the system's efficiency and potential optimizations.

A critical element of these simulations involved three specific terrestrial sites for satellite signal reception and transmission: Cebreros, Spain (Latitude: 40.4522° N, Longitude: -4.2282° W), Malargue,

Argentina (Latitude: -35.775° S, Longitude: -69.397° W), and New Norcia, Australia (Latitude: -31.0481° S, Longitude: 116.191° E). These sites host essential ground stations for receiving and sending signals from interplanetary probes, such as BepiColombo, and are located in strategic regions to ensure global coverage. The weather forecasts and atmospheric attenuation estimates for each of these sites were used to assess possible transmission optimizations based on local atmospheric conditions, thus improving the reliability and efficiency of communications.

Thanks to CRESCO6's ability to run high-intensity computational simulations, it was possible to evaluate the impact of specific atmospheric conditions at each site and adjust transmission parameters in real-time, making the communication system in **Fig.2** more robust and adaptable. This approach allowed for identifying solutions that can also be implemented on lighter computing architectures without sacrificing system accuracy and reliability.

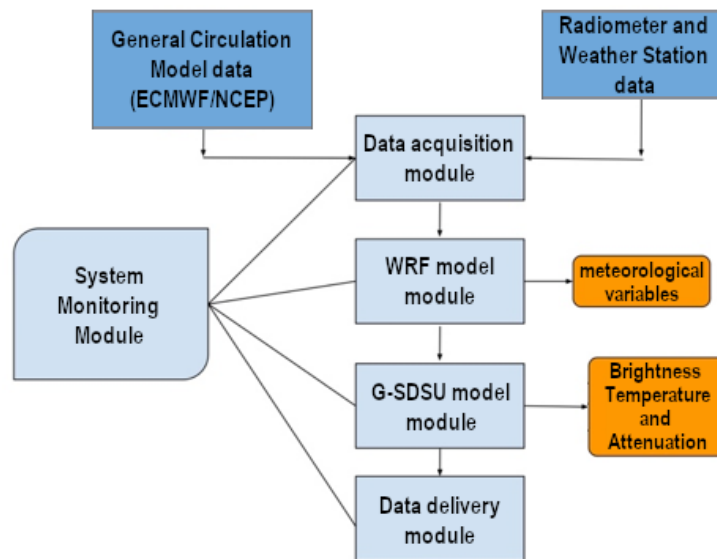


Fig.2: Radio Propagation System Design

The entire study was also greatly supported by the use of Grafana, a powerful open-source platform for monitoring and data visualization (<https://grafana.com>). Grafana enabled the real-time tracking of key metrics and facilitated the analysis of large datasets generated during the simulations, providing intuitive and customizable dashboards that greatly enhanced the efficiency and accuracy of the research.

3 Replacing the Microwave Radiative Transfer Model with an Artificial Neural Network

The Microwave Radiative Transfer Model, used to calculate signal attenuation due to interaction with the atmosphere, represents one of the main computational bottlenecks in satellite transmission optimization systems. While highly accurate, this model requires significant computational resources, making it difficult to implement on lighter platforms.

A promising alternative is the use of ANNs. Neural networks have been demonstrated as universal approximators of nonlinear functions, according to the Universal Approximation Theorem [3, 4], making them particularly well-suited for simulating complex processes such as those described by the atmospheric radiative transfer equation. This ability to approximate complex nonlinear functions allows ANNs to replicate the behavior of the traditional radiative model with high accuracy but with a significantly reduced computational load.

The data collected through the G-SDSU model during the 15 months of simulations, including weather forecasts and atmospheric attenuation estimates, will be used to train the neural network. Training the neural network will allow it to accurately replicate the results of the physical model, offering a more computationally efficient alternative. Once trained, the neural network will be able to perform radiative transfer simulations quickly and accurately, reducing computation times and allowing implementation on less powerful platforms, such as cloud systems or small embedded devices.

This solution not only drastically reduces computational load but also enables real-time or near-real-time calculation of signal attenuation, further improving the efficiency of satellite communications under variable atmospheric conditions. The use of ANNs to simulate radiative transfer represents a step forward in automating and optimizing satellite communications, especially in space missions that require reliable and timely transmissions.

4 Conclusions

In summary, the Radio Propagation predictive system, through its integration of the WRF and G-SDSU models, is pivotal in generating precise atmospheric attenuation predictions over the receiving sites. The system's reliance on sophisticated computational resources underscores the need for high-powered, high-efficiency processing capabilities. However, the operational and logistical demands, particularly the substantial power requirements and the need for a dedicated facility, present significant challenges.

The shift towards utilizing Deep Neural Networks (DNN) represents a transformative approach in atmospheric modeling and prediction. By replacing the G-SDSU model with a DNN, not only it is anticipated a significant reduction in computational load and power consumption, but it can also be foreseen enhanced flexibility and scalability in the deployment of the predictive system. This transition to a more efficient and versatile architecture, requiring fewer computational resources, aligns well with the evolving demands of high-precision weather forecasting and atmospheric research.

Moreover, the potential integration of DNNs with existing meteorological and radiometric data opens new avenues for augmenting the accuracy and reliability of radio-propagation forecasts. The synergy between advanced machine learning techniques and traditional weather prediction models promises to yield a more nuanced and comprehensive understanding of atmospheric attenuation. The dual objectives of validating the DNN's performance against the G-SDSU model and demonstrating its superiority in incorporating real-time observational data set a clear roadmap for the project.

Success in these areas would not only mark a significant milestone in computational meteorology but also enhance our predictive capabilities, leading to better-informed decisions in radio-propagation management. Access to the existing extensive datasets along with generation of new dedicated data will be a crucial factor in training and refining the DNN, ensuring that the system is robust, reliable, and capable of handling the diverse and dynamic nature of atmospheric phenomena. As continuous advances are made, the development and iterative improvement of the system on a dedicated development platform will ensure that the predictive system remains at the forefront of technological innovation and scientific excellence in atmospheric prediction and analysis with contained costs.

Acknowledgments

The authors would like to extend their sincere gratitude to ENEA-Portici for providing the invaluable computational resources necessary to conduct this study. Additionally, we express our deep appreciation to the University of Rome "La Sapienza," especially to Prof. Frank Marzano, whose visionary insights into radio propagation forecasting systems profoundly influenced this research. His exceptional leadership in guiding a team of scientists through such a critical investigation remains an enduring legacy. Though his untimely passing is deeply felt, his contributions continue to inspire and shape our work.

References

- [1] J. G. Powers, J. B. Klemp, W. C. Skamarock, C. A. Davis, J. Dudhia, D. O. Gill, J. L. Coen, D.J. Gochis, R. Ahmadov, S. E. Peckham, G. A. Grell, J. Michalakes, S. Trahan, S. G. Benjamin, C. R. Alexander, G. J. Dimego, W. Wang, C. S. Schwartz, G. S. Romine, Z. Liu, C. Snyder, F. Chen, M. J. Barlage, W. Yu, and M. G. Duda. The Weather Research and Forecasting Model: Overview, System Efforts, and Future Directions. *Bulletin of the American Meteorological Society* 98(8), pp. 1717-1737, (2017).
- [2] H. Masunaga, T. Matsui, W.-K. Tao, A. Y. Hou, C. Kummerow, T. Nakajima, P. Bauer, W. Olson, M. Sekiguchi, and T. Y. Nakajima. Satellite Data Simulator Unit: Multi-Sensor and Multi-Frequency Satellite Simulator package. *Bulletin of American Meteorological Society* 91, pp. 1625–1632, (2011).
- [3] G. Cybenko. Approximation by superpositions of a sigmoidal function. *Mathematics of Control, Signals, and Systems (MCSS)* 2(4), pp. 303-314, (1989).
- [4] K. Hornik. Approximation capabilities of multilayer feedforward networks. *Neural Networks* 4(2), pp. 251-257 (1991).

EVALUATION OF THE CAPABILITIES OF THE AMS-MINNI SYSTEM TO SIMULATE AIR QUALITY IN ITALY DURING THE CALENDAR YEAR 2019

Gino Briganti¹, Andrea Bolignano⁵, Andrea Cappelletti¹, Ilaria D'Elia³, Massimo D'Isidoro², Mihaela Mircea², Antonio Piersanti², Felicita Russo², Maria Gabriella Villani⁴, Lina Vitali²

¹ ENEA Territorial Office of Pisa

² ENEA Bologna Research Centre

³ ENEA Rome Headquarters

⁴ ENEA Ispra (VA) c/o JRC

⁵ ENEA Casaccia Research Centre - Rome

ABSTRACT. In this article, a synthesis of the methodology, the results and the validation of the air quality simulation in Italy for the year 2019 are presented. ENEA is required to provide air quality numerical simulations at the national scale, in accordance with the Legislative Decrees 155/2010 and 81/2018. The computational complexity required the use of the high-performance Computing on CRESCO infrastructure, in particular Cresco 6 grid.

1 Introduction

AMS- MINNI is the Atmospheric Modeling System of the Italian National Integrated Model to support international negotiations on atmospheric pollution (MINNI). It was developed by ENEA and funded by the Italian Ministry of the Environment and Energy Security. The model computes anthropogenic, biogenic, and other natural emissions, as well as meteorological parameters and air quality concentrations, with hourly time resolution across the Italian territory. ENEA is required to carry out national air quality simulations and make the results available, in accordance with the Legislative Decrees 155/2010 and 81/2018. Since 2019, these simulations have been produced every four years (before it was one simulation every five years). After the AMS-MINNI simulation for the calendar year 2010 and 2015, this work refers to the outcomes for the calendar year 2019. The same models constituting the AMS-MINNI suite were used for the development of the forecast operational modelling system FORAIR-IT [1], which currently produces daily three days air quality forecast data over Italy at about 4 km resolution, and over Europe at about 20 km resolution. Thanks to this expertise, since June 2022 MINNI has been producing data for the Copernicus Services devoted to Air Quality, namely contributing to the CAMS regional ENSEMBLE production [2].

Key updates in the 2019 simulation compared to 2015 include the adoption of the WRF meteorological model, the expansion of the simulation grid extent, while maintaining a fixed resolution of approximately 4 km. The transition to the WRF model was driven by the discontinuation of support for the previously used RAMS code. The simulation domain was also expanded to include Lampedusa Island, where ENEA's Atmospheric Observatory plays a crucial role in validating the model and enhancing the FARM chemical model through new algorithm development.

Both the meteorological and air quality outputs were validated to ensure the accuracy of the simulation. Specifically, air quality validation was conducted using the official DELTA Tool software [3], in accordance with the FAIRMODE (Forum for Air Quality Modelling in Europe [4]) evaluation methodology and criteria (<http://fairmode.jrc.ec.europa.eu/>).

2 Simulation set up

AMS-MINNI calculates concentrations and depositions by means of the chemical transport model FARM (Flexible Air Quality Regional Mode [5]), a three-dimensional Eulerian model with first-order closure that simulates the transport, turbulent dispersion, and multiphase chemistry of atmospheric pollutants. Meteorological fields were generated using the three-dimensional non-hydrostatic meteorological model WRF (Weather Research and Forecasting [6]). The hourly gridded emissions used by FARM were prepared by the emission processor EMMA [7], which disaggregates annual data from emission inventories by applying daily, weekly, and seasonal activity profiles, spatial proxies, and chemical speciation profiles linked to specific activities. The emission inventory was based on the ISPRA database, disaggregated at the provincial level and referred to the official 2021 Submission. The diagnostic meteorological post-processor SURFPRO [8] was used to compute key atmospheric parameters, such as the Planetary Boundary Layer (PBL), horizontal and vertical diffusivity coefficients, other turbulence scales, deposition velocities for different chemical compounds, and natural emissions (e.g., sea salt and dust) based on meteorological fields and land use data. Tables 1 and 2 summarize the WRF and FARM setups, respectively.

Table 1: WRF 4.1.2 settings used for the year 2019 simulation.

Microphysics	WRF Single Moment 6-class scheme
Cumulus Parameterization	Off
PBL Scheme	Mellor Yamada Janjic (MY)
Surface layer	Monin-Obukhov/Janjic Eta
Land Surface	Noah LSM
Longwave/Shortwave Radiation	RRTMG
Landuse database	Corine Land Cover 2012 (mapped to USGS 33 classes)
Number of vertical layers	35
Vertical extent	~20000 m
Initial & boundary conditions	3D CAMS global reanalyses
Data assimilation	Spectral Nudging mode, using Global Telecommunication System (GTS) surface measurements (SYNOP)

Table 2: FARM 5.1 settings used for the year 2019 simulation.

Country covered	Italy
EPSG map projection	4326
Model domain/ spatial coverage	lat/lon - SW corner (4.375,34.32), NE corner (21.125,49.48)
Nesting	Two-way nesting with master domain SW corner (-12,32), NE corner (28.2,58.8), horizontal resolution (0.3,0.2) degrees
Spatial resolution	~ 4 km (0.05,0.04) degrees
Initial & boundary conditions	3D CAMS global reanalyses.
Data assimilation	no

3 Validation outcomes and Discussion

Overall, WRF performed very well across all adopted metrics (CORR, BIAS, IOA, and RMSE [9]). Temperature statistics were calculated using data from 205 stations located below 300 m, 104 stations at mid-altitudes, and 99 stations above 800 m. For relative humidity, statistics were derived from 169 stations below 300 m, 49 at mid-altitudes, and 53 above 800 m. Wind speed statistics were based on data from 96 stations below 300 m, 24 at mid-levels, and 23 above 800 m. For all three variables, the model results closely matched the benchmarks suggested in the literature [10]. For instance, in Fig. 1,

the BIAS distribution is presented as a whisker plot, with stations classified by elevation, showing an overall good agreement with observations.

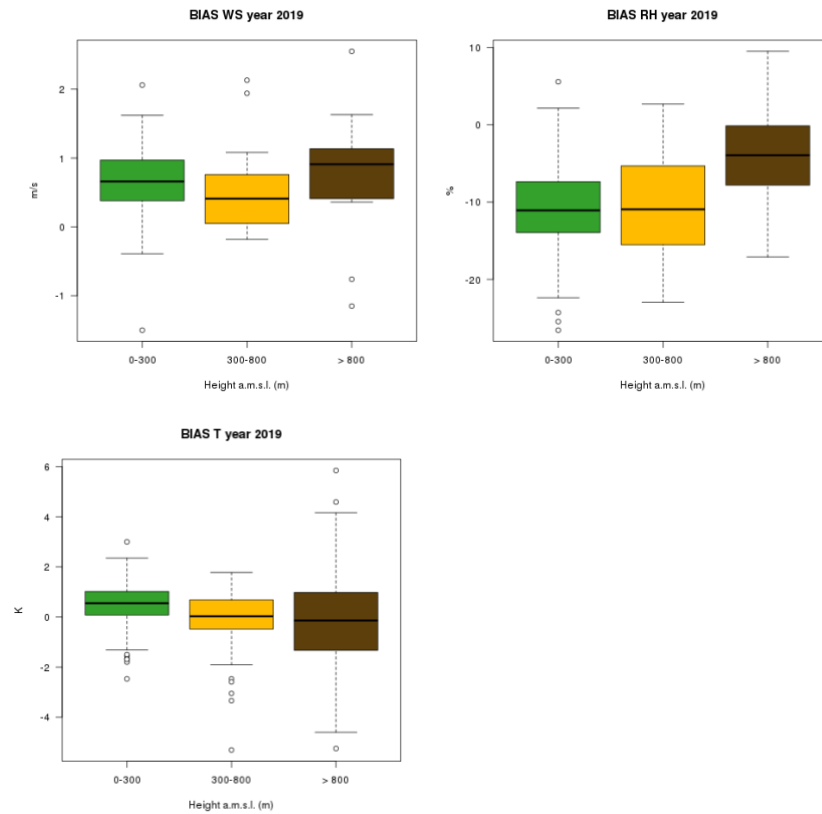


Fig.1: WRF performances (BIAS). From left: relative humidity, temperature, wind speed.

The FAIRMODE approach [11], specifically designed to support the validation of applications related to air quality assessment in the context of the AQD 2008/50/EC, was used for air quality validation. The FAIRMODE methodology essentially compares (Table 3a) the root mean square error (RMSE) with a quantity proportional to the measurement uncertainty (RMS_U). The metric used to assess the quality of a model is the Modelling Quality Index (MQI). The rationale is that a model application can be considered “fit for purpose” if the model-measurement differences remain confined within a given ratio (β , currently set equal 2) of the measurement uncertainty. Alongside MQI, Modelling Performance Indicators (MPIs) are defined for BIAS, model standard deviation (σ_M), and correlation (CORR) (Table 3b). For brevity, only the evaluation of particulate matter PM_{2.5}, one of the most critical pollutants, is presented here. Very good performances were achieved, as it can be inferred from all *MQOs* (Modelling Quality Objectives) and *MPCs* (Modelling Performance Criteria) outcomes (Fig. 2). *MQO_{HD}* is fulfilled for all the 177 valid stations (bottom/left Fig. 2), except for one, an urban station for which *SD* difference is the main reason for the *MQO_{HD}* non-compliance (top/right Fig. 2). In general, the Target Plot points out that *CRMSE* (Centred Root Mean Square Error) is dominated by poor correlation (CORR) in most of the cases. Concerning *BIAS*, both positive and negative values were obtained, being the latter ones more frequent, indicating a general underestimation of PM_{2.5} concentration.

4 Some details on computational setup

The hybrid MPI/OMP version of FARM-5.1 was used, with 12 simultaneous runs (one for each month), utilizing 96 cores per month with 24 OMP threads. The elapsed time was approximately 1.33 hours per simulated day.

WRF model daily simulations used 288 cores with 12 OMP threads, taking approximately 40 minutes per simulated day.

Table 3a: Model quality indicators and objectives and reference diagrams for hourly and daily time series (HD) and for yearly averages (YR).

MQI	MQO	Reference Diagrams
$MQI_{HD} = RMSE/(\beta RMS_U)$	$MQI_{HD} \leq 1$	Assessment Target Plot. Geo Map
$MQI_{YR} = \bar{M} - \bar{O} /[\beta U_{95}(\bar{O})]$	$MQI_{YR} \leq 1$	Assessment Target Plot

Table 3b: Model performance indicators and criteria and reference diagrams for BIAS, CORR, NMSD and high percentiles.

MPI	MPC	Reference Diagrams
$MPI_{BIAS} = BIAS /(\beta RMS_U)$	$MPI_{BIAS} \leq 1$	Scatter Plot. Summary Report, row 1 in section TIME
$MPI_R = (1 - CORR)/\left(0.5 \beta^2 \frac{RMS_U^2}{\sigma_O \sigma_M}\right)$	$MPI_R \leq 1$	MPC Plot. Summary Report, row 2 in section TIME
$MPI_{NMSD} = NMSD /\left(\beta \frac{RMS_U}{\sigma_O}\right)$	$MPI_{NMSD} \leq 1$	MPC Plot. Summary Report, row 3 in section TIME
$MPI_{perc} = M_{perc} - O_{perc} /[\beta U_{95}(O_{perc})]$	$MPI_{perc} \leq 1$	Summary Report, row 4 in section TIME

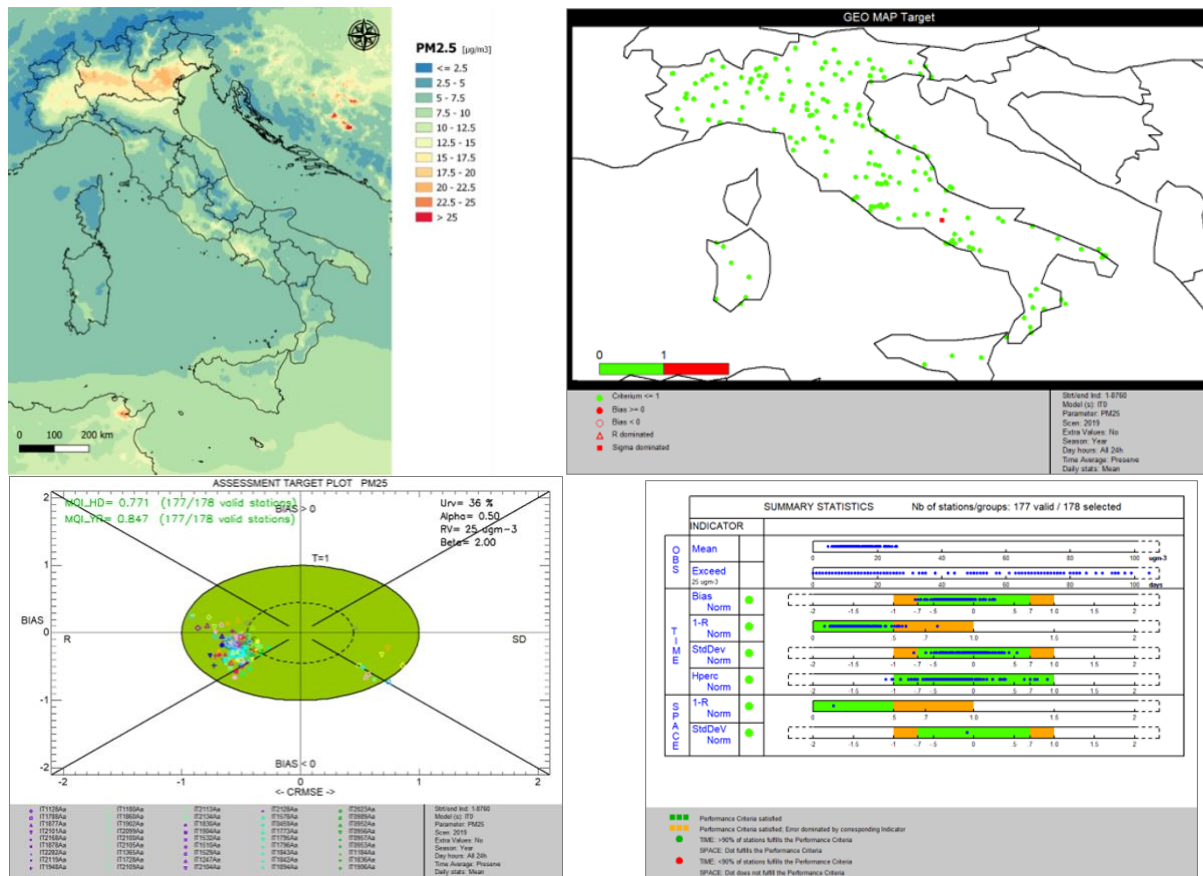


Fig.2: FARM performances (PM2.5). Top: annual mean concentrations (left) and spatial distributions of criterion fulfilment outcomes (right). Bottom: assessment target plot (left) and benchmarking performance summary report for daily mean (right).

References

- [1] M. Adani, D'Isidoro M., M. Mircea, G. Guarnieri, L. Vitali, I. D'Elia, L. Ciancarella, M. Gualtieri, G. Briganti, A. Cappelletti, A. Piersanti, M. Stracquadanio, G. Righini, F. Russo, G. Cremona, M. G. Villani, and G. Zanini. Evaluation of air quality forecasting system FORAIR-IT over Europe and Italy at high resolution for year 2017. *Atmospheric Pollut. Res.*, **13**, 101456 (2022). <https://doi.org/10.1016/j.apr.2022.101456>
- [2] <https://www.regional.atmosphere.copernicus.eu/> (Link visited on September 24, 2024)
- [3] P. Thunis, E. Georgieva, and A. Pederzoli. A tool to evaluate air quality model performances in regulatory applications. *Environ. Model. Softw.*, **38**, 220–230 (2012). <https://doi.org/10.1016/j.envsoft.2012.06.005>.
- [4] <http://fairmode.jrc.ec.europa.eu/> (Link visited on September 24, 2024)
- [5] FARM model <http://www.farm-model.org> (Link visited on September 24, 2024)
- [6] W. C. Skamarock, J. B. Klemp, J. Dudhia, D. O. Gill, Z. Liu, J. Berner, W. Wang, J. J. Powers, M. G. Duda, D. Barker, and X.-Y. Huang. A description of the advanced research WRF model version 4.1 (2019). <https://doi.org/10.5065/1dfh-6p97>.
- [7] Emission Manager. Modular processing system for model-ready emission input preparation. *Arianet s.r.l. Software Manual*. (2014).
- [8] SURFPRO3 - User's guide (SURFace-atmosphere interface PROCessor, Version 3). *Arianet s.r.l. Software manual.*, R2011.31, 2011.
- [9] J. C. Chang and S. R. Hanna. Air quality model performance evaluation. *Meteorol. Atmos. Phys.* **87**, 167–196 (2004). <https://doi.org/10.1007/s00703-003-0070-7>
- [10] C. Emery, E. Tai, G. Yarwood. Enhanced Meteorological Modeling and Performance Evaluation for Two Texas Ozone Episodes. *Report to the Texas Natural Resources Conservation Commission*, prepared by ENVIRON, International Corp, Novato, CA.
- [11] Janssen, S. and Thunis, P. FAIRMODE Guidance Document on Modelling Quality Objectives and Benchmarking (version 3.3), EUR 31068 EN. *Publications Office of the European Union*, Luxembourg, 2022, ISBN 978-92-76-52425-0, <https://doi.org/10.2760/41988>, JRC129254, 2022.

A ROBUST STATISTICAL PROCESS MONITORING FRAMEWORK

Christian Capezza, Fabio Centofanti, Antonio Lepore, Biagio Palumbo

Department of Industrial Engineering, University of Naples Federico II, Naples, Italy

ABSTRACT. Modern data sets are often contaminated with anomalous observations that can seriously decrease the performance of control charting procedures, especially in complex and high-dimensional settings. To mitigate this issue, we show how to apply in a transparent set of steps a new general framework, named robust multivariate functional control chart (RoMFCC), for the statistical monitoring of a resistance spot welding process in the automotive industry that is robust to functional casewise and cellwise outliers. RoMFCC is implemented in the R package `funcharts`, which is available online on CRAN.

1 Introduction

Monitoring the quality of a resistance spot welding (RSW) process in the automotive industry allows the structural integrity and solidity of the welded assemblies in each vehicle. RSW stands out as the most widely utilized method for connecting metal sheets in the body-in-white assembly of automobiles [1], primarily due to its suitability for large-scale manufacturing. The RSW is an autogenous welding process, that is, two overlapping galvanized steel sheets are fused together without the need for filler material. This fusion is achieved by applying pressure to the weld area from opposing sides using copper electrodes. When voltage is applied to the electrodes, a current is generated that passes through the material between them. This current, in turn, produces heat which brings the temperature of the metal at the faying surfaces of the workpieces to the melting point. As a result, the molten metal forms a so-called weld nugget while it cools and solidifies under the mechanical pressure of the electrodes.

In the realm of online measurements for the parameters of the RSW process, the dynamic resistance curve (DRC) is recognized as the comprehensive technological signature of the metallurgical progression of a spot weld [2], and therefore the multivariate vector of DRCs pertaining to the same subassembly can be used for statistical process monitoring (SPM) purposes. The RSW process quality is directly affected by electrode wear since the increase in weld numbers leads to the modification of the electrical, thermal, and mechanical contact conditions at electrode and sheet interfaces. Therefore, to counteract the wear problem, electrodes undergo periodic renovations. In this setting, a paramount issue refers to the prompt identification of mean shifts in DRCs caused by electrode wear. To illustrate the challenges associated with this real-life problem, we analyze DRCs that are courtesy of Centro Ricerche Fiat, recorded at the Mirafiori Factory during lab tests and acquired during RSW processes made on car bodies of the same model. A body is characterized by a large number of spot welds with different characteristics, e.g., the thickness and material of the sheets to be joined together and the welding time. We focus on monitoring a set of ten spot welds made on the body by one of the welding machines. For each assembly to be monitored, where the total number of assemblies in the data set is 1839, the quality characteristic of interest is a vector of ten DRCs collected with 1 ms frequency and normalized on the time domain $[0, 1]$, which can be modeled as multivariate functional data or profiles [3].

Control charts are usually implemented in two phases. In Phase I, historical process data are used to set control chart limits to be used in Phase II, i.e., the actual monitoring phase, where current observations falling outside the control limits signal a possible out-of-control (OC) process. In classical SPM applications, historical Phase I data is assumed to come from an in-control (IC) process. However, this assumption is not always valid. As an example, Figure 1 shows 100 DRCs corresponding to 10 different spot welds, measured in $m\Omega$, that are acquired during the RSW process. Several outliers are visible that should be taken into account to set up an effective SPM strategy. Indeed, control charts are very sensitive to the presence of outlying observations in Phase I, which can lead to inflated control limits and reduced

power to detect process changes in Phase II. In addressing outliers within the Phase I sample, SPM methods commonly employ two alternatives, known as the diagnostic and robust approaches [4]. The diagnostic approach relies on standard estimates following the exclusion of sample units flagged as outliers. However, this method may overlook more moderate outliers that aren't always straightforward to identify accurately. However, the robust approach incorporates all data points and aims to identify a robust estimator, thus mitigating the influence of outliers on final results [5].

Several robust approaches for the SPM of a multivariate scalar quality characteristic have been proposed in the literature, while, to the best of authors' knowledge, a robust approach able to successfully capture the functional nature of a multivariate functional quality characteristic has not been devised in the SPM literature so far. Additionally, when confronted with numerous functional variables, the absence of robust approaches capable of handling outliers is further compounded by the curse of dimensionality. Traditional robust multivariate estimators assume the so-called casewise contamination model for the data, where most cases are contamination-free. However, [6] show that these traditional estimators are affected by the problem of propagation of outliers and, when the dimensionality of the data is high, contamination can more realistically occur in each component independently (componentwise). In the latter case, the fraction of perfectly observed cases can be rather small and the traditional robust estimators may fail. Furthermore, both forms of contamination may occur together, e.g., when monitoring complex data such as profiles or images. The SPM of the RSW process allows the application of a transparent set of steps of the robust multivariate functional control chart (RoMFCC) proposed by [7]. The RoMFCC method is implemented in the R package `funcharts`, available online on CRAN [8] and at <https://www.sfere.unina.it/software/>.

2 The Robust Multivariate Functional Control Chart

The RoMFCC represents a novel general framework for SPM tailored for multivariate functional data that relies on the following four main elements: (I) a functional univariate filter (FUF), (II) robust functional data imputation, (III) casewise robust dimensionality reduction, and (IV) a monitoring strategy. The FUF is used to identify functional cellwise outliers to be replaced by missing components and is an extension of the filtering proposed by [9]. Specifically, the proposed FUF obtains for each observation and each component of the quality characteristic distances from the center of the data which are robust to the presence of possible anomalous observations. Such distances rely on the robust estimation of the principal component directions obtained by considering the extension, referred to as RoMFPCA, of the ROBPCA approach for robust principal component analysis [10] to multivariate functional data. Then, observations with the largest functional distances are labeled as functional cellwise outliers and thus replaced by missing components. The proportion of flagged cellwise outliers is defined by comparing the distance empirical distribution with the distribution that the distances follow in the absence of anomalous observations. Missing components are imputed through a robust functional data imputation method referred to as RoFDI. The RoFDI method extends to the functional setting the robust imputation approach of [11] that sequentially estimates the missing part of an incomplete observation so that the imputed observation has the minimum distance from the space generated by the complete realizations. Also in this step, such distance is obtained by considering the RoMFPCA method. Moreover, to address the correlation bias issue typical of deterministic imputation approaches, the imputed components are randomly perturbed by random errors making the RoFDI a stochastic imputation method. The FUF and the RoFDI methods allow the dataset to be free of cellwise outliers, however, casewise outliers could still be present in the sample. To reduce the infinite dimensionality of the multivariate functional data by being robust towards casewise outliers, we use the RoMFPCA approach. It is well known that the standard multivariate functional principal component analysis is not robust to outliers, which reflects the functional principal component analysis by probably providing misleading results. The proposed RoMFPCA applies the ROBPCA approach to a specific transformation of the coefficients corresponding to the multivariate functional data obtained by the basis function expansion method [3]. To take into account differences in degrees of variability and units of measurement among components, the data are first standardized. The (IV) element of the RoMFCC is based on the consolidated monitoring strategy for a multivariate functional quality characteristic and on Hotelling's T^2 and SPE control charts. The former assesses the stability of the quality characteristic in the finite-dimensional space spanned by the first principal components identified through the

RoMFPCA, whereas the latter monitors changes along directions in the complement space. Under the assumption of multivariate normality, the control limits of Hotelling's T^2 control chart can be obtained considering the given quantiles of a chi-square distribution. The RoMFCC collects elements I-IV in a Phase II monitoring strategy, where a set of Phase I observations, which can be contaminated with both functional casewise and cellwise outliers, is used for the design of the control chart.

3 Results

The data set analyzed is composed of 1839 multivariate profiles, each of which consists of ten DRCs. The Phase I sample is composed of 919 observations corresponding to spot welds made immediately before electrode renewal, whereas the remaining 920 observations are used in Phase II to evaluate the proposed chart performance. We expect that the mean shift of Phase II DRCs caused by electrode wear should be effectively captured by the proposed control chart. As shown in Figure 1, data are plausibly contaminated by several outliers. However, the Phase I data set could still contain casewise functional observations that are not identified in this step. Our method is expected to be robust to both types of outliers. Figure 3 shows the application of the RoMFCC. The vertical line separates the monitoring statistics calculated for the tuning set, on the left, and the Phase II data set on the right, while the horizontal lines define the control limits. Note that, a significant number of tuning set observations are signaled as OC in Figure 3. This is expected because these points may include functional casewise outliers not filtered out by the FUF. In the monitoring phase, many points are signaled as OCs by the RoMFCC. In particular, the RoMFCC signals 72.3% of the Phase II data set observations as OC. This shows that the proposed method is particularly sensible to mean shifts caused by increased electrode wear.

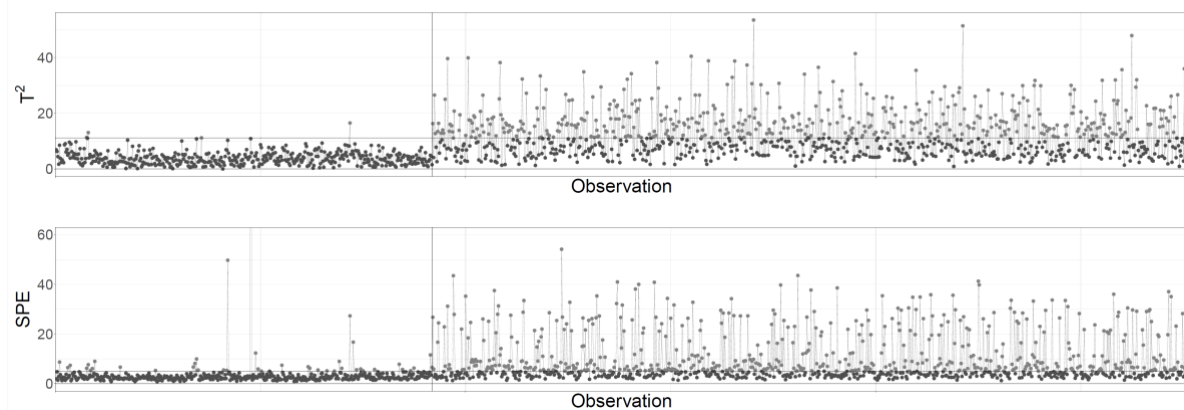


Figure 1. Hotelling's T^2 and SPE control charts for the RoMFCC in the real-case study.

Finally, the proposed method is evaluated against various competing methods. First, we examine control charts designed for multivariate scalar data, constructed based on the average value of each component of the multivariate functional data. This includes the multivariate classical Hotelling's T^2 control chart, denoted as M, alongside the multivariate iterative variant, labeled as Miter, wherein outliers identified by the control chart in Phase I are iteratively eliminated until all data are assumed to be in control (IC). Additionally, we consider the multivariate robust control chart introduced by [12], referred to as MRo. We further consider also two approaches recently appeared in the profile monitoring literature, i.e., the multivariate functional control charts, referred to as MFCC, proposed by [13], and the multivariate iterative functional control charts variant, referred to as MFCCiter, where outliers detected by the control chart in Phase I are iteratively removed until all data are assumed to be IC. The performance of the RoMFCC and the competing methods is assessed by means of the true detection rate (TDR), which is the proportion of points outside the control limits. Table 1 shows the estimated TDR values for all the considered competing methods. Similarly to [14], the uncertainty of TDR is quantified through a bootstrap analysis. Table 1 reports the mean TDR of the empirical bootstrap distribution, and the corresponding bootstrap 95% confidence interval (CI) for each monitoring method. The bootstrap analysis shows that the RoMFCC outperforms the competing control charts; indeed, bootstrap 95% confidence intervals are strictly above those of all considered monitoring approaches. Non-functional

approaches, that is, M, Miter, MRo, show worse performance than functional counterparts because they are not able to satisfactorily capture the functional nature of the data, and robust approaches always improve non-robust ones. Thus, the RoMFCC emerges as the most effective method for quickly identifying OC conditions in the RSW process attributable to increased electrode wear, particularly in scenarios where functional outliers contaminate the Phase I sample.

	TDR	Mean TDR	CI
M	0.336	0.335	[0.305,0.368]
Miter	0.462	0.461	[0.428,0.496]
MRo	0.513	0.512	[0.481,0.547]
MFCC	0.541	0.541	[0.511,0.574]
MFCCiter	0.632	0.632	[0.595,0.664]
RoMFCC	0.723	0.723	[0.695,0.753]

Table 1. Estimated TDR, mean TDR, and CI.

4 Conclusion

The robust multivariate functional control charts (RoMFCC) framework of [7] is applied to the monitoring of a resistance spot welding (RSW) process in the automotive industry, through the observations of dynamic resistance curves available for each spot weld that are often contaminated by functional casewise and cellwise outliers. Its practical applicability is illustrated in a transparent set of steps, i.e., a functional univariate filter, a robust functional data imputation of missing values, a casewise robust dimensionality reduction, and a Phase II monitoring strategy. The RoMFCC framework is the first monitoring scheme capable of monitoring a multivariate functional quality characteristic while being robust to functional case-wise and cell-wise outliers. Its effectiveness is evaluated through a comprehensive Monte Carlo simulation study, where it is benchmarked against several competing monitoring methods. The RoMFCC ability to estimate the data distribution without the need for outlier removal positions it as superior to the competitors across all examined simulated scenarios, as well as in the identification of out-of-control conditions of the dynamic resistance curves associated with the RSW process, mainly due to the electrode wear, which is known to degrade the weld quality.

References

- [1] Zhou, K & Cai, L (2014), ‘Study on effect of electrode force on resistance spot welding process,’ *Journal of applied physics*, 116(8), p. 084902.
- [2] Capezza, C, Centofanti, F, Lepore, A & Palumbo, B (2021), ‘Functional clustering methods for resistance spot welding process data in the automotive industry,’ *Applied Stochastic Models in Business and Industry*, 37(5), pp. 908–925.
- [3] Ramsay, JO & Silverman, BW (2005), *Functional Data Analysis*, Springer, doi:10.1007/b98888.
- [4] Hubert, M, Rousseeuw, PJ & Segaert, P (2015), ‘Multivariate functional outlier detection,’ *Statistical Methods & Applications*, 24(2), pp. 177–202.
- [5] Maronna, RA, Martin, RD, Yohai, VJ & Salibián-Barrera, M (2019), *Robust statistics: theory and methods* (with R), John Wiley & Sons.
- [6] Alqallaf, F, Van Aelst, S, Yohai, VJ & Zamar, RH (2009), ‘Propagation of outliers in multivariate data,’ *The Annals of Statistics*, pp. 311–331.
- [7] Capezza, C, Centofanti, F, Lepore, A & Palumbo, B (2024), ‘Robust Multivariate Functional Control Chart,’ *Technometrics*, doi:10.1080/00401706.2024.2327346.
- [8] Capezza, C, Centofanti, F, Lepore, A, Menafoglio, A, Palumbo, B & Vantini, S (2024a), *funcharts: Functional Control Charts*, R package version 1.4.1, <https://CRAN.R-project.org/package=funcharts>.
- [9] Agostinelli, C, Leung, A, Yohai, VJ & Zamar, RH (2015), ‘Robust estimation of multivariate location and scatter in the presence of cellwise and casewise contamination,’ *Test*, 24(3), pp. 441–461.
- [10] Hubert, M, Rousseeuw, PJ & Vanden Branden, K (2005), ‘ROBPCA: a new approach to robust principal component analysis,’ *Technometrics*, 47(1), pp. 64–79.
- [11] Branden, KV & Verboven, S (2009), ‘Robust data imputation,’ *Computational Biology and Chemistry*, 33(1), pp. 7–13.

- [12] Chenouri, S, Steiner, SH & Variyath, AM (2009), 'A multivariate robust control chart for individual observations,' *Journal of Quality Technology*, 41(3), pp. 259–271.
- [13] Capezza, C, Centofanti, F, Lepore, A, Menafoglio, A, Palumbo, B & Vantini, S (2023), 'funcharts: Control charts for multivariate functional data in R,' *Journal of Quality Technology*, 55(5), pp. 566–583.
- [14] Centofanti, F, Lepore, A, Menafoglio, A, Palumbo, B & Vantini, S (2021), 'Functional regression control chart,' *Technometrics*, 63(3), pp. 281–294.

HIGH PRESSURE DIRECT NUMERICAL SIMULATION OF TURBULENT PREMIXED $\text{NH}_3/\text{H}_2/\text{N}_2$ – AIR SLOT FLAME AT HIGH EQUIVALENCE RATIO

Donato Cecere^{1*}, Matteo Cimini¹, Simone Carpenella² and Eugenio Giacomazzi¹

¹Laboratory of Sustainable Combustion and Advanced Thermal and Thermodynamic Cycles, ENEA, 00124 Rome, Italy

²Department of Civil, Computer Science and Aeronautical Technologies, Roma Tre University, 00146 Rome, Italy

ABSTRACT. This work numerically investigates a premixed $\text{NH}_3/\text{H}_2/\text{N}_2$ -air slot flame at high equivalence ratio and pressure. The main goal is to study the interaction between turbulence and combustion, presenting insights into NO_x productions. Key findings emphasize the effect of the H_2 preferential diffusion on the flame local equivalence ratio, which decreases for negative curvatures, resulting in a NO peak that exceeds the corresponding value in laminar flames. In the post flame zone, the NO concentration is lower than 150 dry-ppm.

1 Introduction

Hydrogen and its derivatives, such as ammonia, are identified as key carbon-free energy carriers for global decarbonization and managing renewable energy intermittency [1]. Regardless of challenges like NO_x emissions [2], stability, and reactivity, ammonia has advantages over hydrogen, such as higher density and cost-effective storage [3]. Recent research indicates that a two-stage Rich-Quench-Lean (RQL) [4] strategy improves flame stability and reduces emissions in ammonia-fired combustors. Moreover, high-pressure staged combustion can achieve NO_x levels comparable to natural gas turbines [5]. For these reasons, this study uses Direct Numerical Simulations (DNS) to explore the flame structure, stabilization, and NO_x formation in a rich premixed $\text{NH}_3/\text{H}_2/\text{N}_2$ slot jet flame at high pressure, addressing the interaction between turbulent flame dynamics and ammonia combustion.

2 Computational Setup

A fuel mixture of 5% NH_3 , 15% H_2 , and 80% N_2 by volume ($\phi=1.5$) is injected, through a slot of width H , into a co-flow of equilibrium burnt gases at 25 bars. The co-flow gases have an adiabatic temperature of 2133 K and a speed of 7 m/s. The fuel is at 750 K and has a velocity of 35 m/s, resulting in a Reynolds number of approximately 41505 (Kolmogorov scale η around 10 μm), a nominal Karlovitz number (Ka) of 38.92, and a nominal Damköhler number (Da) of 1.43. The dimensions of the computational domain are 8.75 H in the streamwise direction, 6.25 H in the crosswise direction and H in the spanwise one (see Fig. 1). The jet and the coflow are separated by walls of thickness $H/4$. The final DNS grid consists of approximately 1.55 billion cells.

The chemical reactions are modelled using the Jiang chemical kinetics mechanism enhanced for NO_x formation in high-pressure NH_3 combustion. Molecular transport in the mixture is modelled using the Hirschfelder and Curtiss expression accounting for preferential diffusion and considering the Soret thermo-diffusive effect and pressure gradient diffusion. The Wilke's formula for viscosity and the Mathur's expression for the thermal conductivity are used to evaluate mixture-average properties. Preferential diffusion is modelled based on the Hirschfelder and Curtiss law.

The numerical simulation is conducted using the in-house parallel code HeaRT [5] and ENEA's supercomputing facility CRESCO [6]. The code solves the compressible N-S equations, discretized using staggered finite-difference schemes. Each chemical species has its individual transport equation. Diffusive fluxes are calculated using a second-order accurate centred scheme; convective terms are modelled through the AUSM⁺-up method, coupled with a third/fifth-order accurate WENO interpolation to minimize spurious oscillations. Homogeneous and isotropic turbulence is prescribed in the central premixed jet mixture and coflow burned gases using synthetic generation methods. The flame regime, based on the inlet parameters, falls within the thin reaction zones (TRZ) according to the Borghi-Peters diagram.

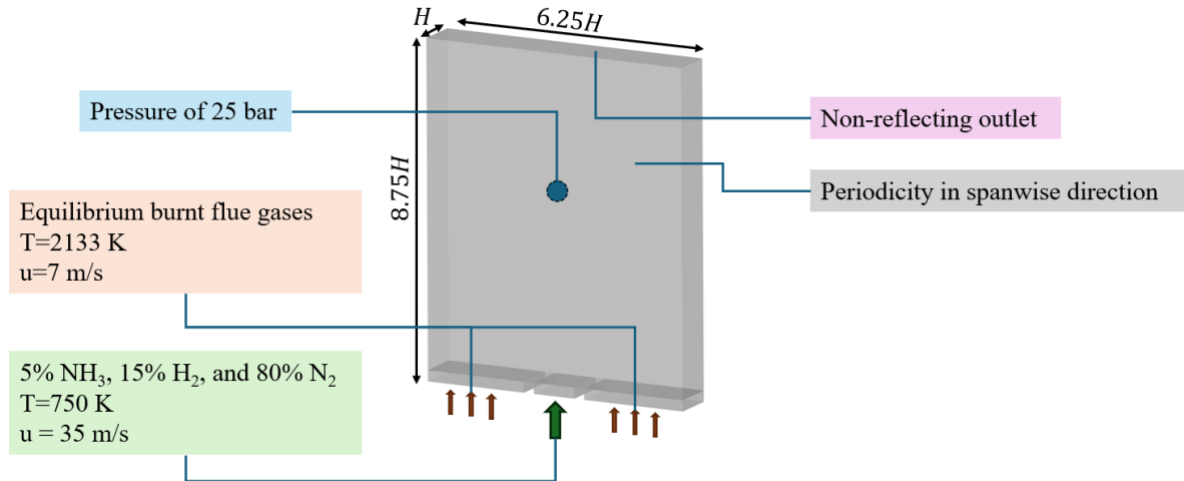


Fig.1: Schematic of the computational domain and boundary conditions for the DNS simulation

3 Results

Figure 2 illustrates the configuration of the slot turbulent flame showing an isosurface at $c=0.76$ (value of the maximum HRR in the laminar flame), coloured with the HRR. Two additional slices in the figure, show the NO mass fraction at $z=0$ and the momentum x-component at the inlet. Turbulent vortices cause the flame to wrinkle fast, which increases fuel consumption quickly since the flame surface is augmented. The flame front tends to corrugate significantly as it gets turbulent, creating a chaotic path with alternating positive and negative curvatures. Since local enrichment of the mixture can cause a decrease in NO and vice versa, the influence of curvature on combustion is important in the creation of NO, since the equivalence ratio fluctuates in the range $1.36 \div 1.85$, rising for positive curvatures.

Analysis of reaction paths shows that, for values of the local equivalence ratio approximately 1.4 less than the nominal one, the NO generation peaks are situated at severe negative curvatures. The HNO path is the most pertinent production rate path in this location. The large concentration of N radicals ($>150\%$ than positive curvature) reacts with the corresponding concentrations of OH and O at negative curvature areas to create NO and HNO radicals. The N_2O and N_2 pathways are the most significant pathways in the consumption of NO [8].

To examine the behaviour of NO production, a continuous zone with alternating positive and negative curvatures was selected inside the flame, as shown in Fig. 3. For this zone, in the local point of maximum (minimum) curvature, the flux diagram of the NO formation reaction path via N is evaluated (see Fig. 4). As result, when the curvature is negative, the NO local production is driven by the HNO decomposition with a third body, which agrees with [8]. Other NO formation mechanisms are due to the reaction of O_2 with N, and the reaction of H with HNO. When the curvature becomes positive, the major production mechanisms remain unaltered. Nevertheless, the conversion of HNO in the NO production process gains weight, while the conversion of N and NH loses relevance. This behaviour can be explained by the fact that zones with positive curvature are affected by a greater H_2 concentration that reacts, producing H_2O with O and OH favouring their depletion.

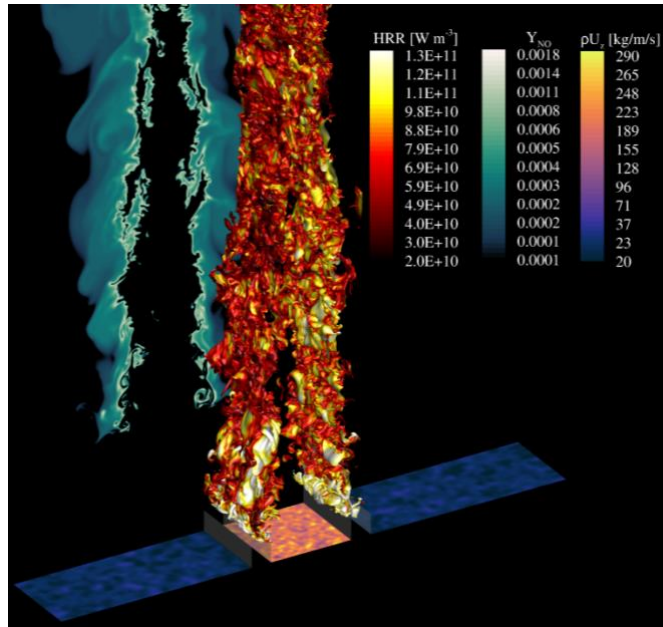


Fig.2: Volume rendering of the isosurface at $c=0.76$ coloured with the HRR, NO slice at $z=0$, and momentum fluctuations slices at the slot inlet. Instantaneous taken at $t=0.0052$ s from the start of the simulation.

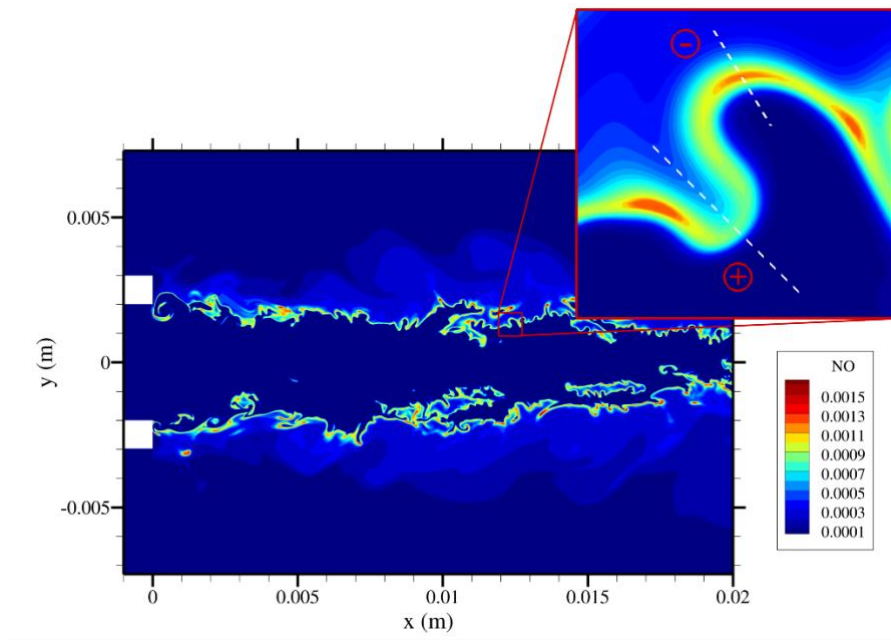


Fig.3: Slice at $z=0$ m and zoomed-in view of NO mass fraction profile.

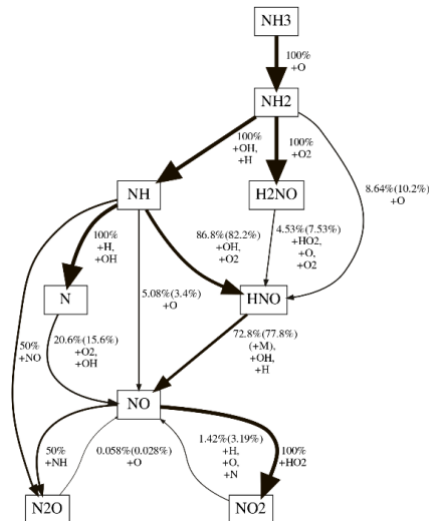


Fig.4: Local reaction path diagram of NO formation via N in the flame zone of negative and positive (parenthesis values) curvature.

4 Conclusion

The article investigated the turbulent premixed combustion of a fuel mixture derived from NH_3 partial decomposition in a coflow of burnt gases at 25 bars by means of DNS. The three-dimensional instantaneous flow field were analyzed, showing the complex structure of this slot flame configuration. The path analysis has been conducted in a local zone of positive and negative curvature, highlighting the driving mechanism in the NO formation. In the post-flame zone ($c > 0.9$), the NO concentration peaks at around 150 dry-ppm, which is significantly higher than 10 ppm observed in the post-flame zone of a laminar flame. This difference is due to the laminar flame's NO equilibrium values being measured at much longer residence times compared to the much shorter 5-20 ms range typical of modern gas turbine combustors.

Acknowledgments

This study was performed within the Italian project "RICERCA E SVILUPPO DI TECNOLOGIE PER LA FILIERA DELL'IDROGENO POR-H2" ("Research and Development of Technologies for Hydrogen Chain", POR-H2, WP2, LA2.2.5), funded by the European Union (NextGenerationEU) through the Italian Ministry of Environment and Energy Security, under the National Recovery and Resilience Plan (PNRR, Mission 2, Component 2, Investment 3.5, project code I83C22001170006)

References

- [1] International Energy Agency. Global Hydrogen Review. Technical report, IEA, Paris, 2021.
- [2] U.J. Pfahl et al. Combust. Flame, 123:140–158, 2000.
- [3] C. Zamfirescu and I. Dincer. Fuel Process. Technol., 90:729–737, 2009.
- [4] E.C. Okafor et al. Proc. Combust. Inst., 37:4597–4606, 2019.
- [5] S. Gubbi et al. ACS Energy Letters, 8:4421–4426, 2023
- [6] E. Giacomazzi, D. Cecere, M. Cimini, S. Carpenella, Energies, 16, 2023.
- [7] G., Ponti, Proceedings of the 2014 Int. Conference on HPC and Simulation, 1030-1033, 2014.
- [8] S. Karimkashi et al. Combustion Science and Technology, 1-30, 2023.

EXTREME MEDITERRANEAN CYCLONES IN AN ATMOSPHERE-ONLY VS AN OCEAN-COUPLED REGIONAL MODEL

Marco Chericoni^{1,2*}, Alessandro Anav², Giorgia Fosser¹ and Gianmaria Sannino²

¹*Scuola Universitaria di Studi Superiori IUSS Pavia, 27100, Italy*

²*Agenzia nazionale per le nuove tecnologie, l'energia e lo sviluppo economico sostenibile ENEA, 00196, Roma, Italy*

¹ Corresponding author. E-mail: marco.chericoni@iusspavia.it.

ABSTRACT. Complex air-sea interactions play a major role in both the variability and the extremes of the Mediterranean climate. This study investigates the differences between an atmosphere-only and an ocean-coupled model in reproducing Mediterranean cyclones and their associated atmospheric fields. To this end, two simulations are performed using the ENEA-REG regional Earth system model at 12 km atmospheric horizontal resolution over the Med-CORDEX domain, both driven by ERA5 reanalysis, for a common 33-year period (1982–2014). The atmosphere stand-alone simulation uses the WRF model with prescribed ERA5 SST, while in the second WRF is coupled to the MITgcm ocean model at horizontal resolution of 1/12°. A cyclone track method, based on sea level pressure, is applied to both simulations and to the ERA5 reanalysis to assess the model capability to reproduce the climatology of intense, potentially most impactful, cyclones. Results show that the seasonal and spatial distribution of the 500 most intense cyclones is similarly reproduced between WRF and ERA5, regardless the use of the coupling.

1 Introduction

The Mediterranean region is intriguing to climate scientists because is a hot spot for climate change. Besides, the ocean and atmosphere interact at the air-sea interface, across a wide range of spatial and temporal scales, generating strong air-sea feedback. These small-scale air-sea feedback processes interact with large scale structures, such as mid-latitude cyclones, entering the Mediterranean basin from the Atlantic region. Mediterranean cyclones formation is very common, making the Mediterranean basin one of the regions with the highest occurrence of cyclones in the world. They often bring extreme precipitation and strong winds, causing significant socio-economic and environmental impacts, particularly in densely populated coastal areas. Thus, a deeper understanding and a more realistic representation of air-sea interaction processes during cyclones is crucial from an impact perspective. Comparing a high-resolution atmosphere-ocean coupled RCM and its atmospheric stand-alone version, this study investigates how the energy redistributes in the entire atmosphere-ocean system, during extreme cyclone events.

The specific questions that are addressed are:

1. Does the high-resolution atmosphere-ocean coupled RCM better represent the climatology of extreme Mediterranean cyclones?
2. Through which physical mechanisms, the explicitly resolved SST distribution and sea surface fluxes impact the precipitation, and the wind speed during extreme cyclones?

2 Climate simulations and cyclone tracking algorithm

2.1 ENEA-REG

To assess the impact of high-resolution atmosphere-ocean coupling on the dynamics of extreme cyclones, two hindcast simulations are performed. The first simulation, referred to as STD, uses the mesoscale Weather Research and Forecasting model (WRF version 4.2.2) with prescribed SST from ERA5 reanalysis [3]. The second simulation (henceforward CPL) uses the ENEA-REG regional Earth system model [1] where WRF has the same set-up and physical parametrizations than STD but is coupled to the Massachusetts Institute of Technology General Circulation Model (MITgcm version c65) extensively used in recent studies to investigate the Mediterranean circulation at different resolutions and time-scales [4]. Thus, the only difference between the STD and the CPL simulation resides in the SST over the Mediterranean Sea, which derives from the ERA5 SST reanalysis (daily, $\Delta x = 0.25^\circ$) in STD, whereas it comes interactively from MITgcm (3-hourly, $\Delta x \approx 1/12^\circ$) in CPL. The WRF horizontal resolution is 12 km, while the ocean component of the CPL has a resolution of $1/12^\circ$ (approximately 10 km). The two simulations initialised and forced by ERA5 reanalysis, respectively for the atmospheric and ocean components, cover the Med-CORDEX region [1] over the period 1982-2014.

3 Cyclotrack

A cyclone track method is applied to both ERA5 and RCM simulations. This method is identical to the one used in [2] (“CYCLOTRACK”) and uses Mean Sea Level Pressure (MSLP) to identify cyclone centres. To identify cyclone centres, a Gaussian filter with a 150 km kernel and sigma value of 2 is first used to smooth the MSLP input fields. Cyclone centres are thus identified as grid points with lower MSLP than their eight neighbour ones. Starting from the deepest cyclone centre, the algorithm constructs possible tracks by connecting centres across consecutive time steps within 250 km radius. Among the candidate tracks, the algorithm will eventually select the one with the least average MSLP difference.

The 500 most intense cyclones have been retained (henceforward called extreme cyclones). Cyclones intensity is considered by the minimum SLP that cyclone attains during its lifetime (i.e. duration of the track).

4 Climatology of extreme Mediterranean cyclones

Figure 1 shows how the mean statistical properties (i.e., intensity, lifetime, and speed) and the seasonal cycle of the extreme cyclones are similarly reproduced between the two RCMs (i.e. STD and CPL) and ERA5. These results are in fair agreement with the most intense cyclones in ERA5 as detected by different cyclone tracking methods and in composite reference tracks for the Mediterranean [4]. Also, the spatial distribution of the extreme cyclones is accurately reproduced by the models, compared to ERA5 (Fig. 2), highlighting the capability of the RCMs to reproduce the climatology of Mediterranean cyclones. Differences between STD and CPL are limited and non-significant, leading at the conclusion that the atmosphere-ocean coupling has only a weak impact on the climatology and statistical properties of extreme Mediterranean cyclones.

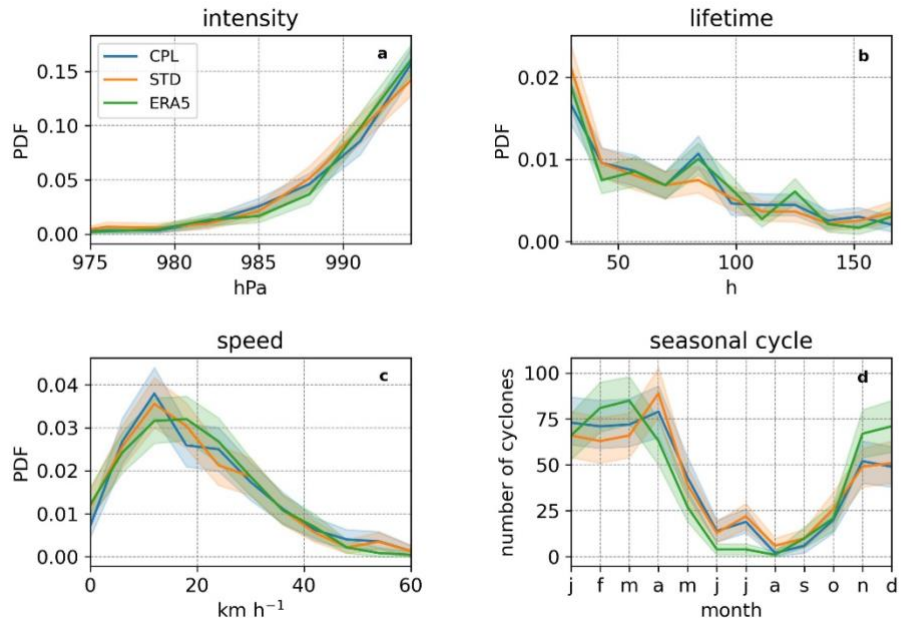


Fig.1: Statistics, intensity (a), lifetime (b) and speed (c), and seasonal cycle (d) of the 500 most intense cyclones in STD, CPL and ERA5. The colour band represent the 2.5-97.5% confidence interval.

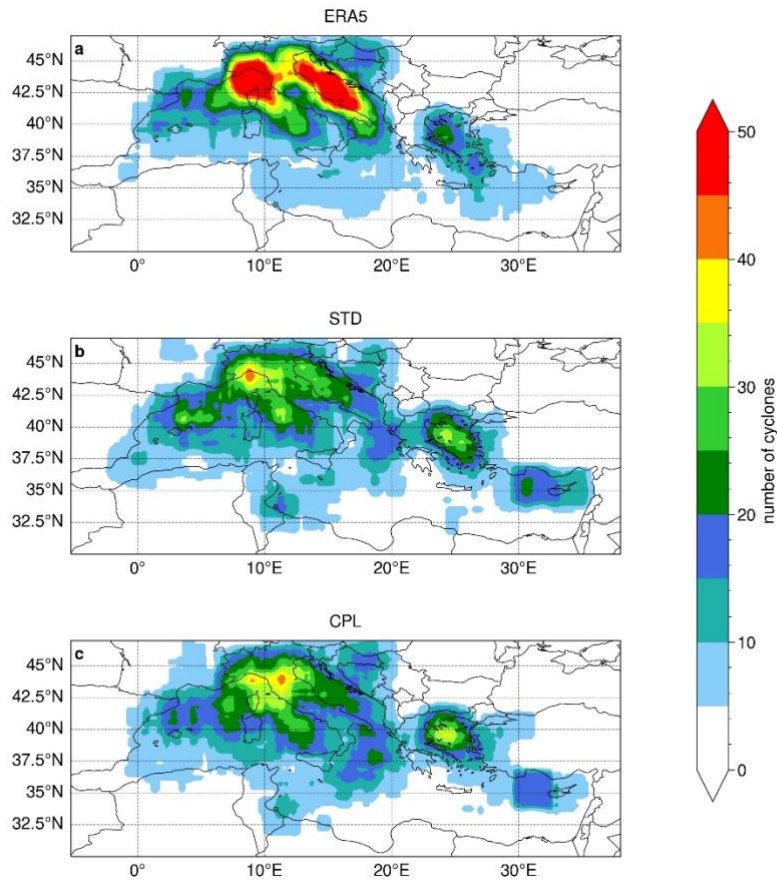


Fig.2: Spatial distribution of the 500 most intense cyclones in ERA5 (a), STD (b) and CPL (c).

Acknowledgments

We acknowledge the World Climate Research Programme, which, through its Working Group on Coupled Modelling, coordinated and promoted CMIP6. The computing resources and the related technical support used for this work have been provided by CRESCO/ENEA-GRID High Performance Computing infrastructure and its staff.

References

- [1] Anav A, Antonelli M, Calmanti S, et al (2024) Dynamical downscaling of CMIP6 scenarios with ENEA-REG: an impact-oriented application for the Med-CORDEX region. *Clim Dyn*. <https://doi.org/10.1007/s00382-023-07064-3>
- [2] Flaounas E, Aragão L, Bernini L, et al (2023) A composite approach to produce reference datasets for extratropical cyclone tracks: application to Mediterranean cyclones. *Weather and Climate Dynamics* 4:639–661. <https://doi.org/10.5194/wcd-4-639-2023>
- [3] Hersbach H, Bell B, Berrisford P, et al (2020) The ERA5 global reanalysis. *Quarterly Journal of the Royal Meteorological Society* 146:1999–2049. <https://doi.org/10.1002/qj.3803>
- [4] Sannino G, Carillo A, Iacono R, et al (2022) Modelling present and future climate in the Mediterranean Sea: a focus on sea-level change. *Clim Dyn* 59:357–391. <https://doi.org/10.1007/s00382-021-06132-w>

STEERED MOLECULAR DYNAMICS SIMULATIONS FOR ANTIBODY-DRUG CONJUGATE CANDIDATE DISCOVERY

Valerio Chiarini^{1*}, Sara Marchio², Simone Giusepponi², Paolo Roberto Saraceni³, Caterina Arcangeli^{3*}, Giuseppe Roscilli¹ and Mariateresa Mancuso³

¹*Takis Biotech, Via di Castel Romano 100, 00128 Rome, Italy*

²*ENEA, TERIN-ICT, via Anguillarese 301, 001123 Rome, Italy*

³*ENEA, SSPT-TECS, via Anguillarese 301, 00123 Rome, Italy*

ABSTRACT. This report presents part of the results obtained by ENEA-Takis Joint Lab MATCH (PNRR-Rome Technopole). Specifically, it includes a molecular dynamics characterization of the binding mechanism between therapeutics monoclonal antibodies (mAb) and tumor antigens, using steered molecular dynamics (MD) simulations. All simulations were performed on the CRESCO6 platform.

1 Introduction

Immunotherapy has revolutionized modern medicine by offering treatments for numerous diseases through a single class of biomolecules: monoclonal antibodies (mAbs) [1,2]. Despite their remarkable effectiveness, identifying suitable mAb candidates for targeted cancer therapy (Antibody-Drug Conjugates, ADCs) remains challenging. These candidates must possess multiple specific characteristics, such as high affinity, monospecificity, and low aggregation, which are essential for human use. Extensive testing and evaluation in preclinical studies and clinical trials are required to determine their efficacy, safety, and potential as new cancer treatments. Given the immense variety of over 10^{13} possible variants, experimental studies alone are prohibitively expensive and time-consuming. To address these challenges, we leverage the High-Performance Computing (HPC) infrastructure of ENEA-CRESCO6 to model molecular interactions, significantly narrowing down the vast pool of potential candidates for experimental validation. Thanks to the capabilities of the CRESCO6 platform, the ENEA-Takis Joint Lab MATCH (Monoclonal Antibody development and Characterization) can effectively tackle this complex task. In this report, we present preliminary results obtained from an HPC-based computational approach to discover mutants of a specific monoclonal antibody developed by Takis company partner. The ideal mutant should exhibit different binding affinities at varying pH levels (7.4 and 5.0) to facilitate antibody recycling and enhance the likelihood of drug release.

2 Computational Methods

Thirteen mutants were rationally designed based on a monoclonal antibody (mAb_{WT}) identified in Takis Laboratories. The structural models of the mutants were generated with Chimera software [3]. Two scenarios were established to simulate both the physiological and late endosomal environments by varying the pH in the simulations. Specifically, the physiological environment was emulated by conditioning the mAb_{WT}, the 13 mutants and the antigen (Ag) separately at pH 7.4 using the PlayMolecule ProteinPrepare tool [4], which identifies the tritable histidine (H) residues in the proteins. The conditioned antibody and antigen were then reconstituted into the bound complex using the

* corresponding authors: caterina.arcangeli@enea.it; chiarini@takisbiotech.it

experimental structure of the latter. Additionally, the wild-type (wt) and each mutant, once bound to the antigen, were conditioned at pH 5 to simulate the late endosomal environment.

All mAb and Ag complexes (mAb:Ag) were placed in a cubic box, solvated with water molecules and the systems were neutralized by adding NaCl. Molecular dynamics (MD) simulations were performed with the GROMACS 2020 package [5], using the CHARMM36 force field [6] in combination with TIP3P [7] water models. Periodic boundary conditions were applied. The mAb:Ag complexes were then energy minimized and equilibrated in two steps by varying the ensembles from NVT to NPT. Five independent unrestrained MD simulation replicas (each 30 ns long) for each system were carried out in NPT ensemble.

The five most diverse binding poses are then extracted from the trajectories, aligned to a pulling reaction coordinate, and used for the steered MD simulations for pulling binding force analysis.

The description of the simulated systems and the simulation details are reported in Table 1.

Table 1: Simulation details, description of the systems and MD simulations carried out.

MD Simulation details		Steered MD Simulation details	
Temperature	310K	Pull type	umbrella
Dielectric constant	1	Pull geometry	COM distance
Integration time step	2 fs	Pull force	600 kJ/mol
Long-range electrostatic force	PME method	Pull velocity	0.005 (nm/ns)
System	Mutated residue into histidine of the VH chain	MD at pH 5.0 and pH 7.4	Steered MD at pH 5.0 and pH 7.4
1. mAb _{wt} :Ag	-	5 replicas, 30 ns	5 replica, 10 ns
2. mAb _{T31H} :Ag	Thr 31	5 replicas, 30 ns	5 replica, 10 ns
3. mAb _{Y32H} :Ag	Tyr 32	5 replicas, 30 ns	5 replica, 10 ns
4. mAb _{G33H} :Ag	Gly 33	5 replicas, 30 ns	5 replica, 10 ns
5. mAb _{W54H} :Ag	Trp 54	5 replicas, 30 ns	5 replica, 10 ns
6. mAb _{N56H} :Ag	Asn 56	5 replicas, 30 ns	5 replica, 10 ns
7. mAb _{D58H} :Ag	Asp 58	5 replicas, 30 ns	5 replica, 10 ns
8. mAb _{Y60H} :Ag	Tyr 60	5 replicas, 30 ns	5 replica, 10 ns
9. mAb _{I100H} :Ag	Ile 100	5 replicas, 30 ns	5 replica, 10 ns
10. mAb _{A101H} :Ag	Ala 101	5 replicas, 30 ns	5 replica, 10 ns
11. mAb _{N102H} :Ag	Asn 102	5 replicas, 30 ns	5 replica, 10 ns
12. mAb _{P103H} :Ag	Pro 103	5 replicas, 30 ns	5 replica, 10 ns
13. mAb _{Y104H} :Ag	Tyr 104	5 replicas, 30 ns	5 replica, 10 ns
14. mAb _{W105H} :Ag	Trp 105	5 replicas, 30 ns	5 replica, 10 ns

3 Results and Discussion

We investigate the structural, dynamical, and functional behavior of specific mAb:Ag complexes consisting of the wild-type (WT) and 13 distinct antibody mutants, where 13 different residues at specific positions within the antibody have been replaced with histidine—a residue known for its sensitivity to pH variations. For each system five MD simulation replicas have been performed at the pH 7.4 and pH 5.0. A total of 280 independent simulations, each 30 ns long (for a total of 8.4 microsecond) have been obtained. The molecular configurations have been extracted from the 280 MD trajectories and clustered [8] in order to find representative conformations to be used as input for the steered MD simulations. A total of 280 independent steered MD simulations, each 10 ns long (for a total of 2.8 microsecond) have been obtained. Figure 1 shows the structural representation of a typical mAb:Ag conformation that will be subjected to steered MD simulations.

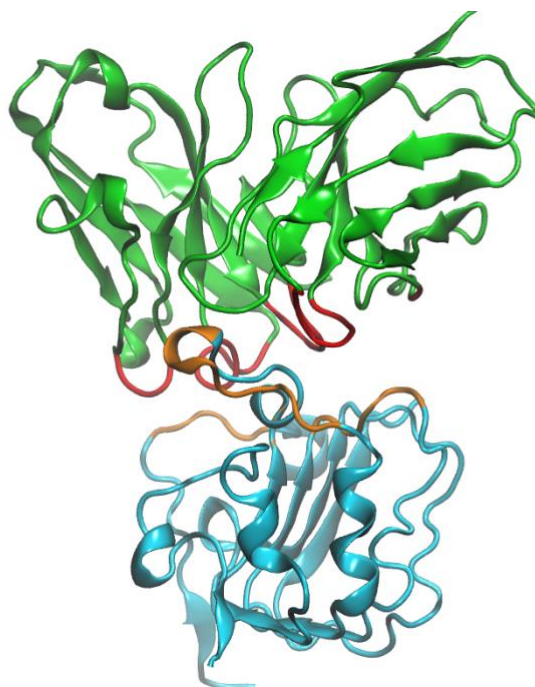


Figure 1: Structural representation of the mAb:Ag complex. Upper (green) the monoclonal antibody (mAb). Lower (cyan) the antigen (Ag). The interacting residues are coloured in red (mAb) and orange (Ag).

The mAb:Ag complex was placed in a rectangular box, as shown in Figure 2, the antigen was positionally restrained and an harmonic force was applied to the mAb through a theoretical spring of precise elastic constant to move it away at a given rate (nm/ns). The resulting evolution of the accumulated-force profile describes the resistance of the interaction to the pulling and, henceforth, the binding strength, which is mediated among the five replicas (Figure 3).

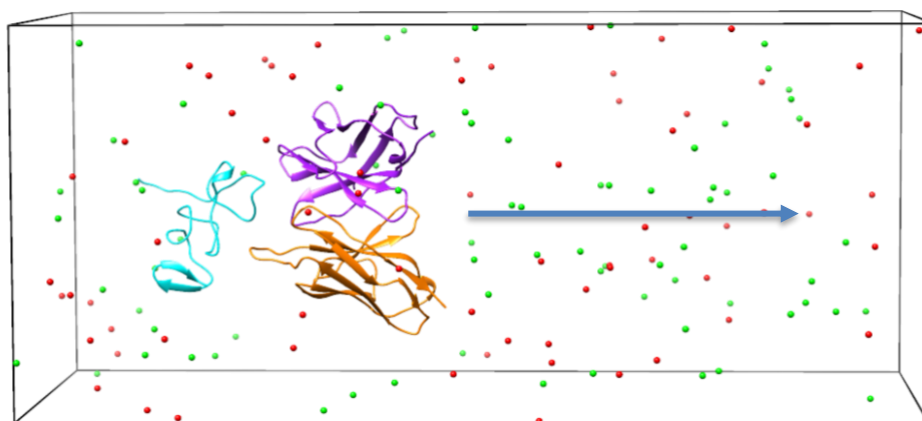


Figure 2: Typical set-up for a steered MD simulation. The antigen is coloured in cyan; the chains of the mAb is coloured in purple and orange. The direction of the pulling force is indicated by the arrow.

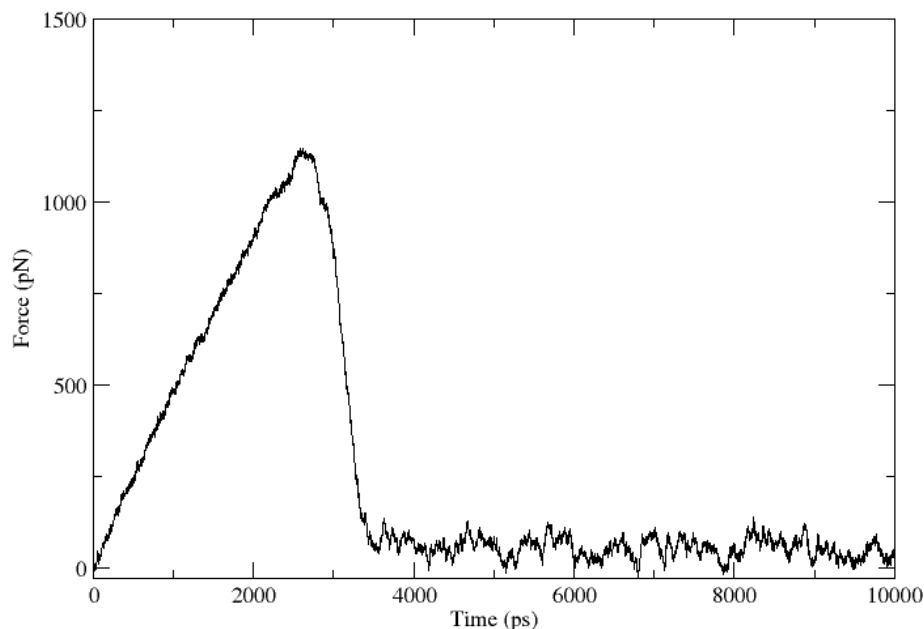


Figure 3: Typical binding-force profiling by steered MD simulation. The force as a function of the simulation time represents the pulling curve and is indicative of the binding strength between the Ag and the mAb under investigation.

Pulling curves for each wild type (WT) and mutant were generated at different pH values and plotted as a function of simulation time. As shown in Figure 4, the analysis of the curves indicates that the WT, the mutants T31H, Y32H, and Y60H exhibit a more pronounced antigen binding strength at pH 7.4. Conversely, the antigen-D58H complex is more stable at pH 5.0, suggesting that this mutant could be a promising candidate for therapeutic molecules targeting acidic environments in tumors.

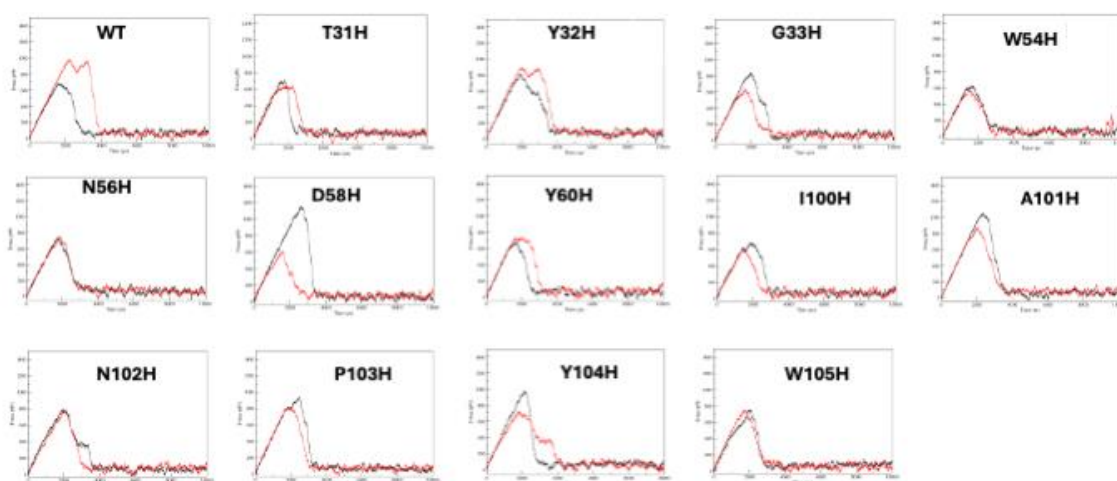


Figure 4: Pulling curves for mAb:Ag complex as a function time. Red, pH 7.4; Black, pH 5.0.

4 Conclusions

The analysis of the pulling curves highlighted that while some mutants showed no difference between the two pH conditions, other mutants showed differential behavior (higher binding at pH 5 and lower at pH 7.4). In particular, the D58H mutant showed very different profiles. If confirmed, this mutant can be considered a promising candidate for antibody-drug conjugate since, if on one side at pH 5 a lower binding capacity favors antibody recycling, higher binding is preferable in the context of tumorigenic environment, that is notoriously acid. Promising candidates will proceed to drug conjugation and further testing.

Acknowledgement

This work was supported and funded by the Project ECS 0000024 Rome Technopole - CUP B83C22002820006, National Recovery and Resilience Plan (NRRP), Mission 4, Component 2 Investment 1.5, funded from the European Union – NextGenerationEU. FP7, JointLab MATCH. Authors acknowledge Guido Guarnieri and Nicolò Colistra from ENEA for their help with the preliminary part of the study.

References

- [1] Hoteit, M., et al. (2021). Cancer immunotherapy: A comprehensive appraisal of its modes of application (Review). *Oncology Letters*, 22, 655. <https://doi.org/10.3892/ol.2021.12916>.
- [2] Esfahani K, et al. (2020). A review of cancer immunotherapy: from the past, to the present, to the future. *Curr Oncol.*, 27(Suppl 2):S87-S97. <https://doi.org/10.3747/co.27.5223>.
- [3] Meng EC, et al. (2023). UCSF ChimeraX: Tools for structure building and analysis. *Protein Science*, 32(11):e4792. <https://doi.org/10.1002/pro.4792>.
- [4] Martínez-Rosell G et al. (2017). PlayMolecule ProteinPrepare: A Web Application for Protein Preparation for Molecular Dynamics Simulations. *Journal of Chemical Information and Modeling*, 57 (7), 1511-1516, DOI: 10.1021/acs.jcim.7b00190.
- [5] Van Der Spoel D, Lindahl, E, Hess B, Groenhof G, Mark AE, Berendsen HJC. Gromacs: fast, flexible, and free. *J Comput Chem*. 2005; 26(16):1701–1718.
- [6] Huang J, MacKerell AD Jr. CHARMM36 all-atom additive protein force field: validation based on comparison to NMR data. *J Comput Chem*. 2013 Sep 30;34(25):2135-45. doi: 10.1002/jcc.23354. Epub 2013 Jul 6. PMID: 23832629; PMCID: PMC3800559.
- [7] Jorgensen WL, Chandrasekhar J, Madura JD, Impey RW, Klein ML. Comparison of simple potential functions for simulating liquid water. *J Chem Phys*. 1983; 79(2):926–935.
- [8] Daura X, Gademann K, Jaun B, Seebach D, van Gunsteren W, Mark, A. Peptide folding: when simulation meets experiments. *Angew Chem Int Ed*. 1999; 38(1-2):236–240.

HIGH FIDELITY NUMERICAL SIMULATIONS OF AMMONIA-HYDROGEN-NITROGEN JET IN CROSS FLOW

Matteo Cimini^{1*}, Donato Cecere¹, Simone Carpenella² and Eugenio Giacomazzi¹

¹*Laboratory of Sustainable Combustion and Advanced Thermal and Thermodynamic Cycles, ENEA, 00124 Rome, Italy*

²*Department of Civil, Computer Science and Aeronautical Technologies, Roma Tre University, 00146 Rome, Italy*

ABSTRACT. This study delves into high fidelity numerical simulations of NH₃/H₂/N₂ jet in an air crossflow. The primary objective is to gain insights into the fundamental mechanisms governing these kinds of flames under high-pressure conditions and complex environments, which are crucial for enhancing combustion efficiency and minimizing pollutant emissions in practical applications.

1 Introduction

In recent years, ammonia has emerged as a promising alternative to fossil fuels, particularly for hydrogen storage, due to its higher density and existing infrastructure [1]. It offers notable advantages over hydrogen, including reduced fire risk and cost-effectiveness [2]. Ammonia is viable for gas turbines, although its combustion challenges, like low flame speed and high NO_x production, need addressing. Blending ammonia with hydrogen or methane enhances combustion stability. Techniques like staged combustion can reduce emissions, and research into catalytic cracking shows potential for efficient ammonia use [3]. Ongoing studies aim to optimize ammonia's role in sustainable fuel technologies.

2 Computational Setup

The three-dimensional compressible Navier–Stokes equations are solved to study the combustion behaviour of a reactive transverse jet of NH₃/H₂/N₂, by means of LES and DNS simulations. The fuel jet has different composition and injection angles (see Table 1), and it is discharged into a crossflow of air at the pressure of 5 bar. The crossflow has a temperature of 850 K and a velocity of 50 m/s, while the fuel jet is at 750 K (a value consistent with the thermal cracking of ammonia) and has a velocity of 150 m/s. A schematic of the computational setup and boundary conditions is depicted in Fig. 1. The physical dimensions of the DNS domain are $L_x \times L_y \times L_z = 25d \times 20d \times 14d$, respectively, in the streamwise, wall-normal, and spanwise directions ($d=0.001$ m is the diameter of the jet hole). The LES simulations have been performed with a longer dimension in the streamwise direction up to 120d. The final DNS mesh has ≈ 683 M cells, while the LES one has ≈ 2 M cells.

The chemical reactions are modelled using the Gotama [4] chemical kinetics mechanism specifically designed for NH₃, blended with H₂, and combustion in air. The Wilke's formula for viscosity and the Mathur's expression for the thermal conductivity are used to evaluate mixture-average properties. Preferential diffusion is modelled based on the Hirschfelder and Curtiss law.

The numerical simulations are conducted using the in-house parallel code HeaRT and ENEA's supercomputing facility CRESCO [5]. The code solves the compressible N-S equations, discretized using staggered finite-difference schemes. Each chemical species has its individual transport equation. Diffusive fluxes are calculated using a second-order accurate centred scheme; convective terms are

modelled through the AUSM⁺-up method, coupled with a third/fifth-order accurate WENO interpolation to minimize spurious oscillations.

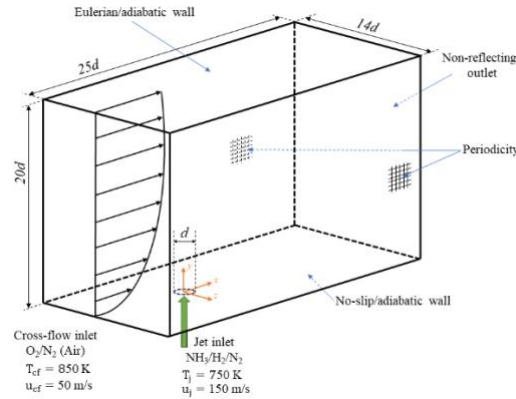


Fig.1: Schematic of the computational domain and boundary conditions for the DNS simulation

Table 1: Test matrix of the computational campaign.

Case	α [deg]	NH ₃ /H ₂ /N ₂ (% by vol.)
LES #1	90	40/45/15
LES #2	75	40/45/15
LES #3	90	80/15/5
LES #4	75	80/15/5
DNS	90	40/45/15

3 Results

3.1 LES approach

In this section, a reduced analysis of the results from LES simulations are reported. The flow-fields and their characteristics are presented and discussed in this section. In Fig. 1 (left), NH₃ and NO mass fraction concentrations are depicted as volume renderings for both simulations set cases of Table 1. In all considered cases, a strong vorticity arises on the leeward side of the flame. This vorticity appears to be significantly more intense in both cases with $\alpha = 75^\circ$. In the same figures the differences in NH₃ concentrations can be seen between the two simulations sets, directly following the simulation setup different settings. Looking at the NH₃ isocontours, together with the vorticities, it can be noted that, in all cases, the observed vorticity on the windward side of the fuel jet, is related to the formation and the expansion of the shear layer, which rolls up into a pattern of Kelvin-Helmholtz hydrodynamic instabilities. This phenomenon is also present, albeit to a lesser extent, on the leeward flame side, but it is not clearly visible.

In Fig. 2 (right), the Heat Release Rates (HRR) together with the stoichiometric mixture fraction ($\xi=0.1433$ for cases #1 and #2, and $\xi=0.1367$ for cases #3 and #4) iso-lines are depicted. It can be noted that the flame results to be anchored, on the leeward fuel jet side near the jet exit, in all the considered cases while the location of the windward fuel jet side flame anchoring is significantly further downstream. As found by Giacomazzi [6], higher HRR can be found on the leeward jet side due to longer residence times. However, comparing the HRR for both fuel mixture compositions, higher values are observed for 80/15/5 NH₃/H₂/N₂ cases. It should also be noted that, on the leeward fuel jet side, also some HRR values can be observed in the fuel-lean areas however, these values are significantly lower than those associated to fuel-rich areas. Finally, far more extended high HRR values areas, can be observed for 90 degrees fuel mixture injection angle cases which agrees with the higher temperature associated with lower strains.

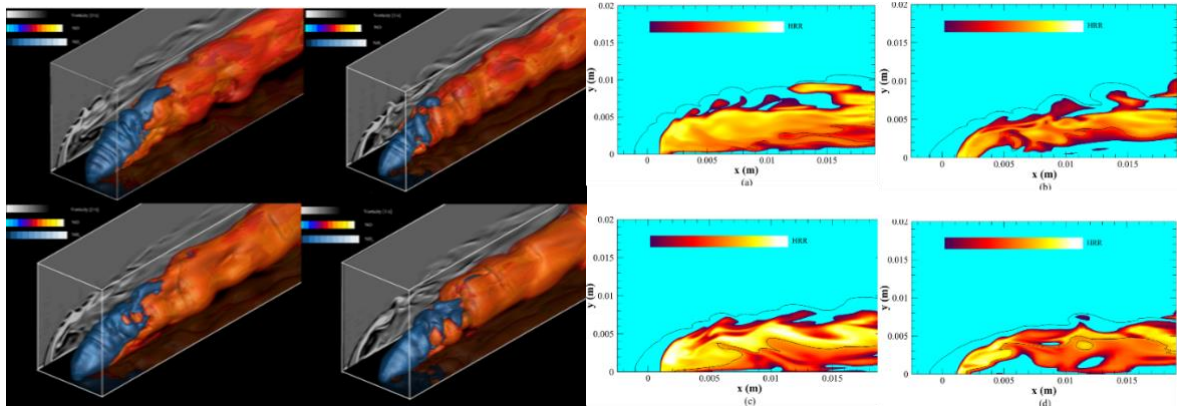


Fig.2: (Left) Volume rendering of NO and NH₃ mass fractions. The slice represents the z-vorticity at z=0. (Right) Instantaneous HRR in the central longitudinal x-y plane. Renderings refer to: 40/45/15 NH₃/H₂/N₂ with $\alpha = 90^\circ$ (a), 40/45/15 NH₃/H₂/N₂ with $\alpha = 75^\circ$ (b), 80/15/5 NH₃/H₂/N₂ with $\alpha = 90^\circ$ (c), 80/15/5 NH₃/H₂/N₂ with $\alpha = 75^\circ$ (d)

3.2 DNS approach

In this section, a reduced analysis of instantaneous quantities from DNS are reported. The complete analysis of this case can be found in [6]. Figure 3 (left) shows some iso-surfaces of the NH₃ concentration and temperature. Vortical structures of the windward shear layer produce mixing with the crossflow air stream by increasing the contact surfaces of the two streams. These coherent structures develop to smaller turbulent scales, enhancing mixing at finer levels. The HRR of the central x-y plane is also depicted on the periodic plane as a projection. The same is done for the HRR in the y-z plane at $x = 7d$ on the outlet plane. High HRR and temperature are observed within the leeward branch of the flow; in the periodic plane of the same picture, the stoichiometric mixture fraction iso-line is also shown with a white line. Although the stoichiometric conditions are reached on both the windward and leeward sides of the fuel jet, no flame develops in the first region due to too short convective times and high strain rates, while the flame can develop around the stoichiometric iso-line in the latter region due to the longer residence times.

Figure 3 (right) shows the vorticity magnitude projected on one of the periodic planes. The flow field is characterized by the formation and expansion of the shear layer, which then rolls up into a clear pattern of Kelvin-Helmholtz hydrodynamic instabilities. These vortical structures are believed to play a crucial role in governing key jet in cross flow processes like mixing and penetration. The instantaneous turbulent structures and the break down phenomenon are also well identified through the Q-criterion (coloured by temperature) in the same figure. Ring-like vortices (RLV) are present in the shear layer, as well as the horse-shoe vortex (HSV), due to the interaction with the crossflow.

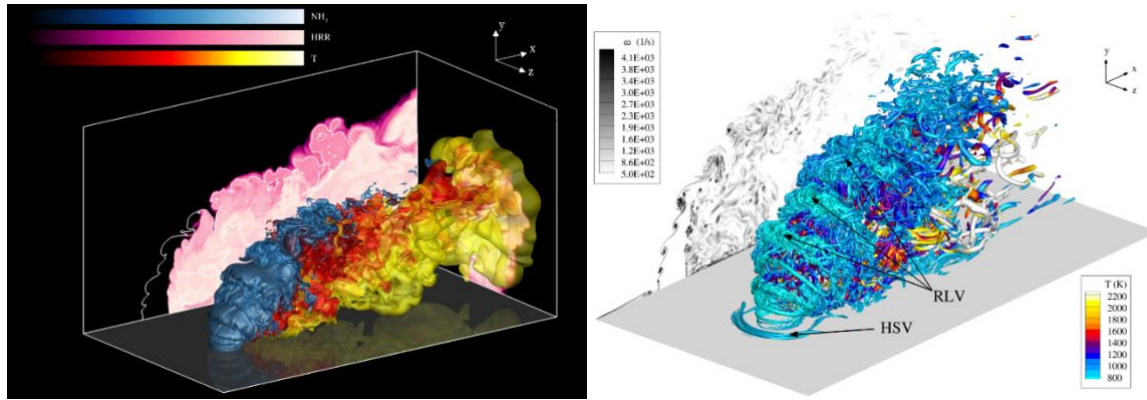


Fig.3: (Left) Volume rendering of temperature and NH₃ mass fraction, and HRR slices at $z = 0$ and $x = 7d$. (Right) Visualization of instantaneous iso-surface of the Q-criterion coloured by the local value of temperature, and vorticity magnitude projected from the mid-plane at $z = 0$. The snapshot refers to $t = 0.00646$ s from the start of the simulation.

4 Conclusion

The article investigated the turbulent non-premixed combustion of a fuel mixture derived from NH₃ partial decomposition in an air crossflow at 5 bar by means of LES and DNS. The three-dimensional LES and DNS instantaneous flow field were analyzed, demonstrating the complex structure of this ideally simple jet in crossflow configuration. The flame develops and anchors on the leeward side of the fuel jet. The flow topology was described, demonstrating the different intensities of the windward and leeward shear layers, the latter having shed vortices with shorter lifetimes due to the damping effect of the reacting region. The main turbulent structures, like ring and horse-shoe vortices, were identified. The results show that the jet in crossflow configuration, nominally non-premixed, can be potentially adopted to generate a non-negligible premixed combustion region.

Acknowledgments

This study was performed within the Italian project "RICERCA E SVILUPPO DI TECNOLOGIE PER LA FILIERA DELL'IDROGENO POR-H2" ("Research and Development of Technologies for Hydrogen Chain", POR-H2, WP2, LA2.2.5), funded by the European Union (NextGenerationEU) through the Italian Ministry of Environment and Energy Security, under the National Recovery and Resilience Plan (PNRR, Mission 2, Component 2, Investment 3.5, project code I83C22001170006)

References

- [1] A., Karabeyoglu et al., AIAA, paper AIAA2012-4055, 2012.
- [2] F. Vitse, et al., J. Power Sources, vol. 142, 1-2, pp. 18-26, 2005.
- [3] D.T., Pratt, Report TS-67-5, 1967; pp.35.
- [4] G.J., Gotama et al., Combustion and Flame, 236, 111753, 2022.
- [5] G., Ponti, Proceedings of the 2014 Int. Conference on HPC and Simulation, 1030-1033, 2014.
- [6] G. Eugenio, et al., Energies, 16(23): 7704, 2023.

AB INITIO STUDY OF THE SURFACE STABILITY OF NI-RICH OXIDES

Andrea Cioffi¹, Valeria Sperati¹, Mariarosaria Tuccillo¹, Priscilla Reale², Sergio Brutti¹

¹ *Department of Chemistry, University of Rome La Sapienza, P.le Aldo Moro 5, 00185 Roma, Italy*

² *ENEA, Via Enrico Fermi 45, Frascati, Italy*

ABSTRACT. Ni-rich NMC electrodes are at the centre stage of innovation in the field of secondary aprotic batteries, being the replacement of Co with Ni and effective strategy to enhance the performance and minimize the content of a critical raw material in the formulation. In the frame of this innovation path, the SIGNE EU project aims to deliver an innovative NMC material with minimized cobalt content and maximized Ni content. Under the umbrella of the SIGNE project, a computational study of the structural and thermodynamic stability of LiNiO₂ and its surfaces have been carried out using the density functional theory and the so-called supercell approach. This is a preliminary study to pave the way for a rational comprehension of the parasitic chemistry of electrolyte components reacting with the surface of this complex positive electrode material.

1 State of the art and rationale of the research activity

In recent years the research of novel battery chemistries is pushed ahead driven by: (a) the worldwide commercial increase of the energy storage device demand and (b) the rising constraints in terms of environmental benignity of processes and materials.^[1,2] In this respect cobalt, that was the key-transition metal for the early commercialization of Li-ion batteries is currently at the centre stage of any research activity in this field due to its earth-crust scarcity, commodity costs and, mainly, environmental and health incompatibility.^[3] In fact, cobalt is the redox active centre of the LiCoO₂ layered phase that is the prototype of most positive electrode materials currently implemented in Li-ion batteries.^[4] In this context, EU policies have been categorizing battery chemistries in generations based on the TRL (technology readiness level) and TtM (time to market) descriptors.^[5] Furthermore, EU also identified key-technologically relevant commodities that pose strategic drawbacks (the so-called Critical Raw Materials list, CRM)^[6] for the entire union in the next decades. Among the innumerable innovative battery chemistries, the so called Gen3a and Gen3b will be commercialized in the next five years: among the many remarkable improvements that will be delivered to the market, both Gen3 batteries aims at minimizing, or even removing cobalt from the formulation, being this atomic specie one of the most critical in the CRM list.^[6] An effective replacement of LiCoO₂ from the battery formulation requires reliable alternative materials with similar or even improved performance. Among the possible options, LiNiO₂ and the so-called Ni-rich layered oxides are at the same time promising and challenging. In fact, LiNiO₂ has the same layered and effective crystal structure of LiCoO₂ and can theoretically deliver more than 150 mAhg⁻¹.^[7,8] However, LiNiO₂ reacts with air to form highly insulating LiOH and Li₂CO₃ precipitates over the crystallite particles and it is thermodynamically less stable than LiCoO₂, thus opening the door to structural degradations upon cycling.^[9]

The SIGNE project funded by the EU through the HE programme (Grant agreement ID: 101069738, started in September 2022, duration 48 months) aims at demonstrating and upscaling to prototype level a novel battery chemistry (Gen3b) based on a Ni-rich layered oxide with general stoichiometry LiNi_{0.8+x}Mn_{0.1+y}Co_{0.1-x-y}O₂ (NMC). Among the many research activities carried out within the SIGNE project, a computational workload is implemented to investigate the NMC cathode material with atomistic simulation at DFT level of theory. The goal is to deliver a comprehensive description of the crystal and electronic structure of this phase, evaluate the surface thermodynamic stability and study the spontaneous reactivity of the NMC surface with other molecular species (i.e. aprotic electrolyte components). In this respect the computational resources of CRESCO have been supporting this research activity in 2023, in particular in the preliminary structural and thermodynamic study of the LiNiO₂ bulk and surfaces. Calculations in the framework of the density functional theory (DFT) have been performed using the Vienna ab initio Simulation Package (VASP) also using the Alloy Theoretic

Automated Toolkit (ATAT) software package for the setup of supercells and slabs. The rationale of the computational work is shown in the Figure 1.

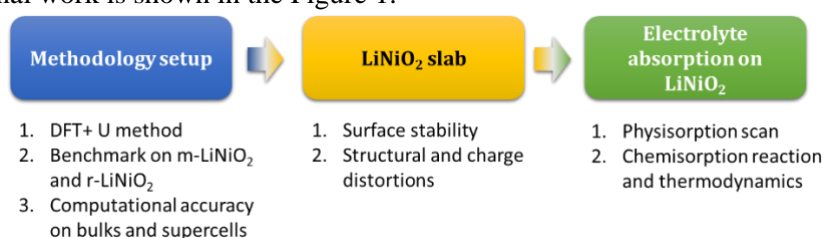


Figure 1. Rationale of the DFT analysis of the Ni-rich NMC cathode

2 Results

The electronic structure of the LiNiO₂ lattices have been modelled to deliver a comprehensive description of the prototypal phase to mimic NMC cathodes. In fact, the bulk structure of NMC matches the hexagonal hR12 metastable lattice of LiNiO₂ (Figure 2a) in the monoclinic lattice m8C., whereas the thermodynamic ground state of the stoichiometric lithium nickel oxide is a monoclinic mC8 lattice (Figure 2b). The computational accuracy of the adopted DFT+U method has been computed by converging kinetic energies and k-points on both the hR12 and the mC8 polymorphs of LiNiO₂. Overall feasible (and scalable) calculation parameters can achieve computational accuracies below 5 mV at⁻¹.

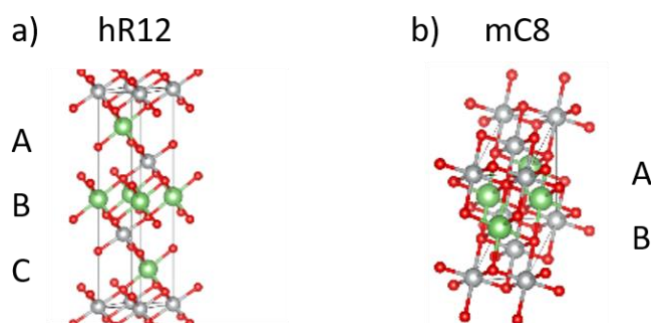


Figure 2. Representation of the unit cell of LiNiO₂ a) in the rhombohedral lattice hR12, b) in the monoclinic lattice m8C.

The computed crystallographic and electronic structure features of the LiNiO₂ bulks match very well to the experimental data: the calculated values are given in Table 1. Mean errors of the structural model are < 2.52 % and the Ni charge state μ_{Ni} can be accurately predicted from the computed magnetic moments.

The modelling of the supercells has been implemented by DFT+U using PAW pseudopotentials and the converged kinetic energy cut-offs for bulks: calculations have been carried out at Γ . Supercells are preliminary step to mimic surfaces and therefore a realistic prediction of energies and structures passing from bulk to supercells is a prerequisite to deliver reliable predictions on surfaces. Overall, energetic stability predictions on supercells match those on bulks for both mC8 and hR12 prototypes confirming a good robustness of the chosen methods.

The local coordination of the Ni ions in the supercell have been modelled by DFT+U. For hR12, a supercell size of 3x3x1 unit cells was chosen (Figure 3a)) and for mC8, a supercell size of 3x2x2 unit cells was chosen (Figure 3b)).

Table 1. Computational lattice parameters obtained from DFT for hR12 lattice and mC8 lattice.^[10]

	hR12	mC8
a/A	2.884 (2.879)	5.288 (4.969)
b/A		2.867 (2.877)
c/A	14.271 (14.203)	5.387 (5.199)
$b/^\circ$		115.41 (109.2)
$V/A^3 \text{ at}^{-1}$	8.566 (8.460)	8.566 (8.715)
μ_{Ni}	1.342 (1)	1.123 (1)

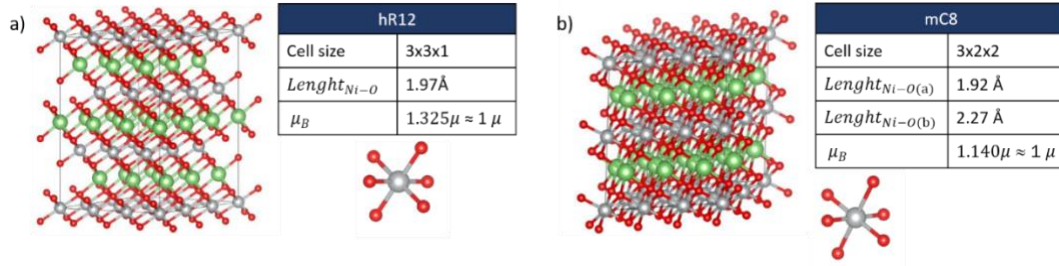


Figure 3. Representation of supercells in the a) hR12 lattice and b) mC8 lattice.

Both hR12 and mC8 supercells mimic the computational bulk structures as well as the experimental data with Ni being in the 3+ oxidation state and Ni-O bond lengths comparable to experimental values. In both structures, there is Jahn-Teller-distortion introduced by Ni³⁺ atoms which are Jahn-Teller active. However, octahedral distortion is far more pronounced for mC8 than for hR12. From the experimental point of view NMC materials crystallize in the hR12 structure that is also the most stable lattice from the thermodynamic point of view.^[11] In fact, our modelling suggests that the hR12 lattice is more stable compared to the mC8 one by 80 and 40 meV at⁻¹ in the case of the periodic lattices and the supercell models, respectively. Owing to this we limited the subsequent research activities about surfaces only to the hR12 prototype.

The analysis of the structure/stability/bonding environment of the LiNiO₂ prototypical lattice in proximity to the crystal surface requires the identification of the crystal cuts able to describe the most stable ordered crystallographic planes shown on the surface of LiNiO₂ crystallites. A recent study^[12] suggests that, among all the possible exposed surfaces of LiNiO₂ crystals in the Wulff-crystal shapes of the hR12 lattice, the (003), the (110) and (104) surface planes are the most stable (Figure 4).⁷ It is to be noted that the (003) surfaces can end with three different compositions: i.e. all Li ions, all O ions or all Ni ions. On the other hand, both the (110) and the (104) one ends with a mixed composition by exposing a squared 2D grid alternating lithium, oxygen and nickel ions.

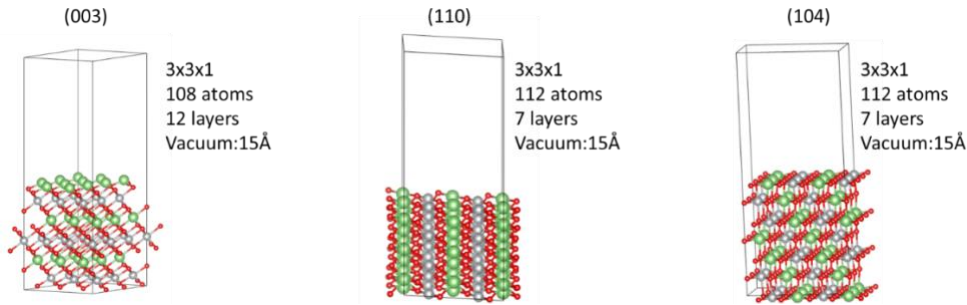


Figure 4. Representation of the (003) and (104) surfaces of the hR12 lattice of LiNiO₂.

The three prototypical crystal surfaces have been optimized in respect to all the atomic positions and the corresponding structural and thermodynamic features outlined.

Surface energies (γ_{hkl}) have been evaluated with the following equation:

$$\gamma^{hkl} = \left(\frac{1}{2S} \right) (E_{slab}^{hkl}(n) - nE_{bulk})$$

where S , E_{slab}^{hkl} and E_{bulk} , are the surface area, the cohesion energy of the slab and the cohesion energy of the bulk, respectively. Structural distortions have been evaluated by computing the mean atomic displacement (σ^2) in respect to the bulk with the following equation.

$$\sigma^2 = \sum_{i=1}^N \frac{[(x_i - x'_i)]^2 + [(y_i - y'_i)]^2 + [(z_i - z'_i)]^2}{N}$$

Where (x_i, y_i, z_i) and (x'_i, y'_i, z'_i) are the positions of analogue atoms in the bulk and in the slab respectively. Computational results are shown in the Figure 5.

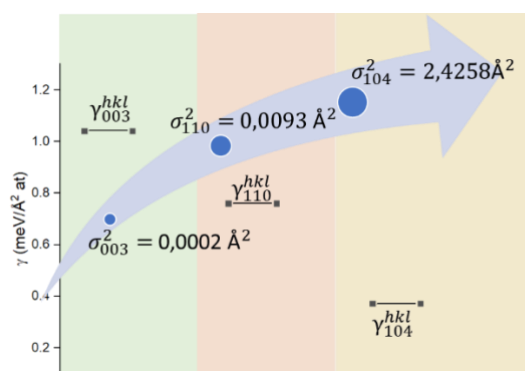


Figure 5. Surface stabilities and atomic displacements of the LiNiO₂ slabs

Surface stabilities and atomic displacements of the LiNiO₂ slabs. Overall, the (104) surface of LiNiO₂ monoclinic lattice is the most stable one and shows also the larger atomic displacement, thus suggesting an extended surface reconstruction and charge transfer from bulk to surface.

Acknowledgments

The authors want to acknowledge the financial support of the European Union's Horizon Europe transport program under the project SiGNE (grant agreement No 101069738).

References

- [1] M. J. Burke, J. C. Stephens, *Energy Res Soc Sci* **2018**, 35, 78.
- [2] J. F. Peters, M. Baumann, B. Zimmermann, J. Braun, M. Weil, *Renewable and Sustainable Energy Reviews* **2017**, 67, 491.
- [3] P. Ferro, F. Bonollo, *Mater Des* **2019**, 177, DOI 10.1016/j.matdes.2019.107848.
- [4] J. Kalkhoff, G. G. Eshetu, D. Bresser, S. Passerini, *ChemSusChem* **2015**, 8, 2154.
- [5] E. Hossain, H. M. R. Faruque, Md. S. H. Sunny, N. Mohammad, N. Nawar, *Energies (Basel)* **2020**, 13, 3651.
- [6] European Commission, *Publications Office of the European Union* **2017**.
- [7] S. Yamada, M. Fujiwara, M. Kanda, *J Power Sources* **1995**, 54, 209.
- [8] F. Li, Z. Liu, J. Shen, X. Xu, L. Zeng, B. Zhang, H. Zhu, Q. Liu, J. Liu, M. Zhu, *J Mater Chem A Mater* **2021**, 9, 2830.
- [9] P. Teichert, G. G. Eshetu, H. Jahnke, E. Figgemeier, *Batteries 2020, Vol. 6, Page 8* **2020**, 6, 8.
- [10] M. Bianchini, M. Roca-Ayats, P. Hartmann, T. Brezesinski, J. Janek, *Angewandte Chemie International Edition* **2019**, 58, 10434.
- [11] T. Yoshida, K. Hongo, R. Maezono, *Journal of Physical Chemistry C* **2019**, 123, 14126.
- [12] E. Cho, S. W. Seo, K. Min, *ACS Appl Mater Interfaces* **2017**, 9, 33257.

PRODUCT AND MANUFACTURING PROCESS OPTIMIZATION USING ADVANCED CALCULATION MODELS ON HPC AND CLOUD PLATFORMS

Leonardo Cosma^{1*}, Antonio Gerardi¹, Annalisa Cassinelli¹, Rosario Dotoli¹ and Alberto Scalise²

¹*Cetma, S.S.7 km 706+030 c/o Cittadella della Ricerca, 72100, Brindisi, Italy*

²*ENEA, TERIN-ICT-IGEST Lab - S.S.7 km 706+030 c/o Cittadella della Ricerca, 72100, Brindisi, Italy*

ABSTRACT. A web application has been developed to allow non-specialised users to launch and monitor complex and resource-demanding calculations on the ENEA's CRESCO6 cluster. An appropriate workflow has been set-up with the aim to optimize a specific manufacturing process, the polymer extrusion, integrating a CFD calculation model based on the OpenFOAM code. The obtained results demonstrate that companies, especially Small and Medium Enterprises, can leverage HPC technology to improve their productivity overcoming the traditional barriers constituted by high infrastructural and technical investments.

1 Introduction

Information and Communication Technologies (ICT) have become crucial in manufacturing, yet less than a quarter of European companies, and even fewer in Italy, utilize these tools due to the technical and infrastructural demands typically met by larger firms. To boost small and medium-sized enterprises (SMEs), scalable technological solutions are necessary.

The advent of advanced design tools, High-Performance Computing (HPC) and Cloud platforms, offers pay-per-use services that could digitalize SME production efficiently. This shift towards cloud computing allows for extensive data processing and analysis outside the company, facilitating the creation of digital twins for precise scenario predictions. This transition is part of the move towards Industry 4.0, integrating automated production with advanced design tools to enhance product development, reduce physical prototyping, and improve product quality from the design stage. The OPTIMUM project exemplifies this by developing a new design process using advanced models tailored for SMEs, leveraging HPC and Cloud for strategic optimization.

2 Solution implementation

The implemented solution is a web application called OPTIMUM which is the entry point for the user to define, submit and check results of simulation jobs. Actual calculation jobs are executed in the CRESCO6 HPC cluster, but it is possible to add further HPC cluster specifying the appropriate connection parameters.

The end user, after logging in, is shown a list of the jobs already defined and can define a new job by clicking an appropriate button on the UI (User Interface). After selecting the type of simulation to be launched, the corresponding form with the appropriate controls is shown where all the simulation parameters can be defined.

The user can then start the simulation and upon its completion, download locally an archive file containing all the significant results.

The connection between the application and the HPC cluster is implemented by transferring input and output files via the cluster SCP (Secure Copy) endpoint and launching the script for the job execution via an SSH (Secure Shell) command. The launch script on the HPC cluster takes care of:

1. Determining which type of simulation must be launched.
2. Creating a working directory and setting up all the necessary input files.
3. Submitting the job via the LSF job scheduler.
4. Executing the appropriate post-processing operations when the simulation job is concluded.

For each of the defined type of simulation jobs, suitable pre- and post-processing operations are selected and executed.

The interaction between the users, the application and the Cresco6 cluster is represented in Fig. 1.

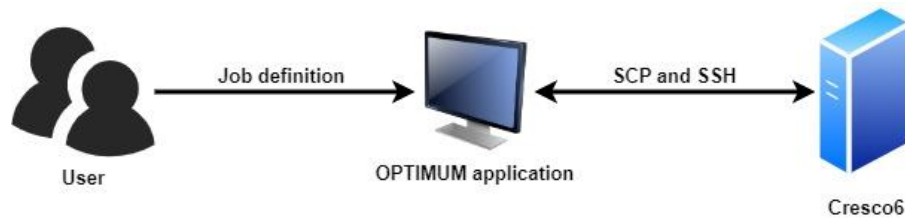


Fig. 1: Interaction between user, application and Cresco6

3 Case study

A case study has been conducted as part of the project activities, carrying out the following steps:

1. Identification of the manufacturer requirements.
2. Identification of the input and output parameters.
3. Setup of the numerical model able to reproduce the physical process.
4. Validation of the numerical model.
5. Definition of the workflow (scripts, templated input files) able to calculate the requested outputs via pre-processing, solution of the numerical model and post-processing.
6. Definition of the simulation job type on the application, so the user could launch simulation directly from the web interface.

3.1 Problem definition

Polymer extrusion for gaskets involves feeding raw polymer material into an extruder, where a rotating screw heats and pressurizes it to a molten state. The molten polymer is then forced through a die that shapes it into the desired gasket profile. Finally, the extruded gasket is cooled, typically by water or air, to solidify and maintain its shape.

One of the main problems of the extrusion process is the “die swelling”: once out from the die, the melt tends to dilatate, and this in turns cause the section to change its shape and size. The final shape and size of the gasket are due mainly to the viscoelastic behaviour of polymers and are dictated by several process parameters: temperatures, pressures, material flow rate, geometry of the die and so on. Since specific size and shape are desired, several combinations of parameters must be evaluated to find the right combination and obtain the desired geometric result. Moreover, changing the die geometry is particularly costly due to the need to physically manufacture a new die every time a modification is needed.

In **Fig. 2** the scheme of the extrusion process is shown, and the zone included into the numerical model is highlighted.

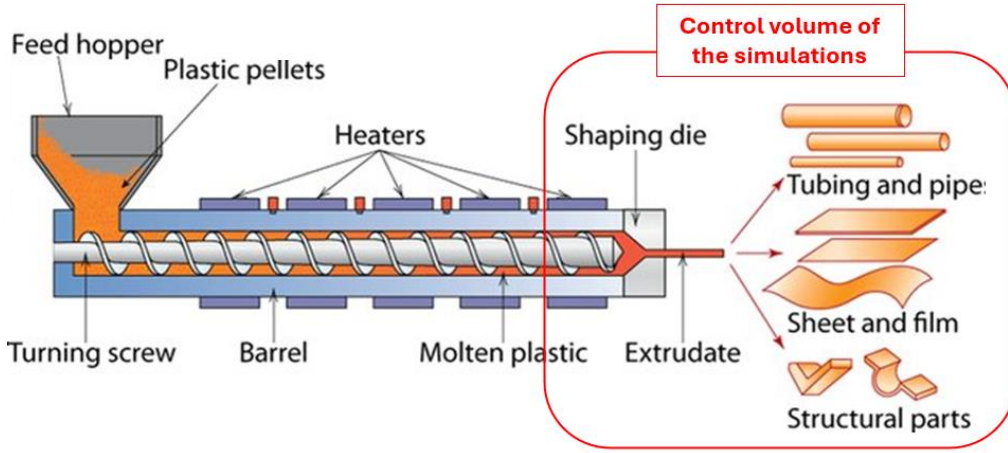


Fig. 2: Polymer extrusion and control volume of the simulations

3.2 Numerical model

The numerical simulation of the extrusion process allows to evaluate the influence on the gasket geometry of all the processing parameters and, most importantly, of the die geometry, greatly reducing the costs and time needed by the design phase of a new product.

The extrusion process is modelled via the Navier-Stokes (NS) equations that prescribe the conservation of mass, momentum and energy [1]:

$$\frac{\partial \rho}{\partial t} + \nabla(\rho \mathbf{u}) = 0 \quad (1)$$

$$\rho \left(\frac{\partial \mathbf{u}}{\partial t} + \mathbf{u} \cdot \nabla \mathbf{u} \right) = -\nabla p + \rho \mathbf{g} + \nabla \cdot \boldsymbol{\sigma} \quad (2)$$

$$\rho \left(\frac{\partial e}{\partial t} + \mathbf{u} \cdot \nabla e \right) = -p \nabla \mathbf{u} + \boldsymbol{\sigma} : \mathbf{u} + k \nabla T \quad (3)$$

To track the motion on the polymer, the Volume of Fluid (VOF) approach is integrated into the NS equations. The VOF method enables to track and locate the interface between the polymer and the surrounding air, thus allowing the correct evaluation of the gasket section. The volume fraction of the polymer α is defined as a new quantity: it varies between 0 (absence of polymer) to 1 (presence of polymer) and is solved adding a new equation to the NS system:

$$\frac{\partial \alpha}{\partial t} + \mathbf{u} \cdot \nabla \alpha = 0 \quad (4)$$

In the other equations the material properties corresponding to the air or the polymer are assigned depending on the value locally assumed by α .

Finally, the expression of the last term of the equation (2) considers the actual viscoelastic behaviour of the polymer. For non-Newtonian fluids, the term depends on the velocity gradient via the viscosity of the material η which is not a constant but varies with the shear rate $\dot{\gamma}$

$$\nabla \cdot \boldsymbol{\sigma} = \eta(\dot{\gamma})(\nabla \mathbf{u} + \nabla \mathbf{u}^T) \quad (5)$$

and for the viscosity the Bird-Carreau model is assumed:

$$\eta(\dot{\gamma}) = \eta_0 [1 + (\lambda \dot{\gamma})^2]^{\frac{n-1}{2}} \quad (6)$$

with constants η_0 , λ and n to be determined experimentally.

The open-source code OpenFOAM has been used to solve the equations of the model using the Finite Volume Method (FVM) technique [2].

3.3 Model validation and application

To validate the approach, the extrusion of a medium-complex geometry has been modelled and the obtained section size and shape has been compared against available experimental measures. In **Fig. 3** the discretized domain and the obtained extruded polymer are shown. The accuracy of the model has been at 5%, meaning that a maximum error of 5% is expected when comparing experimental and numerical measures of thickness or length of the extruded section.

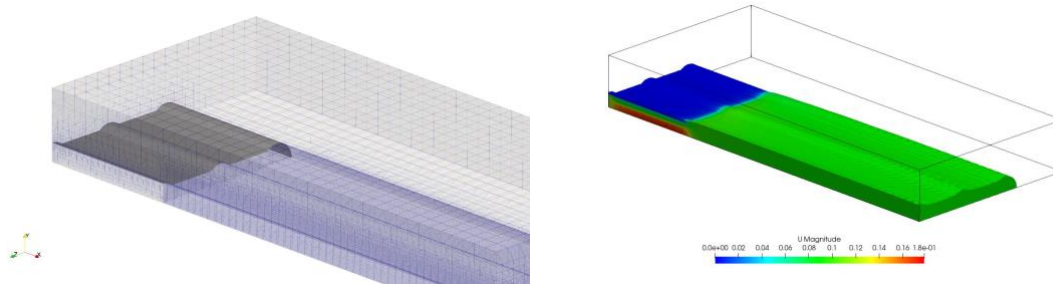


Fig. 3: Validation model: CFD mesh (left) and polymer extrusion (right)

Once validated, the model has been integrated into a workflow able to build the numerical model, solving it by submitting the calculation on the Cresco6 cluster and obtaining the final geometry of the gasket at the end of the process. The input parameters of the workflow are the thermophysical properties of the polymer, the flow rate, the geometry of the die and the process temperature.

The developed workflow has been used to optimize the process parameters obtained the desired geometry for a complex gasket. The geometry and the discretization of the calculation domain is shown in **Fig. 4**.

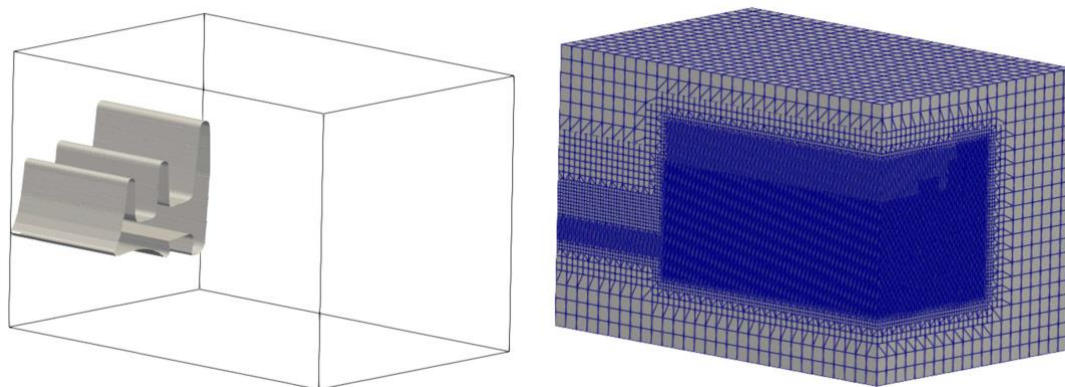


Fig. 4: Case study: geometric domain (left) and CFD mesh (right)

The calculation model is made of 8.5 million cells and requires 20000 iterations. A scalability test has been executed to determine the optimal resource allocation on the Cresco6 cluster. Results are shown in Table 1. The chosen configuration is the 2 nodes – 96 processes, which gives a wall time of about 13 hours. As a comparison, on a modern workstation with 8 cores, the same simulation would have required 13 days.

Table 1: Scalability test.

Allocated nodes	Allocated processes	Wall time	Speed up	Efficiency
1	48	76500s	-	-
2	96	44800s	1.77	0.885
4	192	38500s	2.06	0.515

In **Fig. 5** the output of the workflow is shown. On the left, an axonometric view of the melt flowing outside of the die is shown, while on the right a comparison between the target section (blue) and the extruded section (red) is reported.

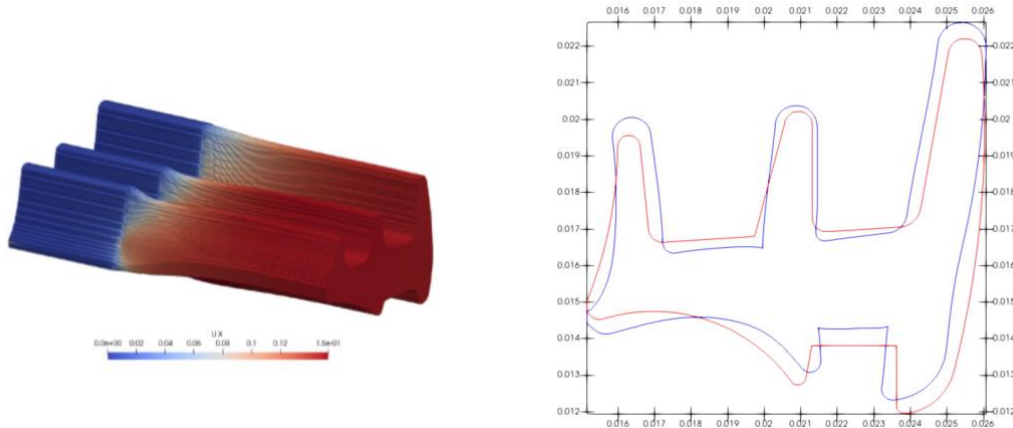


Fig. 5: Case study: melt view (left) and section analysis (right)

The estimated development time for a new gasket is of about 50 working days, while the costs development is estimated at about 20000 € (including personnel, material, energy consumption and external suppliers). By using the developed application and including the simulation workflow into the company business process, the total development time is reduced to half the initial at 25 working days. By reducing experimental tests and the number of sacrificial matrices to be produced, obviously, both the material used and energy consumption can be halved, along with their associated costs.

In the specific case of the window seal, only one die has been produced, potentially reducing procurement costs, barring market fluctuations.

4 Conclusion

In conclusion, a web application able to define and manage job calculations on the Cresco6 cluster has been developed. The user can define different kind of simulation jobs to be executed and the web application can launch and monitor jobs on the cluster via specific protocols to exchange data and execute commands.

A specific workflow for the simulation of the polymer extrusion process has been setup, integrating a validated CFD numerical model based on OpenFOAM open-source code. The obtained results demonstrated not only the validity of the numerical approach but also the economic benefit for the company that integrated this approach in its business process.

Acknowledgments

This research is part of the Project “*OPTIMUM - Ottimizzazione di Prodotti/processi nelle Imprese Manifatturiere mediante l'Utilizzo di Modelli di calcolo avanzati su piattaforme HPC e Cloud*” supported by “Asse 1 - Azione 1.1.3. del Programma Operativo Nazionale «Imprese e Competitività» 2014-2020 FESR” of the Italian Ministry of Economic Development (PON MISE - Prog. n. F/190112/01/X44 - CUP: B98I20000200005).

The computing resources and the related technical support used for this work have been provided by CRESCO/ENEAGRID High Performance Computing infrastructure and its staff [3]. CRESCO/ENEAGRID High Performance Computing infrastructure is funded by ENEA, the Italian National Agency for New Technologies, Energy and Sustainable Economic Development and by Italian and European research programmes, see <http://www.cresco.enea.it/english> for information. CETMA's authors are grateful to Mr. Alberto Scalise (ENEA) for his continuous support during the research activities.

References

- [1] P. K. Kundu et al., Fluid Mechanics, 5th edition, 2012, Academic Press.
- [2] C. Greenshields and H. Weller. Notes on Computational Fluid Dynamics: General Principles. 2022, CFD Direct Ltd
- [3] F. Iannone et al., "CRESCO ENEA HPC clusters: a working example of a multifabric GPFS Spectrum Scale layout," 2019 International Conference on High Performance Computing & Simulation (HPCS), Dublin, Ireland, 2019, pp. 1051-1052, doi: 10.1109/HPCS48598.2019.9188135.

SCALE-RESOLVING SIMULATIONS OF THE FLOW FIELD DEVELOPING AROUND CIRCULAR CYLINDERS IN TANDEM CONFIGURATION FOR FAR-FIELD AEROACOUSTIC PREDICTION

Valerio D'Alessandro^{1*} and Matteo Falone¹

¹*Università Politecnica delle Marche, Dipartimento di Ingegneria Industriale e Scienze Matematiche, Via Brecce Bianche 12, 60131, Ancona, Italy*

ABSTRACT. The prediction of the aerodynamic noise produced by bluff bodies is important in broad range of engineering applications. However, a good balance between accuracy and required computational resources is not easy to find. In this work, the capabilities of a hybrid RANS/LES approach supported by Curle's acoustic analogy in predict the flow/aeroacoustic fields developing around two circular cylinders in tandem arrangement is investigated. It was found that the adopted modelling is suitable for describing the main flow characteristics, while some inaccuracies were noticed in the aeroacoustic prediction.

1 Introduction

The evaluation and the control of the self-noise produced by the aerodynamic interaction between the incoming flow and bluff bodies is an important issue in many engineering applications, such as automotive external mirrors, aircraft landing-gears, antennas and built environment.

Experimental studies have been conducted to quantify the resulting flow/aeroacoustic fields and to provide a benchmark for a numerical approach to the problem, [1-2]. In fact, computational studies could help to better investigate the aeroacoustic noise radiated by the rigid bodies.

In this context, Direct Numerical Simulation (DNS) and Large-Eddy Simulation (LES) could be appealing because of their capabilities in accurately predict the relevant features of such problems. However, the main drawbacks of high-resolution scale-resolving strategies is related to the computational effort they require, especially for high Reynolds number flows.

Differently, Reynolds-Averaged Navier-Stokes equations (RANS) approach supported by the adoption of an acoustic analogy can be low resources demanding. Nevertheless, RANS models are limited in accuracy for complex flows involving large turbulent structures, such separation around bluff-bodies.

To overcome these problems, a hybrid RANS/LES modelling is suitable to face this well-known benchmark, thanks to its capabilities in combine the advantages of the two approaches, [3]. In particular, the Improved Delayed-Detached-Eddy Simulation (IDDES) model seems to be the best candidate because was developed to avoid typical issues related to hybrid formulations, i.e. Grid-Induced Separation, Modeled-Stress Depletion and log-layer mismatch, [4].

For these reasons, in this work a campaign of computations is performed to test the effectiveness of a scale-resolving approach in predict the flow and aeroacoustic fields developing around two circular cylinders in tandem configuration. The Spalart-Allmaras (SA) IDDES formulation was adopted to compute the flow features and the Curle's analogy was employed to evaluate the acoustic pressure.

2 Model description

2.1 Governing equations

The adopted flow model relies on unsteady, incompressible Navier-Stokes equations handled with a hybrid RANS/LES approach that operates like RANS in the near-wall regions and like LES in separated

* Corresponding author. E-mail: v.dalessandro@univpm.it

flow zones. It employs the Spalart-Allmaras IDDES formulation, [5], in which the minimum wall distance d in the SA-RANS model is replaced by a modified length scale \tilde{d} as follows:

$$\tilde{d} = \tilde{f}_d(1 + f_e)d + (1 - \tilde{f}_d)C_{DES} \Delta. \quad (1)$$

The blending function \tilde{f}_d and the elevating function f_e in eq.1 depend both on the grid spacing and the flow field, C_{DES} is equal to 0.65 and sub-grid length scale Δ is defined as in Shur et al., [5]:

$$\Delta = \min\{\max[C_w d, C_w h_{\max}, h_{wn}], h_{\max}\}, \quad (2)$$

where C_w is equal to 0.15, h_{\max} is the maximum local grid spacing and h_{wn} denotes the grid step in wall normal direction.

Aeroacoustic perturbation is computed in the far-field starting from the instantaneous flow pressure p , deriving from the computations. Specifically, Curle's analogy for low Mach number flows was used to evaluate the acoustic pressure, [6]:

$$p(\mathbf{x}, t) - p_\infty = \frac{1}{4\pi} \int_S l_i n_j \left(\frac{1}{a_\infty r} \frac{\partial p}{\partial t} \delta_{ij} + \frac{p}{r^2} \delta_{ij} \right) dS \quad (3)$$

In eq. 3, S is the surface of the emitter body, r is the distance between the source and the observer, n_j is the surface normal pointing toward the fluid, l_i is a unit vector pointing from the source to the observer and p_∞ and a_∞ represent the reference pressure and the free stream speed of sound respectively.

2.2 Numerical approximation

The unstructured, cell-centred finite volume approach available within OpenFOAM library was adopted to achieve the governing equations solution. A high-resolution NVD Gamma scheme was used for convective terms approximation, except for momentum fluxes that are discretized with the hybrid approach proposed by Travin et al., [7], to ensure the computations stability. Diffusive contributions are second-order approximated, while time integration technique relies on an implicit, three level, second-order scheme. Furthermore, the Pressure-Implicit with Splitting Operators (PISO) procedure was employed for pressure-velocity coupling.

2.3 Computational details

The cylinders arrangement here considered has streamwise gap spacing of $L/D = 3.7$ as showed in Fig. 1. The Reynolds number based on the cylinder diameter D is equal to $1.66 \cdot 10^5$ and the reference Mach number is set $M_\infty = 0.1274$ in Curle's acoustic analogy. Moreover, acoustic data were collected according to the microphone A in the experiments, $\mathbf{x}/D|_{micA} = \{-8.33, 27.817, 0\}$ with respect to the centre of the front cylinder.

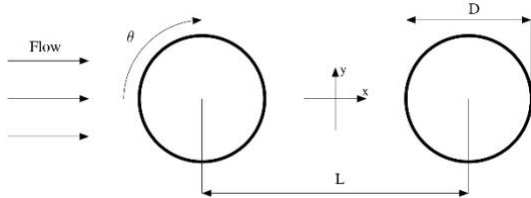


Fig. 1: Schematic of circular cylinder in tandem configuration.

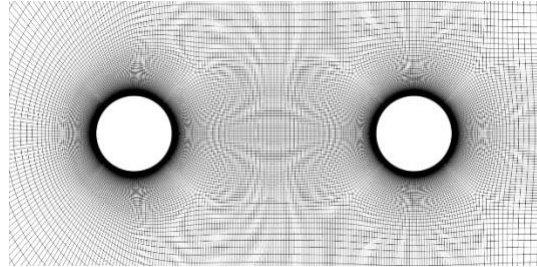


Fig. 2: C-type fully structured mesh, near wall and gap region refinement.

The 3D computational domain was discretized following two different strategies. In the first one, three OH-type fully structured grids were adopted, while in the second one, two C-type fully structured meshes were built in order to reduce the cells number and the consequent computational time. The main features of the used meshes are summarized in Tab. 1.

Cells were clustered near the cylinders wall and in the gap region (Fig. 2) to provide a $y^+ > 1$ and a proper discretization between the rigid bodies. Dimensionless time step was set to $0.0015 D/U_\infty$, ensuring a CFL number lower than 0.8. For all computations, statistics were collected over $200 D/U_\infty$ time units after the fully development of the flow field.

Table 1: Computational grids main features.

Grid	Type	Spanwise extension z/D	Cells number in z	Total cells number
G1	OH	3	80	$6.6 \cdot 10^6$
G2	OH	3	96	$7.5 \cdot 10^6$
G3	OH	6	192	$15 \cdot 10^6$
G4	C	3	40	$2.5 \cdot 10^6$
G5	C	3	40	$3 \cdot 10^6$

3 Results

In this section the obtained results are compared with the experimental data from Basic Aerodynamic Research Tunnel (BART), [1], and Quiet Flow Facility, [2], at NASA Langley Research Centre.

Fig. 3 shows the time-averaged pressure coefficient, $c_p = 2(p - p_\infty)/(\rho U_\infty^2)$, on the front cylinder surface. It is evident that results deriving from G1 to G4 are in a very good agreement with QFF data, while G5 produces an overestimation in c_p in the separated flow region $110^\circ < \theta < 250^\circ$. This is probably due to the cylinder circumferential discretization that, in this case, provides a non-uniform cells distribution along the surface. The not correct reconstruction of the flow field around the upstream cylinder affects also the downstream one. In fact, G5 totally fails in predicting the rear cylinder pressure coefficient behaviour in proximity to the stagnation point, as noticeable in Fig. 3. Conversely, the adoption of the other grids provides more reasonable results, quite aligned with the experimental data.

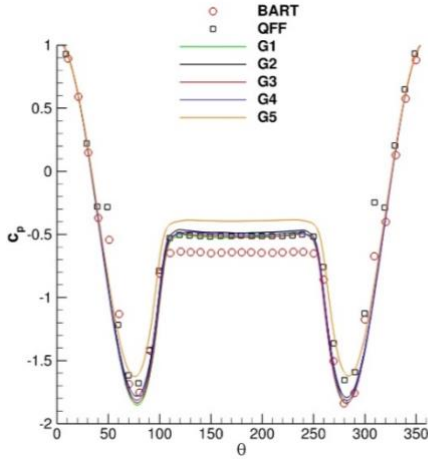


Fig. 3: Time-averaged pressure coefficient – front cylinder.

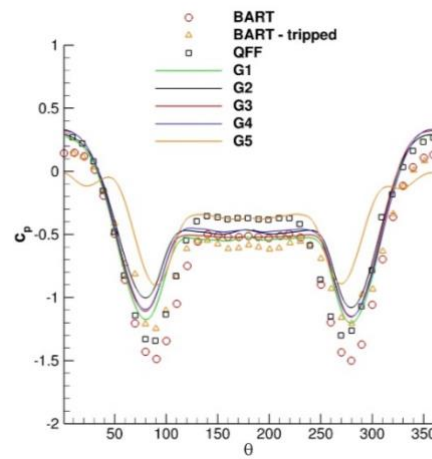


Fig. 4: Time-averaged pressure coefficient – rear cylinder.

For what concerns the fluctuating pressure coefficient, $c_{p,rms}$, the above-described trend is confirmed: the flow field developed around the front body is satisfyingly described in the first four computations, as showed in Fig. 5. However, this is not true when the rear cylinder is considered. In this case, $c_{p,rms}$ is not well predicted, especially in its peaks next to the separation points, i.e. $\theta \cong 110^\circ$ and $\theta \cong 240^\circ$. It was shown that for the considered case, the pressure fluctuation on the downstream cylinder and the consequent lift oscillation produces the principal tone in the far-field acoustic spectra, [3]. Considering this evidence, it is obvious that the discrepancy between the computed data and the experimental ones highlighted in Fig. 6 are reflected in the aeroacoustic predictions.

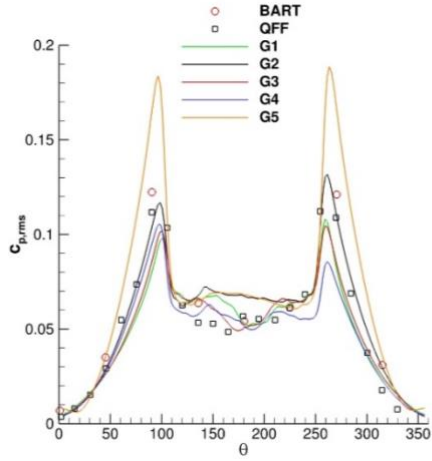


Fig. 5: Fluctuating pressure coefficient – front cylinder.

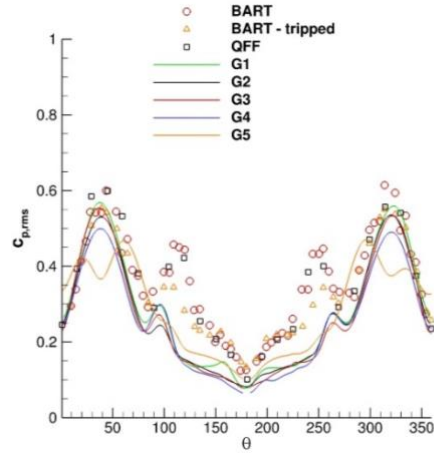


Fig. 6: Fluctuating pressure coefficient – rear cylinder.

The acoustic spectra of the fluctuating pressure computed in correspondence of microphone A is plotted in Fig. 7. As expected, our computations slightly underestimate the tonal peak both in amplitude and in frequency. Moreover, only G3 computation is able to capture the first harmonic, while the second one is not noticeable in none of our simulations. Obtained results suggest the sensitivity of the acoustic pressure to the spanwise domain width and its discretization.

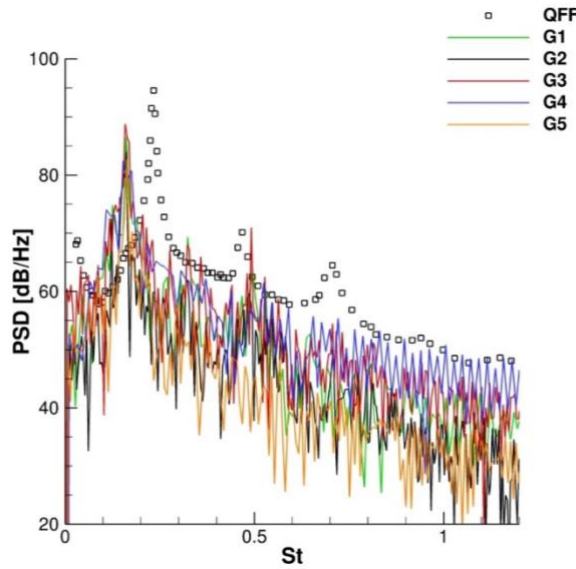


Fig. 7: Acoustic spectra comparison at microphone A.

4 Conclusions

In this work, a suite of simulations of the NASA tandem cylinders benchmark were performed. A scale-resolving Spalart-Allmaras IDDES approach was adopted to compute the flow field, while Curle's analogy was employed to evaluate the far-field aeroacoustic features. Obtained results show that our modelling is suitable for describe the main flow characteristics.

However, some discrepancies between the acoustic experimental data and the computed were found. It was noticed that in our approach the predicted acoustic pressure strongly depends on the spanwise extension of the domain and its discretization. Further investigations will be devoted to evaluate the best combinations of turbulence modelling and sub-grid length scale definition able to minimize the computational effort and provide accurate results.

Acknowledgments

The computing resources and the related technical support used for this work have been provided by CRESCO/ENEAGRID High Performance Computing infrastructure and its staff [8]. CRESCO/ENEAGRID High Performance Computing infrastructure is funded by ENEA, the Italian National Agency for New Technologies, Energy and Sustainable Economic Development and by Italian and European research programmes, see <http://www.cresco.enea.it/english> for information."

References

- [1] L. Jenkins, D. Neuhart, C. McGinley, M. Khorrami, M. Choudhari. Measurements of Unsteady Wake Interference Between Tandem Cylinders, 36th AIAA Fluid Dynamics Conference and Exhibit, 2006.
- [2] D.P. Lockard, M.R. Khorrami, M.M. Choudhari, F.V. Hutcheson, T.F. Brooks, D.J. Stead. Tandem cylinder noise predictions, 13th AIAA/CEAS Aeroacoustics Conference, 2007.
- [3] D.P. Lockard. Summary of the tandem cylinder solutions from the benchmark problems for airframe noise computations-I workshop, 49th Aerospace Sciences Meeting Including the New Horizons Forum and Aerospace Exposition, 2011.
- [4] V. D'Alessandro, S. Montelpare, R. Ricci. Detached-eddy simulations of the flow over a cylinder at $Re=3900$ using OpenFOAM, *Comput. & Fluids*, 2016.
- [5] M.L. Shur, P.R. Spalart, M.K. Strelets, A.K. Travin. A hybrid RANS/LES approach with delayed-DES and wall-modelled LES capabilities, *Int. J. Heat Fluid Flow*, 2008.
- [6] N. Curle. The influence of solid boundaries on aerodynamic sound, *Proc. Roy. Soc. Lond. A*, 1955.
- [7] A. Travin, M. Shur, M. Strelets, P.R. Spalart. Physical and numerical upgrades in the detached-eddy simulation of complex turbulent flows, *Advances in LES of Complex Flows, Fluid Mechanics and Its Applications*, 2004.
- [8] F. Iannone et al., "CRESCO ENEA HPC clusters: a working example of a multifabric GPFS Spectrum Scale layout," 2019 International Conference on High Performance Computing & Simulation (HPCS), Dublin, Ireland, 2019, pp. 1051-1052, doi: 10.1109/HPCS48598.2019.9188135.

PRELIMINARY CFD SIMULATION RESULTS OF THE NACIE-UP WIRE WRAPPED PIN BUNDLE FOR THE IAEA NACIE-CRP

Roberto Da Via^{13*}, Francesco Lodi¹, Giacomo Grasso¹

¹ENEA NUC-ENER-PRO, C.R. "E. Clementel", via Martiri di monte sole 4, 40129 Bologna, Italy

ABSTRACT. The present paper provides the preliminary results obtained by means of Computational Fluid Dynamic simulations of turbulent flows, in mixed convection regime, inside the NACIE-UP 19 wire wrapped pin bundle. The results were obtained in the context of the IAEA Coordinated Research Project on the NACIE-UP facility. A fork of the open-source CFD code OpenFOAM, developed at ENEA within the PRO laboratory, has been used to perform the simulations on ENEA CRESCO6 High Performing Computing system.

1 Introduction

The IAEA Coordinated Research Project on the NACIE-UP facility [1] is a benchmark test which aims at contributing to simulation code validation, at investigating the applicability of existing simulation codes to heavy liquid metals and at investigating the heat exchange in wire wrapped fuel bundles. The benchmark is based on the experimental data collected by ENEA on the NACIE-UP facility and focuses on the transition from forced to natural convection regime in turbulent Lead Bismuth Eutectic flows. The facility is a loop circuit with a test section consisting of 19 wire-wrapped and electrically heated pins arranged in hexagonal lattice [2]. The benchmark, with the available experimental data, is designed to allow the validation of Computational Fluid Dynamic, sub-channel and system codes. The project activities span over a time range of 4 years and involve blind and non-blind simulations of three experimental tests performed by ENEA in 2017, namely ADP06, ADP07 and ADP10. Each test consists of a steady-transient-steady state sequence of flow conditions, with the first and the latter steady states being in forced and natural convection regimes, respectively. The three tests differentiate for scheme of active and non-active pins (in terms of producing thermal power) in the bundle: in ADP10 all pins produce the same thermal power, in ADP06 only the 7 inner pins are active (with uniform thermal power), while in ADP07 a 120-degree sector of 9 pins is non-active. For each test, the thermal power produced by each pin is kept constant, during the test, and the transient condition is initiated by a shutdown of the feed pump, allowing the natural circulation regime to develop. The NUC-ENER-PRO laboratory is involved in the benchmark for the validation of sub-channel code ANTEO+ and of CFD code OpenFOAM, whose results obtained for the first-year activities of the benchmark are shown in the following.

2 The software

The numerical simulations have been performed using a custom fork, developed within the PRO laboratory, of OpenFOAM [3]. In this fork, additional turbulent heat transfer models, particularly suited for liquid metal turbulent flows, have been implemented and it is in the interest of the PRO laboratory to validate them against the experimental data available in the CRP. The computational grids have been generated using *hexaBundleMesher*, an in-house developed meshing algorithm for bare and wire wrapped hexagonal pin bundles. Due to the necessity of simulating the heat transfer across the pins, as

¹³ * Corresponding author. E-mail: roberto.davia@enea.it

will be discussed in the following, the algorithm has been extended to also generate the discretization pin internal layers, so to have a mesh structure for each material composing the real pin.

3 The geometrical and computational model

The pin bundle of the NACIE-UP facility is made of 19 electrically heated pins arranged in hexagonal lattice. The diameter of each pin is equal to 6.55 mm, the wire diameter and axial pitch are 1.75 and 262 mm, respectively, and the lattice pitch is 8.4 mm. The length of the pin wire wrapped section is 1441 mm, while the active part is 600 long [2]. By indicating with $z=0$ the axial location where the active part begins, the bundle ends at $z=700$ mm. In the region prior to the beginning of the heated section, a small thermal power is produced by the pin and no experimental data is available. For this reason, the length of the computational domain has been shortened and spans from $z=-348$ mm up to $z=700$ mm. This allows us to obtain a fully developed flow condition at the entry of the heated section, but with a smaller domain.

As the simulated problem consists of a conjugated heat transfer, between the LBE flow and the heated pins, the OpenFOAM application `chtMultiRegionFoam` has been used. This application requires the generation of separate meshes for each material layer and for each unconnected domain.

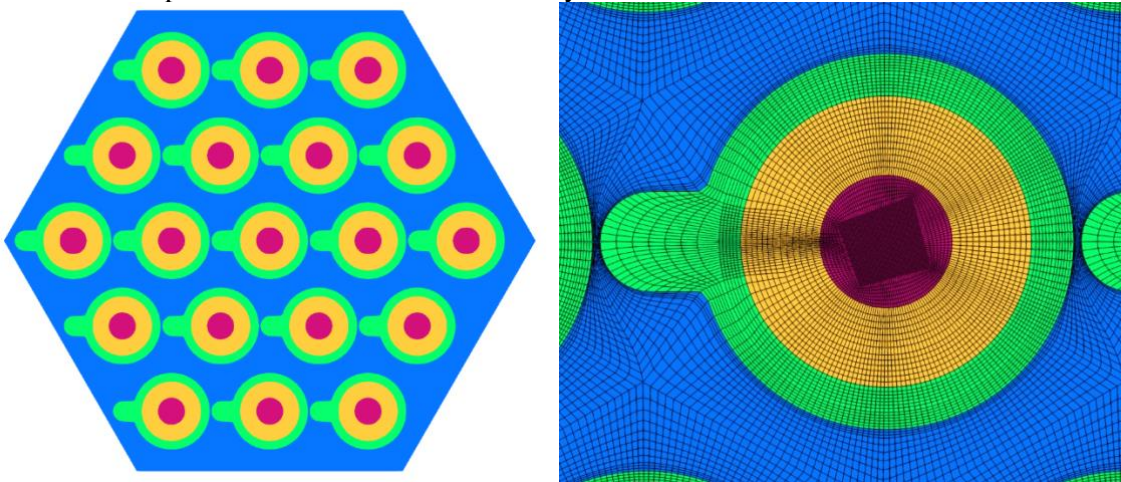


Figure 1: Cross section view of the wire wrapped fuel bundle geometry (left) and close-up view of the conformal mesh for the fluid and pin layer domains.

Since the pins have been split into an inner copper layer, where a volumetric heat source is applied, an intermediate layer of bohrium-nitride and an outer layer of cladding material (including the wrapping wires), the whole model counts 57 meshes for the pin layers (2×10^6 cells for each layer of cladding and bohrium nitride, 2.9×10^6 cells for each copper region) and a mesh (44×10^6 cells) for the fluid domain. A cross-section view of the pin bundle, with regions of same materials highlighted with same colors, is shown on the left of Figure 1, while on the right the grid resolution, with conformal discretization at material interfaces, can be seen, still from the bundle cross-section. The setup shown in Figure 1 is the last that has been simulated and it is labelled as Fluid Cladding Bohrium-nitride Copper (FCBC) case. A first test was performed only considering the Fluid and Cladding (FC) domains, with a uniform heat flux imposed on the inner boundary of the cladding layer in place of the volumetric heat source imposed in the copper region.

The turbulence models used with the `chtMultiRegionFoam` are the `kw-SST` [4], for the dynamical turbulence, and the Kays correlation for the turbulent Prandtl number [5]. On the inlet section a fixed mass flow rate condition has been set, with associated values for the turbulence quantities, while on the outlet section outflow boundary conditions have been set. Standard wall functions have been used on the fluid-cladding boundary interfaces, while for the pin layers the top and bottom boundaries are considered adiabatic. The heat exchange through the coupled boundaries is handled by OpenFOAM

with proper boundary conditions. The temperature dependent physical properties of the four different materials are set according to [2].

Table 1: Reference values of inlet temperature, mass flow rate and thermal power for the simulated steady state cases of ADP06 and ADP10

Case	Q [kW]	T _{ss1} [°C]	Mfr _{ss1} [kg/s]	T _{ss2} [°C]	Mfr _{ss2} [kg/s]
ADP06	250	228	2.66	208	2.56
ADP10	250	225.4	1.33	207.6	1.33

4 Results

The computed results are for the steady state conditions of ADP06 and ADP10, i.e., the target cases scheduled for the first-year activities of the benchmark. The reference values of thermal power generated by the pins, coolant inlet temperature and mass flow rate are reported in Table 1.

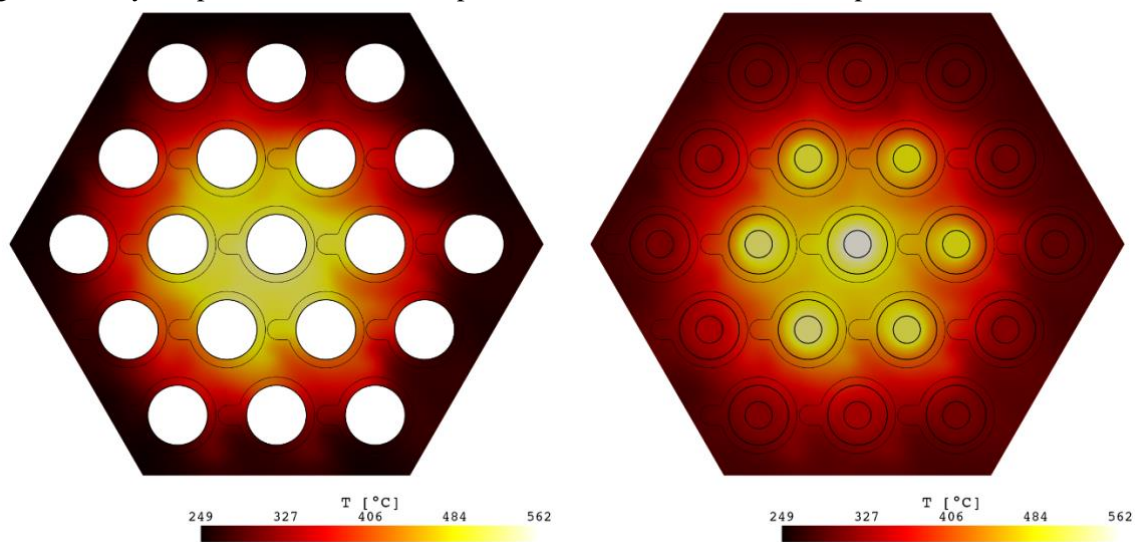


Figure 2: Comparison of FC (left) and FCBC (right) temperature fields on bundle cross section on the same axial location for steady state 2 condition of ADP06 case.

Here we compare the results of the FC and FCBC cases obtained for the second steady state condition of ADP06 test case. Since only the 7 inner pins are active, this test allows us to better understand some peculiarities of the heat exchange that are less evident in the case of all active pins. In the computational models of FC and FCBC cases, for the non-active pins, on the inner surface of the cladding material an adiabatic boundary condition is set (FC), while no volumetric heat source is set on the copper regions (FCBC). In Figure 2, a comparison of temperature distributions of FC and FCBC cases, on the bundle cross section taken at $z=562$ mm (the last monitored plane with the experimental setup), is shown. The non-active pins of the FCBC case act as important means for heat diffusion, as the coolant temperature in the region close to the wrapper is higher than that of FC case. In Figure 3 a similar comparison is shown for the temperature values computed along several axial locations on pin #3 outer surface. For the same positions, experimental data are reported as reference values. The modeling of the pin inner layers allows us to obtain more accurate results as FCBC case results are much closer to reference experimental data.

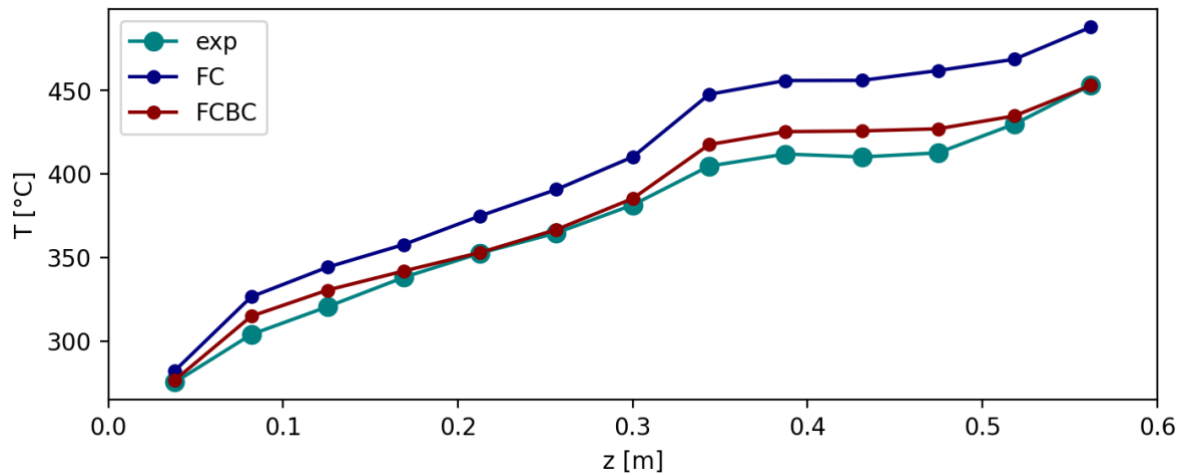


Figure 3: Comparison of temperatures from FC and FCBC cases, along several pin #3 outer surface axial location, for steady state 2 of ADP06 with experimental values

5 Conclusions

The present paper summarizes a part of the results obtained by the PRO laboratory during the first-year activities of the ongoing IAEA NACIE CRP. In this context, CFD simulations of turbulent flows inside the NACIE-UP 19 wire wrapped pin bundle have been performed using OpenFOAM code. The simulated tests differ in the scheme of active and non-active pins of the bundle, showing that, when non active, the pins act as important means for heat diffusion. This outcome has been obtained by comparing the obtained CFD results with the experimental data made available by ENEA in the CRP.

Acknowledgment

The data and information presented in the paper are part of an ongoing IAEA coordinated research project on "Benchmark of Transition from Forced to Natural Circulation Experiment with Heavy Liquid Metal Loop – CRP- I31038"

References

- [1] Benchmark of Transition from Forced to Natural Circulation Experiment with Heavy Liquid Metal Loop, <https://www.iaea.org/projects/crp/i31038>
- [2] Di Piazza, I., Hassan, H., Lorusso, P., Martelli, D. Benchmark specifications for NACIE-UP facility: non-uniform power distribution tests, 2022, ENEA, Italian National Agency for New Technologies, Energy and Sustainable Economic Development, Italy. NA-I-R-542.,
- [3] Official OpenFOAM v9 github repository: <https://github.com/OpenFOAM/OpenFOAM-9>
- [4] Menter, F. R., Kuntz, M., and Langtry, R. (2003). Ten Years of Industrial Experience with the SST Turbulence Model. *Turbulence, Heat and Mass Transfer 4*, ed: K. Hanjalic, Y. Nagano, & M. Tummers, Begell House, Inc., 625 - 632.
- [5] Kays, W. M. (May 1, 1994). "Turbulent Prandtl Number—Where Are We?" *ASME. J. Heat Transfer*. May 1994; 116(2): 284–295

SIMULATING 3D CHROMOSOME STRUCTURE THROUGH POLYMER PHYSICS AND HIGH-PERFORMANCE COMPUTING

Florinda Di Pierno^{1,4}, Alex Abraham^{2,4}, Sougata Goha^{2,4}, Francesca Vercellone^{3,4}, Andrea Fontana^{2,4}, Simona Bianco^{2,4}, Andrea Maria Chiariello^{2,4}, Mattia Conte^{2,4*} and Andrea Esposito^{2,4*}

¹*Dipartimento di Ingegneria Chimica dei Materiali e della Produzione Industriale (DICMaPi), Università di Napoli Federico II, Piazzale Vincenzo Tecchio 80, 80125, Naples, Italy*

²*Dipartimento di Fisica, Università di Napoli Federico II, Complesso Universitario di Monte Sant'Angelo, 80126, Naples, Italy*

³*DIETI, Università di Napoli Federico II, Biennio Ingegneria, Via Claudio 21, 80125, Naples, Italy*

⁴*INFN Napoli, Complesso Universitario di Monte Sant'Angelo, 80126, Naples, Italy*

**Corresponding authors. Email: andrea.esposito@na.infn.it; mattia.conte@na.infn.it*

ABSTRACT. Recent advances in Molecular Biology are providing innovative tools to investigate the complex three-dimensional (3D) organization of the genome within the cell nucleus. These progresses drive the development of quantitative models from mathematics and physics to uncover the mechanisms underlying chromosome folding. In particular, Polymer Physics models combined with high-performance computing (HPC) simulations play a crucial role in understanding how genome organizes to bring specific genes and regulatory elements into spatial proximity. Despite these advances, the very molecular details of such an organization remain elusive. Here, we discuss a recent study that employs Polymer Physics and Machine Learning to study the 3D folding of mammalian chromosomes, showing that a combinatorial arrangement of few binding site types, corresponding to specific chemical species, is sufficient to explain complex patterns of genomic contacts genome-wide. These findings emphasize the importance of integrating theoretical models, experimental data, and HPC tools to unravel the principles of chromosome folding and its functional implications.

1. Introduction

The 3D organization of the genome within the cell nucleus is a key aspect of cellular function and gene regulation [1–4]. Recent advances in molecular biology, driven by technologies like Hi-C [5–9], GAM [10–13] and SPRITE [14, 15], have significantly enhanced our understanding of how chromatin is folded in the cell nucleus [16, 17]. The genome is structured into hierarchical layers, including Topologically Associating Domains (TADs) [3, 18–20], loop domains [21, 22] and larger chromatin compartments such as A/B compartments [5, 23], sub-TADs [24] and meta-TADs [25]. These structures are not merely architectural, but functionally critical, as they facilitate interactions between regulatory elements and their target genes, crucial for gene expression [20, 26]. Disruptions of this spatial organization have been associated with numerous diseases, highlighting its biological significance [4, 27–31].

Despite these advancements, the molecular mechanisms underlying genome folding remain poorly understood. It is still largely unknown how the multitude of specific DNA contacts, such as those between transcribed and regulatory regions, are orchestrated by epigenetic signals and chromatin-organizing molecules like, for instance, transcription factors (TFs). To address this challenge, quantitative models [32–50] and computational approaches [45, 51–64] powered by high-performance computing (HPC) [65–67] have been developed to interpret experimental genomic dataset and infer chromosome architecture. Among these approaches, the Strings and Binders Switch (SBS) model [40, 68–78] provides a quantitative framework by conceptualizing the genome as a polymer chain with specific binding sites that interact through thermodynamic mechanisms to form loops and higher-order structures [33–35, 40, 42–44, 71, 73, 79–82].

In this report, we focus on PRISMR [72, 81, 83, 84], a machine-learning method designed to decode experimental bulk contact (e.g., Hi-C) data and infer the optimal (minimal) arrangement of binding sites that best explains genome-wide chromatin contact patterns.

By applying PRISMR to high-resolution Hi-C data across various cell types, we gain insights into how different binding site types contribute to the 3D organization of the genome [85]. Our findings indicate that few types of PRISMR-inferred binding sites are sufficient to explain data with high accuracy and their combinatorial arrangement correlates well with the transcriptional state of chromosomes, as marked by epigenetic data [85]. Through extensive numerical and in-silico validations, including comparisons with independent experimental datasets and predictions of the impact of genomic mutations, we also show how HPC resources can enhance the analysis of large-scale genomic data, deciphering the complex interplay between chromatin structure and function.

2. Modelling 3D genome organization with Polymer Physics: the SBS Model and the PRISMR approach

To investigate chromosome three-dimensional (3D) organization, we employed the Strings and Binders Switch (SBS) model, a well-established framework rooted in Polymer Physics. In this model, chromatin is represented as a self-avoiding chain composed of polymer beads, which act as binding sites that interact with diffusive molecular binders (**Fig. 1a**). Each bead represents a coarse-grained genomic position, and only binders matching the color-coded binding site can form interactions, facilitating the formation of chromatin loops and other complex 3D structures.

A key feature of the SBS model is its ability to simulate chromatin folding based on both binder concentration and binding energy. When these factors exceed a critical threshold, the polymer transitions from a loosely connected, coil-like state (in the SAW universality class) to a compact, globular structure [71, 86]. This change is driven by polymer microphase separation, promoting the clustering of homologous binding sites, and organizing chromatin into specific contact domains (**Fig. 1e**) [40, 71, 87, 88].

The SBS model simulates these interactions using classical polymer thermodynamics [89], allowing distal chromatin segments to come into contact through binder-mediated bridging. This makes the SBS model a powerful tool for simulating genome-wide chromatin architecture and exploring the molecular mechanisms driving its organization, which is crucial for understanding how chromatin domains form and regulate gene expression and nuclear architecture.

To determine the arrangement of binding sites along the SBS polymer, we employed PRISMR, a machine learning procedure based on Polymer Physics. PRISMR infers the minimal polymer model that best matches experimental contact matrices, such as Hi-C or GAM data, allowing for the reconstruction of 3D chromosome structures and predictions of how genomic mutations can impact chromosome organization.

In PRISMR, chromatin is modelled as a polymer chain of beads, with each bead representing a genomic region. The algorithm iteratively optimizes the distribution of binding sites (color-coded) along the polymer chain, which interact with binders to mediate contacts between distant genomic loci and form loops. This optimization is achieved using a simulated annealing (SA) Monte Carlo procedure [90–94], minimizing the difference between experimental and model-predicted contact matrices.

PRISMR performs multiple iterations to identify the optimal number and arrangement of binding sites while avoiding overfitting. This approach produces a minimal yet accurate representation of chromatin 3D conformation using only bulk contact (e.g., Hi-C) data, with no need for prior knowledge of specific molecular factors. In addition to fitting contact matrices, PRISMR can integrate epigenetic data to assign molecular barcodes to the inferred binding domains, helping characterize their functional roles in chromatin organization (see below).

This combination of the SBS model with PRISMR enables a comprehensive analysis of genome-wide chromatin folding, offering insights into the mechanisms underlying genome architecture and its impact on gene regulation and cellular function.

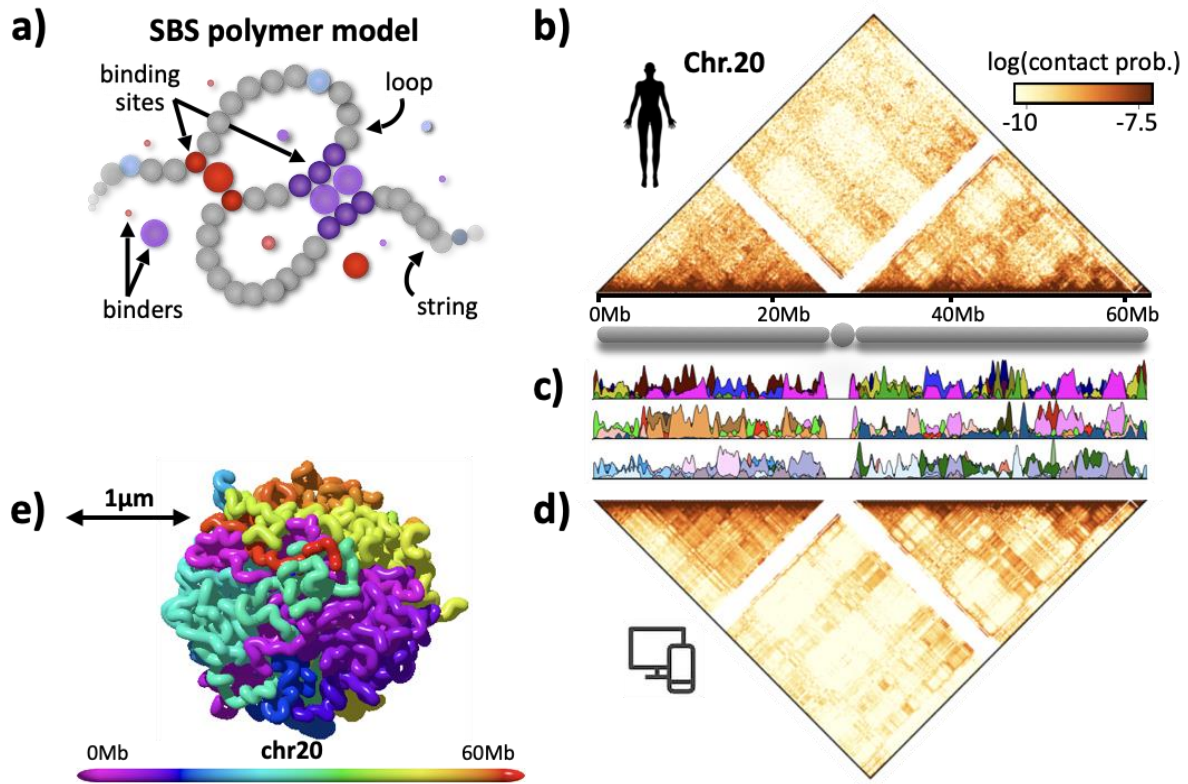


Fig. 1: a) Schematic of the SBS polymer model: in the model, diffusing molecules bridge distant cognate binding sites, forming loops. Each coloured bead represents an individual binding site, and its genomic location encodes the 1D information necessary to generate the 3D chromatin structure via polymer interactions. b) In situ Hi-C data for the entire chromosome 20 at 5 kb resolution in human GM12878 cells [21]. c) The positions and abundances of different types of binding sites (binding domains) along chromosome 20 are shown here as inferred by the PRISM method [72, 81, 83, 84]. For visualization, different domains, represented by distinct colours, are displayed in groups of 10 across different rows. d) The model-inferred contact matrix for chromosome 20 has very high Pearson, distance-corrected Pearson, and stratum-adjusted correlation coefficients (SCC) with Hi-C data ($r = 0.97$, $r' = 0.85$, and $SCC = 0.92$, respectively). e) A snapshot of the 3D structure of chromosome 20 based on the SBS model. Items adapted from [85].

3. PRISM-based Inference of Chromatin Architecture in Human Cells

To investigate the 3D organization of full-length chromosomes, we applied PRISM to high-resolution Hi-C data from the human GM12878 cell line [5–9]. The algorithm uses a simulated annealing Monte Carlo procedure to search for the best SBS model by optimizing the types and the distribution of binding sites, initially tuning parameters on chromosome 12 before applying them to other chromosomes.

Through this genome-wide application, PRISM successfully inferred SBS polymer models for each chromosome, capturing the hierarchical nature of genome organization, including TADs, loops, and larger chromatin domains. Interestingly, we found that a limited number of distinct binding site types (colors) is sufficient to accurately explain the complexity of genome-wide chromatin contacts. For example, for a medium-sized chromosome such as chr12, the optimal number of binding site types was determined to be $n = 30$. While the parameters varied slightly for smaller (chr19) and larger chromosomes (chr8), the variation in binding site types and other parameters remained modest (~15%), ensuring robustness across the genome [85].

The PRISM-inferred chromatin contacts matrices closely matched the experimental Hi-C data across all chromosomes. **Fig. 1** illustrates how the algorithm integrates Hi-C data with the SBS model to infer the spatial arrangement of chromatin. Interestingly, the arrangement of the binding domains along a

chromosome is highly non-trivial: the different types of binding sites do not simply occupy separate, contiguous regions but are spread across the entire chromosome and often overlap with each other (**Fig. 1c**).

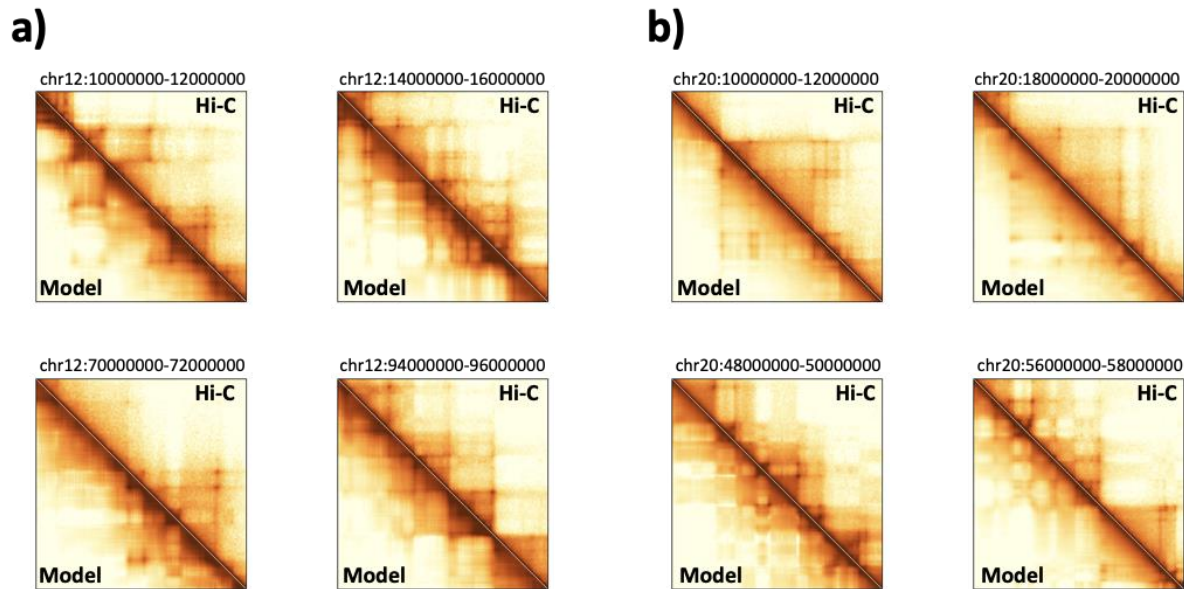


Fig.2: Comparison between Hi-C (upper triangle) and PRISMR (lower triangle) contact matrices of several 2Mb-wide genomic regions along chromosome 12 **a**) and chromosome 20 **b**). Although derived from chromosome-wide contact matrices, the PRISMR inferred SBS models do not miss shorter-scale structures at the TAD and sub-TAD level, including loops. Items adapted from [85].

Fig.1b and **1d** illustrate the high concordance between model predicted contact matrices (lower triangles) and the in situ Hi-C matrices (upper triangles) at 5 kb resolution for chromosome 20. The strong correlation between PRISMR and experimental data was quantitatively confirmed by high Pearson r , distance-corrected Pearson r' , and stratum-adjusted correlation coefficients (SCC) [95] with PRISMR achieving correlation coefficients for chromosome 20 of $r = 0.97$, $r' = 0.85$, and $SCC = 0.92$ (**Fig.1d**). These results demonstrate its precision in reconstructing 3D chromatin structures. Furthermore, the 3D structure of chromosome 20 inferred with the SBS model (**Fig. 1e**) highlights PRISMR's capability in capturing genome-wide chromosomes architecture.

In addition to large-scale features, PRISMR effectively identifies finer structures such as TADs and loops. **Figure 2** compares the experimental Hi-C matrix (upper triangle) and the PRISMR-predicted matrix (lower triangle) for selected 2 Mb genomic regions on chromosome 20. These results emphasize PRISMR's ability to integrate polymer models with computational approaches to reconstruct both large-scale chromatin compartments and smaller, more intricate structures, providing a comprehensive genome-wide view of chromatin organization.

4. Conclusions

In this study, we demonstrated that Polymer Physics models and machine learning techniques enable to accurately reconstruct the 3D architecture of chromosomes across entire genomes. Specifically, the PRISMR algorithm proves to be a powerful tool to infer the minimal set of 1D binding domains sufficient to recapitulate 3D genome-wide contact patterns. These findings shed light on the molecular mechanisms driving chromosome architecture, highlighting the importance of understanding how specific interactions can lead to the spontaneous folding of chromatin into functional 3D structures. The combinatorial code linking 1D chromatin states with 3D organization has significant implications for understanding gene regulation and the spatial organization of genomes in health and disease.

A key strength of the PRISMR methods is its versatility, as it can use input from a range of experimental data types, such as Hi-C [85] or GAM [96], without requiring additional molecular information. This

makes it adaptable for studying various genomes beyond human [81, 85], enabling key molecular insights into genome organization in other species as well. The ability of PRISMR to capture complex chromatin patterns underscore the critical power of computational tools and high-performance computing (HPC) in managing large-scale dataset in biologically relevant contexts.

As the complexity of chromatin folding grows, so does the need for more robust and detailed models. The application of HPC resources, like those provided by ENEA [97], enables the efficient simulation of such detailed molecular dynamics [98, 99]. This computational robustness is crucial for modeling large systems, as the complexity and accuracy of the simulations whether they involve polymer length, molecule numbers, or the integration of multiple molecular processes directly depend on the available computational power.

Integrating Polymer Physics models with experimental data, machine learning, and HPC will be essential for advancing our understanding of 3D genome organization. The substantial development of these computational approaches holds the potential for more accurate models that can reveal deeper insights into chromatin architecture and its functional implications across different cell types and organisms.

References

- [1]. Pombo, A., Dillon, N.: Three-dimensional genome architecture: players and mechanisms. *Nat Rev Mol Cell Biol.* 16, 245–257 (2015). <https://doi.org/10.1038/nrm3965>
- [2]. Dekker, J., Mirny, L.: The 3D Genome as Moderator of Chromosomal Communication. *Cell.* 164, 1110–1121 (2016). <https://doi.org/10.1016/j.cell.2016.02.007>
- [3]. Dixon, J.R., Gorkin, D.U., Ren, B.: Chromatin Domains: The Unit of Chromosome Organization. *Mol Cell.* 62, 668–80 (2016). <https://doi.org/10.1016/j.molcel.2016.05.018>
- [4]. Spielmann, M., Lupiáñez, D.G., Mundlos, S.: Structural variation in the 3D genome. *Nat Rev Genet.* 19, 453–467 (2018). <https://doi.org/10.1038/s41576-018-0007-0>
- [5]. Lieberman-Aiden, E., van Berkum, N.L., Williams, L., Imakaev, M., Ragozy, T., Telling, A., Amit, I., Lajoie, B.R., Sabo, P.J., Dorschner, M.O., Sandstrom, R., Bernstein, B., Bender, M.A., Groudine, M., Gnirke, A., Stamatoyannopoulos, J., Mirny, L.A., Lander, E.S., Dekker, J.: Comprehensive Mapping of Long-Range Interactions Reveals Folding Principles of the Human Genome. *Science* (1979). 326, 289–293 (2009). <https://doi.org/10.1126/science.1181369>
- [6]. Boettiger, A.N., Bintu, B., Moffitt, J.R., Wang, S., Beliveau, B.J., Fudenberg, G., Imakaev, M., Mirny, L.A., Wu, C., Zhuang, X.: Super-resolution imaging reveals distinct chromatin folding for different epigenetic states. *Nature.* 529, 418–422 (2016). <https://doi.org/10.1038/nature16496>
- [7]. Cattoni, D.I., Cardozo Gizzi, A.M., Georgieva, M., Di Stefano, M., Valeri, A., Chamouset, D., Houbbron, C., Déjardin, S., Fiche, J.-B., González, I., Chang, J.-M., Sexton, T., Marti-Renom, M.A., Bantignies, F., Cavalli, G., Nollmann, M.: Single-cell absolute contact probability detection reveals chromosomes are organized by multiple low-frequency yet specific interactions. *Nat Commun.* 8, 1753 (2017). <https://doi.org/10.1038/s41467-017-01962-x>
- [8]. Bintu, B., Mateo, L.J., Su, J.-H., Sinnott-Armstrong, N.A., Parker, M., Kinrot, S., Yamaya, K., Boettiger, A.N., Zhuang, X.: Super-resolution chromatin tracing reveals domains and cooperative interactions in single cells. *Science* (1979). 362, (2018). <https://doi.org/10.1126/science.aau1783>
- [9]. Finn, E.H., Pegoraro, G., Brandão, H.B., Valton, A.-L., Oomen, M.E., Dekker, J., Mirny, L., Misteli, T.: Extensive Heterogeneity and Intrinsic Variation in Spatial Genome Organization. *Cell.* 176, 1502–1515.e10 (2019). <https://doi.org/10.1016/j.cell.2019.01.020>
- [10]. Pombo, A.: Advances in imaging the interphase nucleus using thin cryosections. *Histochem Cell Biol.* 128, 97–104 (2007). <https://doi.org/10.1007/s00418-007-0310-x>
- [11]. Beagrie, R.A., Scialdone, A., Schueler, M., Kraemer, D.C.A., Chotalia, M., Xie, S.Q., Barbieri, M., de Santiago, I., Lavitas, L.-M., Branco, M.R., Fraser, J., Dostie, J., Game, L., Dillon, N., Edwards, P.A.W., Nicodemi, M., Pombo, A.: Complex multi-enhancer contacts captured by genome architecture mapping. *Nature.* 543, 519–524 (2017). <https://doi.org/10.1038/nature21411>
- [12]. Finn, E.H., Misteli, T.: Genome Architecture from a Different Angle. *Dev Cell.* 41, 3–4 (2017). <https://doi.org/10.1016/j.devcel.2017.03.017>
- [13]. Beagrie, R.A., Thieme, C.J., Annunziatella, C., Baugher, C., Zhang, Y., Schueler, M., Kukalev, A., Kempfer, R., Chiariello, A.M., Bianco, S., Li, Y., Davis, T., Scialdone, A., Welch, L.R., Nicodemi, M., Pombo, A.: Multiplex-GAM: genome-wide identification of chromatin contacts yields insights overlooked by Hi-C. *Nat Methods.* 20, 1037–1047 (2023). <https://doi.org/10.1038/s41592-023-01903-1>

- [14]. Quinodoz, S.A., Ollikainen, N., Tabak, B., Palla, A., Schmidt, J.M., Detmar, E., Lai, M.M., Shishkin, A.A., Bhat, P., Takei, Y., Trinh, V., Aznauryan, E., Russell, P., Cheng, C., Jovanovic, M., Chow, A., Cai, L., McDonel, P., Garber, M., Guttman, M.: Higher-Order Inter-chromosomal Hubs Shape 3D Genome Organization in the Nucleus. *Cell*. 174, 744-757.e24 (2018). <https://doi.org/10.1016/j.cell.2018.05.024>
- [15]. Quinodoz, S.A., Bhat, P., Chovanec, P., Jachowicz, J.W., Ollikainen, N., Detmar, E., Sohalim, E., Guttman, M.: SPRITE: a genome-wide method for mapping higher-order 3D interactions in the nucleus using combinatorial split-and-pool barcoding. *Nat Protoc*. 17, 36–75 (2022). <https://doi.org/10.1038/s41596-021-00633-y>
- [16]. Kempfer, R., Pombo, A.: Methods for mapping 3D chromosome architecture. *Nat Rev Genet*. 21, 207–226 (2020). <https://doi.org/10.1038/s41576-019-0195-2>
- [17]. Fiorillo, L., Musella, F., Conte, M., Kempfer, R., Chiariello, A.M., Bianco, S., Kukalev, A., Irastorza-Azcarate, I., Esposito, A., Abraham, A., Prisco, A., Pombo, A., Nicodemi, M.: Comparison of the Hi-C, GAM and SPRITE methods using polymer models of chromatin. *Nat Methods*. 18, 482–490 (2021). <https://doi.org/10.1038/s41592-021-01135-1>
- [18]. Dixon, J.R., Selvaraj, S., Yue, F., Kim, A., Li, Y., Shen, Y., Hu, M., Liu, J.S., Ren, B.: Topological domains in mammalian genomes identified by analysis of chromatin interactions. *Nature*. 485, 376–380 (2012). <https://doi.org/10.1038/nature11082>
- [19]. Nora, E.P., Lajoie, B.R., Schulz, E.G., Giorgetti, L., Okamoto, I., Servant, N., Piolot, T., van Berkum, N.L., Meisig, J., Sedat, J., Gribnau, J., Barillot, E., Blüthgen, N., Dekker, J., Heard, E.: Spatial partitioning of the regulatory landscape of the X-inactivation centre. *Nature*. 485, 381–385 (2012). <https://doi.org/10.1038/nature11049>
- [20]. Bickmore, W.A., van Steensel, B.: Genome Architecture: Domain Organization of Interphase Chromosomes. *Cell*. 152, 1270–1284 (2013). <https://doi.org/10.1016/j.cell.2013.02.001>
- [21]. Rao, S.S.P., Huntley, M.H., Durand, N.C., Stamenova, E.K., Bochkov, I.D., Robinson, J.T., Sanborn, A.L., Machol, I., Omer, A.D., Lander, E.S., Aiden, E.L.: A 3D Map of the Human Genome at Kilobase Resolution Reveals Principles of Chromatin Looping. *Cell*. 159, 1665–1680 (2014). <https://doi.org/10.1016/j.cell.2014.11.021>
- [22]. Rao, S.S.P., Huang, S.-C., Glenn St Hilaire, B., Engreitz, J.M., Perez, E.M., Kieffer-Kwon, K.-R., Sanborn, A.L., Johnstone, S.E., Bascom, G.D., Bochkov, I.D., Huang, X., Shamim, M.S., Shin, J., Turner, D., Ye, Z., Omer, A.D., Robinson, J.T., Schlick, T., Bernstein, B.E., Casellas, R., Lander, E.S., Aiden, E.L.: Cohesin Loss Eliminates All Loop Domains. *Cell*. 171, 305-320.e24 (2017). <https://doi.org/10.1016/j.cell.2017.09.026>
- [23]. Fortin, J.-P., Hansen, K.D.: Reconstructing A/B compartments as revealed by Hi-C using long-range correlations in epigenetic data. *Genome Biol*. 16, 180 (2015). <https://doi.org/10.1186/s13059-015-0741-y>
- [24]. Phillips-Cremins, J.E., Sauria, M.E.G., Sanyal, A., Gerasimova, T.I., Lajoie, B.R., Bell, J.S.K., Ong, C.-T., Hookway, T.A., Guo, C., Sun, Y., Bland, M.J., Wagstaff, W., Dalton, S., McDevitt, T.C., Sen, R., Dekker, J., Taylor, J., Corces, V.G.: Architectural Protein Subclasses Shape 3D Organization of Genomes during Lineage Commitment. *Cell*. 153, 1281–1295 (2013). <https://doi.org/10.1016/j.cell.2013.04.053>
- [25]. Fraser, J., Ferrai, C., Chiariello, A.M., Schueler, M., Rito, T., Laudanno, G., Barbieri, M., Moore, B.L., Kraemer, D.C.A., Aitken, S., Xie, S.Q., Morris, K.J., Itoh, M., Kawaji, H., Jaeger, I., Hayashizaki, Y., Carninci, P., Forrest, A.R.R., FANTOM Consortium, Sempke, C.A., Dostie, J., Pombo, A., Nicodemi, M.: Hierarchical folding and reorganization of chromosomes are linked to transcriptional changes in cellular differentiation. *Mol Syst Biol*. 11, 852 (2015). <https://doi.org/10.15252/msb.20156492>
- [26]. de Laat, W., Duboule, D.: Topology of mammalian developmental enhancers and their regulatory landscapes. *Nature*. 502, 499–506 (2013). <https://doi.org/10.1038/nature12753>
- [27]. Lupiáñez, D.G., Kraft, K., Heinrich, V., Krawitz, P., Brancati, F., Klopocki, E., Horn, D., Kayserili, H., Opitz, J.M., Laxova, R., Santos-Simarro, F., Gilbert-Dussardier, B., Wittler, L., Borschiwer, M., Haas, S.A., Osterwalder, M., Franke, M., Timmermann, B., Hecht, J., Spielmann, M., Visel, A., Mundlos, S.: Disruptions of Topological Chromatin Domains Cause Pathogenic Rewiring of Gene-Enhancer Interactions. *Cell*. 161, 1012–1025 (2015). <https://doi.org/10.1016/j.cell.2015.04.004>
- [28]. Valton, A.-L., Dekker, J.: TAD disruption as oncogenic driver. *Curr Opin Genet Dev*. 36, 34–40 (2016). <https://doi.org/10.1016/j.gde.2016.03.008>
- [29]. Krijger, P.H.L., de Laat, W.: Regulation of disease-associated gene expression in the 3D genome. *Nat Rev Mol Cell Biol*. 17, 771–782 (2016). <https://doi.org/10.1038/nrm.2016.138>
- [30]. Oudelaar, A.M., Hanssen, L.L.P., Hardison, R.C., Kassouf, M.T., Hughes, J.R., Higgs, D.R.: Between form and function: the complexity of genome folding. *Hum Mol Genet*. 26, R208–R215 (2017). <https://doi.org/10.1093/hmg/ddx306>
- [31]. Weischenfeldt, J., Dubash, T., Drainas, A.P., Mardin, B.R., Chen, Y., Stütz, A.M., Waszak, S.M., Bosco, G., Halvorsen, A.R., Raeder, B., Efthymiopoulos, T., Erkek, S., Siegl, C., Brenner, H., Brustugun, O.T., Dieter, S.M., Northcott, P.A., Petersen, I., Pfister, S.M., Schneider, M., Solberg, S.K., Thunissen, E., Weichert, W., Zichner, T., Thomas, R., Peifer, M., Helland, A., Ball, C.R., Jechlinger, M., Sotillo, R., Glimm, H., Korbel, J.O.:

- Pan-cancer analysis of somatic copy-number alterations implicates IRS4 and IGF2 in enhancer hijacking. *Nat Genet.* 49, 65–74 (2017). <https://doi.org/10.1038/ng.3722>
- [32]. Duan, Z., Andronescu, M., Schutz, K., McIlwain, S., Kim, Y.J., Lee, C., Shendure, J., Fields, S., Blau, C.A., Noble, W.S.: A three-dimensional model of the yeast genome. *Nature.* 465, 363–367 (2010). <https://doi.org/10.1038/nature08973>
- [33]. Bohn, M., Heermann, D.W.: Diffusion-Driven Looping Provides a Consistent Framework for Chromatin Organization. *PLoS One.* 5, e12218 (2010). <https://doi.org/10.1371/journal.pone.0012218>
- [34]. Brackley, C.A., Taylor, S., Papantonis, A., Cook, P.R., Marenduzzo, D.: Nonspecific bridging-induced attraction drives clustering of DNA-binding proteins and genome organization. *Proceedings of the National Academy of Sciences.* 110, (2013). <https://doi.org/10.1073/pnas.1302950110>
- [35]. Jost, D., Carrivain, P., Cavalli, G., Vaillant, C.: Modeling epigenome folding: formation and dynamics of topologically associated chromatin domains. *Nucleic Acids Res.* 42, 9553–9561 (2014). <https://doi.org/10.1093/nar/gku698>
- [36]. Giorgetti, L., Galupa, R., Nora, E.P., Piolot, T., Lam, F., Dekker, J., Tiana, G., Heard, E.: Predictive Polymer Modeling Reveals Coupled Fluctuations in Chromosome Conformation and Transcription. *Cell.* 157, 950–963 (2014). <https://doi.org/10.1016/j.cell.2014.03.025>
- [37]. Sanborn, A.L., Rao, S.S.P., Huang, S.-C., Durand, N.C., Huntley, M.H., Jewett, A.I., Bochkov, I.D., Chinnappan, D., Cutkosky, A., Li, J., Geeting, K.P., Gnirke, A., Melnikov, A., McKenna, D., Stamenova, E.K., Lander, E.S., Aiden, E.L.: Chromatin extrusion explains key features of loop and domain formation in wild-type and engineered genomes. *Proceedings of the National Academy of Sciences.* 112, (2015). <https://doi.org/10.1073/pnas.1518552112>
- [38]. Zhang, B., Wolynes, P.G.: Topology, structures, and energy landscapes of human chromosomes. *Proceedings of the National Academy of Sciences.* 112, 6062–6067 (2015). <https://doi.org/10.1073/pnas.1506257112>
- [39]. Serra, F., Di Stefano, M., Spill, Y.G., Cuartero, Y., Goodstadt, M., Baù, D., Marti-Renom, M.A.: Restraint-based three-dimensional modeling of genomes and genomic domains. *FEBS Lett.* 589, 2987–2995 (2015). <https://doi.org/10.1016/j.febslet.2015.05.012>
- [40]. Chiariello, A.M., Annunziatella, C., Bianco, S., Esposito, A., Nicodemi, M.: Polymer physics of chromosome large-scale 3D organisation. *Sci Rep.* 6, 29775 (2016). <https://doi.org/10.1038/srep29775>
- [41]. Fudenberg, G., Imakaev, M., Lu, C., Goloborodko, A., Abdennur, N., Mirny, L.A.: Formation of Chromosomal Domains by Loop Extrusion. *Cell Rep.* 15, 2038–2049 (2016). <https://doi.org/10.1016/j.celrep.2016.04.085>
- [42]. Di Pierro, M., Zhang, B., Aiden, E.L., Wolynes, P.G., Onuchic, J.N.: Transferable model for chromosome architecture. *Proceedings of the National Academy of Sciences.* 113, 12168–12173 (2016). <https://doi.org/10.1073/pnas.1613607113>
- [43]. Di Stefano, M., Paulsen, J., Lien, T.G., Hovig, E., Micheletti, C.: Hi-C-constrained physical models of human chromosomes recover functionally-related properties of genome organization. *Sci Rep.* 6, 35985 (2016). <https://doi.org/10.1038/srep35985>
- [44]. Brackley, C.A., Brown, J.M., Waithe, D., Babbs, C., Davies, J., Hughes, J.R., Buckle, V.J., Marenduzzo, D.: Predicting the three-dimensional folding of cis-regulatory regions in mammalian genomes using bioinformatic data and polymer models. *Genome Biol.* 17, 59 (2016). <https://doi.org/10.1186/s13059-016-0909-0>
- [45]. Buckle, A., Brackley, C.A., Boyle, S., Marenduzzo, D., Gilbert, N.: Polymer Simulations of Heteromorphic Chromatin Predict the 3D Folding of Complex Genomic Loci. *Mol Cell.* 72, 786–797.e11 (2018). <https://doi.org/10.1016/j.molcel.2018.09.016>
- [46]. Shi, G., Liu, L., Hyeon, C., Thirumalai, D.: Interphase human chromosome exhibits out of equilibrium glassy dynamics. *Nat Commun.* 9, 3161 (2018). <https://doi.org/10.1038/s41467-018-05606-6>
- [47]. Nuebler, J., Fudenberg, G., Imakaev, M., Abdennur, N., Mirny, L.A.: Chromatin organization by an interplay of loop extrusion and compartmental segregation. *Proceedings of the National Academy of Sciences.* 115, (2018). <https://doi.org/10.1073/pnas.1717730115>
- [48]. Racko, D., Benedetti, F., Dorier, J., Stasiak, A.: Transcription-induced supercoiling as the driving force of chromatin loop extrusion during formation of TADs in interphase chromosomes. *Nucleic Acids Res.* 46, 1648–1660 (2018). <https://doi.org/10.1093/nar/gkx1123>
- [49]. Crippa, M., Zhan, Y., Tiana, G.: Effective model of loop extrusion predicts chromosomal domains. *Phys Rev E.* 102, 032414 (2020). <https://doi.org/10.1103/PhysRevE.102.032414>
- [50]. Banigan, E.J., Mirny, L.A.: Loop extrusion: theory meets single-molecule experiments. *Curr Opin Cell Biol.* 64, 124–138 (2020). <https://doi.org/10.1016/j.ceb.2020.04.011>
- [51]. Belokopytova, P., Viesná, E., Chyliński, M., Qi, Y., Salari, H., Di Stefano, M., Esposito, A., Conte, M., Chiariello, A.M., Teif, V.B., Plewczynski, D., Zhang, B., Jost, D., Fishman, V.: 3DGenBench: a web-server to benchmark computational models for 3D Genomics. *Nucleic Acids Res.* 50, W4–W12 (2022). <https://doi.org/10.1093/nar/gkac396>
- [52]. Lesne, A., Riposo, J., Roger, P., Cournac, A., Mozziconacci, J.: 3D genome reconstruction from chromosomal contacts. *Nat Methods.* 11, 1141–1143 (2014). <https://doi.org/10.1038/nmeth.3104>

- [53]. Tjong, H., Li, W., Kalhor, R., Dai, C., Hao, S., Gong, K., Zhou, Y., Li, H., Zhou, X.J., Le Gros, M.A., Larabell, C.A., Chen, L., Alber, F.: Population-based 3D genome structure analysis reveals driving forces in spatial genome organization. *Proceedings of the National Academy of Sciences*. 113, (2016). <https://doi.org/10.1073/pnas.1512577113>
- [54]. Li, Q., Tjong, H., Li, X., Gong, K., Zhou, X.J., Chiolo, I., Alber, F.: The three-dimensional genome organization of *Drosophila melanogaster* through data integration. *Genome Biol.* 18, 145 (2017). <https://doi.org/10.1186/s13059-017-1264-5>
- [55]. Serra, F., Baù, D., Goodstadt, M., Castillo, D., Filion, G.J., Marti-Renom, M.A.: Automatic analysis and 3D-modelling of Hi-C data using TADbit reveals structural features of the fly chromatin colors. *PLoS Comput Biol.* 13, e1005665 (2017). <https://doi.org/10.1371/journal.pcbi.1005665>
- [56]. Nir, G., Farabella, I., Pérez Estrada, C., Ebeling, C.G., Beliveau, B.J., Sasaki, H.M., Lee, S.D., Nguyen, S.C., McCole, R.B., Chatteraj, S., Erceg, J., AlHaj Abed, J., Martins, N.M.C., Nguyen, H.Q., Hannan, M.A., Russell, S., Durand, N.C., Rao, S.S.P., Kishi, J.Y., Soler-Vila, P., Di Pierro, M., Onuchic, J.N., Callahan, S.P., Schreiner, J.M., Stuckey, J.A., Yin, P., Aiden, E.L., Marti-Renom, M.A., Wu, C. -ting: Walking along chromosomes with super-resolution imaging, contact maps, and integrative modeling. *PLoS Genet.* 14, e1007872 (2018). <https://doi.org/10.1371/journal.pgen.1007872>
- [57]. Lin, D., Bonora, G., Yardımcı, G.G., Noble, W.S.: Computational methods for analyzing and modeling genome structure and organization. *WIREs Systems Biology and Medicine*. 11, (2019). <https://doi.org/10.1002/wsbm.1435>
- [58]. Zhang, S., Chasman, D., Knaack, S., Roy, S.: In silico prediction of high-resolution Hi-C interaction matrices. *Nat Commun.* 10, 5449 (2019). <https://doi.org/10.1038/s41467-019-13423-8>
- [59]. Fudenberg, G., Kelley, D.R., Pollard, K.S.: Predicting 3D genome folding from DNA sequence with Akita. *Nat Methods.* 17, 1111–1117 (2020). <https://doi.org/10.1038/s41592-020-0958-x>
- [60]. Schwessinger, R., Gosden, M., Downes, D., Brown, R.C., Oudelaar, A.M., Telenius, J., Teh, Y.W., Lunter, G., Hughes, J.R.: DeepC: predicting 3D genome folding using megabase-scale transfer learning. *Nat Methods.* 17, 1118–1124 (2020). <https://doi.org/10.1038/s41592-020-0960-3>
- [61]. Plewczynski, D., Kadlof, M.: Computational modelling of three-dimensional genome structure. *Methods.* 181–182, 1–4 (2020). <https://doi.org/10.1016/j.ymeth.2020.09.013>
- [62]. Wang, Y., Zhang, Y., Zhang, R., van Schaik, T., Zhang, L., Sasaki, T., Peric-Hupkes, D., Chen, Y., Gilbert, D.M., van Steensel, B., Belmont, A.S., Ma, J.: SPIN reveals genome-wide landscape of nuclear compartmentalization. *Genome Biol.* 22, 36 (2021). <https://doi.org/10.1186/s13059-020-02253-3>
- [63]. Shi, G., Thirumalai, D.: From Hi-C Contact Map to Three-Dimensional Organization of Interphase Human Chromosomes. *Phys Rev X.* 11, 011051 (2021). <https://doi.org/10.1103/PhysRevX.11.011051>
- [64]. Marti-Renom, M.A.: Benchmarking experiments with polymer modeling. *Nat Methods.* 18, 456–457 (2021). <https://doi.org/10.1038/s41592-021-01134-2>
- [65]. Iannone, F., Bracco, G., Cavazzoni, C., Coelho, R., Coster, D., Hoenen, O., Maslennikov, A., Migliori, S., Owsiak, M., Quintiliani, A., Palak, B., Pais, V., Robin, F., Rossi, E., Voitsekhovitch, I.: MARCONI-FUSION: The new high performance computing facility for European nuclear fusion modelling. *Fusion Engineering and Design.* 129, 354–358 (2018). <https://doi.org/10.1016/j.fusengdes.2017.11.004>
- [66]. Iannone, F., Ambrosino, F., Bracco, G., De Rosa, M., Funel, A., Guarnieri, G., Migliori, S., Palombi, F., Ponti, G., Santomauro, G., Procacci, P.: CRESCO ENEA HPC clusters: a working example of a multifabric GPFS Spectrum Scale layout. In: 2019 International Conference on High Performance Computing & Simulation (HPCS). pp. 1051–1052. IEEE (2019)
- [67]. Mariano, A., D’Amato, G., Formisano, G., Guarnieri, G., Santomauro, G., Migliori, S.: Crescoware: A Container-Based Gateway for HPC and AI Applications in the ENEAGRID Infrastructure. Presented at the (2022)
- [68]. Nicodemi, M., Prisco, A.: Thermodynamic pathways to genome spatial organization in the cell nucleus. *Biophys J.* 96, 2168–77 (2009). <https://doi.org/10.1016/j.bpj.2008.12.3919>
- [69]. Nicodemi, M., Pombo, A.: Models of chromosome structure. *Curr Opin Cell Biol.* 28, 90–95 (2014). <https://doi.org/10.1016/j.ceb.2014.04.004>
- [70]. Esposito, A., Annunziatella, C., Bianco, S., Chiariello, A.M., Fiorillo, L., Nicodemi, M.: Models of polymer physics for the architecture of the cell nucleus. *WIREs Systems Biology and Medicine.* 11, (2019). <https://doi.org/10.1002/wsbm.1444>
- [71]. Conte, M., Fiorillo, L., Bianco, S., Chiariello, A.M., Esposito, A., Nicodemi, M.: Polymer physics indicates chromatin folding variability across single-cells results from state degeneracy in phase separation. *Nat Commun.* 11, 3289 (2020). <https://doi.org/10.1038/s41467-020-17141-4>
- [72]. Bianco, S., Chiariello, A.M., Conte, M., Esposito, A., Fiorillo, L., Musella, F., Nicodemi, M.: Computational approaches from polymer physics to investigate chromatin folding. *Curr Opin Cell Biol.* 64, 10–17 (2020). <https://doi.org/10.1016/j.ceb.2020.01.002>

- [73]. Chiariello, A.M., Bianco, S., Oudelaar, A.M., Esposito, A., Annunziatella, C., Fiorillo, L., Conte, M., Corrado, A., Prisco, A., Larke, M.S.C., Telenius, J.M., Sciarretta, R., Musella, F., Buckle, V.J., Higgs, D.R., Hughes, J.R., Nicodemi, M.: A Dynamic Folded Hairpin Conformation Is Associated with α -Globin Activation in Erythroid Cells. *Cell Rep.* 30, 2125–2135.e5 (2020). <https://doi.org/10.1016/j.celrep.2020.01.044>
- [74]. Esposito, A., Chiariello, A.M., Conte, M., Fiorillo, L., Musella, F., Sciarretta, R., Bianco, S.: Higher-order Chromosome Structures Investigated by Polymer Physics in Cellular Morphogenesis and Differentiation. *J Mol Biol.* 432, 701–711 (2020). <https://doi.org/10.1016/j.jmb.2019.12.017>
- [75]. Fiorillo, L., Bianco, S., Esposito, A., Conte, M., Sciarretta, R., Musella, F., Chiariello, A.M.: A modern challenge of polymer physics: Novel ways to study, interpret, and reconstruct chromatin structure. *WIREs Computational Molecular Science.* 10, (2020). <https://doi.org/10.1002/wcms.1454>
- [76]. Esposito, A., Bianco, S., Fiorillo, L., Conte, M., Abraham, A., Musella, F., Nicodemi, M., Prisco, A., Chiariello, A.M.: Polymer models are a versatile tool to study chromatin 3D organization. *Biochem Soc Trans.* 49, 1675–1684 (2021). <https://doi.org/10.1042/BST20201004>
- [77]. Chiariello, A.M., Bianco, S., Esposito, A., Fiorillo, L., Conte, M., Irani, E., Musella, F., Abraham, A., Prisco, A., Nicodemi, M.: Physical mechanisms of chromatin spatial organization. *FEBS J.* 289, 1180–1190 (2022). <https://doi.org/10.1111/febs.15762>
- [78]. Conte, M., Chiariello, A.M., Abraham, A., Bianco, S., Esposito, A., Nicodemi, M., Matteuzzi, T., Vercellone, F.: Polymer Models of Chromatin Imaging Data in Single Cells. *Algorithms.* 15, 330 (2022). <https://doi.org/10.3390/a15090330>
- [79]. Barbieri, M., Chotalia, M., Fraser, J., Lavitas, L.-M., Dostie, J., Pombo, A., Nicodemi, M.: Complexity of chromatin folding is captured by the strings and binders switch model. *Proceedings of the National Academy of Sciences.* 109, 16173–16178 (2012). <https://doi.org/10.1073/pnas.1204799109>
- [80]. Brackley, C.A., Johnson, J., Kelly, S., Cook, P.R., Marenduzzo, D.: Simulated binding of transcription factors to active and inactive regions folds human chromosomes into loops, rosettes and topological domains. *Nucleic Acids Res.* 44, 3503–3512 (2016). <https://doi.org/10.1093/nar/gkw135>
- [81]. Bianco, S., Annunziatella, C., Andrey, G., Chiariello, A.M., Esposito, A., Fiorillo, L., Prisco, A., Conte, M., Campanile, R., Nicodemi, M.: Modeling Single-Molecule Conformations of the HoxD Region in Mouse Embryonic Stem and Cortical Neuronal Cells. *Cell Rep.* 28, 1574–1583.e4 (2019). <https://doi.org/10.1016/j.celrep.2019.07.013>
- [82]. Esposito, A., Abraham, A., Conte, M., Vercellone, F., Prisco, A., Bianco, S., Chiariello, A.M.: The Physics of DNA Folding: Polymer Models and Phase-Separation. *Polymers (Basel).* 14, 1918 (2022). <https://doi.org/10.3390/polym14091918>
- [83]. Bianco, S., Lupiáñez, D.G., Chiariello, A.M., Annunziatella, C., Kraft, K., Schöpflin, R., Wittler, L., Andrey, G., Vingron, M., Pombo, A., Mundlos, S., Nicodemi, M.: Polymer physics predicts the effects of structural variants on chromatin architecture. *Nat Genet.* 50, 662–667 (2018). <https://doi.org/10.1038/s41588-018-0098-8>
- [84]. Conte, M., Esposito, A., Fiorillo, L., Annunziatella, C., Corrado, A., Musella, F., Sciarretta, R., Chiariello, A.M., Bianco, S.: Hybrid Machine Learning and Polymer Physics Approach to Investigate 3D Chromatin Structure. Presented at the (2020)
- [85]. Esposito, A., Bianco, S., Chiariello, A.M., Abraham, A., Fiorillo, L., Conte, M., Campanile, R., Nicodemi, M.: Polymer physics reveals a combinatorial code linking 3D chromatin architecture to 1D chromatin states. *Cell Rep.* 38, 110601 (2022). <https://doi.org/10.1016/j.celrep.2022.110601>
- [86]. De Gennes PG.: *Scaling concepts in polymer physics.* , NY (1979)
- [87]. Conte, M., Irani, E., Chiariello, A.M., Abraham, A., Bianco, S., Esposito, A., Nicodemi, M.: Loop-extrusion and polymer phase-separation can co-exist at the single-molecule level to shape chromatin folding. *Nat Commun.* 13, 4070 (2022). <https://doi.org/10.1038/s41467-022-31856-6>
- [88]. Conte, M., Esposito, A., Vercellone, F., Abraham, A., Bianco, S.: Unveiling the Machinery behind Chromosome Folding by Polymer Physics Modeling. *Int J Mol Sci.* 24, 3660 (2023). <https://doi.org/10.3390/ijms24043660>
- [89]. Kremer, K., Grest, G.S.: Dynamics of entangled linear polymer melts: A molecular-dynamics simulation. *J Chem Phys.* 92, 5057–5086 (1990). <https://doi.org/10.1063/1.458541>
- [90]. Kirkpatrick, S., Gelatt, C.D., Vecchi, M.P.: Optimization by Simulated Annealing. *Science* (1979). 220, 671–680 (1983). <https://doi.org/10.1126/science.220.4598.671>
- [91]. Salamon, P., Sibani, P., Frost, R.: *Facts, Conjectures, and Improvements for Simulated Annealing.* Society for Industrial and Applied Mathematics (2002)
- [92]. Henderson, D., Jacobson, S.H., Johnson, A.W.: *The Theory and Practice of Simulated Annealing.* In: Springer (ed.) *Handbook of Metaheuristics.* International Series in Operations Research & Management Science. pp. 287–319. , Boston (2003)
- [93]. Delahaye, D., Chaimatanan, S., Mongeau, M.: *Simulated Annealing: From Basics to Applications.* In: Springer (ed.) *Handbook of Metaheuristics.* International Series in Operations Research & Management Science. pp. 1–35 (2019)

- [94]. Angelini, M.C., Ricci-Tersenghi, F.: Limits and Performances of Algorithms Based on Simulated Annealing in Solving Sparse Hard Inference Problems. *Phys Rev X*. 13, 021011 (2023). <https://doi.org/10.1103/PhysRevX.13.021011>
- [95]. Yang, T., Zhang, F., Yardımcı, G.G., Song, F., Hardison, R.C., Noble, W.S., Yue, F., Li, Q.: HiCRep: assessing the reproducibility of Hi-C data using a stratum-adjusted correlation coefficient. *Genome Res*. 27, 1939–1949 (2017). <https://doi.org/10.1101/gr.220640.117>
- [96]. Fiorillo, L., Bianco, S., Chiariello, A.M., Barbieri, M., Esposito, A., Annunziatella, C., Conte, M., Corrado, A., Prisco, A., Pombo, A., Nicodemi, M.: Inference of chromosome 3D structures from GAM data by a physics computational approach. *Methods*. 181–182, 70–79 (2020). <https://doi.org/10.1016/j.ymeth.2019.09.018>
- [97]. CRESCO - ICT Enea, <https://ict.enea.it/cresco/>
- [98]. Conte, M., Fiorillo, L., Annunziatella, C., Esposito, A., Musella, F., Abraham, A., Bianco, S., Chiariello, A.M.: Dynamic and equilibrium properties of finite-size polymer models of chromosome folding. *Phys Rev E*. 104, 054402 (2021). <https://doi.org/10.1103/PhysRevE.104.054402>
- [99]. Conte, M., Esposito, A., Fiorillo, L., Campanile, R., Annunziatella, C., Corrado, A., Chiariello, M.G., Bianco, S., Chiariello, A.M.: Efficient computational implementation of polymer physics models to explore chromatin structure. *International Journal of Parallel, Emergent and Distributed Systems*. 37, 91–102 (2022). <https://doi.org/10.1080/17445760.2019.1643020>

NUCLEAR ANALYSES FOR EQUATORIAL PORT 12 IN ITER

Davide Flammini¹, Andrea Colangeli¹, Nicola Fomesu¹, Michele Lungaroni¹, Fabio Moro¹, Simone Noce¹, Alberto Previti¹, Rosaria Villari¹

⁽¹⁾ Nuclear Department, ENEA, Via E. Fermi 45, I-00044, Frascati (RM), Italy

ABSTRACT. Nuclear analyses are fundamental to support ITER port integration design and shielding optimization. In this framework, over the last years, ENEA has conducted detailed nuclear assessments on several equatorial diagnostic ports at different design stages. In this report the nuclear analyses for the equatorial port (EP) #12 is described. EP #12 is assumed as the “standard” diagnostic port, and it has already undergone the Final design Review and is now in Manufacturing Readiness Review phase. The study includes modelling and Monte Carlo calculations for neutron and gamma transport, during and at the end of plasma operations from Port Plug to the Port Interspace in a ITER 40° C-model. All the analyses were conducted on CRESCO6 cluster, with the DISUNED v3.1.4 Monte Carlo code, based on MCNP 5. They include the calculation of neutron flux and shutdown dose rate at 12 days after shutdown. The impact of radiation cross-talk with neighbouring ports around EP #12 was assessed along with the breakdown of components.

1 Introduction

The ITER Equatorial Port (EP) #12 is a diagnostic port that will be installed in ITER for the first operations and will host six diagnostics. The diagnostics systems have to be integrated with their apertures that produce severe radiation streaming from the vacuum vessel, posing severe challenge for the maintenance in the region between the closure plate of the port and the biological shield, called Port Interspace (PI) region, where the auxiliary systems are installed. One of the most important challenge in designing a port plug (PP) is indeed to reduce the radiation streaming in the Port Interspace (PI). The simulation presented here uses the MCNP model of the EP #12 developed in [1]. The PI model have been instead developed for this study. The analyses are focused on the neutron field during the operations and on the Shut Down Dose Rate (SDDR) assessment in PI area after the shut down. Targets for SDDR in ITER zone where human access is foreseen for hands-on maintenance are at 100 $\mu\text{Sv/h}$ at 12 days after shut down in PI.

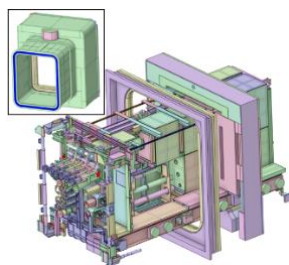


Fig.1: CAD model of the PI systems. In the inset the EP port duct and extension components is shown.

2 Methodology and codes

Monte Carlo simulation have been performed with the DISUNED-v3.1.4 [2], a patch of MCNP5v1.6 [3]. The model generation process is composed by three steps: defeaturing of the original Computer-Aided Design (CAD) model, performed with Ansys/SpaceClaim 2019 [4], conversion from CAD to MCNP with the SUPERMC/MCAM 3.4.0 code [5] and its integration into the ITER MCNP 40° sector model (C-model) [6]. The Vacuum vessel and in vessel coil components have also been updated

according to the last design. In Figure 1, the simplified CAD representation of the PI systems is reported, in Fig 2 the MCNP model of the ITER 40° sector is shown.

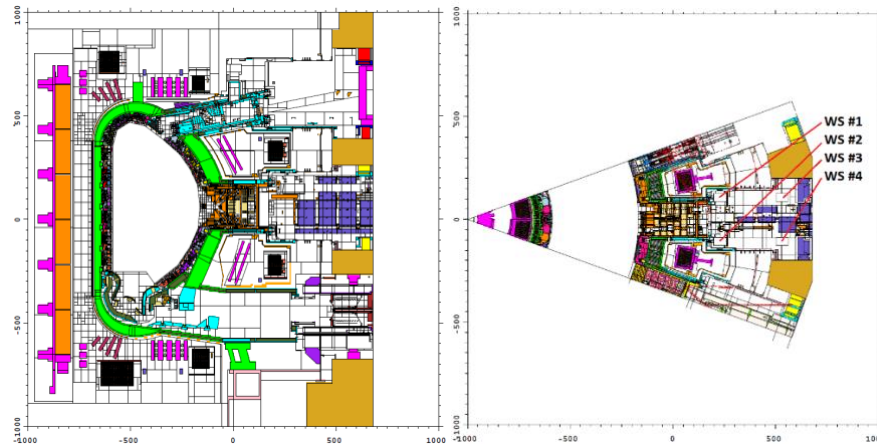


Fig.2: MCNP model of EP and PI #12, integrated into the ITER C-model.

Radiation transport calculations were conducted employing the FENDL3.1d [7] and MCPLIB03/04 [8] nuclear data libraries for neutron and photon transport, respectively and run on CRESCO6 cluster [9]. To enhance efficiency, a weight windows file derived from prior analysis [1] was utilized for variance reduction in PI area. The calculations were executed with up to 10^{10} simulated histories, adopting the standard ITER Deuterium-Tritium Plasma Source, included in the C-model. Special DISUNED library [2] have been used for SDDR calculations. The following quantities have been calculated with cell-based or mesh tallies (track length estimators): SDDR in workstations (WS), SDDR with adjacent port closed, breakdown of components for SDDR, spatial distribution ($10 \times 10 \times 10 \text{ cm}^3$ voxel mesh) of neutron flux and SDDR at 12 days in PI.

WSs represent particular locations where maintenance is foreseen. The WS are boxes roughly representing in dimension an human being ($\approx 60 \times 40 \times 190 \text{ cm}^3$). The position of the workstations is shown in fig. 2. Neutron flux has been normalized to 500 MW of fusion power ($1.973 \cdot 10^{19} \text{ n/s}$ in 40° sector). The SDDR has been calculated with the SA2 irradiation scenario [10].

3 Nuclear analyses and results

The neutron flux ISS area is in the range of $10^9 \text{ n/cm}^2/\text{s}$ at the closure plate down to $10^6 \text{ n/cm}^2/\text{s}$ at the bioshield. Neutron flux distribution along the EP #12 is shown in Fig. 3.

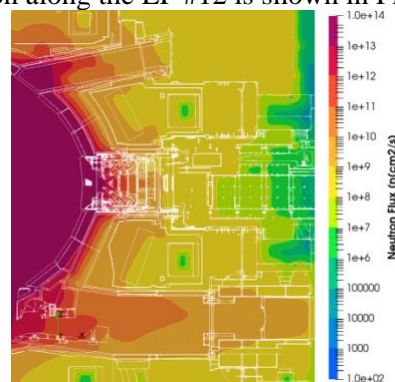


Fig.3: Neutron flux distribution in the vertical midplane along EP #12 from plasma to biological shield.

The SDDR maps at 12 days after the shutdown inside the bioshield are shown in Fig. 4. In the interspace region the SDDR is in the range $10\text{-}10^3 \mu\text{Sv/h}$. The $100 \mu\text{Sv/h}$ line, which delimits the green area include the WS #1 and #2 which are above this value, while #3 and #4 are below this value. This is confirmed by the evaluation of the SDDR in the WS with the cell-based tallies as shown in Table 1. In order to estimate the contribution to the dose in the workstations due by the radiation coming from the EP #12, a calculation in which all the particles coming from all the adjacent ports have been killed. A visual

effect of this modified transport simulation is shown in Fig. 4 right map, while the resulting values are reported in the last two columns of Table 1. The breakdown of components contributing to the dose rate has been calculated with the cell contribution feature of the DISUNED code. This calculates the dose measured in a given tally recording the component that generated the decay photons. The results, reported in Table 2, show that the largest contributors to the dose in WS #1 and #2 are the ISS structures and the EP extension and duct. The latter (shown in the inset of Fig. 1) is a component that is around the WS #1 and #2 which is attached to the vacuum vessel walls of the EP.

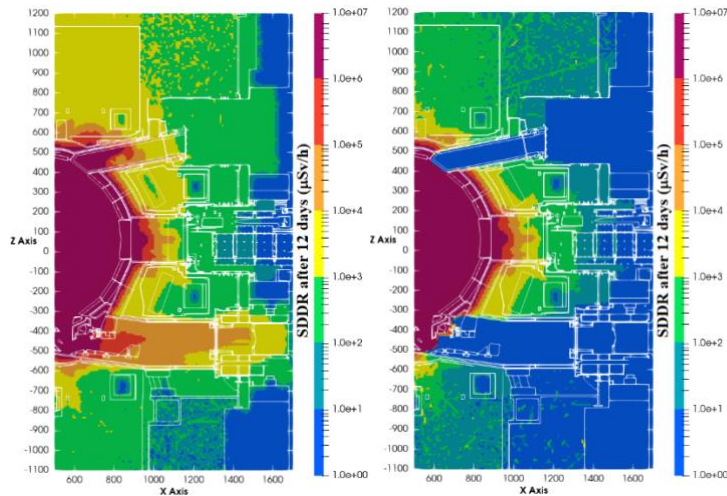


Fig 4: On the left, map of SDDR at 12 days after shutdown in ITER, vertical cut along the midplane of EP #12. On the right the same map, calculated with closed ports.

Table 1: SDDR at 12 days after shutdown calculated in WS#1 to #4 with open and closed ports. The uncertainty value refers to the statistical uncertainty.

WS	SDDR @ 12 days ($\mu\text{Sv/h}$)			
	Open ports	Err. (%)	Closed Ports	Err. (%)
1	354	0.5	273	3
2	453	0.5	362	3
3	70	4	30	1
4	80	5	40	2

From this evaluation it can be inferred that the dose rate is mostly due to the activation of components which are close to the sampling zone rather than the transport of the decay photons generated in highly activated components. The values of SDDR in WS with port closed in this sense show how much the structures surrounding the IS of EP #12 are activated by the neutrons coming from the other ports. A further evidence of this fact is given by the calculation of the contribution to the dose from the ports adjacent to EP #12 (i.e. the cross talk between EP #12 and all other ports) performed with the cell flagging feature of MCNP. In this case the decay photon is flagged when it enters in a port at any point of its history and not only at the moment of its creation. This means that the sum of all contributions can be larger than the total dose because a single decay photon can carry the contribution for more than one port. It is however interesting to compare the contributions among themselves. These are reported in Table 2. The largest contributors are the central ports (both upper and lower), but all the ports contribute, in any case, for less than 10%.

Table 2: Contribution of the SDDR in WS #1 and #2

Components	Contribution to SDDR (%)	
	WS #1	WS #2
DSM #1	2	8
DSM #2	3	6
DSM #3	4	3
ISS	27	51
Bellows and Cryo-flange	2	1

4 Conclusions

Nuclear analyses with ITER C-model along the EPP #12 with a new ISS integrated model has been performed with DISUNED code. Neutrons transport simulations have been performed to calculate the SDDR distribution maps in ISS area at 12 days after shut down. The present configuration of EP #12 will produce a SDDR at 12 days after shutdown at the end of life of ITER which is above the limit in WS #1 and #2. The analysis shows that this effect can be mitigated by enhancing the shielding capability of the port itself. These calculations refer to the SA2 irradiation scenario of ITER.

Acknowledgments

The views and opinions expressed herein do not necessarily reflect those of the ITER Organization.

References

- [1] D. Flammini, et. al. “Neutronic analyses for the equatorial diagnostic port plug #12 in ITER”, *Fusion Engineering and Design* 193 (2023), 113639
- [2] Sauvan, P., Juárez, R., Pedroche, G., Alguacil, J., Catalan, J.P., Ogando, F., Sanz, J., DISUNED system for the determination of decay photon related quantities (2020) *Fusion Engineering and Design*, 151, art. no. 111399
- [3] X-5 Monte Carlo Team, MCNP Version 5, LA-UR-03-1987, LANL, 2008.
- [4] www.spaceclaim.com
- [5] Y. Wu, FDS Team, CAD-based interface programs for fusion neutron transport simulation, *Fus. Eng. Des.*, 84, (2009), 1987 – 1992.
- [6] Leichtle, D., Colling, B., Fabbri, M., Juarez, R., Loughlin, M., Pampin, R., Polunovskiy, E., Serikov, A., Turner, A., Bertalot, L., The ITER tokamak neutronics reference model C-Model (2018), *Fusion Engineering and Design*, 136, pp. 742-746.
- [7] FENDL-3.1d: Fusion Evaluated Nuclear Data Library Ver.3.1d, <https://www-nds.iaea.org/fendl/>
- [8] M. C. White, “Further Notes on MCPLIB03/04 and New MCPLIB63/84 Compton Broadening Data For All Versions of MCNP5”, LA-UR-12-00018 (2012) (Available at https://mcnp.lanl.gov/BUGS/la-ur-12-00018_mcw.pdf)
- [9] G. Ponti et al., "The role of medium size facilities in the HPC ecosystem: the case of the new CRESCO4 cluster integrated in the ENEAGRID infrastructure", Proceedings of the 2014 International Conference on High Performance Computing and Simulation, HPCS 2014, art. no. 6903807, 1030-1033 (<https://www.eneagrid.enea.it/papers.html>).
- [10] M. Loughlin and N. Taylor, “Recommendation on Plasma scenarios”, ITER Report, ITER_D_2V3V8G v1.2, 2009.

PRELIMINARY STUDIES ON DTT TOKAMAK WITH HYMAGYC AND THE HAMILTONIAN MAPPING TECHNIQUE

V. Fusco^{1*}, S. Briguglio¹, G. Vlad¹, C. Di Troia¹, G. Fogaccia¹, X. Wang²

¹*ENEA, Fusion and Nuclear Safety Department, C. R. Frascati, Via E. Fermi 45, 00044 Frascati (Roma), Italy¹⁴*

²*Max-Planck-Institut für Plasmaphysik, Boltzmannstraße 2, Garching D-85748, Germany*

ABSTRACT. Tokamak plasmas, in addition to thermal electrons and thermal ions, host energetic particles. Such particles are characterized by velocities of the order of the Alfvén velocity, thus they can resonantly transfer power to Alfvén modes, driving them unstable; the interaction with the modes can affect the confinement of fast particles themselves, hindering their thermalization in the core plasma, preventing the achievement of burning plasma conditions, and potentially damaging the wall material surrounding the plasma. The study of the dynamics of energetic particles is thus a very important task and appropriate tools have been developed to characterize them. ENEA cresco HPC system have been used to test such tools (the Hamiltonian mapping technique [1]) and adapt them to the hybrid gyrokinetic code HYMAGYC [2].

1 Hybrid gyrokinetic simulations

The code used is HYMAGYC; it is a gyrokinetic hybrid code made of two modules: the fluid module which describes the bulk plasma solving the full MHD linear resistive equations (the field solver originates from the code MARS, which has been transformed from an eigenvalue solver to an initial value one) and the gyrokinetic module that solves the non-linear Vlasov equations with a PIC (particle in cell) technique which describes the energetic particle population. The two modules are coupled by means of the divergence of the pressure tensor of the energetic particles which is added to the fluid momentum equation. A description of the HYMAGYC code can be found in [2] or [3].

The analyzed case refers to the equilibrium [final_eqdskfile_PPFseq3345_DTT2023_04518.eqdsk](#) or [final_eqdskfile_PPFseq3363_DTT2023_04795.eqdsk](#) of the DTT project.

Preliminary MHD studies by means of the linear stability resistive MARS code has been done.

Efforts have been spent to study higher n toroidal modes number as well, as for example $n=7$ and $n=10$; indeed, it is well known that higher toroidal mode numbers could have stronger growth rate when driven by energetic particles.

As a first approach anyway, a low $n=2$ toroidal mode number has been chosen, essentially to set up energetic particles data and avoid infernal modes or edge modes and test the Hamiltonian mapping technique [1]; such diagnostic is important to deeply understand resonant particles dynamics and to analyze the interaction between fast particles and Alfvénic modes and deeply understand saturation mechanism.

In this case, we consider the energetic ion population induced by neutral beam injection (NBI) system; it is represented in this study by an anisotropic slowing down distribution function to better account for the NBI deposition:

¹⁴

Corresponding author. E-mail: valeria.fusco@enea.it.

$$f_{eq} = f_{sd}(\hat{E}, s)\Theta(\alpha, \alpha_0, \Delta)$$

$$f_{sd}(\hat{E}_n, s) = \frac{3}{4\pi} \frac{1}{2^{\frac{3}{2}}} \left(\frac{E_0}{E_c}\right)^{\frac{3}{2}} \hat{n}_H(s) \left(\frac{1}{\log\left(1 + \left(\frac{E_0}{E_c}\right)^{\frac{3}{2}}\right)} \right) \left(\frac{1}{1 + \left(\frac{E_0}{E_c} \hat{E}\right)^{\frac{3}{2}}} \right)$$

$$\Theta(\alpha, \alpha_0, \Delta) = \frac{4}{\Delta\sqrt{\pi}} \frac{e^{-\left(\frac{\cos\alpha - \cos\alpha_0}{\Delta}\right)^2}}{\text{erf}\left(\frac{1 - \cos\alpha_0}{\Delta}\right) + \text{erf}\left(\frac{1 + \cos\alpha_0}{\Delta}\right)}$$

where f_{sd} is the slowing down distribution function and Θ accounts for its anisotropy; \hat{E} is total normalized energy, E_0 is the injection energy, E_c is the critical energy, $\hat{n}_H(s) = n_H(s)/n_H(0)$ is the normalized density profile of the energetic particles, α is the pitch angle, α_0 is the injection angle, Δ the width of the beam around $\cos\alpha_0$.

The width Δ has been obtained fitting a distribution obtained by the ASCOT code with the analytical expression used in HYMAGYC.

As an example, in Fig.1 it is reported the contour plot of the distribution function $f_{eq}(\hat{E}, s)$ integrated in $\cos\alpha$ in the (\hat{E}, s) plane in arbitrary units:

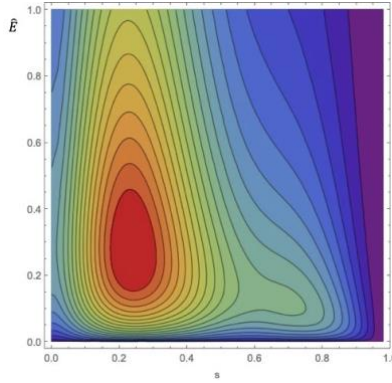


Fig.1: Contour plot of the slowing down distribution function in the (\hat{E}, s) plane, being the injection energy $E_0=510$ KeV, $\alpha_0=-27^\circ$, $\Delta=0.47$, $E_{c0}=230$ KeV

Useful information to recover the analyzed case are the on axis $n_{i0}=2.2250 \times 10^{20} \text{ m}^{-3}$ bulk ion density, $n_{e0}=2.411 \times 10^{20} \text{ m}^{-3}$ electron density, $n_{H0}=7.4039 \times 10^{17} \text{ m}^{-3}$ energetic ion density, $T_{e0}=13.033$ KeV on axis electron temperature whilst the energetic ion density profile and the electron temperature profile are reported in Fig.2.

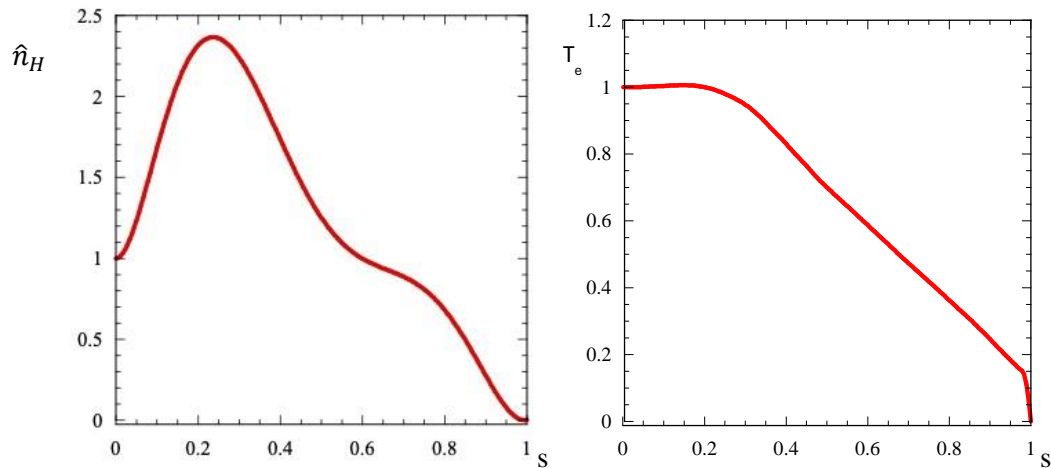


Fig.2: Normalized energetic particle profile \hat{n}_H and electron temperature profile T_e versus s .

Some of the results of the HYMAGYC simulations are shown in Fig.3: the module of the Fourier components of the electrostatic potential versus s (left hand side) and its frequency spectra in the (s, ω) plane (right hand side) for $n=2$.

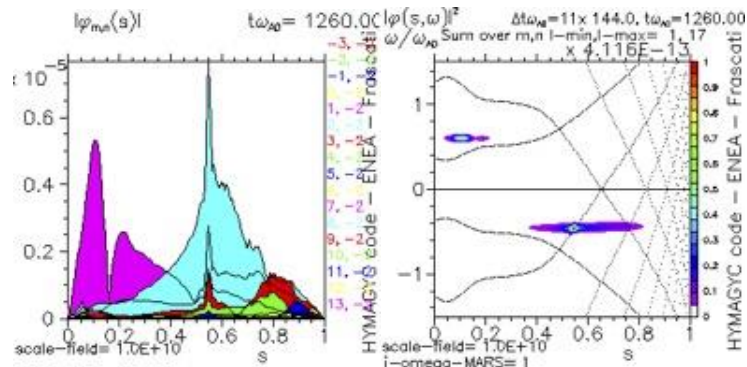


Fig.3: Caption font Scalar potential module versus s (l.h.s) and its frequency spectra in the (s, ω) plane (r.h.s) for $n=2$. The continuous black dots on the right hand side of the plot is the Alfvén continuum in the cylindrical approximation.

The plots show the $(m,n)=(1,2)$ dominant Alfvénic mode located close to the magnetic axis and with positive real frequency, and the $(m,n)=(2,2)$ dominant Alfvénic one, located at mid radius and with negative real frequency. It is well known that they are driven by the gradient of the energetic density profile; indeed, notice that the opposite sign of the frequencies is related to the change of signs around $s \approx 0.25$ of the EP density profile gradient (see Fig. 2). These modes are almost marginally stable in the present study; anyway, to extend the study and adapt the important tools mentioned as the Hamiltonian mapping, the n_{H0} has been heavily enhanced (about 10 times) to obtain clearly growing modes. Fig.4 shows the total energy of the two modes. First, the mid radius mode (red curve in Fig.4) dominates; then, the inner mode overcomes the mid radius one ($t\omega_{A0} \gtrsim 500$ where ω_{A0} is the Alfvén frequency); finally the mid radius mode saturates whilst the inner mode keeps growing and finally saturates as well.

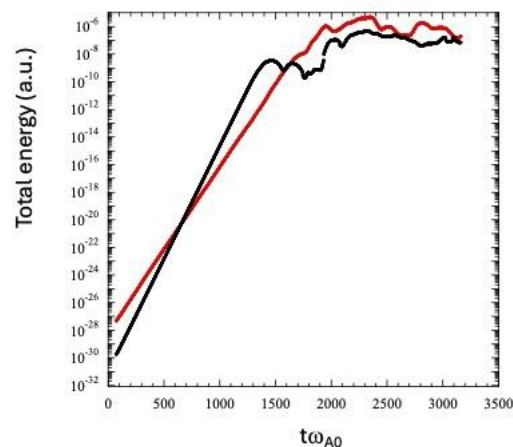


Fig.4: Total energy (arbitrary units) versus time for the inner mode (red line) and outer mode (black line).

2 The Hamiltonian mapping diagnostic

As an example of Hamiltonian mapping diagnostics, Fig.5 depicts the power exchange between the mode and the particles in the reduced spaces $(\mu, v_{||0})$ and $(s, v_{||0})$ after integrating over all the other particle coordinates (μ is the conserved magnetic moment, $v_{||0}$ is the initial "equatorial" parallel velocity). The time chosen (normalized to Alfvén time) selects the mid radius mode.

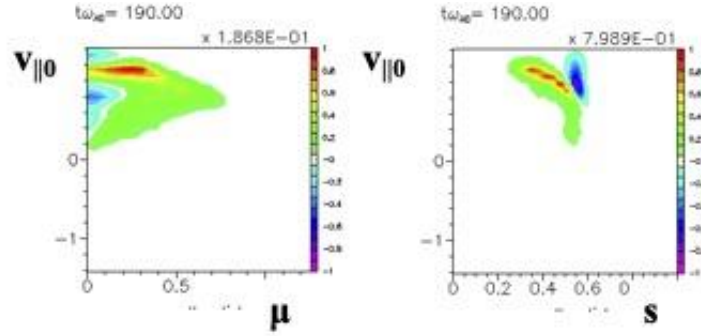


Fig.5: Power exchange between particles and mode at $t\omega_{A0}=190$, normalized to Alfvén velocity.

The resonant phase-space structures are identified by choosing the region where the power exchange is maximum in Fig.5. Such resonant phase-space structures have a remarkable feature: they cannot exchange particles with other structures throughout the evolution of the system because μ and $v_{||0}$ are birth labels for each particle and cannot be modified by the dynamics. Then, the resonant interaction of each structure depends solely on the free-energy source associated with the gradient of the distribution function along the $(\mu, v_{||0})$ structure and thus characterizes the mode, its evolution and, above all, its saturation mechanism during the non-linear phase. Each particle can then be represented by a marker in a space (Θ, s) , where Θ and s are, respectively, the wave phase seen by the particle and its flux coordinate at each crossing of the equatorial plane. Fig. 6 represents the markers in such a plot.

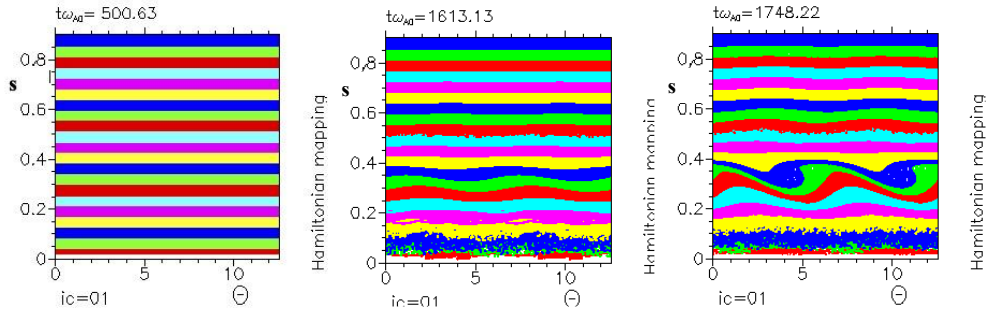


Fig.6: Resonant particles represented by markers in (Θ, s) space at different time (normalized to Alfvén frequency) at $t\omega_{A0}=500$ (linear phase), $t\omega_{A0}=1613$ (early non linear phase), $t\omega_{A0}=1748$ (non linear phase)

During the linear phase the markers drift along Θ ; during the non-linear phase, two types of trajectories identify the evolution of the markers: open trajectories, characterized by a continuous drift along Θ , for particles far away from the resonance ($s \approx 0.35$); closed trajectories constituting an island, for wave-trapped particles near the resonance. Saturation is reached when the free energy source, associated with the density gradient, is reduced (density flattening) and the flattening region extends over the whole power-exchange region. Such investigation allows us to determine the relationship between the radial widths of the island and the consequent saturation level of the field and gives information on the transport of resonant particles which could be eventually responsible of reduced plasma performances.

Acknowledgments

The authors would like to acknowledge the corresponding DTT services (*DTT 2023-PHY-PDG* and *DTT 2023-MHD-MSS*) for supporting such research.

References

- [1] S. Briguglio, X. Wang, F. Zonca et al., Phys. Plasmas 21, 112301 (2014)
- [2] Fogaccia G., Vlad G. and Briguglio S. 2016 Nucl. Fusion 56 112004
- [3] G. Vlad et al 2021 Nucl. Fusion 61 116026

CLASSICAL MOLECULAR DYNAMICS SIMULATIONS OF A PM 0.1 MODEL AND ITS INTERACTION WITH RAFT-LIKE AND NON-RAFT-LIKE BIOLOGICAL MEMBRANES

Sara Giordani¹, Federico Iacovelli², Alice Romeo², Davide Pietrafesa², Mattia Falconi², Barbara Benassi³ and Caterina Arcangeli³

¹*Department of Biochemistry, University of Rome La Sapienza, Viale Regina Elena 332, 00185 Rome, Italy*

²*Department of Biology, University of Rome Tor Vergata, Via della Ricerca Scientifica 1, 00133 Rome, Italy*

³*Laboratory of Health and Environment, Italian National Agency for New Technologies, Energy and Sustainable Economic Development (ENEA), Via Anguillarese, 301, 00123 Rome, Italy*

ABSTRACT. In this report, we present preliminary results from an investigation using numerical simulations to explore the possible interaction modes between PM_{0.1} and biological membranes, with and without lipid-rafts microdomains, resembling the olfactory mucosa. All the simulations were performed on CRESCO6 infrastructure using NAMD 2.3 software [1].

1 Introduction

In the literature, there is strong evidence that increased incidence and mortality of certain diseases such as asthma, chronic obstructive pulmonary disease (COPD), pulmonary fibrosis, neurodegenerative diseases, cancer, and type 2 diabetes are associated with exposure to PM_{2.5} [2]. The fine and ultrafine fractions (PM_{2.5}, PM_{0.1}), which constitute more than 50% of the composition of coarse PM₁₀ particles, are believed to be more toxic as they can reach the lung parenchyma and trigger inflammatory processes in the lungs [3]. Among the organic compounds in particulate matter, polycyclic aromatic hydrocarbons (PAHs) induce genotoxic, mutagenic, and carcinogenic activity. In particular, benzo[a]pyrene has the highest carcinogenic activity. More recently, evidence has emerged regarding the toxicity of ultrafine particles (PM_{0.1}), with sizes smaller than 0.1 μm, underlying neurodegenerative diseases [4,5].

This report presents preliminary results on the investigation of the possible molecular mechanisms by which PM_{0.1} interacts with the membranes of the olfactory mucosa. By employing molecular dynamics simulations, we explored the mode of interaction between PM_{0.1} and the more compact and rigid regions of the membrane, known as lipid rafts, to determine whether they facilitate or hinder its internalization. The results could help elucidate the potential molecular mechanisms underlying the interaction between PM_{0.1} and biological membranes and the mode of PM_{0.1} internalization in human cells, which are still poorly understood to date.

¹ Corresponding author. E-mail: sara.giordani@uniroma1.it

² Corresponding author. E-mail: caterina.arcangeli@enea.it

2 Computational Methods

Three different systems were prepared, each consisting of a structural model of PM_{0.1} and three different membranes mimicking those of the olfactory mucosa. The protocol used for modeling the structure of PM_{0.1}, and the three different membranes is not here described and will be published elsewhere [Giordani et al., manuscript in preparation].

The systems were then solvated, minimized, equilibrated and subjected to MD simulations, as summarized in Table 1.

In particular, all the simulations were performed by using NAMD version 2.13 [1] with the CHARMM36 all-atom force field [6] in combination with TIP3P model [7]. Periodic boundary conditions were applied and after 12000 steps of conjugate gradients minimization [8] and 40 ns of equilibration, unrestrained MD were carried out in the NPT ensemble for 100 ns.

<i>System</i>	<i>Atoms</i>	<i>Water or ions atoms</i>	<i>Total atoms</i>	<i>Production run MD</i>
PM _{0.1} - non raft-like	267.261	610.947	878.208	100 ns
PM _{0.1} - raft-like POPC	255.033	634.203	889.236	100 ns
PM _{0.1} - raft-like PDOPC	255.693	613.038	868.731	100 ns

Table 1: Systems subjected to MD simulations.

The MD simulations were conducted using the CRESCO6 HPC cluster, which allows us to run trajectory's calculations in parallel by employing 12 nodes, totaling 528 processors. The VMD molecular visualization program [9] was used for molecular visualization of the various models and configurations extraction from the trajectories, as well as for some analysis using integrated plugins. All the other analyses were performed via GROMACS 2022 software [10].

3 Results

In order to evaluate changes in the thickness of the membranes interacting with PM_{0.1}, comparative analyses were performed.

Here we report the results about the membrane thickness using "MEMBPLUGIN" [11], the membrane analysis tool, provided by VMD.

During the interaction with the particulate matter no significant changes in thickness were observed in any of the three membranes as shown in Figure 1.

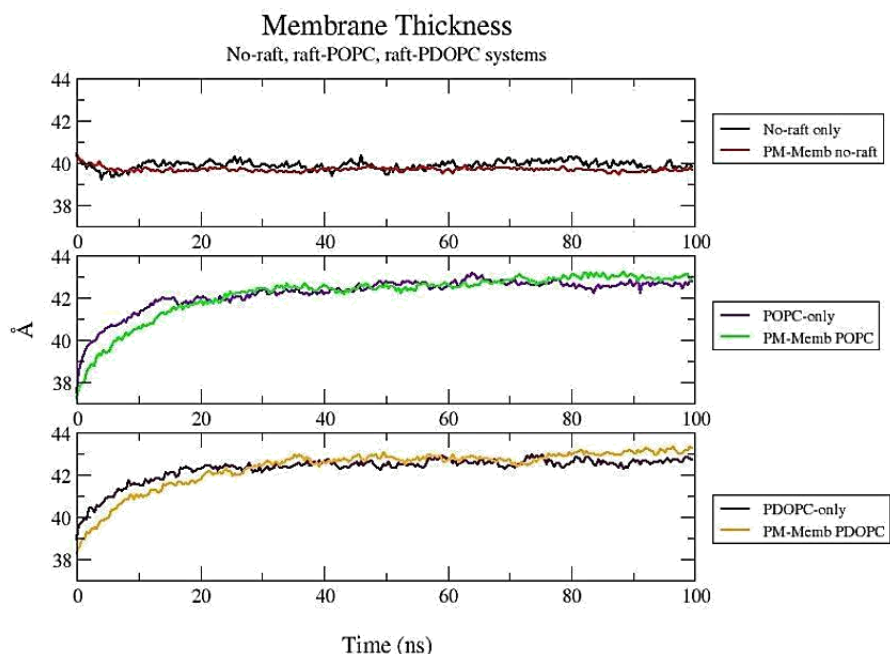


Fig.1: Per-frame bilayer thickness.

In order to better characterize the interaction mechanism between the PM and the membranes the total number of contacts between PM_{0.1} and the atoms of the membrane residues was calculated for each frame. Figure 2 shows that for the PM_{0.1} non-raft-like model, contacts are maintained throughout the entire simulation, peaking at 921 contacts at the 187th frame. Conversely, contacts in the other 2 systems cease completely after a few frames (Fig.3).

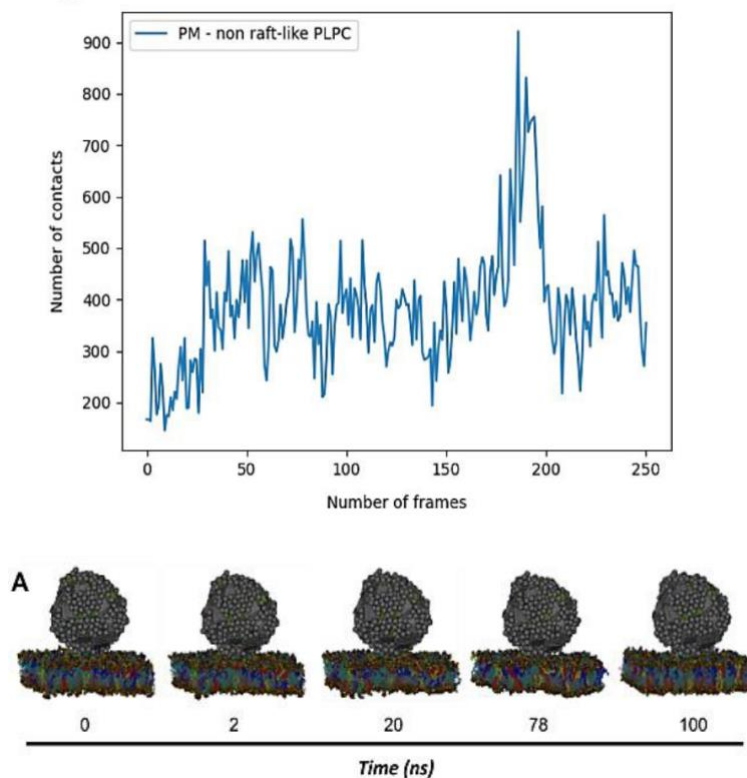


Fig.2: Trend of total contacts calculated for each frame in the PM complex -non-raft -like. (A) Configurations extracted from the trajectories of the three final complexes to highlight the most representative moments of interaction between the 2 systems.

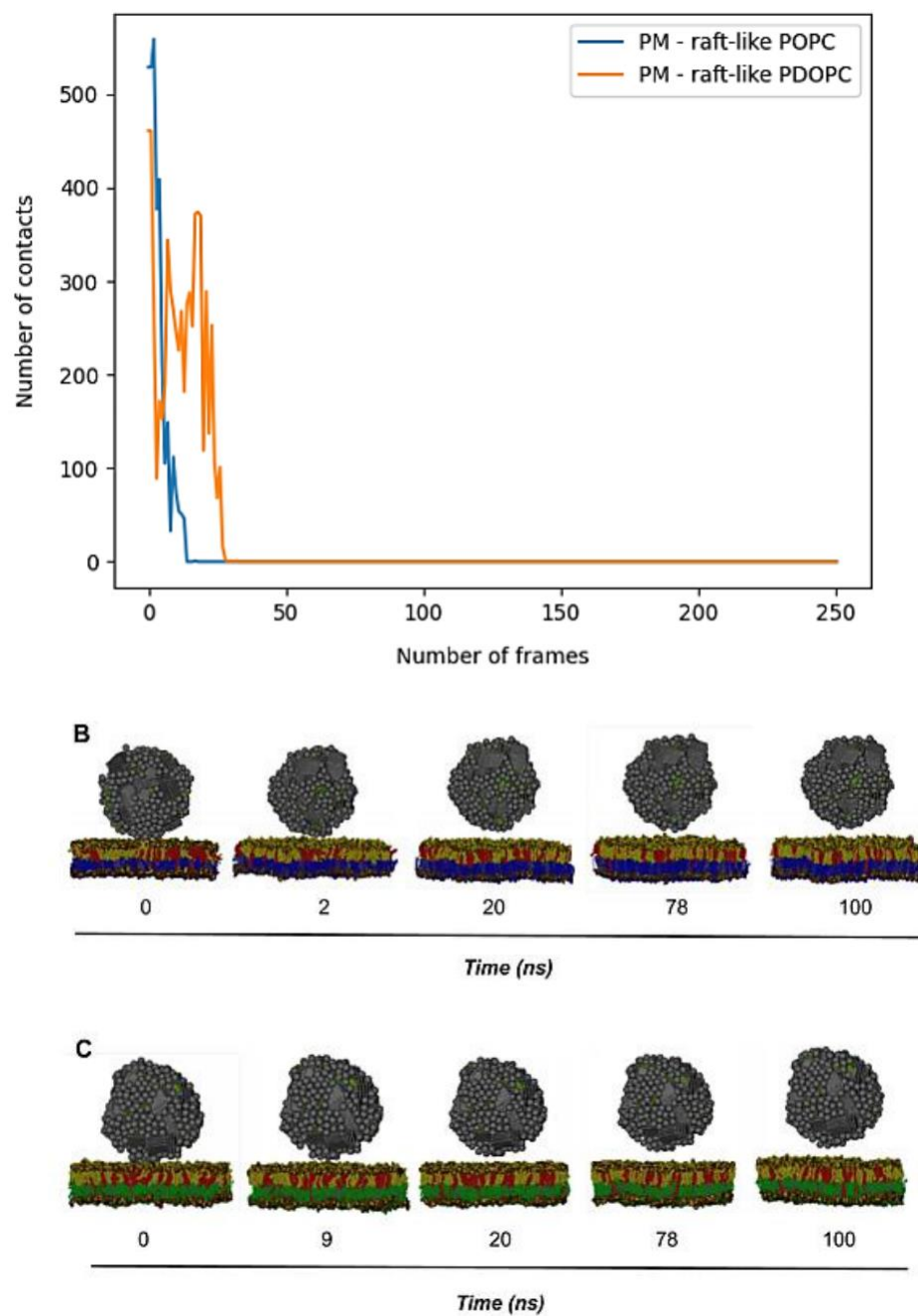


Fig.3: Trend of total contacts calculated for each frame in the two PM complexes - raft-like POPC and raft-like PDOPC. Configurations extracted from the trajectories of the three final complexes to highlight the most representative moments of interaction between the 2 systems. (B) PM_{0.1} - raft-like POPC e (C) PM_{0.1} - raft-like PDOPC.

4 Discussion and Conclusions

Our preliminary findings indicate distinct interaction patterns between PM_{0.1} and the membrane systems, depending on the presence of lipid-raft microdomains. Notably, in the absence of lipid rafts, PM_{0.1} established and maintained a higher number of contacts with the membrane residues, suggesting a more stable interaction. This stability could imply a higher likelihood of PM_{0.1} penetration and accumulation within the olfactory mucosa, potentially leading to adverse biological effects. These interactions could disrupt normal cellular functions, trigger inflammatory responses, or facilitate the translocation of ultrafine particles into the central nervous system via the olfactory bulb. Understanding these interaction mechanisms is crucial for assessing the health risks associated with exposure to ultrafine particulate matter and developing strategies to mitigate their impact on human health.

Our results, therefore, although preliminary, pave the way for further structural studies, including with membrane receptors that may play an active role in PM_{0.1} cellular internalization.

Acknowledgments

The computing resources and the related technical support used for this work have been provided by CRESCO/ENEAGRID High performance Computing infrastructure and his staff. CRESCO/ENEAGRID High performance Computing infrastructure is funded by ENEA, the Italian National Agency for New Technologies, Energy and Sustainable Economic Development and by Italian and European research programmes, see <http://www.cresco.enea.it/english> for information.

References

- [1] Phillips, J.C., Hardy, D.J., Maia, J.D.C., Stone, J.E., Ribeiro, J. V., Bernardi, R.C., Buch, R., Fiorin, G., Hémin, J., Jiang, W., et al. (2020). Scalable molecular dynamics on CPU and GPU architectures with NAMD. *The Journal of Chemical Physics* 153, 044130.
- [2] Moreno-Ríos, A. L., Tejada-Benítez, L. P., and Bustillo-Lecompte, C. F. (2022). Sources, characteristics, toxicity, and control of ultrafine particles: An overview. *Geoscience Frontiers* 13, 101147.
- [3] Mazzoli-Rocha, F., Fernandes, S., Einicker-Lamas, M., and Zin, W. A. (2010). Roles of oxidative stress in signaling and inflammation induced by particulate matter. *Cell biology and toxicology* 26, 481–498.
- [4] Kalia, L. V., and Lang, A. E. (2015). Parkinson's disease. *The Lancet* 386, 896-912.
- [5] Wimo, A., Jönsson, L., Bond, J., Prince, M., Winblad, B., and Alzheimer Disease International (2013). The worldwide economic impact of dementia 2010. *Alzheimer's & dementia: the journal of the Alzheimer's Association* 9, 1–11.
- [6] Huang J, Rauscher S, Nawrocki G, Ran T, Feig M, de Groot BL, Grubmüller H, MacKerell AD Jr. CHARMM36m: an improved force field for folded and intrinsically disordered proteins. *Nat Methods*. 2017 Jan;14(1):71-73.
- [7] Jorgensen, W.L., Chandrasekhar, J., Madura, J.D., Impey, R.W., and Klein, M.L. (1983). Comparison of simple potential functions for simulating liquid water. *J. Chem. Phys.* 79, 926–935.
- [8] S.S. Petrova, A.D. Solov'ev. The Origin of the Method of Steepest Descent. *Historia*
- [9] Humphrey, W., Dalke, A., and Schulten, K. (1996). VMD: Visual molecular dynamics. *Journal of Molecular Graphics* 14, 33-38.
- [10] Abraham, M. J., Murtola, T., Schulz, R., Páll, S., Smith, J. C., Hess, B., and Lindahl, E. (2015). GROMACS: High performance molecular simulations through multi-level parallelism from laptops to supercomputers. *SoftwareX* 1-2, 19-25.
- [11] Guixà-González, R., Rodríguez-Espigares, I., Ramírez-Angueta, J. M., Carrió-Gaspar, P., Martínez-Seara, H., Giorgino, T., and Selent, J. (2014). MEMBPLUGIN: studying membrane complexity in VMD. *Bioinformatics (Oxford, England)* 30, 1478–1480.

HIGH-FIDELITY NUMERICAL SIMULATIONS OF REACTING FLOWS

Davide Laera, Francesco Gabriele Schiavone, Raffaele Intranuovo, Christophe Vankelekom, Sergio Mario Camporeale, and Marco Torresi¹⁵

Department of Mechanics, Mathematics and Management, Polytechnic University of Bari, Via Orabona 4, Bari 70125, Italy

ABSTRACT. Numerical simulations have been performed on CRESCO 6 using the compressible Navier-Stokes solver AVBP 7.14 to investigate different reacting flows. The first paragraph treats OH* analyses in hydrogen-air flames. The second one reports numerical simulations of ammonia-hydrogen-air turbulent flames. The third focuses on the development of a one-step chemical mechanism for hydrogen-air flames. Finally, thermoacoustic instabilities analyses in a micro gas turbine (mGT) are reported in the last paragraph. Simulations are parallelized over 288 CPU (6 nodes) with INTEL MPI libraries.

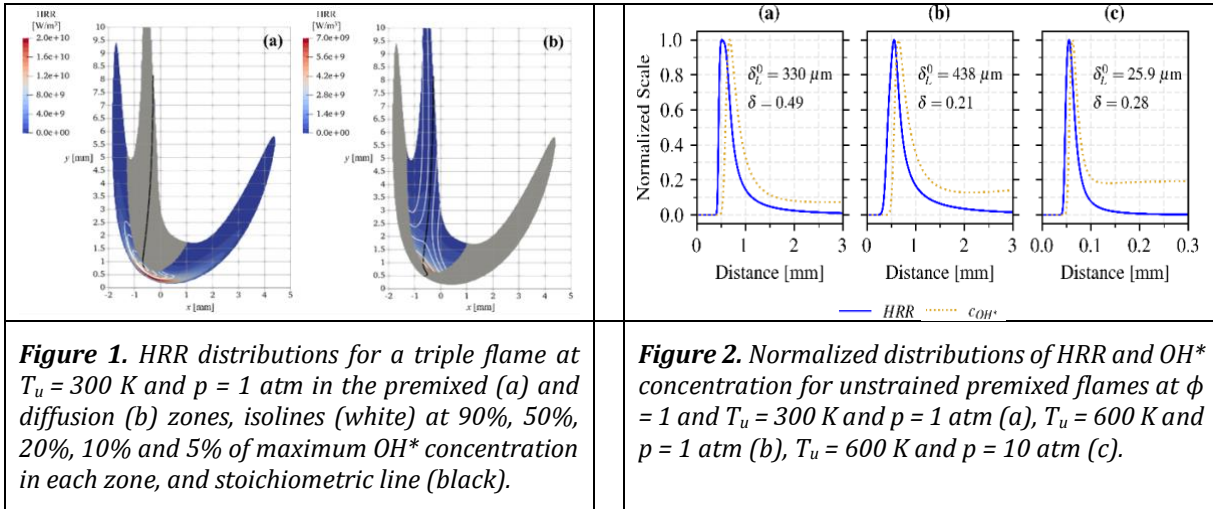
1 Impact of the operating conditions on the correlation between OH* and Heat Release Rate

The distribution of Heat Release Rate (HRR) is fundamental to analyse and predict the structure and dynamics of flames. Nevertheless, HRR direct measurements are impractical, and chemiluminescence is used as a tracer [1]. A good correlation between CH*, OH*, and CO₂* chemiluminescent emissions and HRR is generally observed for steady hydrocarbon flames [1]. For hydrogen (H₂)-air flames, instead, a rather wide distance between the OH* and HRR peaks has been observed, and the correlation between the two quantities has been shown to fail in lean premixed cellular tubular flames [2]. As observed in [3], the fundamental reason leading to these observed differences lies in the interplay between the H-radical pool, the OH* main formation pathways, which are related to the fuel composition, and the heat release process.

The impact of flame regime on the OH*-HRR correlation is analysed by considering a 2D triple flame at $T_u = 300$ K and $p = 1$ atm, for which three zones can be identified: a lean premixed branch, a rich premixed branch, and a diffusion branch. The HRR fields are shown in Fig. 1 for the premixed (a) and diffusion (b) zones, together with isolines (white) of OH* concentration and the stoichiometric line (black). A sensible axial shift can be observed between the HRR and OH* peaks (Fig.2), with the former being located further down, in the rich premixed zone, while the latter is above, close to the stoichiometric line and in proximity of the triple point. On the other hand, the OH* distribution shows to be better correlated to the HRR one, with the two peaks located in the same region and the OH* field able to capture with sufficient adequacy the HRR variation in the whole zone.

This work has been published in “F.G. Schiavone, M. Torresi, S.M. Camporeale, D. Laera, “*Impact of the operating conditions on the correlation between OH* and Heat Release Rate in Hydrogen-Air flames*”. In Proceedings of 46th Meeting of the Italian Section of the Combustion Institute, ISBN 978-88-88104-29-4.”

¹⁵ Corresponding author. E-mail: marco.torresi@poliba.it



2 Direct Numerical Simulation of Ammonia Combustion

In the current energy transition process, ammonia (NH_3) is gaining momentum as a fuel for carbon-free combustion, owing to properties such as high bulk energy density, relatively simple storage if compared with pure hydrogen (H_2), and a global developed economy. Still, given its toxic and corrosive nature, and its unfavourable combustion properties, research is needed to make it a feasible solution [4]. As part of the PRIN PNRR 2022 “Reactant” project, the present work proposes a numerical study to characterize the combustion properties of perfectly premixed NH_3 (pure or doped with H_2) flames when submitted to Homogeneous Isotropic Turbulence (HIT). First, few recent detailed reaction mechanisms [5-6] are compared with an experimental dataset to select the most suitable scheme to predict NH_3 /air laminar combustion properties, i.e., laminar flame speed and adiabatic flame temperature. Then, an Analytically Reduced Chemistry (ARC) version of the selected mechanism is used in the high-fidelity CFD code AVBP (<https://www.cerfacs.fr/avbp7x/>) to perform Direct Numerical Simulations (DNS) of a turbulent 3D stoichiometric flat ammonia flame, a canonical configuration commonly adopted in the literature [7]. Preliminary results (Fig. 3) show hydrogen preferential diffusion on positively wrinkled regions, impacting local equivalence ratio, Heat Release Rate (HRR) and NO_x concentration. Multiple turbulence levels ranging from low to high Karlovitz numbers will be investigated in the future.

This work has been published in: “R. Intranuovo, F.G. Schiavone, D. Laera, “A Direct Numerical Simulation of Ammonia Combustion”. In Proceedings of 46th Meeting of the Italian Section of the Combustion Institute, ISBN 978-88-88104-29-4.”

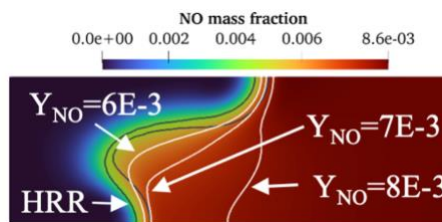


Figure 3. NO mass fraction for $(70\%NH_3+30\%H_2)/air$ flame at $\phi = 1$ ($HRR = 1.9$ GW/m^3).

3 An Arrhenius-based one-step reaction mechanism for hydrogen-air flames simulations

An Arrhenius-based one-step scheme is derived for hydrogen-air combustion simulations. A Pre-Exponential Adjustment [10] approach, based on an explicit analytical dependence of reaction rate parameters on equivalence ratio and pressure is adopted, together with a correction to improve the prediction of thermal flame thickness. The reduced scheme is validated by computations of one-dimensional unstrained and strained laminar premixed flames for a wide range of pressures ([1; 30] atm), unburned gas temperatures ([300; 800] K), and equivalence ratios ([0.4; 6.0]), with a good agreement of predicted main flame parameters between

reduced and reference kinetic schemes. Coupled to a high-fidelity Navier–Stokes compressible solver, the reduced scheme is successfully proved for the numerical simulation of canonical configurations such as one-dimensional and two-dimensional premixed flames under several mixture conditions, with a significant improvement of computational efficiency. The applicability of the scheme for Computational Fluid Dynamics purposes has been subsequently assessed by implementing the thus defined reduced global mechanism in the Navier–Stokes compressible DNS/LES (Large Eddy Simulation) solver AVBP for the computation of canonical configurations such as one-dimensional and two-dimensional premixed flames. Considering a two-dimensional cylindrical expanding flame configuration (Fig.4), the reduced mechanism has shown a significantly good agreement with the reference San Diego mechanism in the prediction of flame structure and properties, and a sensible reduction of computational costs, both in terms of iterations per second and total number of iterations required. The proposed global reaction mechanism aims at a practical solution to avoid computationally expensive numerical simulations of hydrogen-air combustion, especially in a preliminary design phase, optimizing computational resources by delaying the adoption of expensive detailed reaction schemes to more advanced phases of the design process. Moreover, the methodology introduced to develop the reduced mechanism is applicable to other fuels or different mixture conditions of interest, which may be expected to be the subject of further study. Finally, in future work, the performances of the proposed 1S_REV_H2AIR_FGS scheme will be evaluated in partially premixed flames as well as of LES/DNS simulations of turbulent reactive flows.

This work led to the following journal publication: F.G. Schiavone, N. Detomaso, M. Torresi, D. Laera "An Arrhenius-based one-step reaction mechanism for hydrogen-air flames simulations in an extended range of operating conditions." *International Journal of Hydrogen Energy* 57 (2024): 1229-1243.

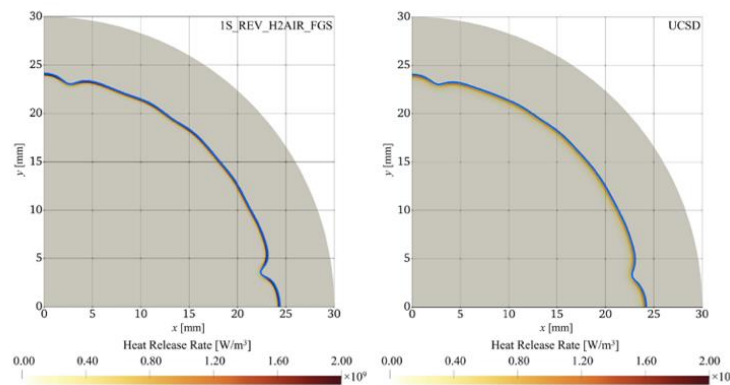


Figure 4. Flame front of the lean 2D cylindrical expanding flame ($\phi = 0.4$) for $r = 24$ mm, identified by the iso-surface of the progress variable $c = 0.5$ (blue line), and superimposed on the Heat Release Rate field. Comparison between CFD simulations performed with reduced scheme developed in this work (left) and reference UCSD mechanism (right).

4 Analysis of Thermoacoustic Instabilities in a Micro Gas Turbine

Micro gas turbines (mGT) are a good candidate to help with the energy transition to overcome the intermittency of renewable energy. Due to a perturbation in the system, thermoacoustic instabilities [8] can occur in the combustor. Consequently, pressure fluctuations may produce vibrations inside the system that will lead to the failure of some components. It can also trigger other instabilities such as flashback and blow-off phenomena due to the interaction with the flame. Many studies have already been performed on laboratory scales or in real industrial gas turbines [8-10] but never on mGT. This work has used numerical simulations and more precisely fully compressible Large Eddy Simulation. Reactive LES simulations have been performed on the *MTT Enertwin* mGT combustor. The results showed a stable V-shape flame (Fig. 5) without any acoustic mode except when the relaxation factor at inlet and outlet are changed. Frequency peaks are excited at approximately 900 and 2200 Hz, which are close to those coming from the experimental data, proving the reliability of the applied procedure.

This work has been published in: “C. Vankelekom, F.G. Schiavone, D. Laera, “*Analysis of Thermoacoustic Instabilities in a Micro Gas Turbine*”. In Proceedings of 46th Meeting of the Italian Section of the Combustion Institute, ISBN 978-88-88104-29-4.”

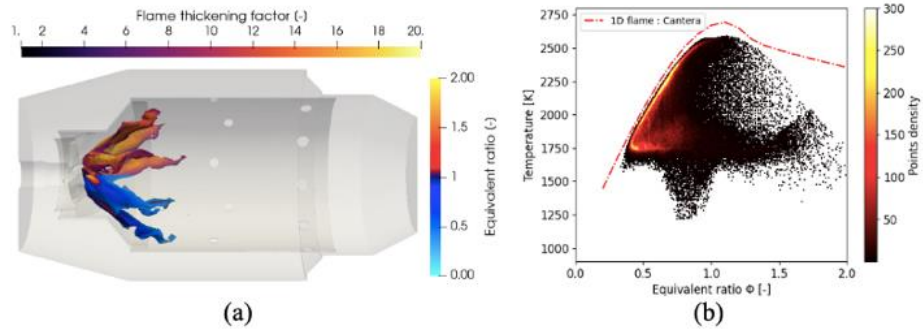


Figure 5. (a) Heat release rate region coloured by the flame temperature and equivalence ratio (b) scatter plot of temperature over local equivalence ratio.

References

- [1] M. Lauer et al., *J. Eng. Gas Turbine Power* 132(6), 061502 (2010).
- [2] G. J. Marshall et al., *Proc. Combust. Inst.* 37(2): 2029-2036 (2019).
- [3] F.G. Schiavone et al., *Proc. Combust. Inst.*, Manuscript accepted for presentation (2024).
- [4] A. Valera-Medina et al., *Energ. Fuels* 35.9: 6964-7029 (2021).
- [5] Y. Zhu et al., *Combust. Flame* 260 :113239 (2024).
- [6] T. Cai et al., *J. Chem. Eng.* 458 :141391 (2023).
- [7] C. Netzer et al., *Combust. Flame* 232 :111520 (2021).
- [8] L.Y. Gicquel et al., *PECS* 38(6) :782-817 (2012).
- [9] A. De Santis et al., *Fuel* 28 :118620 (2020)
- [10] B. Franzelli et al., *Combust. Flame* 159:621-637 (2012)

NON-COVALENT BINDING OF NIRMATRELVIR TO THE SARS-CoV-2 MAIN PROTEASE

Marina Macchiagodena¹, Marco Pagliai¹, Piero Procacci^{1*}

¹University of Florence, Chemistry Dept. U. Schiff, Via della Lastruccia 3, 50019 Sesto Fiorentino, Italy

ABSTRACT. Using massively parallel equilibrium and nonequilibrium molecular dynamics simulation techniques, we examine the non-covalent association of the active principle of the Paxlovid anti-Covid-19 formulation, namely the covalent binder Nirmatrelvir, with the SARS-Cov-2 main protease as a function of the protonation of the HIS41-CYS145 catalytic dyad. The structural characterization of the complexes and the computed binding strengths provide valuable clues on the inhibition mechanism and as to how the potency of the main protease covalent inhibitors could be improved.

1 Background

One year after the World health Organization declared the end to COVID-19 as a global health emergency, the virus is still circulating with immense concern at the health and consequences of the so-called “long covid” affecting mostly vaccinated patients [1]. While m-RNA-based or adenovirus vaccines have helped to substantially reduce the impact of the disease in developed countries, their massive administration did not confer long-standing immunity and did not prevent virus transmission. Waning of immunity from Spike-based M-RNA vaccines during the pandemic has been attributed to the emergence of new variants of the virus, capable of evading the vaccine-induced immune response and invariably involving the exposed Spike protein (S), projecting from the surface of the enveloped SARS-CoV-2. The need for an easily administrable broad spectrum antiviral targeting non-structural viral proteins that are less subject to mutational pressure is hence more urgent than ever.

The 3CLpro SARS-CoV-2 chymotrypsin-like main protease (3CLpro) is probably the most studied biological target for the development of an antiviral compound. This proteinase, generated by self-excision, cleaves at 11 sites the pp1a and pp1ab polyproteins expressed by the virus m-RNA upon cell entry, releasing the viral replication machinery into the host cell.[2] Unlike S, 3CLpro exhibits the desirable feature of having a high degree of homology in the coronaviridae family. For example, the SARS-CoV and SARS-CoV-2 main proteases are 95% homologue and have identical tertiary structure (see 6LU7 and 1UK4 PDB structures) differing by only few aminoacids, all lying at least 1 nm away from the 3CLpro active site.[3]. Because of these features, targeting the SARS-CoV-2 main protease or other non structural proteins may hence constitute a valid approach for an antiviral drug design against future SARS-like outbreaks and, possibly, long covid.

The only available anti-Covid19 drug approved so far by the FDA in May 2023 is the covalent inhibitor PF-07321332 (Nirmatrelvir) of the main protease known, administered in combination with ritonavir in the Paxlovid formulation. PF-07321332 (see Figure 1) is capable of impairing virus replication in human cells at sub-micromolar concentrations.[4] and is based on a peptidomimetic *de novo* design[5], with an electrophilic nitrile warhead for electrophilic attack flanked by two proline-mimetic groups. Upon Nirmatrelvir docking on the catalytic site, the nitrile carbon binds covalently and reversibly the cysteine of the catalytic dyad HIS41-CYS145 of the main protease (see Figure 1). The efficacy of Paxlovid is still under scrutiny and in a recent randomized controlled trial on a sample conducted by Pfizer “sustained alleviation of all symptoms for four consecutive days was not met,” eventually leading to the discontinuation of the enrollment.

A covalent inhibitor such as Nirmatrelvir acts by first non-covalently binding to the protein and then by forming the covalently bound complex according to the combined equilibrium $P + I \rightarrow PI \rightarrow (PI)^{cov}$. The observed inhibition constant, K^{app} , for the reaction $P + I \rightarrow (PI)^{cov}$ is given by

$$K^{app} = \frac{K_i}{(1 + K^{cov})} \quad (1)$$

where K_i is the non covalent inhibition (dissociation) constant, and $K^{cov} = [PI^{cov}]/[PI]$ is the constant regulating the formation of the covalent complex from the non-covalent intermediate. Assuming that $K^{cov} \gg 1$, the strength of the inhibition of a reversible covalent inhibitor is essentially given by the product of two equilibrium constants, i.e. $K_{app} \approx K_i(K^{cov})^{-1}$. In this report, we evaluate the K_i of the non covalent association of Nirmatrelvir with the SARS-CoV-2 main protease as a function on the protonation state of the catalytic dyad HIS41-CYS145 by using the massively parallel virtual Double System Single Box (vDSSB) methodology [6] for computing drug-receptor binding affinities. Structural characterization have been obtained using extensive enhanced sampling simulations of the complexes. The structural features of the non-covalent association are discussed with valuable hints on the overall inhibition mechanism of the main protease by Nirmatrelvir.

2 Methods

The coordinates of the SARS-CoV-2 main protease were obtained from the X-ray structure from Liu et al. [7] (PDB code 6LU7). The initial structures for MD simulations of the complexes were prepared using the well known Vina docking program. We used the AMBER99SB force field with ILDN correction for the protein and we adopted the parametrization provided by the PrimaDORAC web interface[8] for Nirmatrelvir. The TIP3P model was used for the water solvent. The MD simulations were done in cubic boxes of appropriate size in the isothermal-isobaric ensemble using the Parrinello-Rahman Lagrangian in standard thermodynamic conditions. Electrostatics were treated using the particle mesh Ewald method. Binding free energies were computed using the virtual Double System Single Box (vDSSB) alchemical approach, based on a combination of Hamiltonian Replica exchange and nonequilibrium simulations. The vDSSB technique for computing absolute dissociation free energies has been introduced and thoroughly discussed in Ref. [6]. Briefly, the algorithm is based on two massively parallel computational steps executed one after the other. First a Hamiltonian Replica Exchange (HREM) sampling of the ligand-protein complex and of the gas-phase ligand is performed. Second, starting from the HREM-generated initial configurations, the ligand is continuously annihilated in the complex and recoupled in pure solvent in two swarms of hundreds of independent and fast nonequilibrium alchemical trajectories corresponding to two independent embarrassingly parallel jobs. HREM technical specifications (scaling protocol, hot-zone definition, and number of replicas) are identical to those in Ref. [6]. Growth of the ligand in the bulk solvent was achieved in 0.36 ns switching on the Lennard-Jones and the electrostatic interactions in sequence. Annihilation of the ligand in the complex was performed with inverted protocol (electrostatics turned off first followed by the Lennard-Jones interactions) in 0.56 ns. All simulations were done on the CRESCO6 cluster[9] managed by ENEA in Portici using the program ORAC [10]

3 Results and discussion

3.1 Docking results

In Figure 1, we summarize the results obtained with the Vina docking program, using the default settings, for the Nirmatrelvir-Sars-CoV-2 main protease non covalent binding.

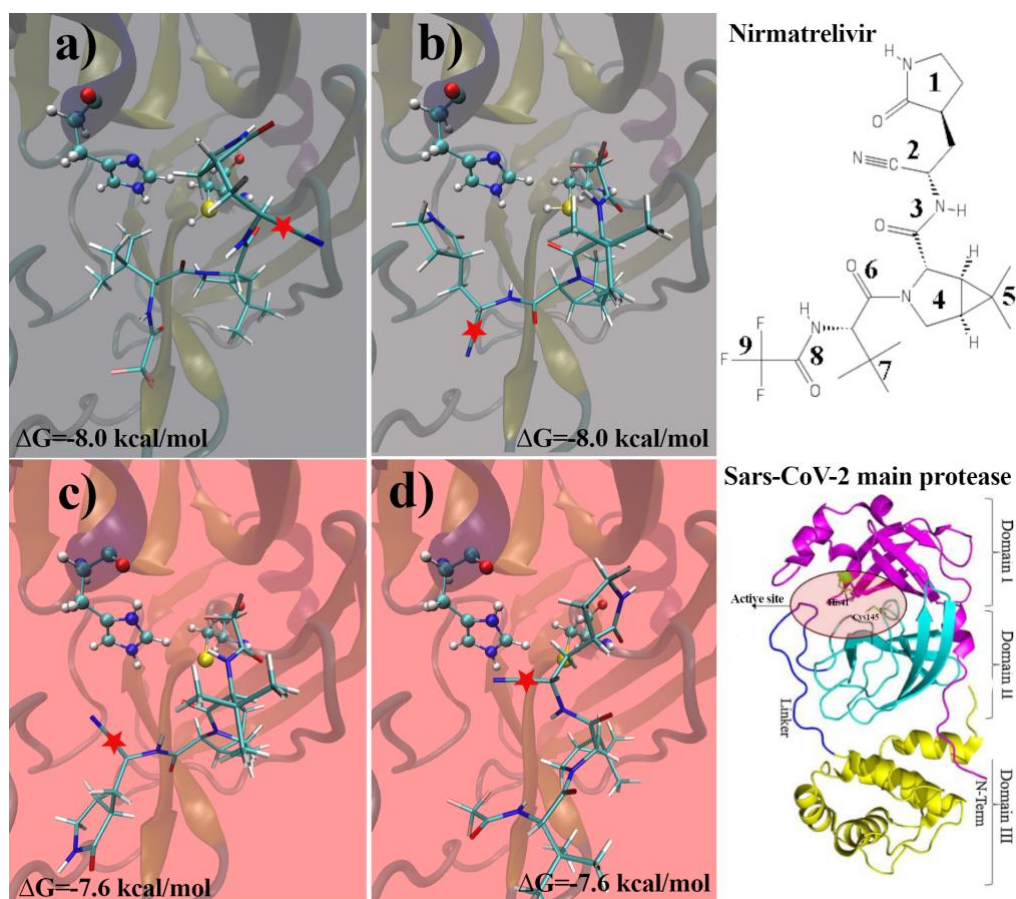


Fig. 1: Lowest Nirmatrelvir (bond representation) energy poses obtained with Autodock Vina for the main protease with the catalytic dyad His41-Cys145 (ball and stick) in the neutral (a, b) and zwitterionic(c,d) form. The nitrile warhead of Nirmatrelvir is marked with a red star. In the righthmost panels, the structure of Nirmatrelvir and of the SarS-Cov-2 main protease are reported.

With the catalytic dyad in the neutral form, we obtain two degenerate optimal poses ($\Delta G = -8.0$ kcal/mol) with a mutual RMSD exceeding 6 Å, with the second pose flipped by $\sim 180^\circ$ with respect to a rotation axis passing by the center of mass (COM) of the ligand and perpendicular to the plane of the figure. The same situation is seen when the catalytic dyad is in the zwitterionic form (i.e. negatively charged CYS145 and positively charged HIS41). We have again two isoenergetic optimal poses ($\Delta G = -7.6$ kcal/mol) with the ligand rotated by 180° with respect to a rotation axis approximately perpendicular to the plane of the figure and passing near the COM of the ligand. In all the four Vina binding poses, the nitrile moiety is rather far from the CYS145 sulfur atom with the distance between the *sp* carbon of the ligand and the cysteine sulfur atom in the range 5-7.5 Å. The closest S(CYS145)-C(nitrile) contact (at ~ 5 Å) is observed for pose of Figure 1d referring to the zwitterionic form of the main protease.

3.2 HREM results

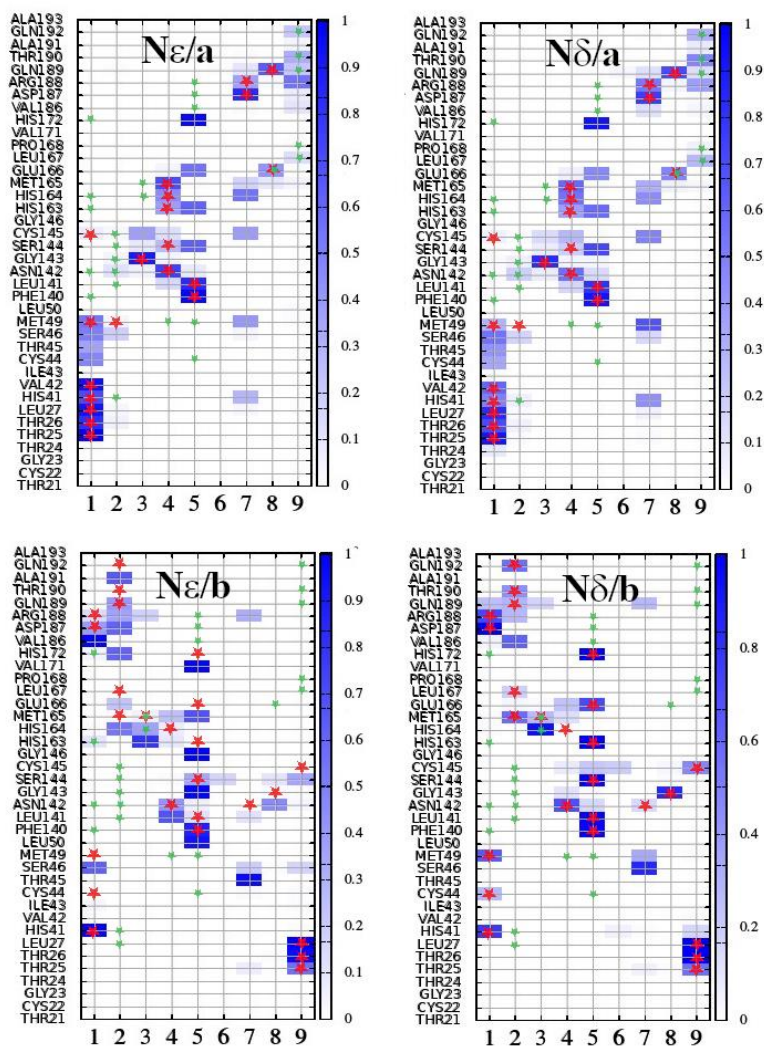


Fig. 2: Nirmatrelvir-main protease heat-map obtained with HREM for the neutral form of the CYS145-HIS41 dyad. Contacts for the Vina starting poses (see Table 1) are indicated with a red star. Green stars refer to the experimental pose (PDB code 7VH8). The x-axis labels refer to the group labels indicated in Figure 1.

For the nirmatrelvir-main protease complex, we launched on CRESCO6 six HREM simulations with hot zone tempering (see Ref. [6]), each lasting 36 ns. The protonation states of HIS41 and the starting Vina optimal poses for this six enhanced sampling simulations are collected in Table 1

Table 1: Protonation states of the initial Vina poses (see Figure 1) in the HREM simulations

Dyad status	His41 tautomer	Vina starting pose (see Figure 1)
Neutral	$N\epsilon$	Pose a)
Neutral	$N\delta$	Pose a)
Neutral	$N\epsilon$	Pose b)
Neutral	$N\delta$	Pose b)
Zwitterionic	$N\epsilon/N\delta$	Pose c)
Zwitterionic	$N\epsilon/N\delta$	Pose d)

Results obtained with HREM for the complexes are shown in the heat-maps of Figures 2 and 3. The ligand has been sectioned into 9 groups (Figure 1 for group labels) with the index (2) referring to the nitrile warhead. A ligand group is assumed to be in contact with a given protein residue if any group-residue atom-atom distance is found below 4.5 Å. The heat-bar on the right of the maps refers to the contact probability.

In general, we note that HREM with hot-zone tempering, while allowing a certain degree of conformational freedom of the ligand in the pocket, does not afford pose swaps. The Vina orientations are approximately conserved in all six cases. Pose swapping implies rotations (see Figure 1) that are possible only if the ligand leaves the binding site, then rebinding with a different orientation.

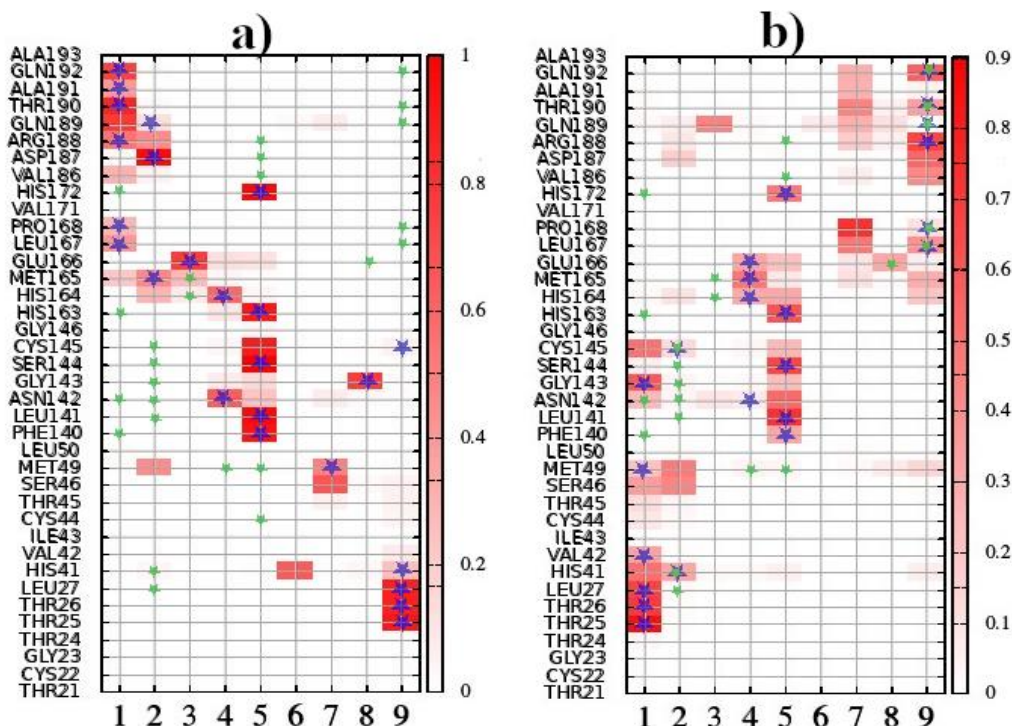


Fig 3: Nirmatrelvir-main protease heat-map obtained with HREM for the zwitterionic form of the CYS145-HIS41 dyad. Contacts for the Vina starting poses (see Table 1) are indicated with a blue star. Green stars refer to the experimental pose 7VH8. The x-axis labels refer to the group labels indicated in Figure 1.

When the dyad is in the neutral form (Figure 2), the Vina pose a) (see Figure 1) is conserved during the HREM simulation with minimal adjustments, irrespective of the tautomeric state of HIS41. When HIS41 is in the N δ state, we observe a weakening of the interaction between HIS4 and the pyrrolidine-2-one moiety (group 1) and a strengthening of the interaction between MET49 and the trimethyl group 7. Starting from the Vina pose b), significant readjustments (see Figure 2) are seen when HIS41 is in the N ϵ form, while for the N δ tautomer the starting Vina pose b) is firmly maintained throughout the whole HREM simulation. As inferred from the maps, the Vina-derived HREM poses are quite far from the experimental covalently bound Nirmatrelvir pose taken from Ref. [11].

When the dyad is in the zwitterionic state, we again see very limited deviations of the HREM heat-maps from the starting Vina poses, irrespective of the HIS41 tautomeric form. Notably, pose d) in this case is not far from the experimental structure [10], with the HREM-derived contacts of the tri-fluoro methyl group and of the nitrile warhead of the ligand closely matching the experimental contacts.

3.3 vDSSB results for dissociation free energies.

As shown in Eq. (1), the inhibition potency depends on two concurrent chemical equilibria. The experimental dissociation free energy is reported to be 13.5 kcal/mol [12]. Assuming that $K_{app} \approx K_i(K^{cov})^{-1}$, the lower is K_i (i.e. the stronger is the non covalent affinity) the weaker the reversible covalent binding of warhead must be. The nitrile moiety is a notoriously a weak electrophile towards cysteine [13].

Table 2: Dissociation Free energies (kcal/mol) for the six Nirmatrelvir-main protease complexes

Dyad status	His41 tautomer	Vina pose	Dissociation free energy
Neutral	N ϵ	a)	11.8 +/- 1.0
Neutral	N δ	a)	4.5 +/- 1.3
Neutral	N ϵ	b)	3.2 +/- 0.8
Neutral	N δ	b)	6.1 +/- 0.5
Zwitterionic	N ϵ /N δ	c)	4.4 +/- 0.5
Zwitterionic	N ϵ /N δ	d)	Non binding

In Table 2, we report the binding affinities of the six variants for Nirmatrelvir-main protease complex. Dissociation free energies of the complexes were obtained by applying the well known Jarzyski theorem to the convolution of the annihilation work of the ligand in a swarm of nonequilibrium simulations starting from the H-REM configurations, and of the recoupling work of Nirmatrelvir in bulk solvent. Remarkably, the highest dissociation free energy is found for the dyad in the neutral form (pose a/state N ϵ) in an orientation that differs significantly from that of the covalently bound ligand in the experimental structure (see Figure 2 N ϵ /a). The closest HREM-sampled variant to the experimental structure of the complex, corresponding to the d) pose with the dyad in the zwitterionic state is found to be a very weak *non-covalent* binder. This result lends further support to an inhibitory mechanism whereby the initial non-covalent addition to the main protease with the dyad in neutral form *precedes* the formation of the thiolate-imidazolium.[*macchia*] The latter is probably sluggishly formed concurrently with a complex ligand relocation in the binding site to form the covalent bond between the nitrile carbon and the cysteine sulfur atom.

In conclusion, the potency of Nirmatrelvir towards the SARS-CoV-2 main protease is largely dominated to the K_i referring to the initial non covalent binding with an estimated contribution to the apparent dissociation constant of only $(K^{cov})^{-1} \simeq 7 \times 10^{-2}$, in full agreement with the weak electrophile nitrile moiety towards cysteine (see Ref. [13]).

Acknowledgments

The computing resources and the related technical support used for this work have been provided by CRESCO/ENEAGRID High Performance Computing infrastructure and its staff. CRESCO/ENEAGRID High Performance Computing infrastructure is funded by ENEA, the Italian National Agency for New Technologies, Energy and Sustainable Economic Development and by Italian and European research programmes (see www.cresco.enea.it for information).

References

- [1] Blanchflower DG and Bryson. A Long COVID in the United States. PLOS ONE **18**, e0292672 (2023).
- [2] Zhang YZ and Holmes EC. A Genomic Perspective on the Origin and Emergence of SARS-CoV-2. Cell **181**, pp 223-227 (2020).
- [3] Macchiagodena M, Pagliai M and Procacci P. Identification of potential binders of the main protease 3CLpro of the COVID-19 via structure-based ligand design and molecular modeling. Chem. Phys. Lett. **750**, pp 137489 (2020).
- [4] Halford B. Pfizer unveils its oral SARS-CoV-2 inhibitor. Chem. Eng. News **99**, pp 7 (2021).
- [5] Westberg M, Su Y, Zou X, Ning L, Hurst B, Tarbet B, Lin MZ. Rational design of a new class of protease inhibitors for the potential treatment of coronavirus diseases. BioRxiv, 09.15.275891 (2020)
- [6] Macchiagodena M, Pagliai M, Karrenbrock M, Guarnieri G, Iannone F and Procacci P. Virtual Double-System Single-Box: A Nonequilibrium Alchemical Technique for Absolute Binding Free Energy Calculations: Application to Ligands of the SARS- CoV-2 Main Protease. J. Chem. Theory Comput. , **16** , pp 7160-7172 (2020)
- [7] Liu X, Zhang B, Jin Z, Yang H and Rao Z. The Crystal Structure of 2019-nCoV Main Protease in Complex with an Inhibitor N3. RSCB PDB, pdbcode: 6LU7 (2020).

- [8] Procacci, P. PrimaDORAC: A Free Web Interface for the Assignment of Partial Charges, Chemical Topology, and Bonded Parameters in Organic or Drug Molecules. *J. Chem. Inf. Model.* **57**, pp 1240-1245 (2017).
- [9] Iannone F, Ambrosino F, Bracco G, De Rosa M, Funel A, Guarnieri G, Migliori S, Palombi F, Ponti G, Santomauro G, Procacci P. CRESCO ENEA HPC clusters: a working example of a multifabric GPFS Spectrum Scale layout. 2019 International Conference on High Performance Computing Simulation (HPCS), pp 1051–1052 (2019).
- [10] Procacci, P. Hybrid MPI/OpenMP Implementation of the ORAC Molecular Dynamics Program for Generalized Ensemble and Fast Switching Alchemical Simulations. *J. Chem. Inf. Model.* **56**, pp 1117-1121 (2016).
- [10] Yao Zhao, Chao Fang, Qi Zhang, Ruxue Zhang, Xiangbo Zhao, Yinkai Duan, Haofeng Wang, Yan Zhu, Lu Feng, Jinyi Zhao, Maolin Shao, Xiuna Yang, Leike Zhang, Chao Peng, Kailin Yang, Dawei Ma, Zihe Rao, Haitao Yang, Crystal structure of SARS-CoV-2 main protease in complex with protease inhibitor PF-07321332, *Protein & Cell*, **13**, Issue 9, pp 689–693 (2022)
- [11] Dafydd RO et al.. An oral SARS-CoV-2 Mpro inhibitor clinical candidate for the treatment of COVID-19. *Science* **374**, pp 1586-1593 (2021)
- [12] Petri L, Egyed A, Bajusz D, Imre T, Hetényi A, Martinek T, Ábrányi-Balogh P, Keserű GM. An electrophilic warhead library for mapping the reactivity and accessibility of tractable cysteines in protein kinases. *Eur J Med Chem.* **207** pp112836.

FIRST-PRINCIPLES METADYNAMICS SIMULATIONS OF PEO/(101)-TiO₂ ANATASE INTERFACES

Arianna Massaro^{1*}, Francesca Fasulo², Ana B. Muñoz-García² and Michele Pavone¹

¹*Department of Chemical Science, University of Naples Federico II, Compl. Univ. Monte Sant'Angelo, Via Cintia 21, Naples, 80126, Italy*

²*Department of Physics "E. Pancini", University of Naples Federico II, Compl. Univ. Monte Sant'Angelo, Via Cintia 21, Naples, 80126, Italy*

ABSTRACT. Structural and dynamic properties of PEO/TiO₂ are investigated *via* metadynamics simulations and Density Functional Tight Binding (DFTB). The conformational freedom of PEO is affected by multiple favourable interactions with the unsaturated Ti sites on surface. Electronic structure analysis performed within DFT reveals that the titania work-function is largely influenced by the dynamical structuring of PEO on anatase surface, the trend correlating with the evolution of dipole moment across the heterogeneous interface over time.

1 Introduction

The research carried out at University of Naples "Federico II" has mainly targeted the characterization of PEO dynamics on (101)-TiO₂ anatase surface to get insights into the polymer structuring and related influence on anatase electronic features. Formed by two versatile and sustainable materials, this heterogeneous interface is technologically appealing for various applications. Even though dynamic features of PEO/anatase interfaces have already been addressed by classical MD methods [1], innovation and relevance of metadynamics (MetaD) approach can properly tackle both the polymer motion and the detailed adsorption/desorption mechanism at the heterogeneous surface [2]. On one hand, the FES for the conformational movements of the polymer chain is expected to be quite flat with multiple equilibrium states structurally similar and lying close in energy. On the other hand, as an enhanced sampling method, MetaD can gain either strongly chemisorbed and desorption states which in principle can be deeply separated by high energy barriers. Thus, we explore the conformational space and the coordination modes adopted by PEO chain interacting with the (101) anatase surface. We perform self-consistent charge (SCC)-DFTB calculations [3,4], which can provide reliable results on structures, electronic features, and energetics for the titania interface, in qualitative agreement with DFT but at a much-reduced computational cost [5,6]. Our findings set solid scientific foundations towards future investigations on structure and dynamics of similar oxide/polymer interfaces.

2 Methods and computational details

The (101) TiO₂ anatase surface is modelled as a 2×2 supercell three-bilayer slab containing 48 TiO₂ f.u. with a 15 Å vacuum along the c direction to avoid interactions between periodic replicas. The PEO model chain is built as a 4 repeating units of ethylene oxide with -CH₃ and -OCH₃ terminus (*i.e.*, CH₃-[OCH₂CH₂]₄-OCH₃) to simulate a PEO-like oligomer. Static geometry optimizations at DFT and DFTB levels of theory are performed within VASP and DFTB+ codes, respectively [7,8]. Dispersion contributions are included as *a posteriori* correction developed by Grimme with Becke-Johnson damping functions (*i.e.*, D3BJ) [9]. For the spin-polarized DFT calculations, the Perdew-Burke-Ernzerhof (PBE) functional within generalized gradient approximation (GGA) is employed to account for exchange-correlation effects [10], the projector-augmented wave (PAW) potentials considered for Ti_pv (3p⁶3d³4s¹), O (2s²2p⁴), C (2s²2p²), and H (1s²) valence electrons [11], and the plane wave (PW) basis sets expanded with 600 eV kinetic energy value. Convergence criteria for energy and force are set to 10⁻⁵ eV and 0.03 eV/Å. For the SCC-DFTB calculations, the MATSCI parameterization of DFTB is selected [4,6]. For MetaD simulations, the DFTB+ package is combined with PLUMED [12]. Atomic motion is propagated through velocity Verlet algorithm with a time step of 0.5 fs. Canonical sampling through a Nosé-Hoover thermostat with a target temperature of 300 K and a coupling strength of 3500 cm⁻¹ is used to impose NVT conditions to the system. The systems are allowed to evolve for 1 ns to ensure the FES convergence. The Gaussian hills sigma is set to 0.05 Å, the height to 4.0 kJ/mol, the

bias factor to 50, and the deposition rate to 100 steps. The k-points sampling is restricted to the Γ -point. Electronic structure analysis is carried out on the minimum-energy geometries along the FES by averaging on 5 snapshots of a specific point: work functions are computed at the PBE(D3BJ) level of theory from the vacuum energy level and the valence band (VB) edge, according to the approach proposed by Toroker *et al.* [13].

3 Results and discussion

The main PEO/TiO₂ anatase interactions are inspected in terms of adsorption of one polymer chain on the (101) termination. Two possible polymer configurations are considered: the helical and the unfolded shape, resembling the crystalline and the amorphous domains, respectively. See Fig.1.

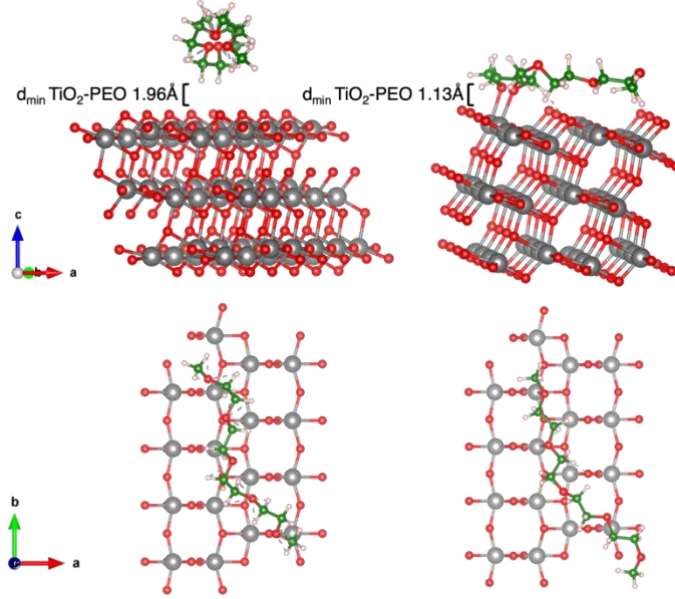


Fig. 1. Side and top views of minimum-energy structures for the PEO/(101)-TiO₂ anatase interface in both **(left)** helical shape and **(right)** unfolded chain conformation obtained at PBE(D3BJ) and DFTB(D3BJ) level of theory. The minimum interfacial distances in both cases are highlighted. Colour code: Ti atoms, grey; O atoms, red; C atoms, green; H atoms, pink.

Adsorption energies are computed according to Eq. (1):

$$E_{ads} = E_{PEO-TiO_2} - (E_{PEO} + E_{TiO_2}) \quad (1)$$

where $E_{PEO-TiO_2}$, E_{PEO} , and E_{TiO_2} are the total energies of the interface, the chain and the pristine anatase slab, respectively. The adsorption energy of the unfolded type is much more negative compared to the helix, as reported in Table 1, which can be ascribed to the strong electrostatic interactions of the exposed PEO oxygen atoms that can establish closer contacts with the Ti atoms on anatase surface.

Table 1. Adsorption energies, E_{ads} , computed according to Eq. (1) at PBE(D3BJ) and DFTB(D3BJ) levels of theory for the two minimum-energy structures of PEO/(101)-TiO₂ anatase interface.

	helical shape	unfolded chain
PBE(D3BJ)	-0.553 eV	-1.683 eV
DFTB(D3BJ)	-0.635 eV	-3.448 eV

Two different CVs are selected to map the MetaD trajectory and describe the dynamical structuring of the interface: (i) the configurational interaction is followed by the number of Ti-O bonds that are formed between the polymer chain and the anatase surface, deemed as the distances below a threshold value of 2.6 Å (*i.e.*, CV1, namely $n(d_{Ti-O})$, is defined as $n = \sum(d_{Ti-O} < 2.6)$ and ranges from 0 to 5); (ii) the conformational space is tracked

by drawing the chain torsion around the central ω (C-C-O-C) dihedral angle, which is evaluated as the cosine function of the dihedral value (*i.e.*, CV2 is $\cos(\omega)$ ranging from -1 to 1). Mono-, bi- and three-coordinated configurations of PEO/anatase represent comparable FES wells, suggesting that PEO can interact with anatase in multiple modes. The flat FES shows three almost degenerate equilibrium states corresponding to skew and eclipsed conformations.

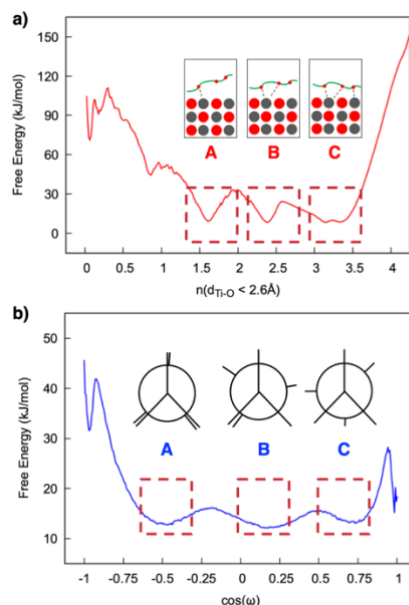


Fig. 2. Converged FESs along 1ns-trajectory reconstructed upon **a)** CV1, number of Ti-O distances; **b)** CV2, cosine of dihedral angle.

Electronic features can also convey dynamical evolution over time. For each structure, we evaluate the work function (WF) as the energy difference of the vacuum energy level at the interface and the TiO_2 VB maximum (VBM):

$$WF = E_{vacuum} - E_{VBM(TiO_2)} \quad (2)$$

The so-obtained values show non-innocent variations, which ultimately attest the intrinsically dynamic feature of the WF: it turns out to be sensitive to the different dipole moments generated across the interface over time. The correlation is clearly visible from the plotted data in Fig. 3: the larger the dipole moment the smaller the work function.

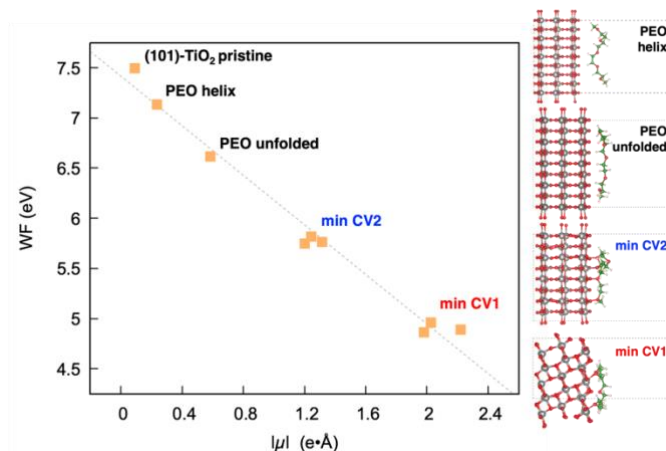


Fig. 3. Plot of WF values calculated at PBE(D3BJ) level of theory as function of dipole moment associated to each configuration.

3 Conclusions

Our theoretical study shows that the FESs for the polymer/crystal system under investigation can be sampled by means of metadynamics simulations. Combined to tight-binding based methods, the MetaD-DFTB(D3BJ) is a promising approach to reliably describe structure, electronic features, energetics and dynamics at an affordable computational cost. These results are gathered in a paper currently under review. The computing resources and the related technical support used for this work are provided by CRESCO/ENEAGRID High Performance Computing infrastructure and its staff; CRESCO/ENEAGRID High Performance Computing infrastructure is funded by ENEA, the Italian National Agency for New Technologies, Energy and Sustainable Economic Development and by Italian and European research programs. See: <http://www.cresco.enea.it/english> for information [14].

References

- [1] O. Borodin, G.D. Smith, R. Bandyopadhyaya, O. Byutner, *Macromolecules* 2003, 36(20), 7873-7883.
- [2] A. Barducci, M. Bonomi, M. Parrinello, *WIREs Comput. Mol. Sci.* 2011, 1 (5), 826-843.
- [3] G. Seifert, *J. Phys. Chem. A* 2007, 111 (26), 5609-5613.
- [4] J. Frenzel, A. F. Oliveira, N. Jardillier, T. Heine, G. Seifert, 2009, 2004-2005.
- [5] D. Sellì, G. Fazio, G. Seifert, C. Di Valentin, *J. Chem. Theory Comput.* 2017, 13 (8), 3862-3873.
- [6] R. Luschtinetz, J. Frenzel, T. Milek, G. Seifert, *J. Phys. Chem. C* 2009, 113 (14), 5730-5740.
- [7] G. Kresse, J. Furthmüller, *J. Phys. Rev. B* 1996, 54 (16), 11169-11186.
- [8] B. Hourahine, et al. *J. Chem. Phys.* 2020, 152 (12), 124101.
- [9] S. Grimme, J. Antony, S. Ehrlich, H. J. Krieg, *Chem. Phys.* 2010, 132 (15), 154104.
- [10] J. P. Perdew, K. Burke, M. Ernzerhof, *Phys. Rev. Lett.* 1997, 78 (7), 1396-1396.
- [11] P. E. Blöchl, *Phys. Rev. B* 1994, 50 (24), 17953-17979.
- [12] G. A. Tribello, M. Bonomi, D. Branduardi, C. Camilloni, G. Bussi, *Comput. Phys. Commun.* 2014, 185 (2), 604-613.
- [13] M. C. Toroker, D. K. Kanan, N. Alidoust, L. Y. Isseroff, P. Liao, E. A. Carter, *Phys. Chem. Chem. Phys.* 2011, 13 (37), 16644-16654.
- [14] G. Ponti, et al. The role of medium size facilities in the HPC ecosystem: the case of the new CRESCO4 cluster integrated in the ENEAGRID infrastructure, *Int. Conf. on High Perform. Comp. & Simul. (HPCS)* pp 1030-1033 (2014).

NUCLEAR ANALYSES IN SUPPORT OF ITER EX-PORT RADIAL NEUTRON CAMERA DESIGN

Fabio Moro¹, Daniele Marocco¹, Francesco Belli¹, Dariusz Bocian², Giorgio Brolatti¹, Silvia Cesaroni¹, Andrea Colangeli¹, Davide Flammini¹, Nicola Fomesu¹, Davide Falco³, Giada Gandolfo¹, Ryszard Kantor⁴, Jerzy Kotula², Domenico Marzullo⁵, Simone Noce¹, Enrico Occhiuto⁵, Rafal Ortwein², Alberto Previti¹, Dustin Sancristóbal⁶, Rosaria Villari¹ and Basilio Esposito¹

⁽¹⁾ Nuclear Department, ENEA, Via E. Fermi 45, I-00044, Frascati (RM), Italy

⁽²⁾ Henryk Niewodniczanski Institute of Nuclear Physics of the Polish Academy of Sciences, ul. Radzikowskiego 152, 31-342 Cracow, Poland

⁽³⁾ NIER Engineering, Via Clodoveo Bonazzi, 2, 40013, Castel Maggiore, Bologna, Italy

⁽⁴⁾ Cracow University of Technology, ul. Warszawska 24, 31-155 Cracow, Poland

⁽⁵⁾ Trieste University, Department of Engineering and Architecture, 34127, Trieste, Italy

⁽⁶⁾ IDOM s.a., Av. de la Fama, 11-15, 08940, Cornellà de Llobregat, Barcelona, Spain

ABSTRACT. The Radial Neutron Camera (RNC) is a diagnostic system located in the ITER Equatorial Port 1 (EP01) composed by two sub-systems (i.e.: in-port and ex-port RNC) probing a poloidal section of the plasma through a set of fan-shaped Lines of Sight (LOS). The RNC is designed to provide a time resolved measurement of the neutron and alpha particles source profiles and of the total neutron source strength, through the application of reconstruction techniques to the line-integrated neutron fluxes.

The Ex-port sub-system is composed by 16 LOS distributed in two different toroidal planes and enclosed in a massive shielding unit, extending from the EP01 closure plate through the Port Interspace, up to the Bioshield Plug. Neutrons, generated in the plasma core, stream through dedicated optical paths hollowed out in the central EP01 diagnostic shielding module and reach the detectors units located at the end of collimating structures. Each detector unit contains one ⁴He gas scintillator, one plastic scintillator as well as one single Crystal Diamond (sCD) matrix.

The performed nuclear analysis allowed the selection of the SWX-277Z-5 castable borated hydrogenated mix as suitable material for the RNC shielding block; moreover, the evaluation of the nuclear heating on the ex-port RNC subcomponents, provided as input for structural analyses, highlighted that the impact of the radiation streaming is negligible with respect to the environmental thermal loads.

1 The ITER Radial Neutron Camera

The Radial Neutron Camera (RNC) [1] is a diagnostic system located in the ITER Equatorial Port 1 (EP01), designed to provide a time resolved assessment of the neutron and α particles source profiles, total neutron source strength and neutron emissivity, through the application of reconstruction techniques to the line-integrated neutron fluxes. Such measurements allow the evaluation of several key parameter necessary for plasma physics studies and control, as well as the estimation of the total fusion power [2, 3]. The RNC is composed by two sub-systems (Fig. 1) probing a poloidal section of the plasma through a set of fan-shaped Lines of Sight (LOS) [4].

The in-port RNC [5, 6], devoted to the plasma edge coverage ($r/a > 0.67$, a = minor radius), consists of a cassette embedded into the EP01 Diagnostic Shielding Module (DSM). It is provided with six LOS equipped with two detectors each: a single Crystal Diamond (sCD) matrix and a ²³⁸U Fission Chamber (FC).

The ex-port sub-system is composed by sixteen LOS distributed in two different toroidal planes and enclosed in a massive shielding unit, extending from the EP01 closure plate through the Port Interspace, up to the Bioshield Plug.

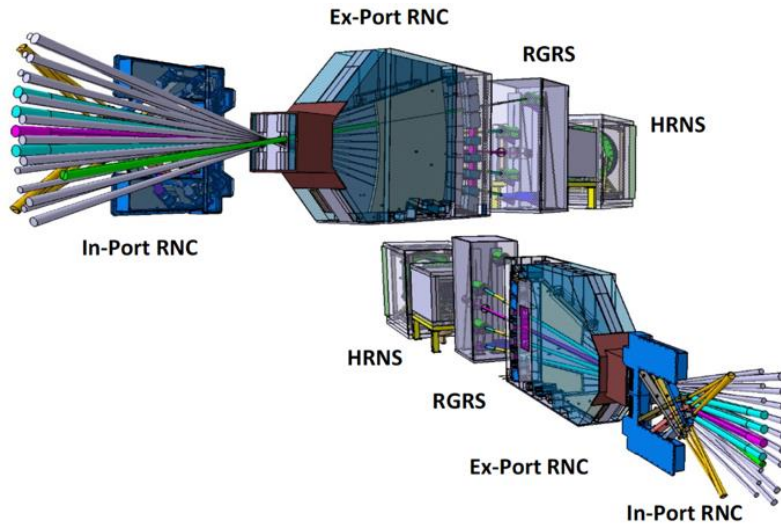


Fig.1: Layout of the RNC showing the in-port LOS (yellow), the ex-port LOS (light purple) and the ones belonging to the interfacing diagnostics RGRS (pale blue) and HRNS (violet).

Neutrons, generated in the plasma core ($r/a < 0.54$), stream through dedicated optical paths hollowed out of the central EP01 DSM and reach the detectors units located at the end of collimating structures. Each detectors unit contains scintillators (gas and plastic) as well as a sCD matrix, enabling spectrometric measurements. The ex-port RNC interfaces with the High Resolution Neutron Spectrometer (HRNS) and the Radial Gamma Ray Spectrometer (RGRS) which have 1 and 3 dedicated LOS respectively (four central collimators of the right set, looking towards the plasma).

Specific calculations have been performed by means of the Monte Carlo MCNP code [7], coupled with the FENDL-3.1d nuclear data libraries [8], aimed at assessing the nuclear loads on the ex-port RNC components during Normal Operating Conditions (NOC), in order to select a suitable material for the shielding block and beam dumps, to assess of the nuclear heating on the detector boxes in support of the cooling system design as well as to evaluate the heat load on the whole structure, providing input for structural analyses.

2 Nuclear analyses

2.1 Integration of the ex-port RNC MCNP geometry in the ITER C-model

The generated ex-port RNC MCNP model has been enclosed into an updated version of the ITER C-model developed by the Port Integrator in which the diagnostic systems located in the EP01 are included in the full central equatorial port.



Fig.2: Poloidal and toroidal section of the ITER MCNP C-model integrating the EP01 features and ex-port RNC.

Such model represents a 40° regular sector of the machine, extended up to the Bioshield plug with complete equatorial, upper and lower ports at the center and half ports at the sides, where periodic boundary conditions are enabled, in order to account for the whole tokamak (Fig. 2). The integrated model has been used to assess the nuclear loads on the diagnostic system in mesh format and on each specific subcomponent, through a suitable tallies definition. The calculations have been performed using the standard ITER plasma source (inductive H-mode, 10 MA/5.3T, 500 MW fusion power, neutron yield: $1.773 \times 10^{20} \text{ s}^{-1}$) embedded in the ITER C-model.

2.2 Assessment of the nuclear loads spatial distribution

The total neutron flux spatial distribution is shown in Fig. 3: the section along the right-hand side collimators set shows the enhanced neutron streaming affecting the central HRNS LOS. The same effect is observed in the left hand side for the third collimator (from the top) that is shared with the RGRS detection system and has a larger diameter.

The neutron flux in the shielding block ‘nose’ area is around $1.3 \times 10^{11} \text{ n/cm}^2/\text{s}$ and it decreases of about 4 orders of magnitude around the detectors’ boxes. The LOS exclusively dedicated to the RGRS and HRNS has no beam dumps, thus the neutrons are allowed to pass through the shielding block and reach the diagnostic systems located backward.

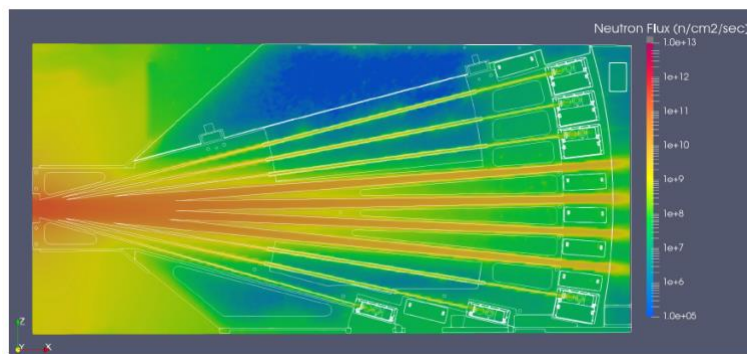


Fig.3: Section of the total neutron flux ($\text{n/cm}^2/\text{s}$) map across the right hand side collimators set.

The nuclear heating data have been provided in 3D map format (Fig. 4), computed on a 2cm mesh voxel size as input for thermal and thermo-mechanical analyses: both the contribution of neutrons and secondary gammas have been taken into account. The results of the calculations highlight that, in the shielding block ‘nose’ where the focal point of the collimators is located, the heat load on the stainless steel reaches a maximum value of $2 \times 10^{-3} \text{ W/cm}^3$. At the detectors boxes, the highest value has been recorded for the central LOS where it reaches $5 \times 10^{-6} \text{ W/cm}^3$.

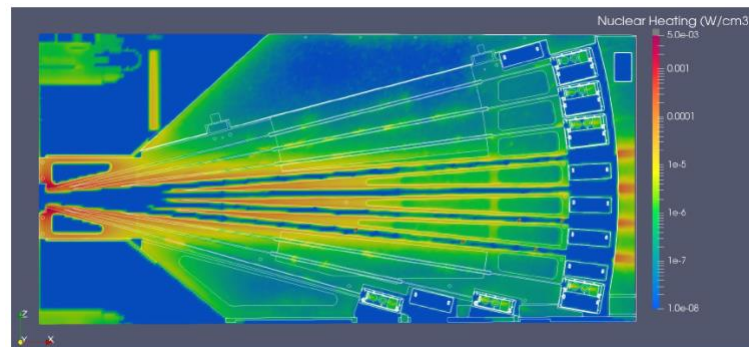


Fig.4: Section of the nuclear heating density (W/cm^3) map across the right hand side collimators set.

The outcome of the nuclear studies has been used as input for thermal analysis on the whole ex-port RNC structure, and to provide guideline for the design development its subcomponents:

- The contribution of the heat load on the ex-port RNC structure due to radiation streaming is negligible with respect to the environmental thermal loads, being the maximum reached temperature below 50°C in the nose area, only +15° with respect to the surrounding air.

- The assessment of the volumetric heat load on the detectors' unit subcomponents showed that the impact of the deposited energy due to neutrons and secondary gammas can be neglected in the design of the dedicated cooling circuit. For instance, the ambient temperature foreseen in the Interspace during NOC ranges between 5-35 °C: even assuming the lower limit (5 °C), the resulting heat load deposited on the detector box is about 5×10^3 W/m³, thus 3 orders of magnitude higher with respect to the one due to nuclear loads.
- The B₄C beam dump located in the back area of the detectors' boxes ensure a reduction of the direct neutron flux of a factor ~70 (the neutron flux impinging on the beam dump in LOS 12 is 4.7×10^7 n/cm²/s, the emerging neutron flux is 6.9×10^7 n/cm²/s).
- Additional calculations, performed to evaluate the nuclear loads on the Position Monitoring System and associated optical fibers, highlight their compliancy in terms of neutron fluence and cumulated dose over the ITER lifetime. The maximum neutron fluence impinging on the PMS sensors is 1.4×10^{17} n/cm² and a cumulative dose of 0.04 MGy is expected, below the radiation hardness design limits.

Acknowledgments

This work was funded by F4E under the contract F4E-FPA-327.

The computing resources and the related technical support used for this work have been provided by CRESCO/ENEAGRID High Performance Computing infrastructure and its staff [9]. CRESCO/ENEAGRID High Performance Computing infrastructure is funded by ENEA.

References

- [1] B. Esposito, *et al.*, 'Progress of Design and Development for the ITER Radial Neutron Camera', *Journal of Fusion Energy*, vol. 41, issue 2, article number 22, 2022.
- [2] D. Marocco *et al.*, 'Combined unfolding and spatial inversion of neutron camera measurements for ion temperature profile determination in ITER', *Nuclear Fusion*, vol 51, Art. no. 053011, 2011.
- [3] D. Marocco *et al.*, 'Neutron measurements in ITER using the Radial Neutron Camera', *Journal of Instrumentation*, vol. 7, no. 3, Art. no. C03033, 2012.
- [4] D. Marocco *et al.*, 'System level design and performances of the ITER radial neutron camera', *Proceedings of the 26th IAEA Fusion Energy Conference, Kyoto*, 2016.
- [5] F. Moro *et al.*, 'The ITER radial neutron camera in-port system: Nuclear analyses in support of its design development', *Fusion Engineering and Design*, vol. 146, pp. 236-241, 2019.
- [6] F. Moro *et al.*, 'Nuclear analyses for the assessment of the loads on the ITER Radial Neutron Camera in-port system and evaluation of its measurement performances', *IEEE Transactions on Plasma Science*, doi: 10.1109/TPS.2022.3185801, 2022.
- [7] Los Alamos National Laboratories, MCNP User's Manual Code Version 6.2, 2017.
- [8] FENDL-3.1d: Fusion Evaluated Nuclear Data Library ver.3.1d, <https://www-nds.iaea.org/fendl/>, 2018.
- [9] F. Iannone *et al.*, 'CRESCO ENEA HPC clusters: a working example of a multifabric GPFS Spectrum Scale layout', *2019 International Conference on High Performance Computing & Simulation (HPCS)*, Dublin, Ireland, 2019, pp. 1051-1052, doi: 10.1109/HPCS48598.2019.9188135.

SASE X-RAY FREE-ELECTRON LASER DRIVEN BY RESONANT MULTI-PULSE IONIZATION ACCELERATION SCHEME

Federico Nguyen^{1*}, Paolo Tomassini², Leonida A. Gizzi³, Luca Giannessi⁴ and Anna Giribono⁴

¹*ENEA, Nuclear Department, I-00044, Frascati, Italy*

²*ELI-NP, R-077125, Magurele, Romania*

³*CNR-INO, I-56124, Pisa, Italy*

⁴*LNF-INFN, I-00044, Frascati, Italy*

ABSTRACT. Laser wakefield accelerators are on the way to provide GeV scale high-brightness electron beams for multidisciplinary applications. In the present work, electron bunches are studied in the framework of a Free-Electron Laser driven by an accelerator in the Resonant Multi-Pulse Ionisation framework. The transport to the undulator is provided by a matched beam focusing with marginal beam quality degradation. Finally, using the CRESCO/ENEAGRID High Performance Computing infrastructure, 3D time-dependent simulations of the produced radiation show that about 10^{10} photons with central wavelength of 0.15nm will be delivered with the electron bunches under consideration.

1 Introduction

Nowadays, Free-Electron Laser (FEL) sources cover a wide range of applications, from materials science with effective technology transfer to industry to biomedical or pharmaceutical research advances. Efficient FEL operation in the X-ray domain requires the establishment of a high gain regime of energy transfer from the electron beam to X-ray photons, to finally yield a high-power laser pulse. This is achieved provided that the beam energy spread, and transverse emittances are sufficiently small to preserve the resonance condition set by the beam energy, the undulator period and deflection strength. The laser wakefield accelerator (LWFA) is a rapidly growing field of research and development in terms of potential flexibility and size reduction to drive an FEL. In the resonant multi-pulse ionization (ReMPI) injection [1], a tightly focused, short-wavelength pulse acts as the ionization pulse. Such a pulse extracts electrons from a dopant (e.g. N, Ar or Kr) and the remaining largest portion of the Ti:Sa pulse is time shaped as a sequence of sub-pulses and focused on the target with a long parabola. In this scheme, plasma density fluctuations result in the most severe source of beam quality fluctuations. Therefore, different electron bunches are simulated varying the plasma density by $\pm 2.5\%$ and by $\pm 5\%$ with respect to the reference condition. FEL performance is evaluated for each of these bunches, assuming to operate the source in self-amplified spontaneous emission (SASE) configuration, that allows the growth of spontaneous radiation power through exponential gain and saturation in the undulators section without any external laser seed. The stability of results upon variation of the starting noise seed is studied in detail for each bunch.

2 Transport of the electron beams accelerated in the ReMPI scheme

In this approach [1], the extracted electrons have small transverse momentum and size after the ionizing pulse passage, due to the pulse low amplitude and size. As a result, a 32pC charge bunch with a normalized emittance of $\epsilon_{nx}=0.083\mu\text{rad}$ along the ionizing pulse polarization is obtained at the capillary target end. Moreover, due to a partial overlapping between the ionizing pulse and the last pulse of the train, a quasi-round beam with normalized emittance $\epsilon_{ny}=0.078\mu\text{rad}$ is achieved. As the ionizing pulse is diffracted away at the capillary entrance, the driving train and the obtained trapped bunch enter the boosting section. Inside the energy boosting section, each sub-pulse (except for the first one) propagates into a plasma wave excited by the previous pulses of the train, so that the time evolution of each pulse is unique in the train and different from a standard evolution

* Corresponding author. E-mail: federico.nguyen@enea.it

of a nonrelativistic pulse inside a capillary. At the end of the capillary density downramp, a $\sim 4.5\text{GeV}$ electron beam with peak current of 3.5kA , projected energy spread of about 2% and slice energy spread at the current peak of 3×10^{-4} is produced, with small differences depending upon variations of the plasma density.

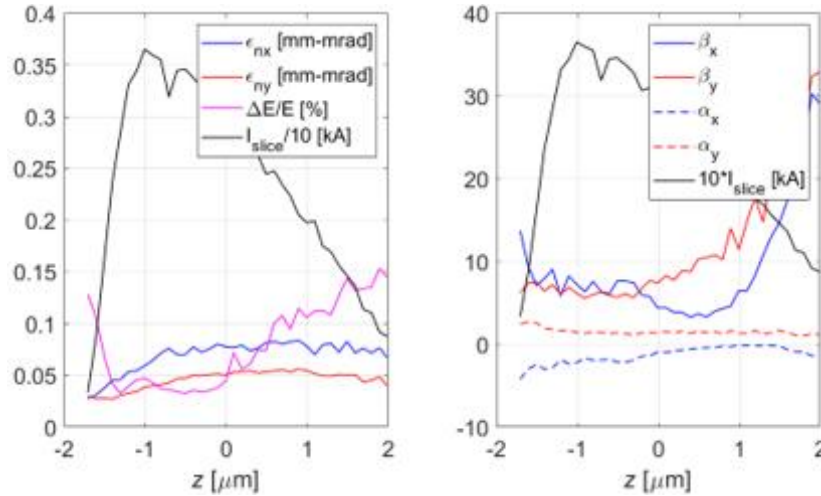


Fig.1: Slice analysis of the reference electron beam, at undulator entrance.

The beam transport and matching to the undulator line are enforced by a 10 m long transfer line consisting in the combination of state-of-the-art permanent and electromagnet quadrupoles. More in detail, the beamline is composed of three triplets of permanent magnet quadrupoles (PMQ) – the single triplet relying on 5-10-5 cm long quadrupoles with a nominal gradient of 450 T/m each spaced by 10 cm center-center – and four electromagnet quadrupoles (EMQ). The position and focusing gradients for PMQ quads have been settled aiming to capture the divergent beam taking advantage of the high magnetic field in a very short distance and trying to avoid spoiling the beam quality because of second order effects. The following EMQs, carry the beam at the undulator entrance and allow for Twiss parameters (α , β , and γ) tuning in a wide range acting only on their magnetic field. The transport beamline aims to carry the electron beam from the ReMPI exit stage and tackles the intrinsic transverse divergence and projected energy spread, potentially leading to emittance spoiling and chromaticity rise. In particular, the associated electron beam dynamics is explored by means of simulations with space-charge effects included, aiming to β values tunable in the range 8-12 m and absolute α functions around 1, with the beam converging in the vertical plane and diverging in the horizontal one. Figure 1 shows the slice analysis of the electron beam: the horizontal emittance along the beam always remains lower than 0.08mm-mrad values.

3 FEL beamline and performance

The undulator parameters chosen for the present study are the following: a planar undulator with undulator period $\lambda_u=14\text{mm}$ and deflection parameter $K=1.145$, capable to operate at a gap of about 5mm and to provide a remanent magnetic field of 1.22T. With the electron bunches under consideration having an average energy of $E_{\text{beam}}=4.5\text{GeV}$, the expected resonant wavelength is $\lambda_R \approx 0.15\text{nm}$ (namely about 8keV photon energy). The undulator beamline consists of 15 modules, each one with length $N_u=140$ periods, $L_u=N_u \times \lambda_u \approx 2\text{m}$, so that the total active length is about 30 meters. With $E_{\text{beam}}=4.5\text{GeV}$ a beam energy, the undulator has almost negligible focusing power, so that to keep the electron beam matched over the whole undulator beamline, the periodic magnetic cell has to include alternate gradient quadrupoles in between undulator modules. Accounting for fluctuations on the plasma density mainly affects the electron beam quality parameters at the undulator entrance and introduce a deviation from the nominal values of the Twiss functions of the beam entering the transport beamline. Four electron bunch distributions produced by varying the plasma density by $\pm 2.5\%$ and by $\pm 5\%$ with respect to the nominal condition, are carried through the same transport line and let interact and radiate through the same undulator beamline, in addition to the reference case.

Since the proposed FEL is designed to operate in SASE configuration, a relevant systematic effect is played by the initial noise power that fluctuates randomly. Therefore, the impact of the starting noise seed on the final

performance is accounted for generating nine additional replicas of the FEL time-dependent simulation obtained by only varying the initial seed, for each bunch coming from the plasma exit, including the modified plasma density bunches. The FEL performance is studied with the GENESIS1.3 simulation code [2], by providing the related full 6D phase space. In particular, the code is used to perform 10 random initial seed simulations times 5 different plasma density samples, namely 50 different FEL simulations. Each simulation has the bunch split in 4500 independent longitudinal slices. The full propagation through the undulator beamline of each slice can be calculated independently in parallel, and it is performed on the CRESCO4 Cluster [3], after having compiled the code with the MPI IMPI-INTEL17 libraries. Results on relevant quantities are obtained by combining the output files resulting from the MPI data decomposition.

Each of the five panels of Figure 2 shows the growth of the pulse energy as a function of the undulator propagation coordinate, for a sample obtained with a different plasma density, specified in terms of fractional difference with respect to the reference value. Every highlighted curve is the average result out of the 4500 slices propagation, and out of 10 different noise seed simulations. On each panel, the highlighted curve is superimposed to the envelope of those 10 simulations and fit to the exponential distribution, for evaluating the gain length L_g from the e^{z/L_g} scaling behavior: upper left box shows fit results and errors. As a result, the gain length value $L_g = 1.8 m$ is obtained, quite consistently among the five samples.

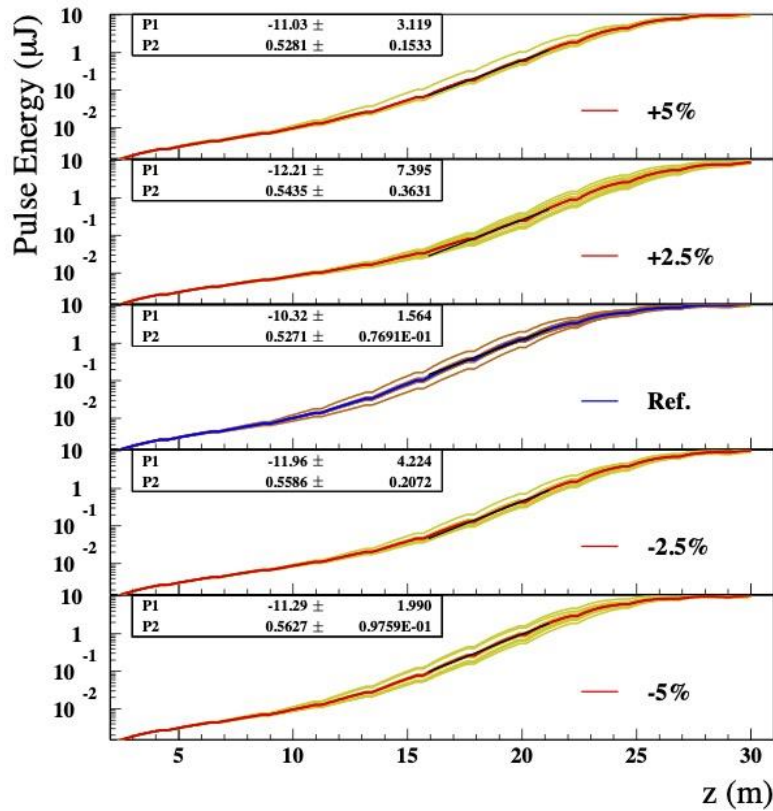


Fig.2: Pulse energy growth as a function of the undulator propagation coordinate for samples with different plasma density. The average growth is fit with an exponential function to estimate the gain length.

At undulator exit, the pulse energy is $E_p = 10.3 \mu J$, that implies a flux of 4×10^{23} photons/s and a brilliance of $3 \times 10^{31} \text{ photons s}^{-1} (\text{mm} \times \text{mrad})^{-2} (0.1\% \text{ bw})^{-1}$, with differences on the order of 9% among the different samples, with no significant trend as a function of plasma density.

In conclusion, by means of numerical simulations, a single-stage 4.5GeV LWFA scheme, along with a state-of-the-art beam transport line accommodating for the relatively large projected energy spread and large beam divergence, is proven to drive a SASE FEL source capable to deliver about 10^{10} photons/shot at 0.15nm resonant wavelength, at the exit of an undulator beamline 30m long.

References

- [1] P. Tomassini *et al.*, Brilliant X-Ray Free Electron Laser Driven by Resonant Multi-Pulse Ionization Injection Accelerator, Proc. FEL2022 Trieste, pp. 191-195 (2022); <https://doi.org/10.18429/JACoW-FEL2022-TUP17> and references therein.
- [2] S. Reiche, GENESIS 1.3: a fully 3D time-dependent FEL simulation code, *Nuclear Instruments and Methods in Physics Research A* **429**, pp. 243-248 (1999).
- [3] F. Iannone *et al.*, CRESCO ENEA HPC clusters: a working example of a multifabric GPFS Spectrum Scale layout, *Proc. Int. Conf. on High Performance Computing and Simulation*, pp. 1051- 1052 (2019).

NATURAL ANTIOXIDANTS AS POTENTIAL INHIBITORS OF PROTEASES FROM SARS-CoV-2

Carla Orlando^{1,2}, Giada Ciardullo¹, Mario Prejanò¹, Nino Russo¹ and Tiziana Marino^{1*}

¹*Dipartimento di Chimica e Tecnologie Chimiche, Laboratorio PROMOCS cubo 14C, Università della Calabria, I-87036 RENDE (CS), Italy.*

²*Department of Biotechnology and Biosciences, University of Milano-Bicocca, Piazza della Scienza 2, 20126 Milan, Italy.*

ABSTRACT. Potential non-covalent inhibition of cysteine proteases (3-chymotrypsin-like protease (M^{pro}), papain-like cysteine protease (PL^{pro}) from SARS-CoV-2 by miquelianin and (+)-catechin has been evaluated throughout molecular dynamics simulations.

1 Introduction

Natural antioxidants have gained popularity in recent years owing to the very promising antiviral action as in particular occurred during the emerged new severe acute respiratory syndrome coronavirus 2 (SARSCoV-2) pandemic. Since the publication of its viral genome, the identified druggable targets as the spike protein, 3-chymotrypsin-like protease (M^{pro}), papain-like cysteine protease (PL^{pro}), and the RNA-dependent RNA polymerase (RdRp) were object of many investigations for drug discovery. [1-3].

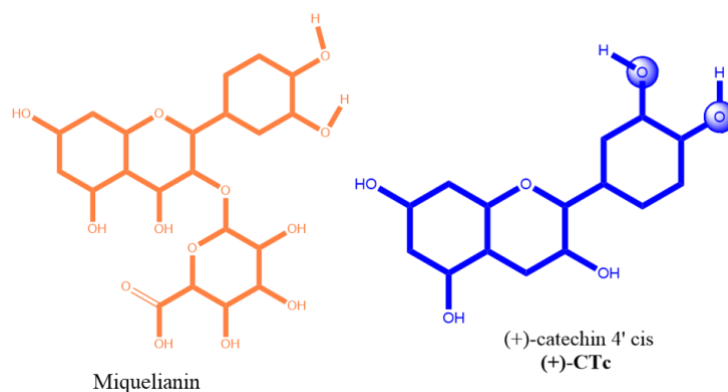
Structural features present in antioxidant molecules as flavonols, have been associated with the non-covalent inhibition of viral proteins [4-6], suggesting that they might have the potential to act as antiviral agents. Indeed, lately, the emergency linked to spread diffusion of SARS-CoV-2 resulted in testing many naturally occurring antioxidants as potential antiviral agents. M^{pro} and PL^{pro}, in particular, are crucial proteins for processing the polyproteins that are translated by the viral RNA [7-9]. Thus, the inhibition represents an important target for future applications. The choice of using M^{pro} and PL^{pro} as molecular targets also lies on the absence of equivalent enzymatic analogues in humans, indicating that there should be no harm from their inhibition. These results induced us to investigate the possible antiviral activity of miquelianin on PL^{pro} [4] and (+)-catechin on M^{pro} and PL^{pro} from SARS-CoV-2, [10] in addition to its ability to scavenge free radicals. [11-13]

Such research can be helpful to find novel antiviral compounds useful in the fight against pandemics in the future. In fact, computer modeling can identify and quantify the atomistic and molecular sources of important physiological processes, providing insights that might validate experimental results or stimulate novel ideas.

2 Computational Methods

Two distinct M^{pro}:ligands (miquelianin and catechin, see Scheme 1) and PL^{pro}:catechin complexes were subjected to molecular dynamics simulations, following the previously approved technique.[4] In detail, the initial structure of the SARS-CoV-2 M^{pro} bound to the non-covalent inhibitor X77 was selected (PDB: 6W63) by including the protonation state calculated for the previous study[4], while the crystallographic structure (PDB: 6W9C) was for PL^{pro} [14]

Molecular docking was carried out using AutoDock version 4.2. [15] aiming to investigate possible binding modes and substrate interactions in the vicinity of the catalytic sites of the of the M^{pro} and PL^{pro}. The docking area was determined using AutoGrid. A size of (38×15×38 Å³), centered at the M^{pro}/PL^{pro} active sites and in the proximity of the catalytic amino acid residues. The genetic algorithm (LGA) was used for the conformational search of the ligand. The final docked poses were grouped using an RMSD tolerance of 2 Å. All MD simulations were carried out adopting the Gromacs package. [16] The ff99SB forcefield was selected to describe the protein.



Scheme 2. Antioxidant molecules used in the simulations.

Parameters for H_4Miq^- and (+)-CTc were obtained were calculated from HF/6-31G* optimizations using the Gaussian09 D.01 code. [17]

The protein systems were initially minimized and relaxed by applying harmonic positional constraints on all atoms ($50 \text{ kcal mol}^{-1} \text{ \AA}^2$) using 5000 steepest descent (SD) steps, followed by 5000 conjugate gradient (CG) steps, while in the second stage of minimization, the entire system was released unconstrained and then a progressive heating was performed up to 300 K for 50 ps, followed by 5 ns at 300 K using Langevin thermostat in NVT ensemble. For the phase productive of the MD simulations, 200 ns trajectories were collected for all the studied systems, keeping the systems at 1 bar pressure in the NPT ensemble and selecting the Berendsen barostat with a time constant $\tau_p = 2.0 \text{ ps}$. In all the simulations, the SHAKE algorithm, and Particle Mesh Ewald (PME) summation method were adopted, with an integration step of 2 fs and a cutoff radius of 10.0 \AA , and the water molecules were treated with the TIP3P scheme.

MM-P/GBSA

Binding free energies between the receptor investigated and the peptide were calculated by solving the linearized Poisson–Boltzmann equation using the Molecular Mechanics Poisson–Boltzmann and Generalized Born surface area (MM-PBSA) methods. The MM-P/GBSA calculation was carried out using the MMPBSA.py [18] module of AMBER16. [19] The snapshots obtained from the whole MD production trajectory of each complex were utilized for calculation. The value of the *igb* flag equal to 5, associated to a salt concentration of 0.1 M, was used.

3 Results

3.1 MD simulations of M^{pro} -ligand complexes

H_4Miq

The computational procedure previously used for other quercetin-like antioxidants based on docking tools and molecular dynamics was employed to explore the non-covalent inhibitory capability of miquelianin species present at physiological pH (7.4) on the SARS-CoV-2 M^{pro} . [4] Since miquelianin is a derivative of quercetin (Scheme 2), additional comparison analysis has been carried out when feasible to demonstrate the impact of sugar in C3. The presence of carboxylic moiety in the sugar ring induced to consider miquelianin in deprotonated form indicated as H_4Miq^- .

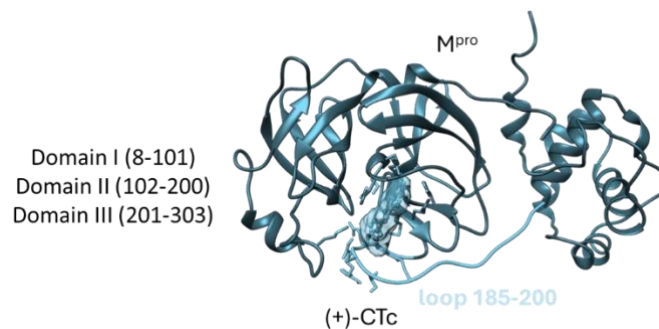


Figure 2: The most representative cluster from MD simulation for $M^{\text{pro}}:(+)\text{-CTc}$.

From the hydrogen bond analysis from the MD trajectory of the complex $M^{\text{pro}}:(+)\text{-CTc}$, the O4'H moiety in (+)-CTc ring B resulted specifically involved in hydrogen bonds, as a donor group, with the main chains of Asp187 and Arg188 with high occupancies. At the same time, it interacts hydrophobically with the Met165 side chain.

PCA was used to determine the larger-scale collective motions occurring in M^{pro} in the presence of catechin (Figure 3). The movement trapped in PC1 related to $M^{\text{pro}}:(+)\text{-CTc}$, emphasizes that domain III does not exhibit significant motions suggesting that the ligand affects the “communication” between the two domains.

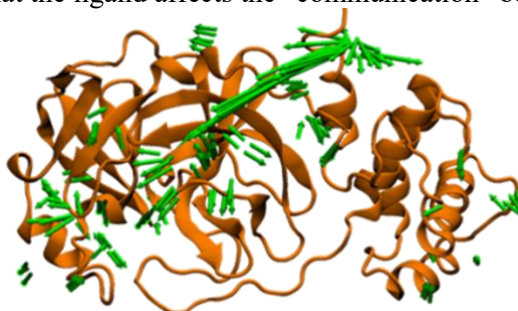


Figure 3: PCA results for $M^{\text{pro}}:(+)\text{-CTc}$.

The binding free energy per amino acid residue was estimated using MM/PBSA calculations, enabling a more quantitative identification of the energetic contributions made by each amino acid residue to the ligand binding. However, analyzing the obtained data emerges that the presence of polar groups on ring A is mandatory to dock the protein in the “primary” pocket in proximity to the catalytic dyad more than catechol moiety on ring B. This feature leads to establish a network of strong interactions with the protein preventing access to the catalytic dyad by natural substrates. The per-residue decomposition free energy analysis, further indicates that only 11 amino acid residues of domain II generate lower binding energy values. A more complete analysis can be found in the ref. [10]

3.2 MD simulations of $PL^{\text{pro}}:(+)\text{-CTc}$

The protein PL^{pro} has 315 residues and a high cysteine residue content. Apart from the catalytic Cys111, the structural zinc ion is bound by four cysteine residues, while the remaining six residues are dispersed throughout the protein structure. PL^{pro} contains a canonical Cys protease catalytic triad (Cys111, His272, and Asp286) very similar to the catalytic site of M^{pro} . Because Cys111 may be sensitive to oxidation, PL^{pro} had poor crystallization characteristics in comparison to M^{pro} .



Figure 5: The most populated cluster from MD of PL^{pro}: (+)-CTc

In the most populated cluster (Figure 5), the (+)-CTc is totally embedded in a region exposed to the solvent resulting surrounded by a layer of water molecules that do not allow establishing direct substrate-protein contacts. This finding emphasizes the different behaviour of the ligand compared to that in M^{pro}.

From MMGBSA an average value of $\Delta G_{\text{bind}} = -7.4$ kcal/mol was found for the PL^{pro}:(+)-CTc system in good agreement with values previously found for inhibitors of PL^{pro}. [21]. This value well accounts for a reduced affinity of (+)-CTc for PL^{pro} if compared to the viral protein M^{pro} above described, suggesting a negligible antiviral effect on this enzyme in silico.

Acknowledgments

"The computing resources and the related technical support used for this work have been provided by CRESCO/ENEAGRID High Performance Computing infrastructure and its staff [22]. CRESCO/ENEAGRID High Performance Computing infrastructure is funded by ENEA, the Italian National Agency for New Technologies, Energy and Sustainable Economic Development and by Italian and European research programmes, see <http://www.cresco.enea.it/english> for information".

References

- [1] Q. Wang, et al. Structural basis for RNA replication by the SARS-CoV-2 polymerase. *Cell* 182, 417-428e413 (2020).
- [2] J. Huang, W. Song, H.Huang, & Q.Sun, Pharmacological therapeutics targeting RNA-dependent RNA polymerase, proteinase and spike protein: From mechanistic studies to clinical trials for COVID-19. *J. Clin. Med.* <https://doi.org/10.3390/jcm9041131> (2020).
- [3] L. Casalino, L. et al. AI-driven multiscale simulations illuminate mechanisms of SARS-CoV-2 spike dynamics. *Int. J. High Perform. Comput. Appl.* 35, 432–451. <https://doi.org/10.1177/10943420211006452> (2021).
- [4] M. Spiegel, G. Ciardullo, T. Marino, N. Russo, Computational investigation on the antioxidant activities and on the M^{pro} SARS-CoV-2 non-covalent inhibition of isorhamnetin. *Front. Chem.* 2023, 11, 1122880.
- [5] M. Spiegel, M. Prejanò, T. Marino, N. Russo Primary Antioxidant Power and M^{pro} SARS-CoV-2 Non-Covalent Inhibition Capabilities of Miquelianin, *Chem. Asian J.* 2024, e202400079
- [6] F. Munafò, E. Donati, N. Brindani, G. Ottonello, A. Armirotti, M. De Vivo, Quercetin and luteolin are single-digit micromolar inhibitors of the SARS-CoV-2 RNA-dependent RNA polymerase. *Sci. Rep.* 2022, 12, 10571.
- [7] Y. Chen, Q. Liu, D. Guo, Emerging coronaviruses: Genome structure, replication, and pathogenesis. *J. Med. Virol.* 2020, 92 (4),418–423.
- [8] K. Anand, J. Ziebuhr, P. Wadhvani, J. R. Mesters, R. Hilgenfeld, Coronavirus main proteinase (3CL^{pro}) structure: basis for design of anti-SARS drugs. *Science* 2003, 300 (5626), 1763–1767.
- [9] L. Lu, S. Su, H. Yang, S. Jiang, Antivirals with common targets against highly pathogenic viruses. *Cell* 2021, 184 (6), 1604–1620.
- [10] G. Ciardullo, C. Orlando, N. Russo, E. Marchese, A. Galano, T. Marino, M. Prejanò Submitted to *Comput. in Biol. Med.* CIBM-D-24-06681R1.
- [11] H. M. Mengist, T. Dilnessa, T. Jin, Structural Basis of Potential Inhibitors Targeting SARS-CoV-2 Main Protease. *Front. Chem.* 2021,9, 7.
- [12] Z. Jin, X. Du, Y. Xu, Y. Deng, M. Liu, Y. Zhao, B. Zhang, X. Li, L. Zhang, C. Peng, Y. Duan, J. Yu, L. Wang, K. Yang, F. Liu, R. Jiang, X. Yang, T. You, X. Liu, X. Yang, F. Bai, H. Liu, X.

- Liu, L. W. Guddat, W. Xu, G. Xiao, C. Qin, Z. Shi, H. Jiang, Z. Rao, H. Yang, Structure of Mpro from SARS-CoV-2 and Discovery of Its Inhibitors. *Nature* 2020, 582, 289–293.
- [13] J. Lee, L. J. Worrall, M. Vuckovic, F. I. Rosell, F. Gentile, A. T. Ton, N. A. Caveney, F. Ban, A. Cherkasov, M. Paetzel, N. C. J. Strynadka, Crystallographic Structure of Wild-Type SARSCoV-2 Main Protease Acyl-Enzyme Intermediate with Physiological C-Terminal Autoprocessing Site. *Nat. Commun.* 2020, 115877.
- [14] <https://doi.org/10.2210/pdb6W9C/pdb>
- [15] G. M. Morris, R. Huey, W. Lindstrom, M. F. Sanner, R. K. Belew, D. S. Goodsell and A. J. Olson, *J. Comp. Chem.*, 2009, 30, 7. <https://doi.org/10.1002/jcc.21256> OK
- [16] M. J. Abraham, T. Murtola, R. Schulz, S. Páll, J. C. Smith, B. Hess, E. Lindahl. GROMACS: High performance molecular simulations through multi-level parallelism from laptops to supercomputers. *SoftwareX*, 1–2, 19–25 (2015).
- [17] M.J. Frisch, G.W. Trucks, H.B. Schlegel, G.E. Scuseria, M.A. Robb, J.R. Cheeseman, D.J. Fox, Gaussian 09. Gaussian, Inc.: Wallingford, CT, USA, (2009).
- [18] B. R., III Miller,; T. D., Jr. McGee, J. M. Swails, N. Homeyer, H. Gohlke, A. E. Roitberg, MMPBSA.py: An Efficient Program for End-State Free Energy Calculations. *J. Chem. Theory Comput.* 2012, 8 (9), 3314.
- [19] D. R.; Roe, T. E. Cheatham, PTRAJ and CPPTRAJ: Software for Processing and Analysis of Molecular Dynamics Trajectory Data. *J Chem. Theory Comput.* 2013, 9 (7), 3084–3095.
- [20] J. Dong, G.-F. Yang, Structure of Mpro complexed with Quercetin. To be published <https://www.rcsb.org/structure/8GQT>.
- [21] M. U. Mirza, S. Ahmad, I. Abdullah, M. Froeyen Identification of novel human USP2 inhibitor and its putative role in treatment of COVID-19 by inhibiting SARS-CoV-2 papain-like (PLpro) protease, *Comp. Biol. Chem.* 2020, 89, 107376. doi.org/10.1016/j.compbiolchem.2020.107376.
- [22] F. Iannone et al., "CRESCO ENEA HPC clusters: a working example of a multifabric GPFS Spectrum Scale layout," 2019 International Conference on High Performance Computing & Simulation (HPCS), Dublin, Ireland, 2019, pp. 1051-1052, doi: 10.1109/HPCS48598.2019.9188135.

FIRST-PRINCIPLES INSIGHTS ON SOLID-STATE PHASE TRANSITIONS IN P2- Na_xMnO₂-BASED HIGH ENERGY CATHODE

Michele Pavone^{1,*}, Aniello Langella¹, Arianna Massaro¹ and Ana B. Muñoz-García²

¹*Department of Chemical Sciences, University of Naples Federico II, Via Cintia 21, Naples, Italy*

²*Department of Physics “E. Pancini”, University of Naples Federico II, Via Cintia 21, Naples, Italy*

ABSTRACT. Using density functional theory (DFT), we investigate phase transitions in P2-Na_xMnO₂ system during charge and discharge. Cooperative Jahn-Teller effects (CJTE) associated to Mn³⁺ JT-active centres, together with changes in Na⁺/vacancy ordering upon desodiation, are highlighted as the main causes driving the phase transitions after Na insertion/extraction. Our theoretical insights can provide advances for future design principles towards more efficient and structurally stable layered oxides as high-energy NIB cathodes.

1 Introduction

The research conducted at the University of Naples “Federico II” has focused on the solid-state phase transitions in P2-Na_xMnO₂ cathode material [1]. Manganese-based layered oxides are promising cathodes for sodium-ion batteries (NIBs) [2]. However, phase transitions compromise structural stability during battery operation [3]. This study provides atomistic insights into P2→P2' and P2→OP4 transitions in the Na_xMnO₂ system. By examining structural and electronic variations at different states of charge, the gliding-driven mechanism is elucidated. The cooperative Jahn-Teller effects (CJTE) associated with Mn³⁺ JT-active centers and changes in Na⁺ orderings drive these transitions. The retention of the P2 structure relies on a delicate balance between electrostatic (Na⁺-Na⁺ intra- and O²⁻-O²⁻ inter-layer repulsions) and covalent (TM-O bond strengths) contributions.

2 Methods and Computational details

We model the P2-, OP4-, and P2' Na_xMnO₂ compounds with varying sodium contents ($x_{\text{Na}} = 0.72, 0.59, 0.47,$ and 0.34). The projector-augmented wave (PAW) method and plane-wave basis sets are employed within VASP code [4-6]. Spin-polarized DFT calculations are conducted within the generalized gradient approximation (GGA) and PBE exchange-correlation functional [7]. To overcome the self-interaction error associated with DFT-GGA for highly-localized electrons, we apply the DFT+U scheme with $(U-J)_{\text{eff}} = 4.0$ eV for the Mn d shell [8-14]. The DFT-D3 method accounts for dispersive forces [15-18]. Energy cutoff value of 750 eV and a $4 \times 4 \times 4$ k-points grid for Brillouin zone sampling are used to converge energy within 10^{-5} eV threshold. Criteria for ionic minimization is set to 10^{-3} eVÅ⁻¹. Structural models consist of $2\sqrt{3} \times 4 \times 1$ supercells for P2 and OP4 systems, and $2 \times 4 \times 1$ supercell for P2', with an equal number of Na atoms for direct comparisons. Each supercell contains 119, 115, 111, and 107 atoms in Na_{0.72}MnO₂, Na_{0.59}MnO₂, Na_{0.47}MnO₂, and Na_{0.34}MnO₂, respectively. Na cations in P2-NMO structures can reside either in face (Na_F, 2b Wyckoff position) or edge sites (Na_E, 2c Wyckoff position) [3]. To accurately consider the configurational entropy of Na_E and Na_F distributions at each stoichiometry, we employ the special quasi-random structure (SQS) approach [19-20], that ensures occupancy of each site consistently respected throughout the analysis [19].

3 Results and discussion

Energy evaluations show that P2-Na_xMnO₂ is the most stable phase for $0.47 \leq x \leq 0.59$, while OP4 is favored at $x_{\text{Na}} = 0.34$ and P2' at $x_{\text{Na}} = 0.72$, consistent with experimental data [19]. To understand the effect of desodiation to the phase stability, we analyze P2-Na_xMnO₂ at various Na compositions.

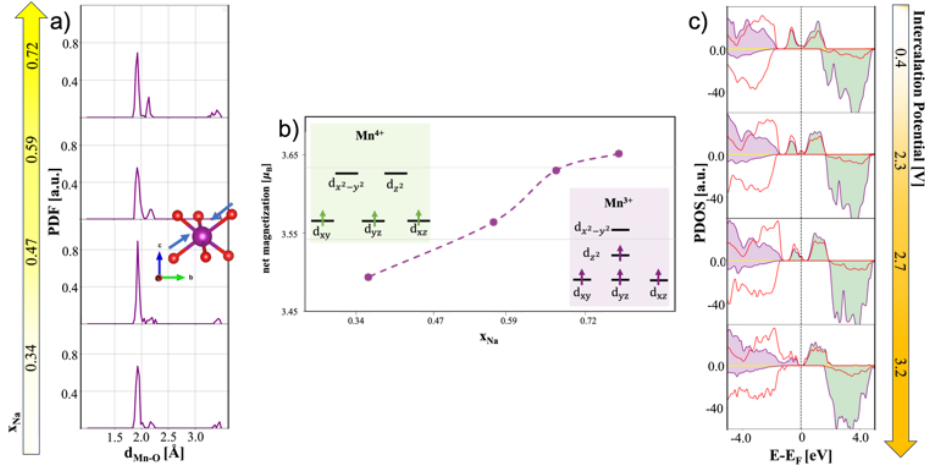


Fig. 1 a) Pair distribution functions (PDFs) of Mn-O distances; b) Net magnetization of Mn atoms; c) PDOS of P2- Na_xMnO_2 computed at the PBE+U-D3(BJ) level of theory. Color code: Na s states, yellow; Mn t_{2g} and e_g bands, violet and green, respectively; O p states, red.

Pair distribution functions (PDF) of Mn-O distances reveal significant structural changes during Na^+ extraction (Fig. 1a). At $x_{\text{Na}} = 0.72$, two Mn-O bond lengths (1.9 Å and 2.2 Å) are observed, the 2.2 Å peak diminished as Na content decreases clearly indicating a JTE. The average magnetization on the Mn sublattice decreases from 3.7 μB to 3.4 μB with Na^+ extraction (Fig. 1b), confirming partial oxidation of Mn^{3+} to Mn^{4+} . The Mn^{3+} exhibit significant axial bond elongation in MnO_6 octahedra. The presence of an electronic JTE is further corroborated by the projected density of states (PDOS) (Fig. 1c) showing the Mn e_g band crossing the Fermi level at high x_{Na} (low voltage) due to JTE with Mn^{3+} . At low x_{Na} , the Mn d band appeared as a single t_{2g} band below the Fermi level, indicating the predominance of Mn^{4+} . JT distortions can induce structural instability and trigger phase transitions in solid-state materials [21]. Understanding whether these distortions are cooperative or localized is crucial. We assess the average structural distortion for each P2- Na_xMnO_2 structure by evaluating the octahedral distortion factor, D_{Oct} , as [22]:

$$D_{\text{Oct}} = \frac{6(l_{\text{long}} - l_{\text{short}})}{(2l_{\text{long}} - 4l_{\text{short}})} \quad (1)$$

where l_{long} and l_{short} are the average values of longer and shorter Mn-O bonds, respectively. The D_{Oct} values (Fig. 2a) show decreasing distortion, but at $x_{\text{Na}} = 0.34$, distortion increases again, suggesting persistent structural distortion even at the lowest Mn^{3+} concentrations. To determine whether this unique D_{Oct} trend is the result of Cooperative Jahn-Teller Effect (CJTE), we analyze the distribution of Mn^{3+} . CJTE often involves unique charge patterns and periodic arrangement. Fig. 2b shows Mn distribution in the a-b plane. At $x_{\text{Na}} = 0.47$, Mn^{4+} adopt an exotic wave-like shape, resulting in minimal distortion. Previous reports on O3-NMO structures have shown that the arrangement of Na^+ is influenced by electrostatic and electronic interactions *via* JTE [23], allowing some Na to occupy highly distorted sites. Our analysis of Na_xMnO_2 models reveal that certain Na^+ undergo significant displacement from their original crystallographic sites (edge and face positions) to intermediate pseudo-octahedral sites, hereafter referred to as “displaced” Na (Na_D). In Fig. 2a, Na_D can be visualized as a pseudo-edge site where the Na^+ resides near two Mn-centered octahedra. We calculate the average displacement of Na^+ at each composition.

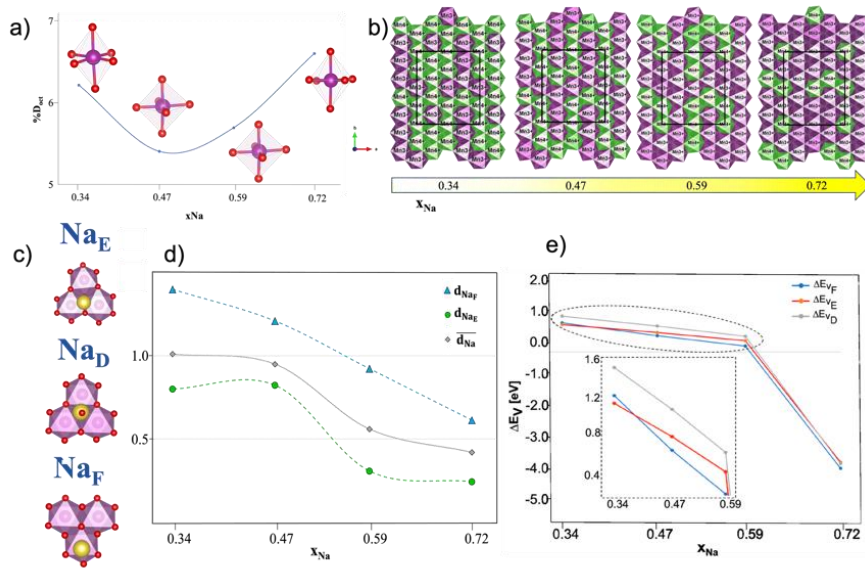


Fig. 2 a) Average octahedral distortion, %D_{oct}, evaluated for MnO₆ octahedra; b) Geometrical distributions of Mn³⁺ and Mn⁴⁺ in the a-b plane. Color code: Mn³⁺-centered octahedra, violet; Mn⁴⁺-centered octahedra, green. c) Top views of different Na crystallographic sites: edge Na_E, face Na_F, and displaced Na_D; d) Average displacement of Na (grey line) and individual contributions from face and edge sites (blue and green lines, respectively); e) sodium vacancy formation energies for each site (edge ΔE_{vE}, face ΔE_{vF}, and displaced ΔE_{vD}).

Fig. 2b shows that most of Na_D originate from displacements from Na_F (blue curve in the plot), while dislocations from Na_E are relatively small (green curve in the plot). To assess the impact of Na_D sites on system stability, we calculate the formation energy of a Na vacancy at each x_{Na} according to the following equation:

$$\Delta E_v = E_{\text{Na}_x\text{MnO}_2} - E_{\text{Na}_{x-1}\text{MnO}_2} + \frac{1}{2} E_{\text{Na}} \quad (2)$$

where $E_{\text{Na}_x\text{MnO}_2}$ and $E_{\text{Na}_{x-1}\text{MnO}_2}$ are the total energies of the system before and after Na removal, respectively, while E_{Na} is the total energy sodium metal [13]. The results show that Na_F sites are more stable than Na_E sites within $0.4 < x_{\text{Na}} < 0.7$, but Na_D sites are even more stable: at high voltages, Na⁺ prefer to occupy pseudo-octahedral sites, leading to a thermodynamically favorable transition from face to pseudo-edge sites. The P2 crystalline form cannot accommodate both octahedral and prismatic coordinations, leading to the need of manganese layer gliding and thus the P2-to-OP4 transition to occur. Changes in Na⁺ ordering drive the solid-state transition toward the OP4 phase. On the other hand, we find that at high sodium content, the increased Na⁺-Na⁺ repulsion and the weaker Mn⁴⁺-O bonds facilitate the P2' phase formation through TMO₂ layer gliding.

4 Conclusions

This study gets insights into phase transitions affecting the P2-Na_xMnO₂ cathode during Na extraction/insertion. By examining structural and electronic changes upon desodiation/sodiation, we identify the atomistic mechanisms driven by JTE/CJTE and key electrostatic/covalent interactions in affecting the structural stability and leading to thermodynamic driving forces that underlie the phase transition to OP4 and P2' at high and low voltage, respectively. Controlling these factors will be key for future development of efficient and structurally stable NIB cathodes.

References

- [1] A. Langella, A. Massaro, A. B. Muñoz-García, M. Pavone, "First-Principles Insights on Solid-State Phase Transitions in P2-Na_xMnO₂-Based High Energy Cathode during Na-Ion Battery Operations," *Chem. Mater.*, 36, 5, 2370–2379, 2024.
- [2] P. Gupta, S. Pushpakanth, M. A. Haider, S. Basu, "Understanding the Design of Cathode Materials for Na-Ion Batteries," *ACS Omega*, 7, 7, 5605–5614, 2022.
- [3] P.-F. Wang, Y. You, Y.-X. Yin, Y.-G. Guo, "Layered Oxide Cathodes for Sodium-Ion Batteries: Phase Transition, Air Stability, and Performance," *Adv. Energy Mater.*, 8, 8, 1701912, 2018.

- [4] G. Kresse, D. Joubert, "From ultrasoft pseudopotentials to the projector augmented-wave method," *Phys. Rev. B*, 59, 3, 1758–1775, 1999.
- [5] G. Kresse, J. Furthmüller, "Efficient iterative schemes for ab initio total-energy calculations using a plane-wave basis set," *Phys. Rev. B*, 54, 16, 11169–11186, 1996.
- [6] P. E. Blöchl, "Projector augmented-wave method," *Phys. Rev. B*, 50, 24, 17953–17979, 1994. d
- [7] J. P. Perdew, K. Burke, M. Ernzerhof, "Generalized Gradient Approximation Made Simple," *Phys. Rev. Lett.*, 77, 18, 3865–3868, 1996.
- [8] V. I. Anisimov, J. Zaanen, O. K. Andersen, "Band theory and Mott insulators: Hubbard U instead of Stoner I," *Phys. Rev. B*, 44, 3, 943–954, 1991.
- [9] S. Tosoni, "A DFT study of Mn₃O₄ Hausmannite thin films supported on coinage metals," *Appl. Surf. Sci.*, 612, 155920, 2023.
- [10] A. Massaro, *et al.*, "Unveiling Oxygen Redox Activity in P2-Type Na_xNi_{0.25}Mn_{0.68}O₂ High-Energy Cathode for Na-Ion Batteries," *ACS Energy Lett.*, 6, 7, 2470–2480, 2021.
- [11] A. Massaro, *et al.*, "Ru-Doping of P2-Na_xMn_{0.75}Ni_{0.25}O₂-Layered Oxides for High-Energy Na-Ion Battery Cathodes: First-Principles Insights on Activation and Control of Reversible Oxide Redox Chemistry," *ACS Appl. Energy Mater.*, 5, 9, 10721–10730, 2022.
- [12] A. Massaro, A. Langella, A. B. Muñoz-García, M. Pavone, "First-principles insights on anion redox activity in Na_xFe_{1/8}Ni_{1/8}Mn_{3/4}O₂: Toward efficient high-energy cathodes for Na-ion batteries," *J. Am. Ceram. Soc.*, 106, 1, 109–119, 2023.
- [13] A. Massaro, *et al.*, "First-principles design of nanostructured electrode materials for Na-ion batteries: challenges and perspectives," *Phys. Chem. Chem. Phys.*, 25, 28, 18623–18641, 2023.
- [14] G. Brugnetti, *et al.*, "Structural Evolution of Air-Exposed Layered Oxide Cathodes for Sodium-Ion Batteries: An Example of Ni-doped Na_xMnO₂," *Chem. Mater.*, 35, 20, 8440–8454, 2023.
- [15] S. Grimme, J. Antony, S. Ehrlich, H. Krieg, "A consistent and accurate ab initio parametrization of density functional dispersion correction (DFT-D) for the 94 elements H-Pu," *J. Chem. Phys.*, 132, 15, 154104, 2010.
- [16] A. Pecoraro, *et al.*, "Structural and electronic properties of defective 2D transition metal dichalcogenide heterostructures," *J. Comput. Chem.*, 41, 22, 1946–1955, 2020.
- [17] A. Massaro, A. Pecoraro, A. B. Muñoz-García, M. Pavone, "First-Principles Study of Na Intercalation and Diffusion Mechanisms at 2D MoS₂/Graphene Interfaces," *J. Phys. Chem. C*, 125, 4, 2276–2286, 2021.
- [18] A. B. Muñoz-García, A. Massaro, M. Pavone, "Ab initio study of PbCr_(1-x)S_xO₄ solid solution: an inside look at Van Gogh Yellow degradation," *Chem. Sci.*, 7, 7, 4197–4203, 2016.
- [19] C. Wang, *et al.*, "Tuning local chemistry of P2 layered-oxide cathode for high energy and long cycles of sodium-ion battery," *Nat. Comm.* 12, 2256, 2021.
- [20] D. Gehringer, M. Friák, and D. Holec, "Models of configurationally-complex alloys made simple," *Comput. Phys. Commun.*, 286, 108664, 2023.
- [21] T. Nagai, Y. Mochizuki, S. Yoshida, T. Kimura, "Chemical Aspect of Displacive-Type Ferroaxial Phase Transition from Perspective of Second-Order Jahn–Teller Effect: NASICON Systems as an Example", *J. Am. Chem. Soc.*, 145, 8090–8098, 2023.
- [22] H. Jung, J. Kim, and S. Kim, "Phonon study of Jahn–Teller distortion and phase stability in NaMnO₂ for sodium-ion batteries," *J. Appl. Phys.*, 132, 5, 055101, 2022.
- [23] X. Li *et al.*, "Direct visualization of the Jahn–Teller effect coupled to Na ordering in Na_{5/8}MnO₂", *Nat. Mater.*, 13, 6, 586–592, 2014.

HEXAGONAL NaCl ATOM-THIN LAYER STRUCTURING ON METHYLAMMONIUM LEAD IODIDE PEROVSKITE: A FIRST-PRINCIPLES INVESTIGATION

Adriana Pecoraro¹, Ana Belén Muñoz-García^{1*}, Gennaro Vincenzo Sannino², Paola Delli Veneri³ and Michele Pavone^{2*}

¹ *Department of Physics “E. Pancini”, University of Naples Federico II, Napoli, Italy*

² *Department of Chemical Sciences, University of Naples Federico II, Napoli, Italy*

³ *Italian National Agency for New Technologies, Energy and Sustainable Economic Development (ENEA), Portici (NA), Italy*

ABSTRACT. Alkali halides are extensively used in Perovskite Solar Cells (PSCs) as interlayers between the active material and the charge selective layers to improve the contact quality. We characterize the structure and the electronic features of atom-thin layers of NaCl on the methylammonium lead iodide (MAPI) perovskite via Density Functional Theory (DFT) calculations. We assess both the role of the MAPI surface termination and stacking. We obtain an exotic honeycomb-like structuring of the salt, also recently observed in experiments on a diamond substrate. We investigate the electronic modifications induced by the salt layer and its ability to improve the defect tolerance of the perovskite surface.

1 Introduction

The selection of charge transport layers (CTLs) is crucial to improve efficiency and stability of PSCs. Salt interlayers between the perovskite and the CTLs can improve the bonding between the two materials and prevent charge recombination. Salts can introduce surface dipoles that enable to tune the work function providing a convenient alignment with the perovskites.¹ Among them sodium chloride, despite its apparent simplicity, shows exotic structures as recently found by Tikhomirova *et al.*² on the diamond (110) surface. Such behavior mainly depends on the interaction with the substrate. Here we report the formation of similar exotic NaCl structuring on a perovskite film by means of state-of-the-art DFT calculations. We consider the MAPI perovskite and investigate modifications of electronic properties due to the presence of the salt layer. We also consider a Iodine vacancy on the perovskite surface to assess the ability of the salt to improve the perovskite defect tolerance. Such defects result in shallow donor states in the band structure that can be responsible for an undesired doping of the absorber material³ and can promote degradation mechanisms. Our calculations reveal that the salt layer can limit the formation of surface vacancies.

2 Computational Models

We consider the (010)-MAPI surface covered by an atom-thin layer of NaCl exposing the most energetically favorable (001) surface.⁴ We consider the orthorhombic low temperature MAPI phase (*Pnma* group) accounting for its two distinct possible terminations, namely the PbI₂- and the MAI- ones. The perovskite slab consists in a 7-layer perovskite slab, sandwiched between two atom-thin salt layers to avoid spurious dipoles. We investigate two different stackings, S1 and S2, differing from a translation of the salt of a ¼ of the unit cell along the *a* direction. The MAPI structure is obtained through geometrical minimization performed within the PBE-D3BJ level of theory. The lattice constants values (*a* = 8.844 Å, *b* = 12.592 Å, and *c* = 8.563 Å), show a good agreement with those measured by both X-ray⁵ and NPD.⁶ The same procedure is adopted to obtain the minimum energy NaCl lattice constant. Its value is 5.59 Å and agrees with the experimental one of 5.64 Å.⁷

3 Results and Discussion

The result of the optimization is a massive reconstruction of the salt for both perovskite terminations and stackings as evident from Figure 1.

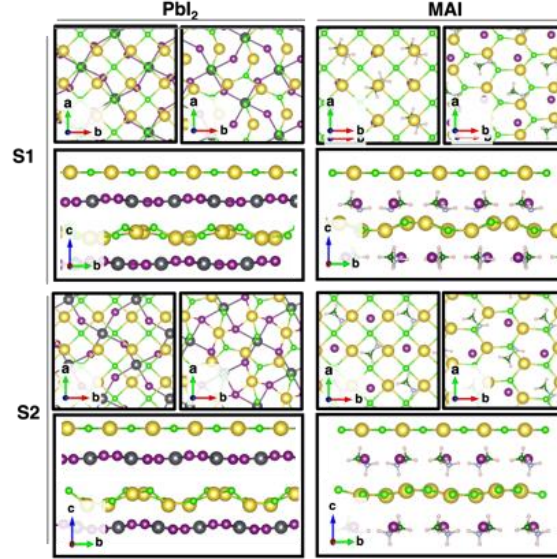


Figure 1. Top views before (left) and after (right) the geometrical optimization for the PbI_2 - and the MAI-terminated MAPI/NaCl interfaces corresponding to stackings S1 and S2. Lateral views before (upper) and after (lower) the optimization for the PbI_2 - and the MAI-terminated MAPI/NaCl interfaces corresponding to stackings S1 and S2. Only the outermost layer of the MAPI slab is shown. Color code: Pb - dark gray; I - violet; C - green; N - light blue; H - light pink; Na - yellow; Cl - light green.

In the MAI-terminated interface, sodium and chlorine atoms reorganize to form a pseudo-hexagonal arrangement independently from the stacking. In both stackings and terminations, the lateral views of the interfaces show a corrugation that is more regular and wavy shaped for the MAI system.

Interaction between the MAPI and the salt buffer can be quantified via calculation of adhesion energy per unit area given by:

$$E_{adh}/A = \frac{E_{int} - E_{MAPI}^{int} - E_{NaCl}^{int}}{A} \quad (1)$$

where E_{int} is the total interface energy, while E_{MAPI}^{int} and E_{NaCl}^{int} are the total energies of the isolated perovskite film and the salt at the interface geometry, respectively. A is the contact area between them. Results are listed in Table 1.

Table 2: Adhesion energies per unit area for both S1 and S2 stackings.

	Energy (eV)	Energy (eV)
	S1	S2
PbI₂	-0.072	-0.077
MAI	-0.040	-0.021

Negative adhesion energies suggest that both heterostructures are favorable to form with PbI_2 termination interacting more strongly with the salt. No dependence on the stacking is observed for the PbI_2 systems while S1 stacking is favored for the MAI system. A charge density difference plot is depicted by Figure 2.

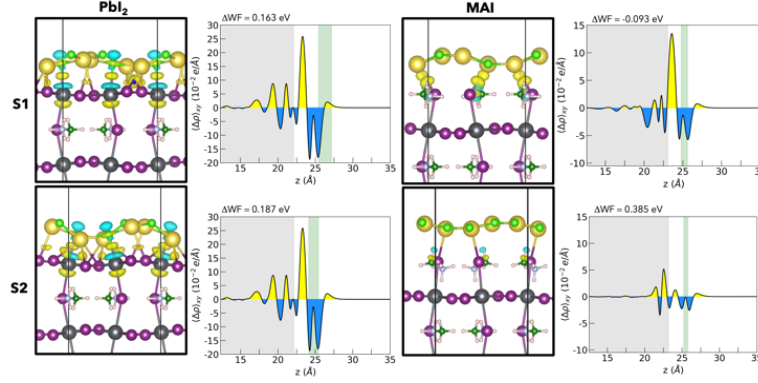


Figure 2. Electron density differences for the interaction between the PbI₂- and the MAI-terminated MAPI film and the NaCl layer (left). Yellow denotes increased electronic density and light blue indicates decreased electronic density. Isosurface value: 0.0025. Planar averages charge density difference for each system (right).

In the PbI₂ case, as similar charge reorganization is observed for the two stackings, while for the MAI system the different stackings result in different interactions reflecting the adhesion energy values. The geometrical reorganization of the salt impacts on the electric properties of the perovskite. We investigate the modification in the MAPI work function (WF) due to the salt. WF is defined as the energy difference between the electrostatic potential in the vacuum and the valence band maximum (VBM). Results obtained for S1 and S2 stackings on PbI₂ - and MAI- terminated systems are reported in Figure 2 together with the planar averaged charge density difference. The WF variation is an important parameter to account in designing well performing interfaces with optimized charge transport features. A WF increase means a lower energy position for both VBM and CBM, within a rigid band model picture. These variations influence the band alignment at interfaces that sets the thermodynamic conditions for the holes and electrons drift across junctions.

Table 2: VBM and CBM energies for both PbI₂ and MAI terminations and stackings, accounting for the WF variations reported for each system in Figure 2. Values reported in the below are calculated from the experimental references (VBM=-5.43 eV and CBM=-3.88 eV).⁸

	PbI ₂	PbI ₂	MAI	MAI
Energies (eV)	S1	S2	S1	S2
VBM	-5.59	-5.62	-5.34	-5.82
CBM	-4.04	-4.07	-3.79	-4.26

Data reported in Table 2 suggest a beneficial role of the NaCl layer that, increasing the WF, gives an optimal band offset (about 0.2 eV) for both stackings of PbI₂-terminated systems with some HTLs such as (CuZnSn₂ - 5.4 eV),⁹ Cu₂O (-5.38 eV),¹⁰ MoS₂ (-5.3 eV),¹¹ that don't match well with the pristine MAPI's valence band level. The WF decrease, experienced by the S1 stacking of the MAI-termination, improves the band offset with the most used P3HT (-5.10 eV)¹² and PEDOT:PSS(-5.10 eV).¹³ On the ETL side, the WF variation for the S2 stacking of MAI-terminated model results in a proper band alignment with the ZnO (-4.4 eV).¹¹ We investigate the presence of a Iodine vacancy for the S1 configuration of both terminations. The vacancy is simulated by removing a neutral iodine atom from the topmost perovskite layer, closer to the salt buffer. The vacancy formation energies calculated as:

$$E_{form} = E_{def} + \frac{1}{2}E_{I_2(g)} - E_{prist} \quad (3)$$

are listed in table 3.

Table 3: Vacancy formation energies calculated at PBE-D3BJ level of theory according to equation (3), for staking S1 of both -PbI₂ and -MAI terminations of the pristine and the salt covered perovskite.

System	Energy (eV)	Energy (eV)
	Pristine	NaCl covered
PbI ₂	2.44	2.78
MAI	2.96	3.01

In all cases the presence of the salt slightly inhibits the defect formation with a more pronounced effect on the PbI_2 system for which energy is increased of about 0.35 eV (~ 8 kcal/mol).

4 Conclusions

In conclusion, we investigate a system composed by a MAPI film with two different terminations, namely MAI and PbI_2 , and covered with an atom-thin layer of NaCl. We observe that the formation of both interfaces is thermodynamically favored and leads to a strong structural reorganization of the salt atoms. In the case of the MAI-terminated model a regular honeycomb-like hexagonal structure of the salt layer is found. Our results reveal that such singular structuring of the salt atom is a consequence of the interaction with the perovskite. We also investigate the electronic effects of the presence of a Iodine vacancy in the material, since these defects are often responsible for low efficiencies in perovskite solar cells. Our calculations reveal that the salt buffer can contribute to inhibit their formation.

Acknowledgments

The computing resources and the related technical support used for this work have been provided by CRESCO/ENEAGRID High Performance Computing infrastructure and its staff; CRESCO/ ENEAGRID High Performance Computing infrastructure is funded by ENEA, the Italian National Agency for New Technologies, Energy and Sustainable Economic Development and by Italian and European research programmes. See: <http://www.cresco.enea.it/english> for information.²⁰

References

- [1] S. Aperi, G. Brocks and S. Tao, *Phys. Rev. Materials*, 2020, **4**, 085403.
- [2] K. A. Tikhomirova, C. Tantardini, E. V. Sukhanova, Z. I. Popov, S. A. Evlashin, M. A. Tarkhov, V. L. Zhdanov, A. A. Dudin, A. R. Oganov, D. G. Kvashnin and A. G. Kvashnin, *J. Phys. Chem. Lett.*, 2020, **11**, 3821–3827.
- [3] J. M. Ball and A. Petrozza, *Nat Energy*, 2016, **1**, 1–13.
- [4] P. W. Tasker, *Philosophical Magazine A*, 1979, **39**, 119–136.
- [5] T. Baikie, Y. Fang, J. M. Kadro, M. Schreyer, F. Wei, S. G. Mhaisalkar, M. Graetzel and T. J. White, *J. Mater. Chem. A*, 2013, **1**, 5628–5641.
- [6] M. T. Weller, O. J. Weber, P. F. Henry, A. M. D. Pumpo and T. C. Hansen, *Chem. Commun.*, 2015, **51**, 4180–4183.
- [7] J. E. Nickels, M. A. Fineman and W. E. Wallace, *J. Phys. Chem.*, 1949, **53**, 625–628.
- [8] C. Zhang, W. Luan and Y. Yin, *Energy Procedia*, 2017, **105**, 793–798.
- [9] A. S. Nazligul, M. Wang and K. L. Choy, *Sustainability*, 2020, **12**, 5138.
- [10] A. M. Elseman, S. Sajid, A. E. Shalan, S. A. Mohamed and M. M. Rashad, *Appl. Phys. A*, 2019, **125**, 476.
- [11] S. Li, Y.-L. Cao, W.-H. Li and Z.-S. Bo, *Rare Met.*, 2021, **40**, 2712–2729.
- [12] Y. Chen, L. Zhang, Y. Zhang, H. Gao and H. Yan, *RSC Adv.*, 2018, **8**, 10489–10508.
- [13] S. Rafique, S. M. Abdullah, M. M. Shahid, M. O. Ansari and K. Sulaiman, *Sci Rep*, 2017, **7**, 39555.

NEUTRONIC MODEL TO FIND PROMISING CANDIDATES AS BURNABLE POISONS IN FAST REACTORS

Roberto Pergreff^{1/6}, Francesco Lodi¹, Giacomo Grasso¹

¹ENEA – Italian National Agency for New Technologies, Energy and Sustainable Economic Development
Via Martiri di Monte Sole 4, 40129 Bologna - Italy

ABSTRACT. Small modular liquid metal fast reactors technology may require viable solutions to reach very long core lifetime or to reduce the reactivity swing as much as possible. For this reason, the use of burnable poisons may soon be a necessary route. Unfortunately, to this date very few materials are known that may be used as burnable poisons in fast reactors. This paper aims to propose a metric by which to predict the neutronic behavior of materials without the need for extensive neutronic calculations for which a detailed description of the system in terms of materials and geometry is required. The values calculated by the model can be used in a comparative analysis to derive a ranking of materials according to their neutronic performances. The model was first tested with seven candidates such as Eu_2O_3 , Gd_2O_3 , Dy_2O_3 , Er_2O_3 , NpO_2 , AmO_2 and B_4C , and then validated against the results obtained with MCNP6.1 for a Lead fast reactor fuel assembly with UO_2 enriched in ^{235}U at 19.75 wt.% in which, one at a time, the various candidates have been added. Despite some small differences from the simulations, the comparison confirmed the prediction ability of the model.

1 Introduction

Recent developments in small modular liquid metal fast reactors technology may require the use of burnable poisons (BPs). In fact, as non-fissile materials which compensate for the excess reactivity of the fuel during the early stages of core operational cycles by virtue of their large neutron absorption cross sections, the burnable poisons can be used either to increase the initial fuel loading on which the core lifetime depends (and therefore the burnup at discharge) or, alternatively, to reduce the reactivity swing thus making the reactor control easier from both design and operation point of views.

However, despite their potential importance for this kind of reactors, to this date very few materials are known as viable burnable poisons. In fact, experiences with burnable poisons in liquid metal fast breeder reactors (LMFBRs) have been rather limited so far, since, being highly stable and easily controllable reactors, the control has usually been carried out with stainless-steel rods filled with boron carbide.

The present study aims to develop a metric to identify promising candidates as burnable poisons for the technology of small – and notably micro – modular liquid metal fast reactors. To this end, a neutronic model was proposed that predicts the neutronic behavior of a candidate in fast spectrum without requiring extensive neutronic calculations for which a detailed description of the system in terms of materials and geometry is required. This model can be considered a semi-quantitative model because it provides values that can be used in a comparative analysis to derive a ranking of materials according to their neutronic performances.

All calculations were performed on CRESCO6, the Linux cluster integrated into the ENEAGRID infrastructure.

2 Methodology and Research Activity

The starting point for the model development was the idea of evaluating the effectiveness of a burnable poison in controlling the positive reactivity over time by separately considering its performance in terms of poisonousness from its performance in terms of burnability. The first characteristic has to do with the ability to provide a negative contribution on reactivity such as to compensate for the initial excess positive reactivity

¹⁶ Corresponding author. E-mail: roberto.pergreff@enea.it.

of the fuel, while the second one is related to the ability to have a burnup kinetics such that the change in reactivity due mainly to fuel depletion is balanced. If the poisonousness is due to the absorption cross section of the burnable poison itself that must be higher or at least comparable to that of the fuel, the burnability is mainly due to absorption cross sections of the isotopes formed by neutron capture in the poison which must be as low as possible.

The performance of a burnable poison in terms of poisonousness is evaluated through an equation which relates at beginning of life (BoL) its negative contribution on the neutron balance to the positive contribution of the fissile material. To appreciate the effective contribution of the burnable poison, this equation is written in terms of microscopic cross sections i.e., net of the atom density of the material itself. Since in the denominator the contribution of the fissile material is greater than 1, the more negative the poisonousness value obtained, the greater the effectiveness of a burnable poison.

The performance of a burnable poison in terms of burnability is made possible by a time-dependent equation which is the product of the change in reactivity due to each transmutation times the total number of times in time t that such transmutation occurs. The second value coincides with the total amount of the daughter isotope produced in time t , net of its initial quantity, if any. In fact, in this case, the production of an isotope as a result of the transmutation or decay of isotopes which do not specifically depend on the initial quantities of the isotopes added as BP must not be taken into account, this production being independent of the BP itself. This equation takes advantage from the fact that, since in fast reactors the spectrum variations are relatively small, the constant cross section approximation can reasonably be performed. A crucial aspect of this equation, which must be evaluated on a case-by-case basis and on which the accuracy of the results depends, concerns the choice of transmutation-decay chains, that is, the number of isotopes included in the chains. In this regard, an isotope can be skipped in the chain only if it has a very short lifetime compared with the rate of transmutations. A chain ends only when one isotope is found in a very small quantity and its daughter isotopes have low absorption cross sections.

3 Results

The model was first tested and then validated against simulations. For both phases, calculations with the general-purpose Monte Carlo radiation-transport code MCNP6.1 [1] were performed. In both phases, the ENDF/B-VIII.0 distribution [2] processed by LANL in ACE format [3] was chosen as evaluated nuclear data library.

The candidates used in the test phase are as follows: Eu_2O_3 , Gd_2O_3 , Dy_2O_3 , Er_2O_3 , NpO_2 , AmO_2 and B_4C . The rare-earth elements were chosen being well-known burnable poisons in Light Water Reactors, while the two minor actinides were selected as they represent the most promising solutions for fast reactors due to their negative contribution to the neutron balance in a fast spectrum [4]. Finally, Boron was considered as it is the reference material for fast reactor control. All elements have been considered with their natural abundance except for Neptunium that is considered as 100% ^{237}Np and Americium considered as 75% ^{241}Am and 25% ^{243}Am . For each candidate, the values of poisonousness and burnability were calculated using the one-group effective cross sections of its isotopes calculated with MCNP6.1 for a hexagonal cell with only UO_2 i.e., for an undoped configuration in which the spectrum is not affected by the presence of the burnable poison.

To validate the results of the test phase, the ranking of the materials obtained with the model was compared with that obtained with MCNP6.1 for a typical lead fast reactor fuel assembly in which, one at a time, the various candidates have been added. In particular, the poisonousness of the materials calculated with the model in the test phase was validated against the ability of the same materials to reduce the initial criticality compared with the reference undoped case (UO_2), while the burnability of the materials calculated with the model in the test phase was validated against their ability to reduce the reactivity swing, obtained as the difference between the multiplication factor at a certain time and that at the initial time.

For this purpose, the following cases were considered:

- one undoped reference case with only UO_2 ;
- seven doped cases with a poison content of 1.5 at.% of which:

- six homogeneous configurations i.e., (U,Eu)O₂, (U,Gd)O₂, (U,Dy)O₂, (U,Er)O₂, (U,Np)O₂ and (U,Am)O₂ with fuel and poison mixed together homogeneously in all FA pins;
- one heterogeneous configuration i.e., with the fuel rods of UO₂ and the poisoned rods of B₄C arranged in different FA lattice positions. A schematic of this assembly is shown in Figure 2 where it is possible to appreciate the positioning of the absorber rods so as to minimize the spatial self-shielding of the poison.

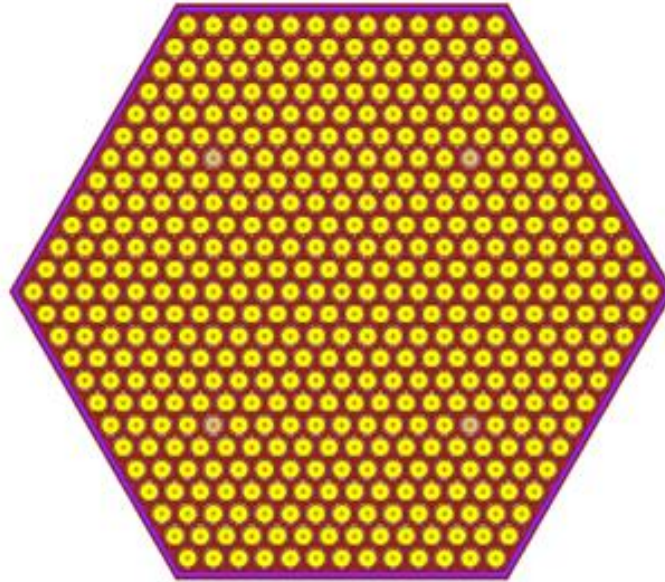


Figure 2. XY view of the FA doped with 4 B₄C rods.

In all cases, the isotopic composition of the Uranium vector is the same as the one used in the test phase with UO₂ enriched in ²³⁵U at 19.75 wt.%. Moreover, to ensure an equal comparison between the cases, the following conditions were applied:

- the total number of fuel and poison molecules in the doped cases was kept the same as that of uranium oxide in the reference case;
- the number of poison molecules in the doped cases was kept the same.

Depletion calculations were carried out to attain, in all doped cases, the same burnup steps as those of the reference case with UO₂. These steps are, in GWd/t_{HM}, as follows: 15.97, 31.94, 47.91, 63.89, 95.83 and 159.71.

The results of the comparison between the simulations and the model are shown in

Table 3. The following is observed:

- about poisonousness, excellent agreement is observed, except for the inversion between the cases with AmO₂ and B₄C. However, these two cases are very close, their discrepancy being little beyond the statistical uncertainty of the calculations themselves.
- about burnability, two different behaviors can be noted:
 - for burnups lower than 47.91 GWd/t_{HM}, excellent agreement is observed, except for Eu₂O₃ and UO₂, whose performance at low burnups is underestimated by the model compared with the simulations. At the same time, both these cases show a correct trend, although not in phase, as burnup increases;
 - for burnups above 63.89 GWd/t_{HM}, excellent agreement is observed. In fact, except for the inversion between Er₂O₃ and UO₂ at 63.89 GWd/t_{HM}, the order is fully respected.

Table 3. Comparison of the material orders obtained from simulations and the model for both poisonousness and burnability as a function of burnup [GWd/t_{HM}].

Burnup	Poisonousness				Burnability		
	0 (BoL)	15.97	31.94	47.91	63.89	95.83	159.71
	Simulations (MCNP)						
Best	Eu ₂ O ₃	AmO ₂					
2	AmO ₂	NpO ₂					
3	B ₄ C						
4	NpO ₂	Ref.	Eu ₂ O ₃				
5	Gd ₂ O ₃						
6	Dy ₂ O ₃	Eu ₂ O ₃	Ref.	Dy ₂ O ₃			
7	Er ₂ O ₃	Dy ₂ O ₃	Dy ₂ O ₃	Ref.	Ref.	Er ₂ O ₃	Er ₂ O ₃
Worst	Ref.	Er ₂ O ₃	Ref.	Ref.			
	Model						
Best	Eu ₂ O ₃	AmO ₂					
2	B ₄ C	NpO ₂					
3	AmO ₂	B ₄ C					
4	NpO ₂	Gd ₂ O ₃	Gd ₂ O ₃	Gd ₂ O ₃	Eu ₂ O ₃	Eu ₂ O ₃	Eu ₂ O ₃
5	Gd ₂ O ₃	Dy ₂ O ₃	Dy ₂ O ₃	Dy ₂ O ₃	Gd ₂ O ₃	Gd ₂ O ₃	Gd ₂ O ₃
6	Dy ₂ O ₃	Er ₂ O ₃	Er ₂ O ₃	Eu ₂ O ₃	Dy ₂ O ₃	Dy ₂ O ₃	Dy ₂ O ₃
7	Er ₂ O ₃	Ref.	Eu ₂ O ₃	Er ₂ O ₃			
Worst	Ref.	Eu ₂ O ₃	Ref.	Ref.	Ref.	Ref.	Ref.

4 Conclusions and future works

Despite some minor differences, the comparison with the results obtained with MCNP6.1 largely confirmed the ability of the model in predicting the performance of materials used as burnable poisons in fast reactors with 1.5 at.% content in the burnup range of 16 to 160 GWd/t_{HM}.

Two future works are noteworthy: the neutronic characterization (i.e., reactivity swing, residual reactivity penalty, neutron spectrum, spectral index and temperature reactivity coefficients) of the materials which were found to be most promising so as to provide design guidance for micro and small modular liquid metal fast reactors and the application of the model to other candidates to find new materials that present neutronic behavior suitable for a burnable poison.

References

- [1] J.T. Goorley et al., Initial MCNP6 Release Overview – MCNP6 version 1.0, LA-UR-13-22934 (2013).
- [2] D. A. Brown et al., ENDF/B-VIII.0: The 8th major release of the nuclear reaction data library with CIELO-project cross sections, new standards and thermal scattering data. Nucl. Data Sheets 148:1-142 (2018). DOI: 10.1016/j.nds.2018.02.001.
- [3] J.L. Conlin et al., Release of ENDF/B-VIII.0-based ACE data files, internal report LA-UR-18-24034, LANL, Los Alamos, 2018.
- [4] H. Guo, T. Kooyman, P. Sciora and L. Buiron. Application of Minor Actinides as Burnable Poisons in Sodium Fast Reactors, Nuclear Technology, (2019).

DEVELOPMENT OF A MULTIPHASE MHD OPENFOAM SOLVER FOR FUSION REACTOR ANALYSIS

Sonia Pignatiello, Lorenzo Melchiorri, Simone Siriano and Alessandro Tassone

Dep. of Astronautical, Electrical and Energy Engineering (DIAEE) - Nuclear Engineering Research Group, Sapienza University of Rome, Corso Vittorio Emanuele II, 244, Roma, 00186, Italy
Corresponding author: sonia.pignatiello@uniroma1.it

ABSTRACT. This contribution addresses the issue of numerically modelling and predicting the Magnetohydrodynamics (MHD) effects on the dynamic of the bubbles in the liquid metal breeder of a fusion reactor. The `mhdInterFoam` numerical code has been developed implementing the MHD equations in the OpenFOAM solver `interIsoFoam` and has been validated against numerical and experimental results from existing literature. Simulations include scenarios with nitrogen bubbles of various sizes (Eötvös number $\approx 1.5 - 8.5$) rising in mercury at room temperature, under a horizontal magnetic field (Hartmann number = 0 - 148). The simulation results show good agreement with experimental findings.

1 Introduction

Liquid metals (LM) are considered for use as coolants and tritium breeders in various Breeding Blanket (BB) concepts, such as the Water-Cooled Lead Lithium BB, and in advanced Plasma-Facing Components (PFC) [1] [2]. A significant drawback of using electrically conductive fluids in magnetic confined fusion reactors is their interaction with the magnetic field, resulting in magnetohydrodynamic (MHD) effects. These effects, generated by the induced Lorentz force within the liquid metal, include changes in velocity distribution, increased pressure losses, and degradation of mass and energy transport processes [3]. Consequently, designing these components requires accurate predictive numerical tools and high-quality numerical data.

An engineering issue in the LM BB design is linked to the production of helium bubbles that can be transported within the main fluid flow [4]. Their presence can lead to safety issues and to a decrease of the BB performances. This work introduces a numerical code, developed using OpenFOAM (OF) and validated against experimental data found in the literature, which is able to predict the MHD effects caused by the motion of a gas bubble within a channel filled with a liquid metal.

2 `mhdInterFoam` code

The `mhdInterFoam` (mIF) is a code capable of carrying out MHD time-dependent simulation of two incompressible, isothermal and immiscible fluids. Currently, it supports only the fluid region, so it is possible to model only ideal electric wall conditions through BCs, such as perfectly electrically insulated and conductive walls. The solver is based on the `interIsoFoam` solver of OpenFOAM v2212. MHD effects were implemented following guidelines from Zhang et al [6]. The `interIsoFoam` solver has been tested by the authors under hydrodynamic conditions for a high-density ratio mixture, successfully simulating various flow regimes for helium bubbles rising in a lead-lithium eutectic alloy [7]. The two-phase modelling is performed employing the Volume of Fluid (VOF) method, a free-surface modelling technique which use a scalar function α that represent the volume fraction of each fluid in a CV. Excluding phase change, the mass of a certain phase must be conserved, thus:

$$\frac{\partial \alpha}{\partial t} + \nabla \cdot (\alpha \mathbf{u}) = 0 \quad (1)$$

In essence, this represents the advection equation of the interface, and its solution must preserve its sharpness. Once the alpha distribution is calculated, material properties are updated within the computational domain according to the following relationship, where β represents a generic property:

$$\beta = \alpha\beta_1 + (1 - \alpha)\beta_2 \quad (2)$$

The VOF method employ a single momentum equation for the whole mixture and below is reported the one implemented in the mIF solver, which includes the Lorentz force:

$$\rho \left[\frac{\partial \mathbf{u}}{\partial t} + (\mathbf{u} \cdot \nabla) \mathbf{u} \right] = -\nabla p + \nabla \cdot \Psi + \mathbf{F}_S + \rho \mathbf{g} + \mathbf{J} \times \mathbf{B}_0 \quad (3)$$

where ρ is the density, \mathbf{u} is the velocity, p is the pressure, Ψ is the viscous stress tensor, \mathbf{g} the gravitational acceleration, \mathbf{J} is the current density, \mathbf{B}_0 is the imposed magnetic field and \mathbf{F}_S is the surface tension force which is modeled as a volumetric force employing the Continuum Surface Force (CSF) technique of Brackbill et al. [8].

To evaluate the Lorentz force, the Electric potential formulation has been used and the equations implemented in the code are respectively the Electric Potential Poisson equation (4) and the Ohm's law (5):

$$\nabla^2 \varphi = \nabla \cdot (\mathbf{u} \times \mathbf{B}_0) \quad (4)$$

$$\mathbf{J} = \sigma(-\nabla \varphi + \mathbf{u} \times \mathbf{B}_0) \quad (5)$$

where φ is the electric potential and σ is the electrical conductivity. To satisfy the charge conservation, a conservative formulation of the Lorentz force and for the current density developed by Ni et al. [5] have been implemented. For more information refer to Ref [9].

3 Code validation

In this section, we present the results of the validation process for the mIF code. This validation involves simulating the rising of a nitrogen bubble in a square channel filled with liquid mercury under the influence of a transversal uniform magnetic field \mathbf{B}_0 . This case was previously explored by Mori et al. [10], where the bubble dynamics for various initial diameters d was investigated under three different magnetic field intensities, ranging from 0.5 to 1.5 T.

The parameter chosen for comparison is the terminal velocity of the bubble. Initially at rest, the bubble undergoes acceleration until it attains a limit velocity, a value contingent upon factors such as the bubble diameter, material properties, and the intensity of the magnetic field. This terminal velocity, apart from minor oscillations, remains relatively constant.

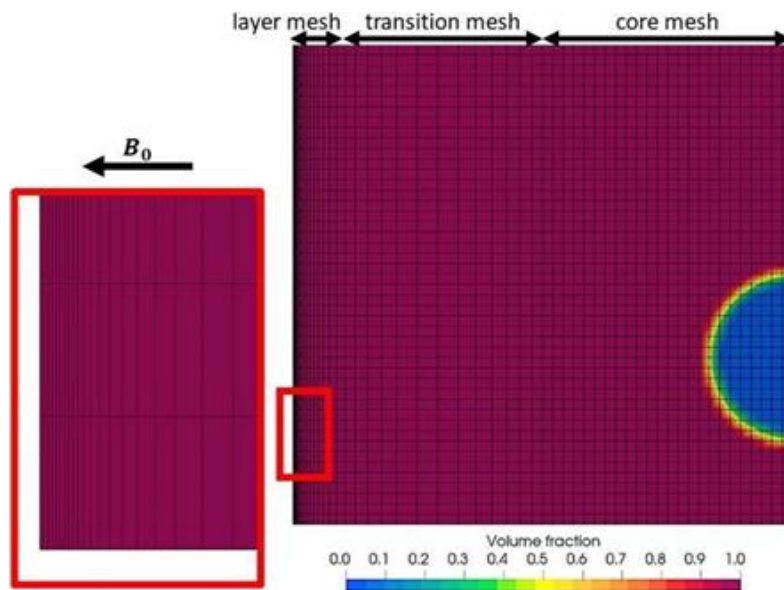


Fig. 1: Example of computational grid used in the study. Detail of the mesh in the Hartmann layer (left box).

The convergence criteria are established by observing this behaviour, deeming the simulation converged when the oscillations remain within a range $\pm 10\%$ concerning the terminal velocity. Achieving this requires a simulation timeframe between 0.21 and 0.25 seconds. The numerical domain is represented as a parallelepiped, with a square base measuring $6d \times 6d$. Depending on the bubble's dimension and magnetic field intensity, the height ranges from $16d$ to $42d$. The spherical nitrogen bubble starts from rest at $1d$ above the bottom wall while the liquid mercury remains stationary.

The simulation considers material properties detailed in Ref [9] and the key dimensionless parameters Reynolds (Re) or Galilei (Ga) number, Eötvös (Eo) number, and Hartmann (Ha) number, varying in the intervals $3200 \leq Re \leq 11800$, $1.5 \leq Eo \leq 8.5$ and $0 \leq Ha \leq 148$. Concerning the BCs, the noSlip condition for velocity and the zeroGradient condition for pressure, volume fraction and electric potential have been applied on all walls. This last condition is in line with the glass channel used by Ref [10]. The mesh configuration includes a core mesh with dimensions $3d \times 3d$ of uniformly sized square elements of $d/n \times d/n$. This is followed by a transition mesh leading to the wall mesh, where elements measure $d/8 \times d/8$. The wall mesh ensures 7 divisions across the MHD layers as shown in Fig 1. The parameter n was determined through a mesh sensitivity analysis, considering values of 11, 16 and 24, using the average terminal velocity up to 0.1 seconds as the comparison parameter. The analysis revealed a mesh-independent solution for $n = 16$ which was then used for all cases. The simulations were performed using CRESCO6 cluster using an average number 350 processors for 336 hours per simulation.

Fig. 2 illustrates the rising velocity of the bubble with a diameter of 5.60 mm moving through a 0.5 T magnetic field. The results from two other codes are also presented, alongside the experimental terminal velocity value of 168 m s^{-1} [8]. Both the mIF solver and Code A simulate a very short-lived initial phase, extending from 0 to approximately 0.1 s, characterised by the rapid bubble acceleration. Then, the velocity reaches a plateau and begins oscillating around a mean value. Code B also reaches this point, albeit with a smoother initial phase. Across all three codes, the average velocity U_T closely aligns with the experimentally measured value. Table 1 collects the results for all the considered bubbles, demonstrating that the code accurately predicts the terminal velocity of the bubbles, with a maximum discrepancy from the experimental data of approximately 10%. The maximum discrepancy is observed for the smallest bubble, and it is likely attributed to the perturbations in the measurement system concerning the motion field of the metal surrounding the bubble [10].

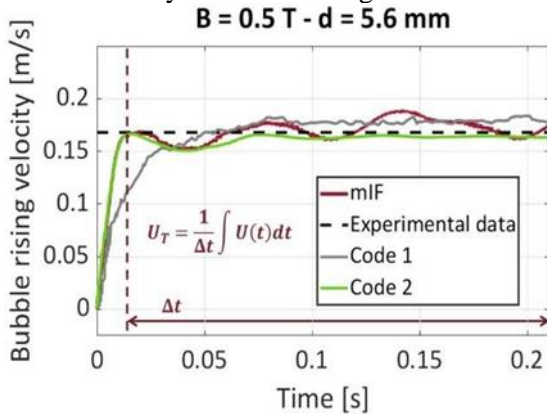


Fig.2: Rising velocity for the bubble with $d=5.6 \text{ mm}$ under a magnetic field with intensity 0.5 T. Code 1 refers to the results in Ref [11] and Code 2 to Ref [6].

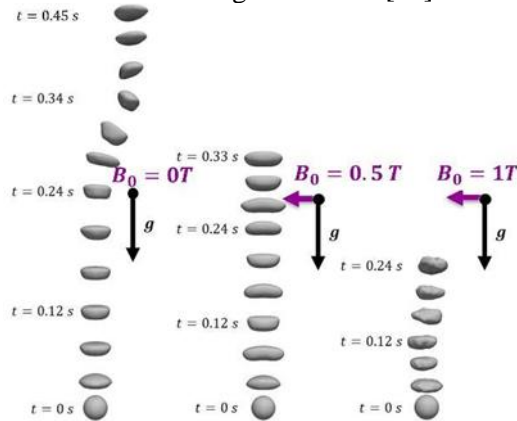


Fig. 3: Shape of the bubble with $d = 5.6 \text{ mm}$ for the hydrodynamic case (left), $B_0 = 0.5 \text{ T}$ (centre) and $B_0 = 1 \text{ T}$

Fig. 3 shows the bubble's shape during ascent at various time steps. Without a magnetic field, the bubble remains ellipsoidal due to low Eötvös and Galilei numbers. With the magnetic field, the bubble still stays ellipsoidal, with the short axis aligned with the magnetic field and the long axis perpendicular. The Lorentz force's braking effect is evident, causing the bubble to rise less and follow an almost straight trajectory within the same timeframe. The obtained results are in good agreement with literature findings.

Table 1: Results of validation. The symbols $U_{T,ex}(mm/s)$ and $U_{T,mIF}(mm/s)$ refer respectively to the experimental value in [10] and the mIF results [9]. $E(U_T)(\%)$ is the relative error between the two values.

$B_0(T)$	$d(mm)$	$U_{T,ex}(mm/s)$	$U_{T,mIF}(mm/s)$	$E(U_T)(\%)$
0.0	2.36	189	207	9.5
0.0	3.87	192	189	-1.6
0.0	5.60	201	203	1.0
0.5	2.36	199	187	-6.0
0.5	3.87	184	174	-5.4
0.5	5.60	168	172	2.4
1	5.6	143	134	-6.3

Acknowledgments

This work has been carried out within the framework of the EUROfusion Consortium and has received funding from the Euratom research and training programme 2014-2018 and 2019-2020 under grant agreement No 633053. The views and opinions expressed herein do not necessarily reflect those of the European Commission.

References

- [1] P. Arena, G. Bongiovì, I. Catanzaro, C. Ciurluini, A. Collaku, A. Del Nevo, P. A. Di Maio, M. D’Onorio, F. Giannetti, V. Imbriani, and et al. "Design and Integration of the EU-DEMO Water-Cooled Lead Lithium Breeding Blanket" *Energies*, 16 (2023).
- [2] Kessel, C. E., Andruczyk, D., Blanchard, J. P., Bohm, T., Davis, A., Hollis, K., Yoon, S. J. "Critical Exploration of Liquid Metal Plasma-Facing Components in a Fusion Nuclear Science Facility". *Fusion Science and Technology*, 75 (2019).
- [3] Müller U., Bühler L. "Magnetofluidynamics in Channels and Containers" *Springer*, Berlin, Heidelberg (2001).
- [4] L. Batet, *et al.* "Numeric implementation of a nucleation, growth and transport model for helium bubbles in lead-lithium HCLL breeding blanket channels: theory and code development" *Fusion Eng. Des.*, 86 (2011)
- [5] Ni M.-J., Munipalli R., Huang P., Morley N.B., Abdou M.A. "A current density conservative scheme for incompressible MHD flows at a low magnetic Reynolds number. Part II: On an arbitrary collocated mesh" *J. Comput. Phys.*, 227 (2007).
- [6] Zhang J., Ni M.J. "Direct simulation of multi-phase MHD flows on an unstructured cartesian adaptive system" *J. Comput. Phys.*, 270 (2014).
- [7] Siriano S., Balcázar N., Tassone A., Rigola J., Caruso G. "Numerical simulation of high-density ratio bubble motion with interIsoFoam" *Fluids*, 7 (2022).
- [8] Brackbill J.U., Kothe D.B., Zemach C. "A continuum method for modeling surface tension" *J. Comput. Phys.*, 100 (1992).
- [9] Siriano S., Melchiorri L., Pignatiello S., Tassone A. "A multi-region and a multiphase MHD OpenFOAM solver for fusion reactor analysis" *Fusion Eng. Des.*, 200 (2024).
- [10] Mori Y., Hijikata K., Kuriyama I. "Experimental study of bubble motion in mercury with and without a magnetic field" *J. Heat Transfer*, 99 (1977).
- [11] Jin K., Kumar P., Vanka S.P., Thomas B.G. "Rise of an argon bubble in liquid steel in the presence of a transverse magnetic field" *Phys. Fluids*, 28 (2016).

MODELLING THE POTENTIAL INTERACTION BETWEEN AIRBORNE PARTICULATE MATTER AND THE SARS-CoV-2 SPIKE PROTEIN

Alice Romeo^{1*}, Roberto Pellegrini^{1,2}, Maurizio Gualtieri^{3,4}, Barbara Benassi², Massimo Santoro², Federico Iacovelli¹, Milena Stracquadanio³, Mattia Falconi¹, Carmela Marino², Gabriele Zanini³, Caterina Arcangeli²

¹*Department of Biology, University of Rome Tor Vergata, Via della Ricerca Scientifica 1, 00133 Rome, Italy*¹⁷

²*Division of Health Protection Technologies, Italian National Agency for New Technologies, Energy and Sustainable Development (ENEA), 00123 Rome, Italy*

³*Division of Models and Technologies for Risks Reduction, Italian National Agency for New Technologies, Energy and Sustainable Development (ENEA), 40129 Bologna, Italy*

⁴*Department of Earth and Environmental Sciences, Piazza della Scienza 1, University of Milano-Bicocca, Milan*

ABSTRACT. The strong impact of the COVID-19 pandemic in Northern Italy regions led to the hypothesis that airborne particulate matter (PM), present at high concentrations in these areas, may act as a carrier for the SARS-CoV-2 virion. To address this controversial issue, in this work, we demonstrated the presence of SARS-CoV-2 RNA genome on PM_{2.5} samples collected in the city of Bologna in winter 2021 and then modelled and simulated the interaction of a simplified PM_{2.5} fragment with the SARS-CoV-2 Spike protein. The simulations highlighted the potential molecular interaction between the protein and the PM, resulting in a binding free energy of -207.2 ± 3.9 kcal/mol, while structural analyses suggested that PM attachment does not induce an alteration in the protein structure and dynamics. Although this simulation cannot assess whether the interactions would be sufficient to carry the virus in the atmosphere or retain its infectiousness after the transport, they suggest the possibility of an association between the PM and SARS-CoV-2, which should be verified by further experimental analyses.

1 Introduction

During the first phases of the COVID-19 pandemic, largest outbreaks were recorded in most polluted areas, particularly the Lombardia, Veneto and Emilia Romagna regions (<https://www.epicentro.iss.it/coronavirus/sars-cov-2-inquinamento-atmosferico>). This evidence led the scientific community to hypothesize a correlation between the rapid diffusion of the virus and the high rates of urban pollution characterizing these areas [1]. Indeed, epidemiological studies reported a positive correlation between high particulate matter (PM) levels and mortality from heart and respiratory conditions in urban areas. Pollution exposure is known to increase the incidence of respiratory viral infections, virus transmissibility, patients' hospitalizations and disease severity [2]. The atmospheric PM is a heterogeneous mixture of air-dispersed particles, composed of a carbonaceous core and several organic (polycyclic aromatic hydrocarbons) and inorganic (transition metals, sulfates and nitrates) components [3]. PM particles have no well-defined shape, and their composition varies according to the source, period of sampling and weather conditions. It has been suggested that air pollution could favour SARS-CoV-2 infection either by inducing negative effects on the host immune system or by acting as a carrier facilitating the transport of viral particles. In this framework, this work has been performed within the scope of the PULVIRUS project (<https://www.pulviris.it/>) to investigate the presence of potential molecular interactions between the organic and inorganic components of a PM_{2.5} model and the SARS-CoV-2 Spike (S) glycoprotein covering the virion surface. This study has been published in [3].

¹⁷ Corresponding author. E-mail: caterina.arcangeli@enea.it.

2 Computational methods

2.1 Molecular modelling and simulation of a PM_{2.5} fragment

A simplified PM_{2.5} fragment was modelled by including representative organic and inorganic components identified in a typical secondary organic (SOA) and inorganic aerosol (SIA) of the Po river Valley (Bologna area), collected during air pollution sampling carried out by the ENEA Laboratory of Atmospheric Pollution. The SIA constituted the predominant component of PM_{2.5} fine particles (52% of the total mass), while the ratio of SOA components was 1:30:30:10:20 for polycyclic aromatic hydrocarbons (PAHs), carbohydrates, alkaloid acids, aromatic acids and aliphatic acids, respectively. Representative compounds have been selected for each chemical class [3] (Table 1). CHARMM parameters for these compounds were generated using the CGenFF program (<https://cgenff.umaryland.edu>) and the CHARMM general force field [4], except those for ammonium, which were already included in the CHARMM force field and those for nitrate, which were obtained from the literature [5]. The PM_{2.5} carbon core was approximated by a 3-layer sheet of graphene with a size 240 x 240 x 162 Å³, modelled using the CHARMM-GUI web interface [6] and parametrized using the CHARMM force field. The final PM_{2.5} model was assembled using the Packmol program [7], randomly inserting the components on one side of the graphene surface (Fig. 1). The model was solvated in a box of TIP3P water molecules, resulting in a system of 920.385 atoms which was simulated through classical molecular dynamics (MD) using the NAMD 2.13 program [8] on 12 nodes of the ENEA CRESCO6 HPC cluster. Details on the simulation protocol are reported in the paper [3]. After an initial equilibration phase, a production run of 190 ns was performed. All analyses have been carried out using the GROMACS 2019 [9] or VMD 1.9.3 [10] programs.

2.2 Modelling and simulation of the PM_{2.5}-virus interface

Using the last frame of the previous simulation, a simplified model of a PM_{2.5}-virus interface was assembled, including a model of the SARS-CoV-2 S ectodomain (residues 1-1147). The structures were approached using the VMD program [10] to mimic an initial interaction between the two interfaces, manually fixing superpositions between the protein surface and surrounding compounds. The assembled structures were parametrized using the CHARMM force field [4, 11] and inserted in a box of TIP3P water molecules, neutralized with KCl ions. This system resulted in a total of 1.589.154 atoms and was simulated as described in the previous section for 100 ns using the NAMD 2.13 [8] program on 12 nodes of the ENEA CRESCO6 HPC cluster.

3 Results

3.1 Analysis of PM_{2.5} assembly

Simulation of the simplified PM_{2.5} model allowed the organic and inorganic compounds to stratify around the graphene layer, mimicking the aerosols' arrangement around the carbon core (Fig. 1). During the simulation, organic molecules distributed over the graphene sheet interacting with the carbon layer or within themselves, forming hydrophobic aggregates of different size already during the first phases of simulation. Once formed, these clusters tend to remain in the solvent establishing few interactions with the graphene surface. Levoglucosan and oxalacetate are the compounds most attracted to the surface, suggesting that graphene can act as an attractive matrix for organic molecules. Distance analysis highlighted that, at the end of the simulation, about 34% of the PM organic compounds are in close contact with the carbon layer, including 97% and 84% of the oxalacetate and levoglucosan molecules, respectively. On the other hand, inorganic PM components randomly diffuse in the solvent without specifically interacting with the graphene.

Table 1: Chemical composition of a typical PM_{2.5} sampled in Northern Italy. Representative molecules for each chemical class selected for building the model are indicated.

Chemical composition		Representative molecule	Pubchem ID	N° of molecules in the model
SOA	PAH	benzo[a]pyrene (BZP)	2336	5
	carbohydrate	levoglucosan (LVG)	2724705	150
	alcaloid acid	palmitic acid (PLX)	985	100
	aromatic acid	phtalic acid (PTX)	1017	50
	aliphatic acid	oxalic acid (OXC)	971	100
SIA	ammonium	NH ₄ ⁺	223	493
	nitrate	NO ₃ ⁻	943	493

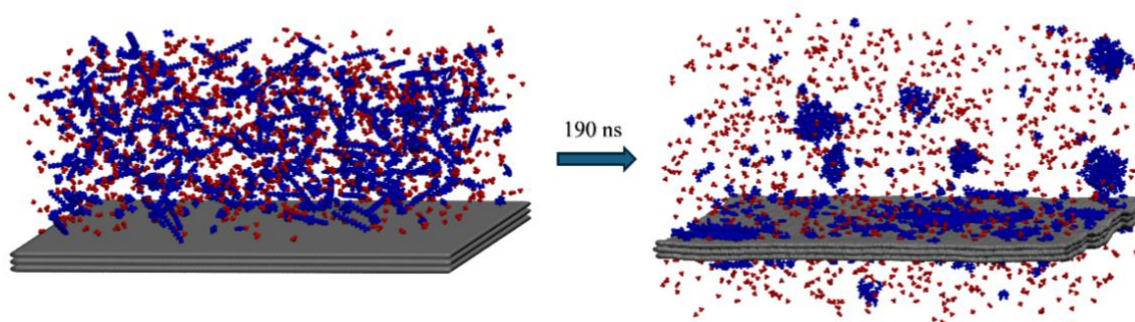


Fig.1: Temporal evolution of PM_{2.5} compounds diffusion over the graphene sheet (in grey as surface). The organic compounds are shown as spheres in blue, while inorganic ions are shown in red.

3.2 Analysis of PM_{2.5} interactions with the SARS-CoV-2 Spike glycoprotein

Distance analysis showed that the S protein rapidly approaches the graphene surface, reducing its distance from about 1.0 nm to 0.2 nm during the first 50 ns of simulation (Fig. 2). This binding is stably maintained and mostly involves the glycans covering the upper protein regions, which extend and adhere to the graphene surface. The strength of this interaction has been quantified over the last 50 ns of simulation using the MM/GBSA method. Results highlighted an interaction energy of -207.2 ± 3.9 kcal/mol at the protein-PM interface, due to favourable non-polar and electrostatic interactions. The protein shows high interaction energies with the organic PM compounds and the inorganic species, evaluated as -118.2 ± 1.7 kcal/mol and -68.7 ± 1.1 kcal/mol, respectively. This suggests that the inclusion of viral surface proteins within this cloud of interactions could represent a capture mechanism for the virus, allowing it to rapidly approach the PM carbon core and stabilizing the virion during the hypothesized transport. Structural analyses have been performed on the S glycoprotein to evaluate if PM_{2.5} attachment could result in an alteration of the protein's structural and functional dynamics, comparing the results to a reference trajectory [12]. Overall, analyses showed that the protein maintains structural parameters and interaction patterns similar to the reference simulation, suggesting that its structure is not compromised by PM interaction and that the virion should retain its ability to bind the host cell receptors after being released [3].

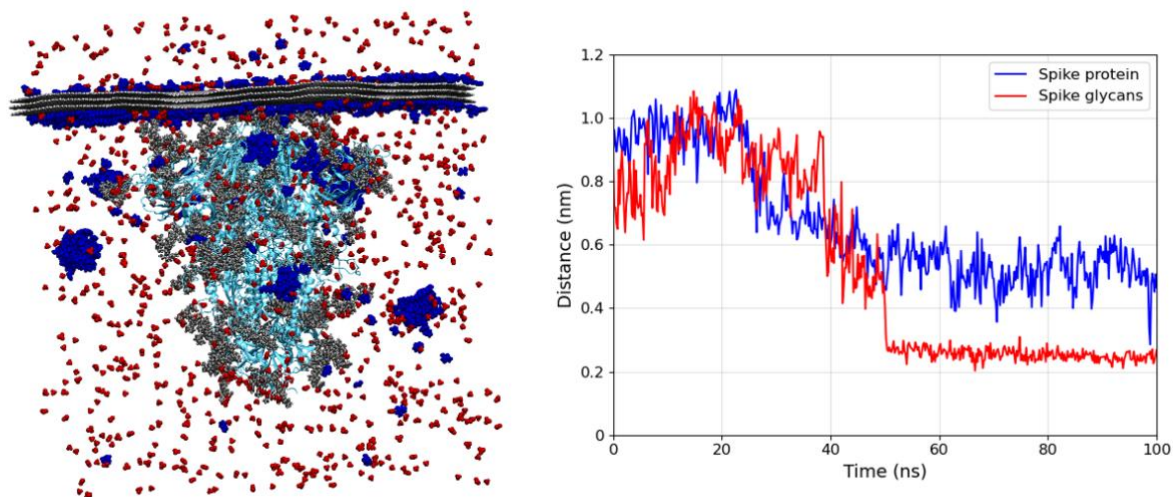


Fig.2: On the left, final frame obtained from the PM_{2.5}-virus simulation. The protein is shown as a ribbon in cyan, and the glycans as spheres in grey. The PM is represented as in Fig.1. On the right, distances calculated between the graphene surface and the S protein residues (blue line) or glycans (red line).

4 Conclusion

Modelling and simulation of a simplified PM_{2.5} fragment allowed, for the first time, to get some insights into the dynamic behaviour and molecular interactions of its organic and inorganic components with the carbon core, approximated by a hydrophobic layer composed of three graphene sheets. Interactions of this final assembled PM_{2.5} model with the SARS-CoV-2 S glycoprotein have been evaluated, following the hypothesis of a possible role of the PM_{2.5} as a SARS-CoV-2 carrier. Since the virus should retain its functionality to be transmitted through pollution particles, the structural integrity of the S glycoprotein has been monitored during the simulation, confirming that the protein maintains its structural dynamics when adhered to the graphene layer, with no alterations observed in the protein fluctuations and only minor differences in its pattern of intra- and inter-chain interactions. The obtained picture would support the hypothesis of a possible interaction between the particulate and the SARS-CoV-2 S proteins, suggesting that the glycans covering the upper protein regions would be responsible for the first attachment to the PM_{2.5} carbon core, while a surrounding cloud of organic and inorganic PM_{2.5} components would trap the protein through an interaction network which could stabilize the virion for airborne transport. However, further investigations are needed to confirm whether these interactions would be sufficient to stably carry the virus in the atmosphere, or whether the virus would retain its activity after transport and release. In conclusion, the results obtained in this work and within the PULVIRUS project contributed to delineating the molecular interactions possibly occurring between PM and SARS-CoV-2, supporting further studies aimed at clarifying the relationship between PM abundance and viruses' airborne diffusion.

Acknowledgements

We acknowledge the PULVIRUS Project (<https://www.pulviris.it/>) that funded this activity and the colleagues from the National and Regional Environmental Agencies involved in the Project. The computing resources and the related technical support used for this work have been provided by CRESCO/ENEAGRID High performance Computing infrastructure and his staff. CRESCO/ENEAGRID High performance Computing infrastructure is funded by ENEA, the Italian National Agency for New Technologies, Energy and Sustainable Economic Development and by Italian and European research programmes, see <http://www.cresco.enea.it/english> for information.

References

- [1] B. Woodby, M.M. Arnold, and G. Valacchi. SARS-CoV-2 infection, COVID-19 pathogenesis, and exposure to air pollution: What is the connection? *Annals of the New York Academy of Sciences* 1486, pp. 15–38, (2021).
- [2] J. Ciencewicky and I. Jaspers. Air pollution and respiratory viral infection. *Inhalation Toxicology* 19, pp. 1135–1146, (2007).
- [3] A. Romeo, R. Pellegrini, M. Gualtieri, B. Benassi, M. Santoro, F. Iacovelli, M. Stracquadiano, M. Falconi, C. Marino, G. Zanini, and C. Arcangeli. Experimental and in silico evaluations of the possible molecular interaction between airborne particulate matter and SARS-CoV-2. *Science of The Total Environment* 895, pp. 165059, (2023).
- [4] K. Vanommeslaeghe, E. Hatcher, C. Acharya, S. Kundu, S. Zhong, J. Shim, E. Darian, O. Guvench, P. Lopes, I. Vorobyov, and A.D. Mackerell. CHARMM general force field: A force field for drug-like molecules compatible with the CHARMM all-atom additive biological force fields. *Journal of Computational Chemistry* 31, pp. 671–690, (2010).
- [5] L.A. Richards, A.I. Schäfer, B.S. Richards, and B. Corry. The importance of dehydration in determining ion transport in narrow pores. *Small* 8, pp. 1701–1709, (2012).
- [6] S. Jo, T. Kim, V.G. Iyer, and W. Im. CHARMM-GUI: A web-based graphical user interface for CHARMM. *Journal of Computational Chemistry* 29, pp. 1859–1865, (2008).
- [7] L. Martínez, R. Andrade, E.G. Birgin, and J.M. Martínez. PACKMOL: A package for building initial configurations for molecular dynamics simulations. *Journal of Computational Chemistry* 30, pp. 2157–2164, (2009).
- [8] J.C. Phillips, R. Braun, W. Wang, J. Gumbart, E. Tajkhorshid, E. Villa, C. Chipot, R.D. Skeel, L. Kalé, and K. Schulten. Scalable molecular dynamics with NAMD. *Journal of Computational Chemistry* 26, pp. 1781–1802, (2005).
- [9] M.J. Abraham, T. Murtola, R. Schulz, S. Páll, J.C. Smith, B. Hess, and E. Lindah, Gromacs: High performance molecular simulations through multi-level parallelism from laptops to supercomputers. *SoftwareX* 1–2, pp. 19–25, (2015).
- [10] W. Humphrey, A. Dalke, and K. Schulten. VMD: Visual molecular dynamics. *Journal of Molecular Graphics* 14, pp. 33–38, (1996).
- [11] J. Huang, S. Rauscher, G. Nawrocki, T. Ran, M. Feig, B.L. De Groot, H. Grubmüller, and A.D. MacKerell. CHARMM36m: An improved force field for folded and intrinsically disordered proteins. *Nature Methods* 14, pp. 71–73, (2016).
- [12] A. Romeo, F. Iacovelli, C. Scagnolari, M. Scordio, F. Frasca, R. Condò, S. Ammendola, R. Gaziano, M. Anselmi, M. Divizia, and M. Falconi. Potential Use of Tea Tree Oil as a Disinfectant Agent against Coronaviruses: A Combined Experimental and Simulation Study. *Molecules* 27, (2022).

MULTIPARTITE ENTANGLEMENT AND QUANTUM FRUSTRATION: SIMULATION AND APPLICATIONS

Paolo Scarafile¹, Angelo Mariano², Saverio Pascazio³

¹*Dipartimento di Fisica, Università di Bari, I-70126 Bari, Italy [pablo.scarafile97@gmail.com]*

²*ENEA, TERIN-ICT Division, Bari local office, I-70121 Bari, Italy*

³*Dipartimento di Fisica and INFN, Università di Bari, I-70126 Bari, Italy*

ABSTRACT. Frustration is a phenomenon commonly encountered in various domains, from social and psychological contexts to the realm of physics. In particular, the concept of frustration has a significant role in quantum systems, where it describes situations in which the individual components of a system cannot achieve a globally optimal state due to conflicting interactions. This report will investigate into the distinction between multipartite and bipartite entanglement, we will introduce computational algorithms for simulating a large number of quantum states, particularly focusing on systems of multiple qubits. We will explain how frustration emerges in these quantum systems and how it can be studied computationally through statistical approaches. Specifically, we will also analyze the distribution of bipartite and multipartite entanglement in frustrated systems, revealing how frustration affects different states, including random states and states with uniform real-phase distributions. Through this analysis, we will highlight the distinct ways in which frustration manifests in different types of quantum states.

1 Introduction

The resources of ENEA GRID/CRESCO HPC have been used in order to investigate the multipartite entanglement of systems of qubits, which is a characteristic and intriguing phenomenon of quantum information theory. Multipartite entanglement has the typical features of a complex phenomenon and a computational approach is required for its analysis [1][2][3][4]. The research was focused on qubits systems, which can be described by the two-dimensional Hilbert space and can be represented as a combination of the two possible outcomes of the bit:

$$|\psi\rangle = a|0\rangle + b|1\rangle \quad (1.1)$$

where a, b are complex numbers, that satisfy $|a|^2 + |b|^2 = 1$

Qubits systems are fundamental in the investigation of the entanglement, because they represent the simplest systems affected by this phenomenon. The analysis of multipartite entanglement, which affects systems with $n > 2$ qubits, differs from the bipartite case because there is not a unique bipartition of the system (for example a system of 4 qubits can be bi-partitioned in 3 different ways) and a direct evaluation of the amount of entanglement does not exist. Moreover, with an increasing number of subsystems an exponential growth of the number of bipartitions arises, making the multipartite entanglement even more challenging. For this reason, information about the multipartite entanglement has to be extracted by analyzing the distributions of the purities associated to each bipartite entanglement [2][3][4]. It is convenient a statistical approach, analyzing the distributions of bipartite entanglement associated to the single bipartitions. This can be made computationally, simulating an enormous number of states.

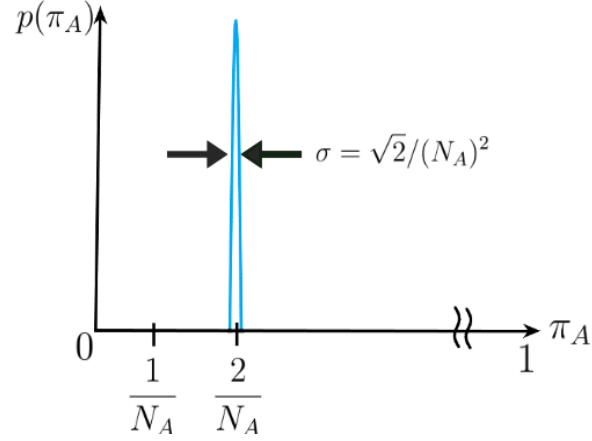


Figure 1: Typical shape of the distribution of bipartite entanglement in a system of n qubits, in the case random states

Another crucial phenomenon investigated in the research, which is directly correlated to multipartite entanglement is Quantum Frustration [2][3][4]. It expresses the impossibility of existence of perfect maximally multipartite entangled states, or simply perfect MMES. In other word, the presence of Quantum Frustration reduces the amount of entanglement in the qubits systems. It can be also studied computationally, analyzing the distributions of the potential of multipartite entanglement:

$$\pi_{ME}(|\psi\rangle) = \binom{n}{n_A}^{-1} \sum_{A=|n_A|} \pi_A(|\psi\rangle) \quad (1.2)$$

2 Computational Approach

The research was based on the simulation of quantum qubits states in two different sub-manifolds. The pseudo-random states and the uniform real-phased states:

$$|\psi\rangle = \sum_{k=0}^{2^{n-1}} c_k |k\rangle \text{ where } c_k \in \mathbb{C} \quad (2.1)$$

$$|\psi\rangle = \frac{1}{2^n} \sum_{k=0}^{2^{n-1}} \xi_k |k\rangle \text{ where } \xi_k = \{-1, +1\} \quad (2.2)$$

In order to simulate these states two distinct and scalable procedure have been introduced. For the pseudo-random set, a quantum circuit has been used, coded using the Qiskit library [6], as shown ion Figure 2 [6]:

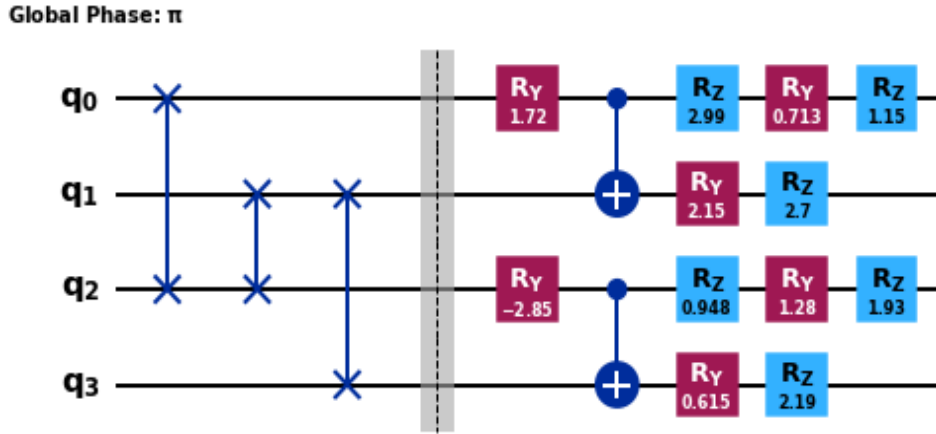


Figure 2: The pseudo-random state generator circuit consists of m layers. Each of them is divided in a random permutation section (first part of the circuit), followed by random two-qubit gates and rotations (second part). When the number of qubits is odd, one of the qubits is idle in each layer. In this figure, a circuit with $n = 4$ qubits and just one layer is shown for illustration purposes [6].

The method used for the creation of the uniform real phased states is the following:

1. the creation of cyclic permuted python vectors with value +1 and -1;
2. the initialization of these vectors in quantum states using a proper quantum gate of the Qiskit library.

Using these computational methods, the following number of states have been simulated for number of qubits from 3 to 12, in Table 1:

Qubits	Pseudo-random states	Uniform real-phased states
3	2×10^6	128
4	2×10^6	32678
5	2×10^6	2×10^6
6	2×10^6	2×10^6
7	2×10^6	2×10^6
8	2×10^6	2×10^6
9	2×10^6	2×10^6
10	2×10^6	2×10^6
11	10^6	10^6
12	10^6	10^6

Table 1: Number of states simulated per number of qubits for both pseudo-random and uniform real-phased states

For each number of qubits, all the possible reduced density matrices have been evaluated, tracing out the qubits related to the sub-system A . For each density matrix the purity has been calculated. Both the trace operations and the purity calculations have been performed using proper functions of the Qiskit library. The purpose of this procedure was to collect the values of purities for each bipartition for all the states. However, in the computational process two major problems arise:

1. time of runs
2. quantity of storage needed

These problems arise because the number of states to be simulate was enormous and the amount of data to be collected for each state exponentially grew with the number of qubits of the system. For 3 qubits, the amount of data for each state was of 3 distinct data, meanwhile for 12 qubits was of 462. It is evident that locally, it would be impossible to simulate all the states and collect all these data. Indeed, the possibility to compute all the simulations on the ENEA-GRID/CRESCO HPC cluster, allows to identify potential errors quicker, but also to reduce the time of the simulation by means of job scheduling and parallelization[7]. Four distinct histograms for any number of qubits have been computed, from 3 to 12, varying type of data and sub-manifold: In Figure 3, the histograms associated to 12 qubits are chosen as a representative case:

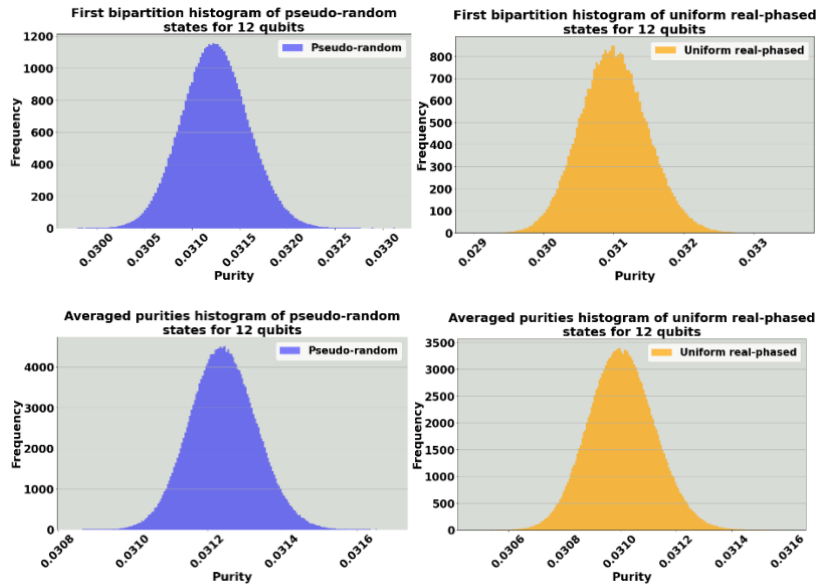


Figure 3: Histograms associated to 12 qubits. On the top, the bipartite entanglement distributions with respect the first bipartition for pseudo-random state (blue) and uniform real-phased (orange). On the bottom, the bipartite entanglement distributions with respect the first bipartition for pseudo-random state (blue) and uniform real-phased (orange).

3 Analysis And Results

Two main analysis have been performed. The first one has the aim to investigate the bipartite entanglement associated to all the balanced bipartitions relative to the sub-manifold chosen, the second one has the aim to analyze the distributions of the potential of multipartite entanglement in order to investigate how differently the frustration appears in the sub-manifolds. Both of them were composed by three distinct sections:

1. Comparison of the parameters of the distributions
2. L^1 distance evaluation
3. Gaussian approximation

Starting from the first analysis, the values of the parameters have been plotted as function of the number of qubits, as shown in Figure 4:

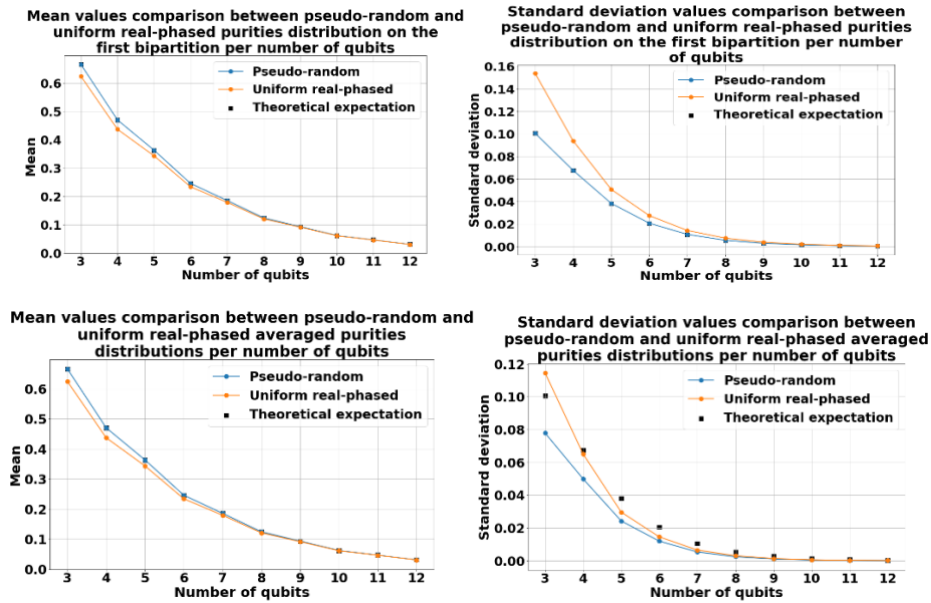


Figure 4: Comparison of mean value and standard deviation of the histograms between pseudo-random state and uniform real-phased varying the number of qubits. On the top in the case of first bipartition purities histogram, on the bottom in case of averaged purities histogram.

The mean of the random distribution is larger than the uniform ones. Moreover, the standard deviation of the random distribution is lower than that of the uniform distribution.

Moving on the second analysis, in order evaluated the distance, the histogram of the absolute difference between distribution of pseudo-random and uniform real-phased states with same number of qubits have been computed. In Figure 5 only the plots associated 12 are shown as a representative case:

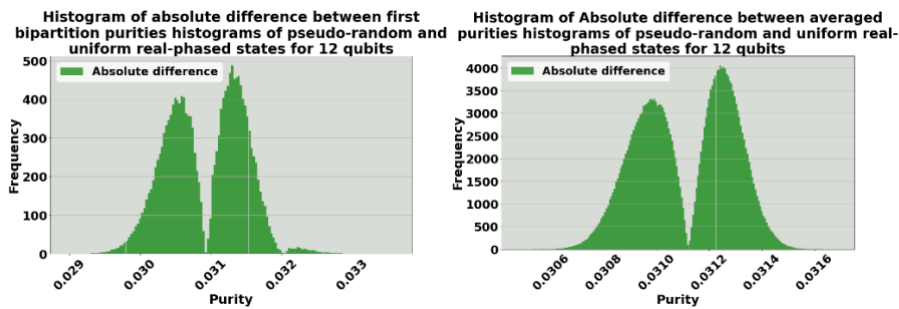


Figure 5: Histograms of absolute difference between pseudo-random state and uniform real-phased for 12 qubits. On the left in the case of first bipartition purities histogram, on the right in case of averaged purities histogram.

The L^1 distance can be easily estimated computing the area of the histograms of the absolute difference. All the values of L^1 distance have been plotted with respect to the number of qubits

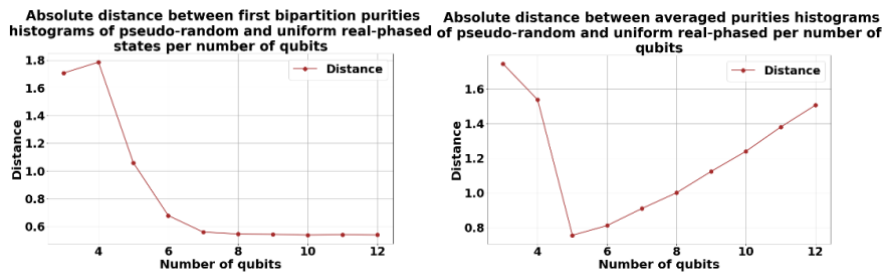


Figure 6: L^1 distance behavior between pseudo-random state and uniform real-phased varying the number of qubits. On the left in the case of first bipartition purities histogram, on the right in case of averaged purities histogram.

4 Conclusion

The results gained suggest that the uniform states are statistically more entangled than the random ones, for all the possible number of qubits of the system. This conclusion is enforced by the corresponding analysis on the averaged distributions over all the bipartitions, where the same behavior has been observed. On the other hand, the quantum frustration would seem to appear stronger for pseudo-random states. Indeed, uniform real-phased states have a mean purity over all the bipartitions, i.e. the potential of multipartite entanglement, smaller than the pseudo-random, proof of a smaller frustration effect. This enforces the conclusion that uniform real phased states are more entangled and less frustrated. Moreover, the analysis of the L^1 distance shows an almost flat region for 7-12 qubits. This strange behavior does not allow strong conclusion about the effective separability of the distributions over the first bipartitions. For the distributions of the averaged purities over all the bipartitions the conclusions are clearer. Indeed, uniform real-phased states tend to separate from the pseudo-random very quickly, with a value about of 1.51 at 12 qubits. The last analysis shown an extremely good Gaussian approximation already at 9-10 qubits in both the cases.

The technical support provided by ENEA-GRID/CRESCO HPC has to be mentioned[7]. CRESCO/ENEAGRID High Performance Computing infrastructure is funded by ENEA, the Italian National Agency for New Technologies, Energy and Sustainable Economic Development and by Italian and European research programmes.

References

- [1]J. Preskil. *Lecture Notes for Ph219/CS219: Quantum Information. Chapter 2*. Update July 2015. url: https://www.lorenz.leidenuniv.nl/quantumcomputers/literature/preskill_2_update.pdf.
- [2]Paolo Facchi. “Multipartite entanglement in qubit systems”. In: *Rendiconti Lincei, Matematica e Applicazioni* 20.1 (Mar. 2009), pp. 25–67. issn: 1720-0768. doi: 10.4171/rlm/532. url: <http://dx.doi.org/10.4171/RLM/532>.
- [3]P Facchi et al. “Multipartite entanglement and frustration”. In: *New Journal of Physics* 12.2 (Feb. 2010), p. 025015. issn: 1367-2630. doi: 10.1088/1367-2630/12/2/025015. url: <http://dx.doi.org/10.1088/1367-2630/12/2/025015>.
- [4]P Facchi et al. “Statistical mechanics of multipartite entanglement”. In: *Journal of Physics A: Mathematical and Theoretical* 42.5 (Jan. 2009), p. 055304.issn: 1751-8121. doi: 10.1088/1751-8113/42/5/055304. url: <http://dx.doi.org/10.1088/1751-8113/42/5/055304>.
- [5]Gabriele Cenedese et al. “Generation of Pseudo-Random Quantum States on Actual Quantum Processors”. In: *Entropy* 25.4 (Apr. 2023), p. 607. issn: 1099-4300. doi: 10.3390/e25040607. url: <http://dx.doi.org/10.3390/e25040607>.
- [6]Qiskit contributors. *Qiskit: An Open-source Framework for Quantum Computing*. 2023. doi:10.5281/zenodo.2573505.
- [7]F. Iannone et al. “CRESCO ENEA HPC clusters: a working example of a multifabric GPFS Spectrum Scale layout”. In: *2019 International Conference on High Performance Computing Simulation (HPCS)*. 2019, pp. 1051–1052.

MONTE CARLO SIMULATION FOR REACTOR CALCULATIONS TO MEDICAL TERBIUM-161 PRODUCTION

Lucrezia Spagnuolo¹, Luigi Lepore^{1*}, Giada Gandolfo¹, Marco Capogni²

¹ENEA, NUC-IRAD-CRGR, Nuclear Material Characterization Laboratory and Nuclear Waste Management
ENEA Casaccia Research Center Via Anguillarese, 301, 00123 Roma, RM, Italy¹⁸

²ENEA, NUC-INMRI, National Institute of Ionizing Radiation Metrology, ENEA Casaccia Research Centre, Via
Anguillarese 301, 00123 Rome, Italy

ABSTRACT. TRIGA (Training, Research, and Isotope production General Atomics) facilities are research reactors widely used for neutron activation analysis and several neutron-related experiments and applications due to the range of thermal neutron fluxes produced.

Neutron fluxes in TRIGA reactors can also be used for radionuclide production, e.g. to generate a new radioactive source for technical applications or medical isotope supply. Neutron activation technique is commonly used, involving exposing an originally non-radioactive material to neutron radiation to induce nuclear reactions and produce specific radionuclides.

The ENEA TRIGA RC-1 reactor is involved in the EU-funded SECURE Project, aiming at studying the feasibility of Italian local production of radionuclides for medical applications. In particular, the ENEA team is investigating the possibility to produce Terbium-161 (¹⁶¹Tb), a promising isotope for targeted radiation therapy favourably better than Lutetium-177 (¹⁷⁷Lu) currently used in cancer therapy, through neutron activation of Gadolinium target highly enriched in Gadolinium-160 (¹⁶⁰Gd) exploiting the reaction channel $^{160}\text{Gd}(n,\gamma)^{161}\text{Gd}(\beta)^{161}\text{Tb}$.

Monte Carlo simulation for radiation transport has been used for reactor calculations to determine neutron fluxes and to obtain correction factors to be applied to the sample under irradiation to obtain more realistic results.

1 Introduction

TRIGA reactors have been proven to be valuable tools for producing medical radioisotopes, even though they provide “lower-magnitude” neutron fluxes compared to production reactors. These facilities can help meet the increasing demand for medical radioisotopes, serving as a local supply source. The role of all nuclear reactors in the supply chain of such radioisotopes should not be underestimated nowadays.

With this purpose, the ENEA TRIGA RC-1 joined the EU-funded SECURE Project (Strengthening the European Chain of sUPply for next generation medical RadionuclidEs). The project aims to make a major contribution to the sustainability of medical radioisotope production and supply for its stable application in diagnostics and therapy within the European context. It is focusing on promising developments in innovative radionuclides, design of irradiation targets, and novel production routes for both currently used and new promising radioisotopes for medical applications.

One of the radioactive nuclides exploited is ¹⁶¹Tb; this is an interesting radionuclide in cancer treatment, showing similar decay characteristics and chemical behaviour to the clinically employed ¹⁷⁷Lu. The therapeutic effect of ¹⁶¹Tb may be enhanced due to the co-emission of a larger number of conversion and Auger electrons, which could be more effective in the treatment of the smallest metastases, as well as single cancer cells [1,2]. The ENEA Casaccia Research Centre is contributing to the project by focusing on the production of the radionuclide ¹⁶¹Tb. This is obtained by neutron activation of a gadolinium target, highly enriched in ¹⁶⁰Gd, with the reaction channel $^{160}\text{Gd}(n,\gamma)^{161}\text{Gd}(\beta)^{161}\text{Tb}$ (or $^{160}\text{Gd}(n,\gamma)^{161}\text{Tb}$ for short) at the TRIGA RC-1 Reactor. Once the irradiation cycle is completed, the target is extracted and sent for chemical processing to obtain: a) the final ¹⁶¹Tb in a salt chemical form i.e. precursor of the radiopharmaceutical product, b) the recovery of the ¹⁶⁰Gd raw materials to produce new targets. The recovery of the raw material allows to start new cycles,

*Corresponding author. E-mail: luigi.lepore@enea.it

maximizing the exploitation of the expensive Gadolinium target highly enriched in ^{160}Gd , and reducing the overall costs.

2 Methodology

Reactor calculation software is an essential tool for predicting the neutron flux and radiation field in nuclear reactors. These calculations are also important for understanding the production of radionuclides by neutron activation, which is a critical aspect of many applications in nuclear medicine, industrial processes, research, and even reactor management and safety.

Reactor calculation codes are mainly based on Monte Carlo methods, where neutrons are uncharged particles that interact with matter in a stochastic way. Simulations results can be very accurate and reliable if the user reproduces all the details of real scenario in the virtual world of simulation. The main purpose of software is to determine neutron fluxes as ‘input data’ to other calculation tools, e.g. for radionuclide activation calculations, decay and transmutation, and radiation shielding analysis.

2.1 Monte Carlo simulation for radiation transport

Currently, the most efficient method to simulate radiation transport in media through complex (many volumes or “cells”, several radioactive sources, and different materials) and large (few centimetres to hundreds of meters) geometries is the Monte Carlo simulation. This approach involves running a lot of ‘histories’ of the particle of interest in order to reproduce all the possible paths travelled by the radiation, into a virtual world. The process is realized by means of random samplings from all the probability density functions ruling physical phenomena. Very complex geometries can be built, and very accurate results can be achieved if all the elements, that are important to the transport of the analysed radiation, are described into the model. Moreover, an adequate computational power should be available for running a statistically significant number of histories. For this work, the MCNPX (Monte Carlo N-Particle eXtended) code has been used, in its version MCNPX 2.5.0 [3].

Simulations have exploited the usage of multi-processing on CRESCO High Parallel Computing Resources extensively. The computing resources and the related technical support used for this work have been provided by CRESCO/ENEAGRID High Performance Computing infrastructure and its staff [4].

CRESCO/ENEAGRID High Performance Computing infrastructure is funded by ENEA, the Italian National Agency for New Technologies, Energy and Sustainable Economic Development and by Italian and European research programmes, see <http://www.cresco.enea.it/english> for information. In particular, the whole Monte Carlo work has requested 60000 hours per core.

2.2 The MCNP TRIGA RC-1 calculation to neutron flux at the Central Thimble

The ENEA TRIGA RC-1 MCNPX model is based on detailed material composition retrieved from plant documentation and schemes [5].

The MCNP input available at the ENEA Research Nuclear Reactor Laboratory can be used for reactor calculations to determine neutron fluxes at specific points of interest. The Central Thimble, being the most intense point for neutron activation, is the focus in the current document of the provided MCNP results. The Central Thimble is expected to use an irradiation capsule whose volume available for sample hosting is a cylinder of 3.6 cm in diameter and 18 cm in height. To account for the vertical variation of the neutron flux versus core height, the irradiation volume is divided for calculation into 9 sub-volumes, 2 cm in height each. Figure 1 shows the MCNP representation of the reactor core, alongside a sketch of the irradiation volume partitioned in 9 sub-volumes labelled from f204 to f294 (the f204 sub-volume is the innermost position). Figure 2 shows the neutron spectra of the sub-volumes at the Central Thimble versus irradiation volume height.

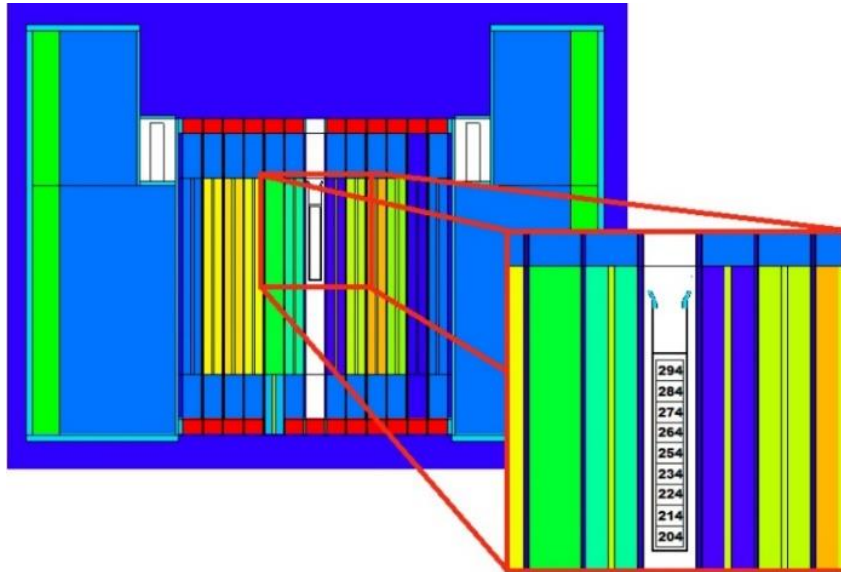


Fig.1 ENEA TRIGA RC-1 in MCNP: section of the reactor core and particular of the Central Thimble irradiation position.

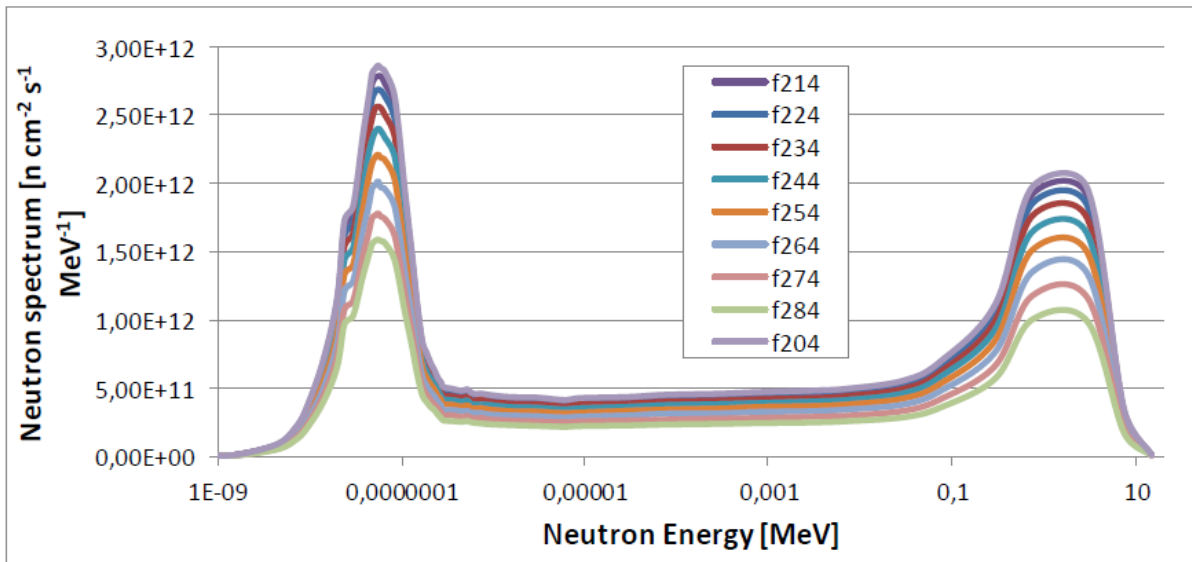


Fig.2 Neutron Spectra at ENEA TRIGA RC-1 Central Thimble vs. irradiation volume height.

Once the neutron flux is determined, it can be compared to the results obtained from the experimental characterization of the neutron flux at the Central Thimble (i.e. the point with the maximum magnitude neutron spectrum available) using neutron activation analyses according to ASTM E626-08/E626-97 procedures and applying spectral unfolding algorithms as described in Chiesa et al. [6].

The following Figure 3 shows the neutron spectra at the Central Thimble center-point calculated using the methodology of reference [6], ASTM E626 methodology with a fission spectrum added, and the MCNP code result. It can be seen that the results obtained using the three methods agree with each other.

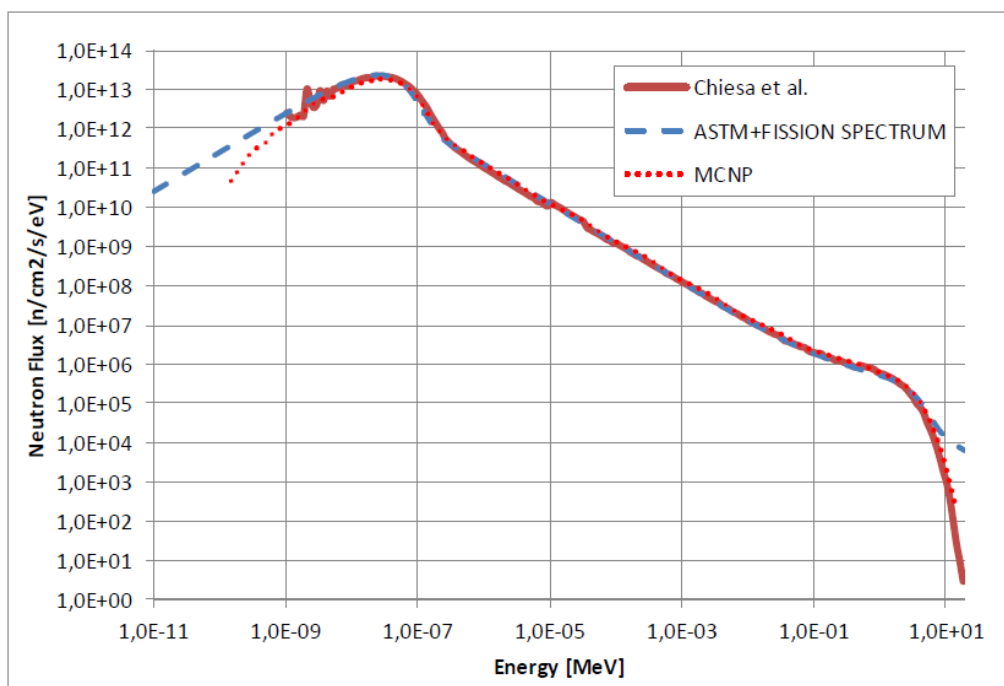


Fig.3 Neutron Spectra at ENEA TRIGA RC-1 Central Thimble center-point calculated with the Chiesa et al. methods [6], the ASTM E626 with fission spectrum added, and with MCNP code for a power of 100 kW.

2.3 Irradiation Calculation at the Central Thimble

The prior determination of the neutron flux is fundamental to initiate activation calculations with other codes also, e.g. with the FISPACT-II Code that allows automated calculations for activation channels that are possible for the irradiated target.

In this work the calculation was performed using 1 g of Gd_2O_3 (Gd enriched at 98.2% in ^{160}Gd). The sample is assumed to be exposed to the maximum reactor power, 1 MW, with the maximum magnitude neutron spectrum available at the ENEA TRIGA RC-1 reactor i.e. inside the Central Thimble with a neutron flux density of $5 \cdot 10^{13} \text{ cm}^{-2} \cdot \text{s}^{-1}$.

From a technical point of view, the reaction channel $^{160}Gd(n,\gamma)^{161}Tb$ has not a particularly favourable microscopic cross section value. It would be more efficient to irradiate a given amount of ^{160}Gd raw material in a high flux neutron source with respect to low magnitude neutron flux facilities, such as a TRIGA reactor. In addition, the irradiation time should be selected to be at least 1÷2 times the half-life of ^{161}Tb , i.e. 7÷14 days. With a given mass of raw material, the saturation activity (the maximum reachable activity) would be reached almost after 21 days continuous irradiation. Achieving such a long period of irradiation is not possible at the ENEA TRIGA RC-1 for two reasons: a) the reactor core may not have enough positive reactivity to sustain this kind of irradiation cycle, and b) there are constraints in the irradiation time (maximum 6 hours per day) leading to an underutilization of the raw material.

The expected irradiation schedule, considering the previous mentioned limits, involves the placement of the sample at the Central Thimble position for 12 days, with 6 hours of irradiation per day, excluding Saturdays and Sundays. In total, the sample will be irradiated for 72 hours.

This irradiation condition allows to reach a final activity of about 6.8 GBq of ^{161}Tb in the irradiated sample.

3 Results and Conclusions

In recent years, there has been an increase of interest in emerging short-lived radionuclides with potential use in human cancer therapy or medical imaging. This growing interest has prompted the scientific community to study the characteristics of these radionuclides, and explore different production methods, including traditional routes. Nowadays, diversification in production methodologies is necessary to ensure the continue and stable supply of radiopharmaceuticals in healthcare facilities, and to prevent any interruptions in providing suitable therapeutic plans to patients.

The use of radionuclides for medical purposes traditionally involves their production inside power reactor plants, but even research reactors and accelerator facilities can also contribute in supplying such radionuclides, and potentially address current shortages in supply chains due to temporary or permanent shutdowns of power reactors.

For this reason, in the framework of the EU-funded SECURE Project (Strengthening European Chain of sUpplY for next generation medical RadionuclidEs), the production capabilities for ^{161}Tb at the ENEA TRIGA RC-1 research reactor have been investigated.

From the calculations made, it emerges that it is possible to obtain an activity of 6.8 GBq of ^{161}Tb starting from 1 gram of Gd_2O_3 , enriched at 98.2% in ^{160}Gd , with 72 hours of irradiation time inside the Central Thimble, the maximum neutron flux irradiation position.

Since ^{161}Tb is a radionuclide still in experimental phase for medical applications, in order to quantify the activity necessary for a therapy, we can refer to therapies carried out with ^{177}Lu (a radionuclide with similar chemical and physical characteristics). A typical therapy with ^{177}Lu consists in 6 injections of 7 GBq each (at 6-week distance).

It should be emphasized that the capsule can be filled with approximately 400 grams of raw material. Therefore, in this way and with this condition, it is possible to conclude that a single irradiation cycle could theoretically serve about 200÷300 patients per month. This calculation takes into account one half-life decay time for ^{161}Tb after the target extraction; this time is necessary to perform chemical processing and separation to produce ^{161}Tb in a suitable radiopharmaceutical form.

References

- [1] N. Gracheva, C. Müller, Z. Talip e e. al., «Production and characterization of no-carrieradded ^{161}Tb as an alternative to the clinically-applied ^{177}Lu for radionuclidetherapy» *EJNMMI Radiopharmacy and Chemistry*, vol. 4, n. 12, 2019.
- [2] S. McNeil, M. Van de Voord, C. Zhang e e. al., «A simple and automated method for ^{161}Tb purification and ICP-MS analysis of ^{161}Tb » *EJNMMI Radiopharmacy and Chemistry*, vol. 7, n. 31, 2022.
- [3] J. F. Briesmeister, Ed., «MCNP: A General Monte Carlo N-Particle Transport Code,» 2000.
- [4] F. Iannone et al., «CRESCO ENEA HPC clusters: a working example of a multifabric GPFS Spectrum cale layout,» in 2019 International Conference on High Performance Computing Simulation (HPCS), 2019, pp. 1051–1052.
- [5] L. Falconi, N. Burgio, M. Palomba, E. Santoro e M. Carta, «A MCNPX TRIGA RC1 Experimental channels model for the design of a new neutronic diffraction facility» in *Proceedings of the Meeting Research Reactors Fuel Management*, Berlin, 2016.
- [6] D. Chiesa, M. Carta, V. Fabrizio, L. Falconi, A. Grossi e M. Nastasi, «Characterization of TRIGA RC-1 neutron irradiation facilities for radiation damage testing» *The European Physical Journal Plus*, vol. 135, n. 349, 2020.

ACCURATE CALCULATIONS OF THE EXCHANGE INTERACTIONS IN MOLECULAR QUBITS AND ORGANIC RADICALS IN THE BULK PHASE AND IN THE PRESENCE OF AN ELECTRIC FIELD

Federico Totti^{1,2*}, Prem Prakash Sahu¹, and Maksim Arsentev¹

¹*Università degli Studi di Firenze, "U. Schiff" Chemistry Department, Via della Lastruccia 3-13, 50019 Sesto Fiorentino (Italy)*

ABSTRACT. The aim of the project is to establish computational protocols that enable accurate computations of magnetic exchange interactions within potential qubit systems, encompassing both gaseous and condensed states- bulk and hybrid. At the same time, the project has been devoted to study the magneto-electric effect starting from simple organic radicals.

1 Introduction

It was found previously that the application of external factors, such as, for example, an external electric field, makes it possible to overcome several functional limitations inherent to materials. The brightest example, this applies to cases where an electric field can open the band gap and reduce the effective mass of an electron and a hole for heterojunctions in graphene and other two-dimensional carbonitride materials[1] for creating 2D channels in high-performance field-effect transistors (FETs), allows to tune band gap in transition metal dichalcogenides, black phosphorus, etc.[2, 3, 4, 5, 6]. Among them, electrostatically tunable bandgap bilayer graphene still has the advantage in front of the device in terms of mobility due to the lower effective mass ($m_{BLG} = \sim 0.037$ [7], $m_{BP} = 0.13$ [8] and $m_{MoS_2} = \sim 0.37$ [9]). Using first-principle calculations and experiments, H. Abbasian[10] studied the effect of local electric fields of opposite directions on the graphene sheets on electronic structure. The self-assembling molecular network (SAN) overlays induce local electric fields in opposite directions on the graphene sheets. The research showed such electric field and combined with gating, can produce a band gap of 254 and 263 meV, with the Fermi levels situated in the middle of these gaps. Moreover, the linearly dispersing bands of graphene remain unchanged in a specific energy range near the Dirac point. Another example is single-molecule magnets (SMM), which possess the potential for various applications in nanotechnology. These include the development of high-density information storage devices. The SMMs must have high anisotropy barrier (U_{eff}) for reversal of magnetization with a significant blocking temperature (T_B), coercivity and ambient stability(11). The key to achieving this lies in improving the barrier height for magnetization reversal (U_{eff}).

Over the past decade, molecular magnets have also carved out some space in the quantum computing field. Indeed, transition metal complexes have become increasingly popular candidates for electron spin-based quantum bits (qubits) due to their synthetic tunability and long achievable coherence times. To thrive in quantum technologies such as computing, sensing, and communication, overcoming decoherence challenges and obtaining multi-qubit architectures suitable as quantum logical gates is pivotal. Recent research on molecular materials for quantum information processing unveiled two promising candidates, that demonstrate prowess in encoding single-qubit and multi-qubit logical operations driven by magnetic exchange interactions: (i) a sulfur-rich [Cu(dttt)₂] system, [(dttt)⁻ = 1,3,2-dithiazole-4-thione-5-thiolate] exhibiting van der Waals-mediated strong antiferromagnetic exchange interactions, reaching an impressive value of 108 cm⁻¹ [12] and

(ii) a ferromagnetic exchange coupling of $J = -8 \times 10^{-3} \text{ cm}^{-1}$ was observed in a heteronuclear $\text{V}^{\text{IV}}\text{O}-\text{Cu}^{\text{II}}$ porphyrin-based complex $[\text{VOCu}(\text{TrPP})_2]$ (TrPP^- = triphenyl porphyrinate) respectively [13].

The aim of the project is to establish computational protocols that enable accurate computations of magnetic exchange interactions encompassing both gaseous and condensed states- bulk and hybrid for the two challenging systems $[\text{Cu}(\text{dttt})_2]$ and $[\text{VOCu}(\text{TrPP})_2]$. At the same time, the project has been devoted to study the magneto-electric effect starting from the simple organic chiral nitronyl-nitroxide radical $\text{C}_{13}\text{H}_{15}\text{N}_4\text{O}_6$ (chiral space group $P4_1$) [14].

2.Results

2.1 $[\text{VOCu}(\text{TrPP})_2]$

In this complex, a distinctive ferromagnetic exchange coupling with a J value of $J = -8 \times 10^{-3} \text{ cm}^{-1}$ was observed, which was also corroborated with the DFT gas-phase calculations. When contemplating the intricacies of packing and intermolecular interactions, it becomes imperative to integrate fundamental periodic boundary conditions. These conditions play a crucial role in obtaining precise calculated values for magnetic exchange interactions, particularly in instances where molecular density functional theory (DFT) calculations prove to be insufficient. To achieve our objective, we utilized the Quantum Espresso v7.2 software package [15], employing the plane-wave (PW) pseudopotential method integrated within it with revPBE functional. Our objective is to enhance the precision of the J value through the correction of intrinsic delocalization in Density Functional Theory (DFT). This correction involves the integration of the Hubbard correction, denoted as DFT + U, which is computed using Linear Response Theory. The U values were determined for V(IV), Cu(II), and the O-atom bonded to V(IV). The resulting computed values for V, Cu, and O atoms are 4.96, 7.37, and 7.84, respectively. Once achieved the relaxed structure by incorporating the U parameters, the Broken-Symmetry Density Functional Theory (DFT) technique was used to compute the magnetic exchange interactions. This step aims to gauge the alignment between our computed value and the one documented in experimental observations. Playing with convergence parameters our efforts have led to significant progress. Initially, we obtained a J value of -0.84 cm^{-1} per $\text{V}^{\text{IV}}\text{O}-\text{Cu}^{\text{II}}$ pair for cutoffs of 90 Ry and 900 Ry. This value was refined to $J = 0.41 \text{ cm}^{-1}$ for 150 Ry and 1800 Ry, and it remained constant even when increasing the cutoffs to 200 Ry and 2400 Ry, and further to 300 Ry and 3600 Ry.

2.2 $[\text{Cu}(\text{dttt})_2]$

The system has an interesting hydrogen-free environment, demonstrating strong antiferromagnetic exchange interactions mediated by van der Waals, with an astounding value of 108 cm^{-1} . In the investigation, gas-phase DFT simulations also indicated a value of 81.8 cm^{-1} . Commencing our computations with a high-quality crystal structure in this investigation was fortunate, eliminating the necessity for extensive geometry relaxation. The bulk phase, characterized by a framework composed of four distinct Cu-atoms, was employed. To initiate the computational process, we began by determining the Hubbard U parameters for the current system. This involved conducting single-point calculations using the HP package within Quantum Espresso[16]. The resulting values were identified as 9.33 for Cu-atoms and 2.94 for S-atoms. By implementing the DFT+U correction with respective U values, we embarked on Broken-Symmetry DFT calculations in the bulk phase. Our investigation unveiled magnetic interactions, yielding $J_1 = 9.22 \text{ cm}^{-1}$, $J_2 = 14.56 \text{ cm}^{-1}$, and $J_3 = 80.73 \text{ cm}^{-1}$, pretty much in alignment with earlier reported results.

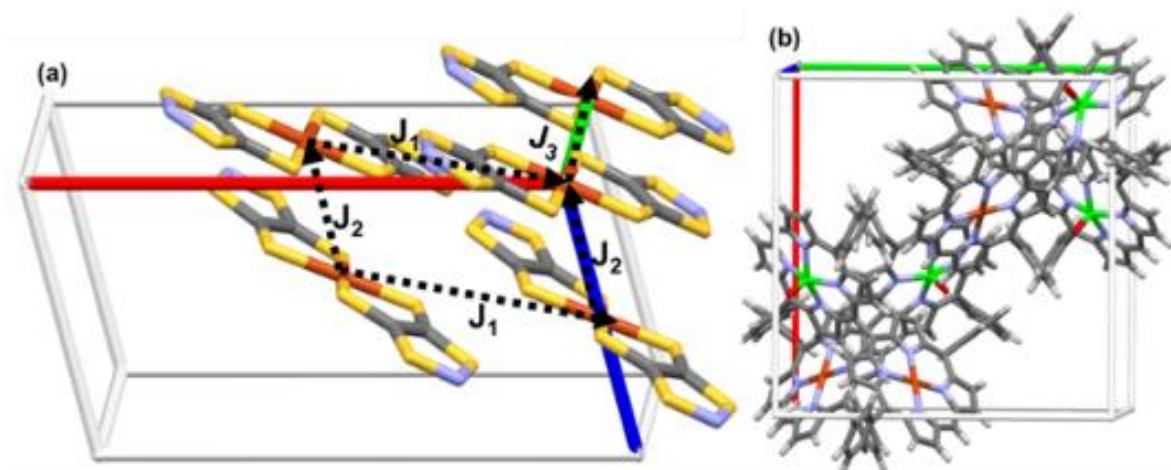


Fig.1: (a) Magnetic exchange pathways of relevance in [Cu(dttt)₂] system;
(b) Primitive cell of the bulk [VOCu(TrPP)₂] system.

2.3 3, 5-dinitrophenyl derivative of nitronyl nitroxide radical

The Plane-Wave Self-Consistent Field (PWSCF) code in the Quantum Espresso package [15] and the rVV10 dispersion correction along with revPBE functional were employed. We calculated the average value J by using the Broken Symmetry for single unit cell, 12.299 K, in perfect agreement with experimental one of 12.3 K [14] while for the slab chosen along z for three unit cells, 12.023 K. The experimental value interchain interaction between spirals was calculated on the basis of data from work of Shiomi *et al.* [14]: the computed value is 0.207 K. A similar value obtained by using the Broken Symmetry Formalism allowed us to obtain 0.269 K, which is also in perfect agreement. However, such a value is distributed extremely unevenly: 9.718 K for the left outermost layer and 13.489 K for the right. The value in the middle of the slab is 11.844 K. The magnetoelectric effect on the J values takes place but is very weak (on the third digits). For most spin configurations the application of the electric field along z decreases the J values.

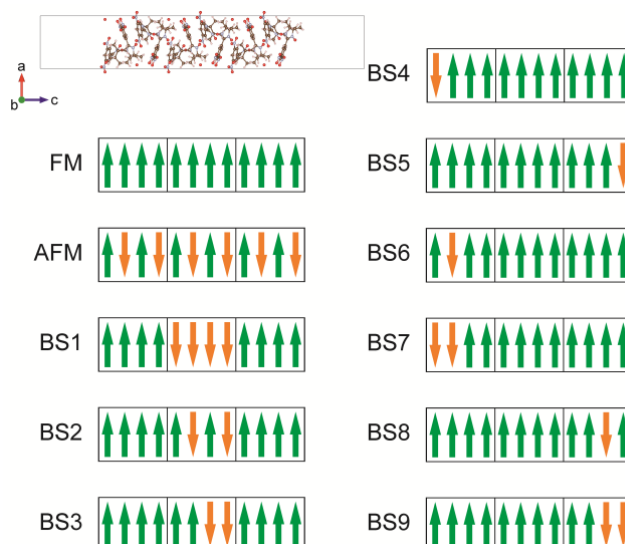


Fig.1: 456-atom 1×1×3 slab of **1R** and the corresponding spin configurations used for the calculation of magnetic exchange coupling constants J within the Broken Symmetry Formalism.

Acknowledgments

This work was supported by the European Union through the Next Generation EU funds through the Italian MUR National Recovery and Resilience Plan, Mission 4 Component 2 – Investment 1.4 – National Center for HPC, Big Data and Quantum Computing – CUP B83C22002830001. The support of MUR through Progetto Dipartimenti di Eccellenza 2018–2022 (CUP B96C1700020008) and 2023–2027 (CUP B97G22000740001 – DICUS 2.0). The computing resources and the related technical support used for this work have been provided by CRESCO ENEAGRID High Performance Computing infrastructure and its staff [15].

References

- [1] X. Cao X, J. Shi, M. Zhang, X. Jiang, H. Zhong, P. Huang, et al. Band Gap Opening of Graphene by Forming Heterojunctions with the 2D Carbonitrides Nitrogenated Holey Graphene, g-C₃N₄, and g-CN: Electric Field Effect. *J. Phys. Chem. C* **120**, pp. 11299–11305, (2016).
- [2] B. Radisavljevic, A. Radenovic, J. Brivio, V. Giacometti, A. Kis. Single-layer MoS₂ transistors. *Nat. Nanotechnol.* **6** pp 147–50, (2011).
- [3] S.-L. Li, K. Wakabayashi, Y. Xu, S. Nakaharai, K. Komatsu, W.-W. Li, et al. Thickness-Dependent Interfacial Coulomb Scattering in Atomically Thin Field-Effect Transistors *Nano. Lett.* **13**, 3546–3552, (2013).
- [4] L. Li, Y. Yu, GJ. Ye, Q. Ge, X. Ou, H. Wu, et al. Black phosphorus field-effect transistors *Nat. Nanotechnol.* **9**, 372–377 (2014).
- [5] H. Liu, AT. Neal, Z. Zhu, Z. Luo, X. Xu, D. Tománek, et al. Phosphorene: An Unexplored 2D Semiconductor with a High Hole Mobility. *ACS Nano* **8**, 4033–4041, (2014).
- [6] W. Feng, W. Zheng, W. Cao, P. Hu, Back Gated Multilayer InSe Transistors with Enhanced Carrier Mobilities via the Suppression of Carrier Scattering from a Dielectric Interface. *Adv. Mater.* **26**, 6587–6593 (2014).
- [7] W. Zhu, V. Perebeinos, M. Freitag, P. Avouris. Carrier scattering, mobilities, and electrostatic potential in monolayer, bilayer, and trilayer graphene. *Phys. Rev. B* **80**, 235402 (2009).
- [8] T. Low, AS. Rodin, A. Carvalho, Y. Jiang, H. Wang, F. Xia, et al. Tunable optical properties of multilayer black phosphorus thin films. *Phys Rev B* **90**, 075434 (2014).
- [9] H. Peelaers, C.G. Van de Walle. Effects of strain on band structure and effective masses in MoS₂. *Phys Rev B* **86**, 241401 (2012).
- [10] H. Abbasian. Gap Opening in Graphene via Locally Introduced Electric Field. *Phys status solidi – Rapid Res. Lett.* **17**, 2200302 (2023).
- [11] S.K. Gupta, T. Rajeshkumar, G. Rajaraman, R. Murugavel. An air-stable Dy(III) single-ion magnet with high anisotropy barrier and blocking temperature. *Chem Sci* **7**, 5181–5191 (2016).
- [12] F. Santanni, M. Briganti, G. Serrano, E. Salvadori, A. Veneri, C. Batistoni, S. F. Russi, S. Menichetti, M. Mannini, M. Chiesa, L. Sorace, and Roberta Sessoli *JACS Au*, **2023**, 3, 1250–1262.
- [13] D. Ranieri, A. Privitera, F. Santanni, K. Urbanska, G.J. Strachan, B. Twamley, E. Salvadori, Y.-K. Liao, M. Chiesa, M.O. Senge, F. Totti, L. Sorace, R. Sessoli. *Angew. Chem., Int. Ed.* e202312936 (2023).
- [14] D. Shiomi, Y. Kanzaki, S. Okada, R. Arima, Y. Miyazaki, A. Inaba, et al. An Enantiopair of Organic Ferromagnet Crystals Based on Helical Molecular Packing of Achiral Organic Radicals. *J Phys. Chem. Lett.* **2**, 3036–3039 (2011).
- [15] Giannozzi P, Baroni S, Bonini N, Calandra M, Car R, Cavazzoni C, et al. QUANTUM ESPRESSO: a modular and open-source software project for quantum simulations of materials. *J. Phys. Cond. Matter* **21**, 395502 (2009).
- [16] F. Iannone, F. Ambrosino, G. Bracco, M. D. Rosa, A. Funel, G. Guarnieri, S. Migliori, F. Palombi, G. Ponti, G. Santomauro and P. Procacci, *2019 International Conference on High Performance Computing and Simulation* pp. 1051–1052 (2019)

ATOMISTIC SIMULATIONS OF QUANTUM DOTS AND OTHER NANOCRYSTALS

Juliette Zito¹, Iyyappa R. Panneerselvam¹, Roberta Pascazio¹, and Gabriele Saleh^{1*}

¹*Nanochemistry, Istituto Italiano di Tecnologia, Via Morego 30, 16163 Genova, Italy*

**Corresponding author. Email: gabriele.saleh@iit.it*

ABSTRACT. Here we report on the atomistic simulations performed on nanocrystals, mainly quantum dots. These simulations, performed on the cresco6 supercomputer, played a key role in complementing experimental information on the atomistic structure of quantum dots, on their optoelectronic properties, and on the effect of different ligands. We combined density functional theory, statistical thermodynamics, and classical molecular dynamics simulations.

1 Introduction

Nanocrystals (NCs) are solid aggregates of atoms possessing dimensions of less than 100 nm. Their (nano)dimensions make their physiochemical properties fundamentally different from their macrocrystals counterpart [1]. NCs made by semiconductor materials take the name of “quantum dots” (QDs). QDs can be produced in solution through colloidal synthesis, and they possess a wide range of peculiar optoelectronic properties [2]. Indeed, they are already used in the display industry [3] and their importance was recognized in the assignment of the 2023 Nobel prize [4]. In our research group, we perform simulations on QDs (and NCs in general), working in close collaboration with the experimentalists in our department. We aim to rationalize experimental findings, to uncover atomistic details not accessible from experimental techniques alone, and to derive models and empirical rules to design QDs with desired properties. We adopt a multitude of simulation techniques, from density functional theory (DFT) to molecular dynamics (MD) based on tailored force fields.

2 Studying the atomistic and electronic structures of quantum dots

DFT simulations can be adopted to obtain the electronic structure (band dispersion, density of states, charge density distribution) of QDs, that lies at the heart of their optoelectronic properties. Moreover, these simulations are necessary to complement experimental data to obtain the atomistic structure of complex QDs such as heterostructures.

2.1 AgBiSCl₂: a new quaternary chalcocalide

Chalcocalides are a new promising class of QDs that feature some of the excellent optoelectronic properties of the well-known metal halide perovskites while having a considerably greater stability. Chalcocalides still lag behind in terms of technologically relevant properties such as the photoluminescence efficiency. Therefore, discovering new chalcocalide QDs is a hot area of research. In this project, a quaternary chalcocalide, AgBiSCl₂ was synthesized in form of QDs using an innovative synthetic protocol. We calculated the band structure of this compound, as well as the charge density distribution of the valence and conduction bands [5]. The results indicated that the band gap was direct and that the valence band had a significant contribution from the *d* orbitals of Ag, besides from anions (S and Cl), as typical in ionic compounds. The simulations were performed with the Vienna ab initio software package (VASP[6]). We adopted a hybrid DFT functional, HSE06[7], computationally demanding but known to provide reliable results especially concerning the electronic structure. Spin-orbital coupling effects were also accounted for. Given the high computational requirements, the VASP run were carried out on cresco6 adopting 1296 cores (27 nodes).

2.2 CsPbBr₃/PbS Nanocrystal Heterostructures

Research has recently expanded in the direction of NCs heterostructures as heterodimer and core-shell geometries have been proven beneficial in terms of stability, bandgap tunability, and the emergence of new properties. In this project, our experimental colleagues reported the synthesis of NCs heterostructures composed of two well-known semiconductor domains, namely CsPbCl₃ and PbS.

Combined with microscopic analysis, DFT atomistic simulations unveiled a well-defined epitaxial interface between the perovskite and lead sulfide domains featuring a continuity of the Pb sublattice across the interface between the two domains: they share a common Pb²⁺ layer at the junction coordinated with Cl⁻ ions on one side and S²⁻ ions on the other side. Moreover, DFT calculations indicated a quasi-type-I band alignment at the heterojunction, with band-edge electrons fully localized in the PbS domain and holes that are instead localized in a region at the interface of the two domains, spanning both of them. These calculations are in accordance with the optical emission spectra of the heterostructures exhibiting PL in the near-infrared region (originating from PbS), but weak PL in the blue region (originating from CsPbCl₃), indicative of predominant carrier transfer from the CsPbCl₃ to the PbS domain upon photoexcitation.

The simulations were performed with the cp2k software [8] on cresco6, generally adopting 96 cores (2 nodes) for geometry optimization and 48 cores (1 node) for electronic structure calculations. The PBE exchange-correlation functional was adopted.[9] All core electrons were included in the pseudopotential, while the valence electrons were described with the DZVP basis set included in the cp2k package and with plane waves having an energy cutoff of 400 Ry.

3 Rationalizing and predicting the role of ligands in quantum dots

Atomistic simulations are employed to study the interaction between the inorganic core of the QDs and ligands, and the effect of the latter on the QDs properties. DFT is adopted to evaluate the ligands' binding energy, besides the electronic properties of QDs. Instead, the dynamic evolution of QD-ligands interactions is conveniently investigated through classical methodologies, as their low computational cost allows for the simulation of realistic models with the same sizes and shapes as in experiments, and long-time molecular dynamics simulations can be performed.

3.1 Exogenous Metal Cations in the Synthesis of CsPbBr₃ Nanocrystals and their Interplay with Tertiary Amines

The current synthetic methodologies of CsPbBr₃ halide perovskite NCs rely on over-stoichiometric amounts of Pb²⁺ precursors, resulting in the presence of unreacted lead ions at the end of the process. To understand the role of excess Pb²⁺ in CsPbBr₃, our experimental team replaced it with different exogenous metal cations (M) in their synthesis scheme of CsPbBr₃ NCs and investigated their effect on the synthesis products. These cations can be divided into two groups: Group 1 delivers monodisperse CsPbBr₃ cubes capped with oleate species (as in the case when Pb²⁺ is used in excess) and with photoluminescence quantum yield (PLQY) as high as 90% with some cations (for example, with M = In³⁺); Group 2 yields irregularly shaped CsPbBr₃ NCs with broad size distributions. In both cases, the addition of a tertiary ammonium cation (TA) during the synthesis, after the nucleation of the NCs, reshapes the NCs to monodisperse truncated cubes. Such NCs feature a mixed oleate/TA surface termination with PLQY values up to 90%.

To understand the binding effects of the different cations in CsPbBr₃, we conducted two main sets of DFT simulations to support the experimental findings. *(i)* We computed the binding energies of the various metal cations M and oleate species, modelled using shorter alkyl chain ligands, i.e., acetate ions. Importantly, the computed metal-carboxylate binding strengths are closely related to the classification of the cations based on their effect in the reaction mixture: Group 1 cations present higher affinities toward carboxylate ions while Group 2 cations consistently show lower affinities toward carboxylate ions. Mg²⁺ represents the only exception to this trend. *(ii)* We computed the binding energies of CsBr, tertiary ammonium-Br, and neutral tertiary amine at the surface of a CsPbBr₃ NC model, reported in **Fig. 1a** along with the associated binding sites are depicted in **Fig. 1b-d**. The neutral tertiary amine showed weak interaction (2.14 kcal/mol), suggesting it cannot change the NC shape. In contrast, the tertiary ammonium ion (TABr) had a binding energy of 33.54 kcal/mol, indicating efficient passivation and potential shape modulation of CsPbBr₃ NCs. The CsX ion pair binding

was energetically favored over TABr by about 20 kcal/mol, suggesting a two-step mechanism where TA cations etch outer layers before binding, in agreement with the size reduction observed with direct TABr treatment.

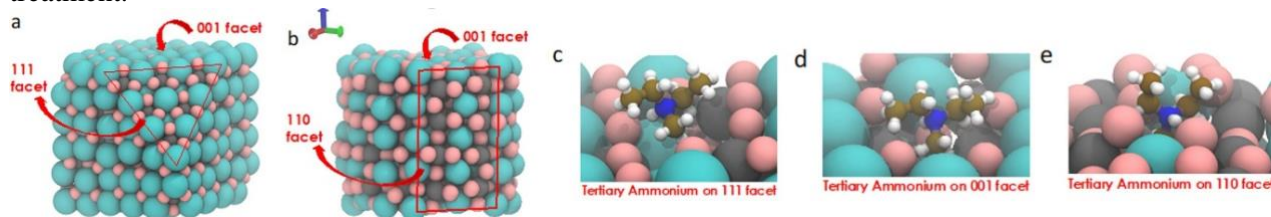


Fig. 1 (a, b) Ball representation of the CsPbBr₃ NC model. The Miller indices of the facets are highlighted. (c, d, e) Binding geometries of a tertiary ammonium on various facets.

We conducted atomistic simulations at the DFT level using the PBE exchange–correlation functional [9] and a DZVP basis set on all atoms, as implemented in CP2K 6.1.[8] All the simulations have been performed in vacuum. For this work, the simulations were run using a minimum of 48 cores and a maximum of 144 cores, depending on the system size.

3.2 Molecular dynamics simulations reveal how ligands determine the shape of InAs quantum dots

This project tackled the rationalization of the role played by different ligand precursors and their ratios in of the synthesis of III-V QD models, particularly colloidal InAs tetrapods, through the amino-As route.[10] A previous experimental systematic investigation suggested that various combinations of trioctylamine (TOA) and oleylamine (OA) provided good control over the size distribution, giving out tetrahedral InAs NCs, while a TOA:OA volume ratio of 4:1 produced InAs tetrapods. Further experimental characterizations suggested that the morphology of the tetrapods plays an important role in shaping their properties. We thus employed classical MD simulations to shed light on the role played by different TOA and OA volume ratios in the resulting structural features of the InAs QDs. In particular, we performed canonical (NVT) ensemble MD simulations at constant particle number N , volume V , temperature T (300 K) to locate Cl ions in the surface of a non-neutral, experimentally-realistic 4.0 nm InAs core, equilibrating the system. The NVT MD simulations employed a 0.5 fs integration timestep for a total of 2000 steps (100 ps). As for the simulations involving the different reaction conditions, NVT and isothermal-isobaric (NpT) equilibrations at constant particle number N , pressure p (1 atm), temperature T (473 K) were conducted for the TOA:OA mixtures at different ratios (for a total 1 ns NVT equilibration and ca. 50 ns per MD simulation on all OA:TOA ratios). Overall, these MD simulations indicated that TOA, given its steric hindrance and reduced basicity, binds weakly to the edges and corners of InAs NCs. Conversely, OA tends to strongly passivate (111) facets. The combined use of these ligands, particularly at higher TOA:OA ratios, promotes growth along the $\langle 111 \rangle$ directions, forming tetrapods. This work therefore suggests the use of ligand mixtures as a rational design strategy to produce larger NCs while maintaining control over their dimensions and distribution, altering the reaction kinetics and promote the formation of tetrapod-shaped QDs.

The classical MD simulations in this project were all conducted using the GROMACS 2021 package [11] using 48 cores (1 node). The temperature in the systems were equilibrated using the velocity-rescaling thermostat, while the pressures were equilibrated using an extended-ensemble Parrinello-Rahman approach. A smooth particle mesh Ewald method (SPME) using beta-Euler splines and a 1 nm short-range cut-off for was employed the computation of both the LJ and Coulombic terms of all MD simulations. The FF parameters for the InAs core and the Cl anions had been determined in a previous work,[12] while the ligand and solvent bonded and non-bonded FF parameters, as well as the charge parameters for their tails, were retrieved from the CHARMM207 FFs.

4 Nanostructures for hydrogen evolution reactions

The production of hydrogen from water electrolysis, is one of the most promising routes to free the society from its dependence on fossil fuels. However, given the high cost of the adopted catalysts, this route still lacks market competitiveness. In this work, a low-cost, highly efficient electrode made of ruthenium-copper nano-heterostructures deposited on TiO₂ was developed. We performed extensive DFT simulations to understand

the atomistic structure of the developed catalyst and the energetics of the various reaction steps leading to hydrogen formation from water [13]. Initially, many Ru-Cu structures were simulated, in order to understand what structures were most stable and were thus likely to form in the real sample. Subsequently, the energetics of the key reaction steps, namely the Volmer step and hydrogen desorption, were investigated for all possible reaction sites on the candidate surfaces. A mechanism for hydrogen evolution on our newly developed catalyst was thus derived based on the computational results. Geometry optimizations and binding energy calculations were performed through the VASP code[6], adopting the PBE functional [9]. The simulations were carried out mainly on cresco6, using a number of cores from 48 to 576, depending on the size of the system.

Acknowledgments

The projects reported here were funded by the programme MiSE-ENEA under the Grant “Italian Energy Materials Acceleration Platform – IEMAP”.

References

- [1] Kovalenko, M. V. *et al.* Prospects of nanoscience with nanocrystals. *ACS nano* 9, no. 2 (2015): 1012-1057.
- [2] Debasis, B., Qian, L., Tseng, T.K. and Holloway, P. H. Quantum dots and their multimodal applications: a review. *Materials* 3, no. 4 (2010): 2260-2345.
- [3] Steckel, J. The Impact of Colloidal QD Science and Technology on the Display Industry. *Information Display* 40.3 (2024): 11-12.
- [4] The Nobel Prize in Chemistry 2023: <https://www.nobelprize.org/prizes/chemistry/2023/summary/>
- [5] Quarta, D., Toso, S., ..., Saleh, G., *et al.* "Direct Band Gap Chalcohalide Semiconductors: Quaternary AgBiSCl₂ Nanocrystals." *Chemistry of Materials* 35, no. 23 (2023): 9900-9906.
- [6] Kresse, G., and Furthmüller, J. Efficient iterative schemes for ab initio total-energy calculations using a plane-wave basis set. *Physical review B* 54, no. 16 (1996): 11169.
- [7] Krukau, A. V. *et al.* Influence of the exchange screening parameter on the performance of screened hybrid functionals. *The Journal of chemical physics* 125, no. 22 (2006).
- [8] VandeVondele, J., & Hutter, J.. An efficient orbital transformation method for electronic structure calculations. *The Journal of chemical physics*, 118(10) (2003): 4365-4369.
- [9] Perdew, J. P., Burke, K., & Ernzerhof, M.. Generalized gradient approximation made simple. *Physical review letters*, 77(18) (1996): 3865.
- [10] Liu, Z., Pascazio, R. *et al.* Colloidal InAs Tetrapods: Impact of Surfactants on the Shape Control. *Journal of the American Chemical Society* 145.33 (2023): 18329-18339.
- [11] Hess, B., *et al.* GROMACS 4: algorithms for highly efficient, load-balanced, and scalable molecular simulation. *Journal of chemical theory and computation* 4.3 (2008): 435-447.
- [12] Dumbgen, K. C., Pascazio, R., *et al.* Classical Force Field Parameters for InP and InAs Quantum Dots with Various Surface Passivations. *The Journal of Physical Chemistry A*, 127, 15 (2023) 3427-3436.
- [13] Zuo, Y., Bellani, S., Saleh, G. *et al.* Ru–Cu Nanoheterostructures for Efficient Hydrogen Evolution Reaction in Alkaline Water Electrolyzers. *J. Am. Chem. Soc.*, 145, 39 (2023) 21419-21431.